

Comprehensive throughflow method for steam turbine development

Andrej Vasilj

Department of Engineering
University of Cambridge

This dissertation is submitted for the degree of
Doctor of Philosophy

Queens' College

March 2021

Declaration

I hereby declare that except where specific reference is made to the work of others, the contents of this dissertation are original and have not been submitted in whole or in part for consideration for any other degree or qualification in this, or any other university. This dissertation is my own work and contains nothing which is the outcome of work done in collaboration with others, except as specified in the text and Acknowledgements. This dissertation contains fewer than 65,000 words including appendices, bibliography, footnotes, tables, and equations and has fewer than 150 figures.

Andrej Vasilj
March 2021

Comprehensive throughflow method for steam turbine development

Andrej Vasilj

Wetness formation in condensing nozzle flow has been well researched and very good agreement has been achieved between theory and experimental measurements. However, condensation in steam turbines is much more complex and optical measurements show a much broader droplet spectrum than in nozzles and steady cascade expansions. The dominant theory explaining this behaviour is that large-scale fluctuations in static temperature (comparable to temperature drop in a turbine stage) are caused by unsteady blade wake segmentation by subsequent blade rows, also known as wake chopping, and have a substantial influence on the condensation process.

To better understand these phenomena, a widely used stochastic wake-chopping model is implemented within a well-established throughflow framework, examining the impact of wake chopping on generated droplet size spectra and thermodynamic relaxation losses. A comprehensive sensitivity study of the predicted droplet spectra to modelling parameters and inlet temperatures (changing the nucleation zone location) is performed to discern the effects of flow phenomena from modelling limitations.

To aid the understanding of how the broadening of droplet spectra affects other phenomena in turbines, a deposition model is implemented, combining inertial and turbulent diffusion contributions. The inertial deposition rate is determined by performing 3D droplet tracking through a representation of the steam flow field while turbulent deposition rate is based on empirical deposition measurements in vertical pipe flow, using a coarse estimate of friction velocity. While the choice of friction velocity model is likely to have a strong impact on the deposition rates, most studies use flat-plate boundary layer equations whose flow assumptions strongly deviate from the flow in turbine blade passages. Therefore, a deposition rate sensitivity study is performed, and a better friction velocity guess is obtained using high-fidelity numerical simulations. Additionally, the impact of wake chopping on deposition rates is studied.

The developed models are integrated within the throughflow framework in an iterative fashion, whereby pressure and efficiency trajectories are provided to the wake chopping model which returns improved droplet spectrum, wetness, and thermodynamic relaxation loss predictions to update the flow field. The model performance is validated against existing experimental measurements and published CFD results for a model four-stage, low-pressure steam turbine, over a broad range of operating conditions. These show impressive agreement between measured and computed turbine performance, with wake chopping calculations capturing even the minute changes in flow parameters. Furthermore, computed droplet size spectra (converted to light extinction) agree remarkably well with light extinction measurements, suggesting that the developed model can be used as a predictive tool for turbine design.

Dedicated to my parents, Diana and Miro, and my sister Ana.

Acknowledgements

First and foremost, I would like to thank my supervisor, Dr. Alexander J. White for his guidance throughout this project. I would also like to extend my gratitude to my advisor, Dr. Graham Pullan, and the Cambridge (almost-) Isentropic team, in particular Dr. Sebastian Schuster, Dr. Jörg Starzmann, and Dr. David Redpath, whose friendship and experience helped me progress immensely. Thanks to Dr. Kane Chandler from General Electric for providing a valuable experimental dataset, thus enabling the validation efforts presented in this thesis. Special thanks and farewell to Dr. Brian Haller, a great supporter of wet-steam research, who, sadly, never saw the completion of this project.

I will always fondly remember the times at the Hopkinson Lab, in large part due to the fruitful discussions and relaxing coffee breaks with Max, Lee, Aaron, Savvas, Jenna, Nick, Shrey, Jocelino, and James.

I would also like to acknowledge the many friends I made during my stay in Cambridge, in particular, Johan, David, Audrey, Chelsea, Lin, Daniel, Charles, Kosta, Ankita, Luz, Matt, Margarita, Aracely, Le, Chris, Krishan, Aaron, Arian, and Henry. Queens' and 65 Panton St. will always remain a home-away-from-home.

A big thank you to Andrea for her love, care, and making the pandemic lockdown as enjoyable as possible; to Nikola for being the best friend one can hope for and the ultimate WoT platoon-mate; and to Dr. Uma, for being a great listener.

Special thanks to Ana for the long discussions about modelling, improving my knowledge of statistics, and for being there for me every step of the journey. Your support has been truly invaluable.

I am forever indebted to my family, Miro, Diana, and Ana, who have always and unreservedly supported me throughout my professional and personal growth. I owe this achievement to them.

This project was sponsored by the EPSRC and General Electric, to whom I am grateful.

Slap

Dobriša Cesarić (1902–1980)

Teče i teče, teče jedan slap;
Što u njem znači moja mala kap?

Gle, jedna duga u vodi se stvara,
I sja i dršće u hiljadu šara.

Taj san u slапu da bi mogo sjati,
I moja kaplja pomaže ga tkati.

Waterfall

Dobriša Cesarić (1902–1980)

A waterfall flows, and flows, and flows;
What does my little drop mean to it, who knows?

Look, a rainbow over the water flies,
And shimmers and trembles in thousands of dyes.

But for this dream in the water to shine,
It is also brought out by this droplet of mine.

Table of contents

List of figures	xv
List of tables	xvii
Nomenclature	xix
1 Introduction	1
1.1 Recent developments in the global energy market	1
1.2 Wetness effects in condensing steam turbines	3
1.3 Research aims	4
1.4 Structure of the Thesis	5
2 Literature review	7
2.1 Introduction	7
2.2 Nucleation and droplet growth	8
2.2.1 Nucleation	8
2.2.2 Droplet growth	11
2.2.3 Experimental measurements and validation	13
2.3 Other drivers of condensation in turbines	15
2.3.1 Wake chopping	16
2.4 Deposition	20
2.4.1 Inertial deposition modelling	20
2.4.2 Turbulent deposition modelling	21
2.4.3 Deposition measurements	27
2.5 Wetness loss mechanisms in steam turbines	28
2.6 Summary	31
3 Unsteady wake segmentation	33
3.1 Introduction	33

3.2	Streamline equilibrium description of the flow field	33
3.2.1	Supersonic/transonic flow treatment	38
3.2.2	Strengths and limitations of the streamline equilibrium method	39
3.2.3	Real gas properties of steam	41
3.3	Condensation and droplet growth modelling	42
3.4	Unsteady wake segmentation modelling	46
3.4.1	Model integration with a flow solver	49
3.4.2	Random-walk wake-chopping model	51
3.4.3	Gaussian wake profile	52
3.5	Test case – repeating stage turbine design	56
3.5.1	Convergence	58
3.6	Sensitivity to modelling assumptions	58
3.6.1	Fixed expansion rate	58
3.6.2	1D expansion rate	61
3.6.3	2D expansion rate	64
3.6.4	Wetness and thermodynamic relaxation loss sensitivity	68
3.7	Conclusions	71
4	Droplet deposition modelling	73
4.1	Introduction	73
4.2	Inertial deposition	74
4.2.1	Coordinate system definition and coordinate transformations	76
4.2.2	Leading edge collection efficiency	79
4.2.3	Calculation procedure	80
4.2.4	Analysis of droplet trajectories	81
4.3	Turbulent deposition	84
4.4	CFD study of turbine blade skin friction coefficient	88
4.4.1	Non-equilibrium two-phase flow solver	89
4.4.2	White's cascade test case	91
4.4.3	Comparison with experimental measurements	92
4.4.4	Breakdown of factors influencing the skin friction coefficient (C_f) .	96
4.5	Impact of skin friction coefficient on droplet deposition	101
4.5.1	Influence of different models: Schlichting vs. CFD	102
4.5.2	Sensitivity to small variations in C_f	105
4.6	Importance of droplet spectrum accuracy	107
4.6.1	Effect of wake chopping and expansion rate variation	107
4.6.2	Effect of wake decay rate	108

4.6.3	Effect of wake width	111
4.6.4	Effect of wake asymmetry	112
4.7	Conclusions	114
5	Comparison with experiments	117
5.1	Introduction	117
5.2	Unified streamline equilibrium model	117
5.2.1	Convergence and comparison with other methods	118
5.3	Validation case: four-stage LP turbine	120
5.3.1	Experimental measurements	120
5.3.2	Numerical calculations	122
5.3.3	Inlet mass flow rate	123
5.3.4	Pressure probes	123
5.3.5	Turbine performance	128
5.3.6	Wetness and subcooling	134
5.3.7	Sauter mean diameter	136
5.3.8	Light extinction measurements	138
5.3.9	Nucleation zone migration between blade rows	142
5.4	Conclusions	145
6	Conclusions and future work	147
6.1	Conclusions	147
6.1.1	Summary	147
6.1.2	Unsteady wake segmentation	148
6.1.3	Droplet deposition	149
6.1.4	Comparison with turbine measurements	150
6.2	Future work	151
References		155
Appendix A	Scaling blade pressure curves based on blade loading	169
Appendix B	Wake functional form derivation	171
B.1	Linear function	171
B.2	Quadratic function	173
B.3	Step function	176
B.4	Summary of solved functions	177

Appendix C Drag coefficient expressions	179
Appendix D Correction for non-continuum gas effects	181
Appendix E Skin friction coefficient – CFD data	183
Appendix F Pressure probe comparison data	185

List of figures

1.1	Global energy outlook, reported in [74].	2
2.1	The Gibbs free energy of droplet formation and the critical droplet radii.	9
2.2	Langmuir's droplet growth model.	12
2.3	Droplet spectrum comparison between nozzles and turbines, shown in [186].	15
2.4	Illustration of unsteady wake segmentation by subsequent blade rows.	17
2.5	Pipe flow particle deposition measurements, shown in [181].	22
2.6	Impact of turbophoresis on different droplet sizes.	25
2.7	Wetness loss breakdown for a 1000 MW nuclear LP turbine, from [120].	31
3.1	Grid of streamlines and quasi-orthogonals on the meridional plane.	34
3.2	Coordinate systems of a fluid parcel in streamline equilibrium.	35
3.3	SLEQ code flow chart.	37
3.4	Axial velocity profile comparison, extracted from [33].	40
3.5	Schematic of polytropic efficiency assignment across the pitch.	47
3.6	ChopCode flow chart.	50
3.7	Schematic of wake representation across the pitch, $\bar{\eta} = 90\%$, $\sigma_w = 0.04$	53
3.8	Artificial blade wake profiles.	55
3.9	Pressure distributions in the repeating-stage model turbine.	57
3.10	Wake chopping convergence over a range of pathline calculations.	59
3.11	Wake shape influence assuming a fixed expansion rate and no wake decay.	60
3.12	Wilson zone length in a repeating stage turbine.	62
3.13	Droplet spectrum sensitivity to wake decay, assuming a 1D \dot{p} variation.	63
3.14	Droplet spectrum sensitivity to wake decay, assuming a 2D \dot{p} variation.	64
3.15	Impact of 1D and 2D \dot{p} variation on droplet size spectrum for a fixed wake decay rate.	65
3.16	Wake shape influence assuming 2D \dot{p} variation and wake decay.	66

3.17 Wake width influence assuming 2D \dot{p} variation, Gaussian wake profile, and wake decay.	67
3.18 Influence of wake asymmetry assuming 2D \dot{p} variation and wake decay.	68
3.19 Wake chopping impact on wetness and thermodynamic loss.	69
4.1 Base vector rotation in the cylindrical coordinate system.	77
4.2 Leading edge collection efficiency based on the droplet Stokes number.	80
4.3 Deposition code flow chart.	82
4.4 Pitchwise droplet trajectories for a range of droplet sizes.	83
4.5 Meridional trajectories for droplets of different sizes.	85
4.6 Turbulent deposition curve, extracted from [174].	86
4.7 Blade geometry and computational domain.	92
4.8 Block structured finite-volume mesh (fine resolution).	93
4.9 Mesh structure details	94
4.10 H2 steam cascade case.	95
4.11 L2 steam cascade case.	96
4.12 Definition of suction and pressure side surfaces.	97
4.13 Skin friction coefficient distribution along the blade.	97
4.14 Streamwise pressure gradient and skin friction coefficient along the blade pressure side.	98
4.15 Streamwise pressure gradient and skin friction coefficient along the blade suction side.	99
4.16 Difference in C_f between flat plate equations and CFD results.	100
4.17 Effect of flow incidence angle on skin friction coefficient.	101
4.18 Droplet size spectrum and estimated C_f at the last stage stator inlet.	102
4.19 Fractional deposition rate in the last stage stator.	103
4.20 Change in τ_{d+} based on the used $C_f(\text{Re})$ function.	104
4.21 Deposited liquid mass fraction for different C_f models.	105
4.22 Total deposition variation.	106
4.23 Change in total deposition rates with C_f variation.	106
4.24 Effect of wake chopping and pressure variation on deposition rates – part 1.	109
4.25 Effect of wake chopping and pressure variation on deposition rates – part 2.	110
4.26 Impact of wake decay rate on total deposition rates(2D \dot{p} variation case)	111
4.27 Impact of wake width on total deposition.	112
4.28 Impact of wake asymmetry ratio on total deposition.	113
5.1 Convergence of sleqWake calculations	119

5.2	Experimental rig schematic, adapted from [22].	121
5.3	Throughflow calculation computational grid.	122
5.4	Measured and calculated inlet mass flow rates for a range of θ_{01}	124
5.5	Pressure variation with θ_{01} , upstream of the penultimate stage.	126
5.6	Pressure variation with θ_{01} , between the penultimate stage stator and rotor. .	127
5.7	Pressure variation with θ_{01} , downstream of the penultimate stage	129
5.8	Comparison of wake chopping results to measured total-to-static efficiency and CFD wetness loss prediction.	131
5.9	Wake chopping, measured, and CFD specific work output.	133
5.10	Wake chopping, measured, and CFD wetness and subcooling	135
5.11	Wake chopping and CFD Sauter mean diameter.	137
5.12	Wake chopping and measured light extinction upstream and downstream of the penultimate stage.	140
5.13	Mie extinction coefficients for a range of droplet size parameters.	142
5.14	Upstream migration of the condensation zone when decreasing θ_{01}	143
F.1	Static pressure at the casing on planes 31, 32, and 41.	186
F.2	Static pressure at the hub and casing on plane 42.	186
F.3	Static pressure at the hub and casing on plane 51.	187
F.4	Static pressure at the hub and casing on plane 52.	187
F.5	Static pressure at the hub and casing on plane 61.	188
F.6	Static pressure at the hub and casing on plane 62.	188
F.7	Casing static pressure variation with θ_{01} on planes 31 to 42.	189
F.8	Casing static pressure variation with θ_{01} on planes 51 to 62.	190
F.9	Hub static pressure variation with θ_{01} on planes 42 to 61.	191

List of tables

3.1	ChopCode input data	51
3.2	Wake shape definitions	54
4.1	Boundary conditions	93
4.2	Fraction of deposited liquid mass for a range of wake decay rates.	111
4.3	Fraction of deposited liquid mass for a range of wake widths.	112
4.4	Fraction of deposited liquid mass for a range of wake asymmetry ratios. . .	113
E.1	Reynolds number variation	184
E.2	Incidence angle variation	184

Nomenclature

Roman Symbols

a	Acceleration vector
<i>b</i>	Local blade thickness parameter
<i>c</i>	Blade chord length
C_C	Cunningham correction factor for non-continuum gas effects
C_D	Drag coefficient
c_p	Specific heat capacity at constant pressure
d_{LE}	Axial unit-vector
<i>E</i>	Light extinction coefficient
\mathbf{e}_θ	Circumferential unit-vector
\mathbf{e}_r	Radial unit-vector
\mathbf{e}_z	Axial unit-vector
<i>F</i>	Gibbs free energy
<i>f</i>	Specific Gibbs free energy
\mathbf{F}_D	Resulting external force on a droplet
F_{LE}	Fraction of droplets deposited on a blade leading edge
F_q	Blade force in the <i>q</i> direction
<i>g</i>	Turbidity

G_d	Mass flow rate of particles to the wall per unit wall area (deposition rate)
G_{d+}	Non-dimensional deposition rate per unit wall area
h	Enthalpy
h_0	Stagnation enthalpy
h_{lg}	Condensation/vapourisation latent heat
I	Rothalpy // Streamline index
I_λ	Incident intensity of monochromatic light of wavelength λ
$I_{0\lambda}$	Incident intensity of monochromatic light of wavelength λ in a dry case (no droplets)
J	Steady nucleation rate // Quasi-orthogonal index
k	Boltzmann's constant
k_g	Thermal conductivity of vapour
Kn	Knudsen number
l	Distance travelled by the light beam
M	Mach number
m	Meridional axis
\dot{m}	Mass flow rate
m_i	Liquid mass in the size group i
m_m	Molecular mass of water
M_{rel}	Relative Mach number
N	Number of discrete droplet size groups
n_i	Number of droplets in the size group i
N_v	Number of droplets per unit volume
O	Blade opening
\mathbf{P}	Reference plane from which angles in cylindrical coordinates are determined

p	Reference vector, orthogonal to the axial coordinate z
P	Blade pitch
p	Pressure
Pr	Prandtl number
P_{wet}	Power lost due to the thermodynamic wetness loss
q	Quasi-orthogonal line direction
q_c	Condensation coefficient
R	Specific gas constant
r	Droplet radius // Local streamsurface radius
r_c	Radius of curvature
r_*	Critical droplet radius
S	Supersaturation ratio
s	Specific entropy
s_t	Streamwise direction
s_{th}	Specific entropy increases due to the heat transfer between droplets and steam
T	Thermodynamic temperature
t	Time
U	Uniform distribution
u_*	Friction velocity
\mathbf{v}	Velocity vector
V	Volume
v	Velocity // Specific volume
w	Relative velocity
y_i	Wetness fraction of the size group i

Greek Symbols

α	Heat transfer coefficient // Angle between the QO and the streamsurface
α_g	Coefficient of steam expansion at constant pressure
α_{ht}	Heat transfer coefficient
α_i	Surface heat transfer coefficient for droplet group i
α_s	Dimensionless droplet size parameter
β_{TE}	Blade outlet angle
σ_w	Wake width
Δ	Increment
ΔT	Vapour subcooling
Δt_{ls}	Residence time of a fluid parcel in the last stage stator
$\Delta \mathbf{v}$	Velocity slip vector
η	Polytropic efficiency
$\bar{\eta}$	Circumferentially and time averaged polytropic efficiency
η_c	Droplet collection efficiency
η_{TS}	Total-to-static efficiency
κ	Heat capacity ratio
λ	Wavelength
λ_g	Mean free path of a vapour molecule
μ	Dynamic viscosity
ν	Kinematic viscosity
ν_y	Young's correction factor
Ω	Angular velocity of the shaft
ϕ	Meridional pitch angle

Φ_D	Correction function for particle drag force
ϕ_K	Kantrowitz' non-isothermal correction factor
ψ	Non-dimensional mass flow function
ρ	Density
σ	Specific surface free energy (surface tension)
τ_{d+}	Non-dimensional particle relaxation time
τ_f	Time scale associated with the flow
τ_s	Wall shear stress
τ_w	Wake decay time constant
θ	Temperature in degrees Celsius
ξ	Blade row loss
ξ_{wet}	Thermodynamic wetness loss

Superscripts

*	Sonic conditions
---	------------------

Subscripts

01	Total value at the inlet (e.g., inlet total temperature)
D	Drag
eq	Equilibrium conditions
g	Gas phase (vapour)
i	i -th droplet size group
$i.$	Isothermal
in	Inlet conditions
is	Isentropic
l	Liquid phase (water)

<i>LE</i>	Leading edge
<i>m</i>	Meridional component
<i>n.i.</i>	Non-isothermal
<i>r</i>	Radial component
<i>s</i>	Saturation conditions
<i>s_{aero}</i>	Aerodynamic entropy
<i>θ</i>	Circumferential component
<i>v</i>	Per unit volume
<i>w</i>	Blade wake
<i>z</i>	Axial component

Acronyms / Abbreviations

1D	One dimensional
2D	Two dimensional
3D	Three dimensional
<i>A</i>	Mesh aspect ratio
CFL	Courant-Friedrich-Levy number
DNS	Direct numerical simulations
E	East neighbouring point
\mathbb{E}	Expected value
HP	High pressure
i.i.d.	Independent and identically distributed (random variable)
<i>IND</i>	Role of the quasi-orthogonal (LE/TE/Duct/Blade passage)
LE	Blade leading edge
LES	Large eddy simulations

LP Low pressure

MFP Mean free path of molecules

N North neighbouring point

CPU Central processing unit

P Current point

QO Quasi-orthogonal line

RANS Reynolds-averaged Navier Stokes

S1 Blade-to-blade calculation

S2 Hub-to-tip calculation

SLEQ Streamline Equilibrium flow solver

S South neighbouring point

TE Blade trailing edge

Var Variance

W West neighbouring point

Chapter 1

Introduction

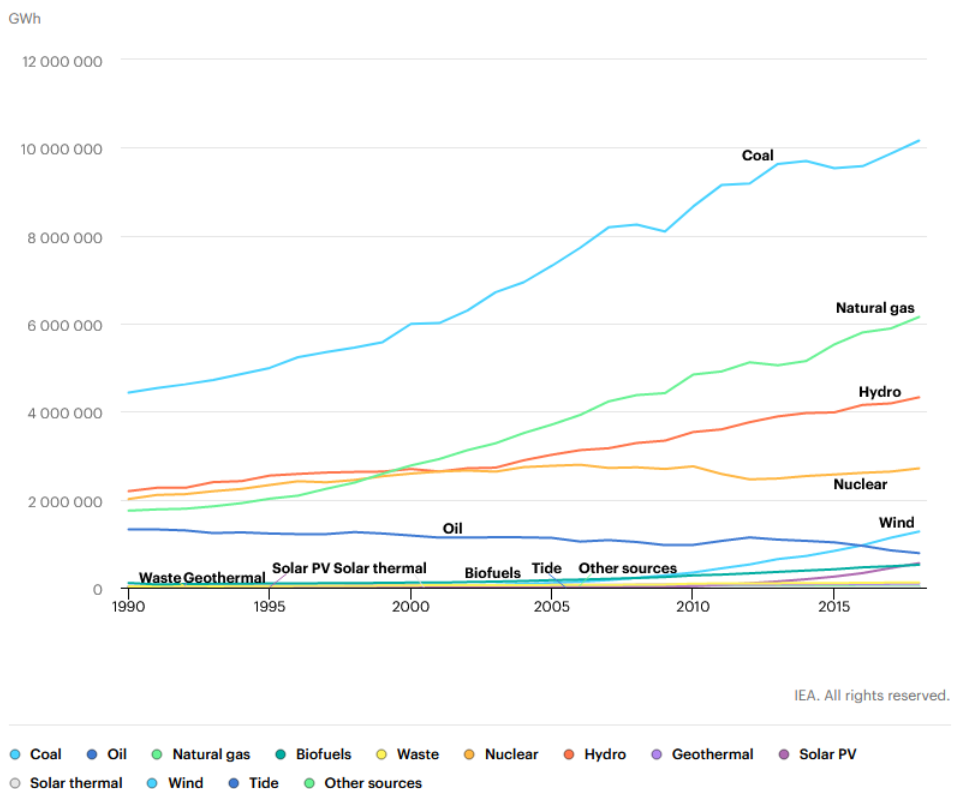
1.1 Recent developments in the global energy market

Back in 2004, the international energy agency (IEA) predicted that global energy demand would reach approximately 23 TW by 2025, indicating an ever-growing world-wide demand. This number was, however, already surpassed in 2013 as the globally improving living standard and technological aspirations of developing countries have been driving the energy requirements. As shown in fig. 1.1a, the global energy grid still largely relies on fossil fuel to keep up with the demand, with coal contributing almost twice as much as the second-placed natural gas. Renewable sources, while rapidly increasing in capacity, still contribute only a small proportion on the global scale.

Naturally, the increase in electricity demands is in clear conflict with the emission goals placed to tackle climate change. The focus of the Paris climate agreement [76], signed in 2016 by 196 states, is to limit global warming by well below 2 °C compared to the pre-industrial era by achieving the global peaking of greenhouse gas emissions as soon as possible. This is supposed to be followed up by a goal of reaching climate-neutrality by the mid-century. Although the data post-Paris agreement shows a slower rise in CO₂ emissions (see fig. 1.1b) due to a decrease in carbon intensity of energy generation, there is still no consensus that the peak has been reached.

Steam turbine cycles play a large role in achieving this goal, as they generate around 48% of electricity and more than 32% of combined heat and power in the United States.¹ Their relevance is also increasing, as indicated by a 2021 report by GlobalData, a data analytics company. The aggregate value of the global steam turbine market is projected to rise to \$36.7bn between 2019 and 2023, fuelled by the increasing demand for uninterrupted

¹<https://www.energy.gov/sites/prod/files/2016/09/f33/CHP-Steam%20Turbine.pdf>



(a) Total global energy supply by source, in GWh, [75].

(b) Power sector CO₂ emissions in the Sustainable Development Scenario (SDS), in Gt, [74].

Fig. 1.1 Global energy outlook, reported by the International Energy Agency (IEA) [74, 75].

power in developing countries such as China and India, and growing co-generation and combined-cycle operations.²

Stemming from Charles Parson's turbine design in 1884, which produced 7.5 kW of electricity at 1.6% thermal efficiency, modern turbines and steam cycles have been continuously optimised, reaching up to 64% thermal efficiency in combined cycles.^{3,4} Continuous efficiency improvements, achieved by increasing the maximum cycle pressure, drive the steam expansion deeper into the wet steam region. However, the presence of a dispersed liquid phase was shown to adversely affect both turbine performance (loss increase in stages operating with wet steam) and lifespan of blades (erosion damage) [27]. This was addressed by limiting the low pressure (LP) turbine outlet wetness to 12%, which placed restrictions on further pressure increases. Further improvements (1950s) were made by adding a reheat cycle, whereby (high pressure) HP turbine outlet flow is reheated to peak temperature (thus reducing wetness downstream), and by introducing intermediate pressure (IP) turbines to the cycle. The addition of a second reheat cycle was considered, but the benefits were strongly outweighed by the costs. Nowadays, multiple stages in LP turbines operate with wet steam and, in nuclear plants, often the entire LP and parts of HP turbine operate with wet steam.

1.2 Wetness effects in condensing steam turbines

Phase change can happen in two ways. Individual molecules can attach to impurities (e.g., dust particles) or surrounding surfaces, and nucleate immediately upon steam crossing the saturation line, maintaining the flow at near-equilibrium. This process is often observed in our surroundings (e.g., rain formation) and is known as heterogeneous nucleation. The dominant method, however, is homogeneous nucleation, whereby steam crosses the saturation line into a meta-stable, supersaturated state, and becomes subcooled. The condensation occurs through the formation of small molecular clusters and the process increasingly becomes thermodynamically favourable with increase in steam subcooling. Latent heat release due to condensation brings the steam back to near-equilibrium conditions. While the condensation mechanisms in steady flow (e.g., nozzles and steady cascades) are well understood, optical measurements in operating condensing steam turbines show significantly broader, skewed droplet spectra, with a larger mean diameter, as well as large static temperature fluctuations at the turbine outlet, comparable in magnitude to a temperature drop in a blade row. Multiple explanatory theories have been proposed (nucleation in blade vortices [47], heterogeneous

²<https://store.globaldata.com/report/gdpe1061emr-steam-turbines-for-thermal-power-update-2019-global-market-size-average-price-equipment-market-share-and-key-country-analysis-to-2023/>

³<https://www.mhi.co.jp/technology/review/pdf/e581/e581070.pdf>

⁴<https://www.modernpowersystems.com/features/featuret-point-2-goes-commercial-8127325/>

nucleation [149], and unsteady blade row interaction [59]), and the majority of researchers agree that unsteady blade row interaction (also known as wake chopping) is the dominant effect. Wake chopping assumes that periodic segmentation of “hot” blade wakes (higher dissipation than the core of the flow) by the relative motion of subsequent blade rows creates the observed complex temperature fluctuations which postpone nucleation (very sensitive to local subcooling) and axially stretch the nucleation zone.

The wetness-related efficiency decrease is caused by multiple mechanisms [120]. The largest contributor is the thermodynamic relaxation loss generated by the irreversible heat transfer between the droplets at saturation temperature and the subcooled steam. Changes to the flow field (e.g., condensation shocks) increase aerodynamic losses, and the velocity slip between droplets and the surrounding steam (large density difference) induces kinematic relaxation loss. A portion of droplets acquiring velocity slip deposit on the nearby blade surfaces (difference in velocity triangles), thus causing breaking loss, and forming rivulets and liquid films on the blades. Liquid films are centrifuged towards the trailing edges (centrifuging loss), where they break down and form coarse water droplets – the primary source of erosion damage to downstream blade rows.

The complex interaction between the mentioned loss sources determines the total wetness loss and makes the prediction computationally expensive, even though individual mechanisms are considered to be well understood. Hence, simple empirical rules (e.g., the Baumann rule – each 1% wetness increase leads to a 1% increase in total energy loss) are still widely used. Considering that wetness loss can reach up to 5% of total energy output [143], the ability to systematically analyse wetness loss and optimise the turbine design accordingly is of considerable interest.

1.3 Research aims

Even though wetness formation and related losses are considered to be well understood, there are some areas that require a deeper understanding before wetness-loss-based turbine optimisation can be performed. Examples include the influence of wake chopping on the turbine flow field, nucleation process, and subsequent two-phase flow mechanisms (e.g., deposition rates, relaxation losses). Hence, this thesis has three primary objectives:

- (i) Perform an in-depth sensitivity study of the leading wake chopping model to: (a) examine the sensitivity of the model to key parameters, (b) understand which features of the results are products of physical phenomena and which of modelling limitations (i.e., the reliability of results needs to be determined to use the model as a predictive

- tool), and (c) study how wake chopping affects other parameters (e.g., thermodynamic relaxation loss) and phenomena (e.g., droplet deposition).
- (ii) Develop a coarse droplet deposition model that includes both inertial and turbulent diffusion contribution. Using the model, investigate: (a) how important wake chopping is or subsequent phenomena (e.g., comparing calculated deposition rates based on a droplet spectrum from a wake chopping calculation vs. a spectrum from a steady throughflow calculation vs. a representative Sauter mean diameter), (b) in case wake chopping has a large impact, how sensitive are deposition rates to wake chopping modelling parameters, and (c) how sensitive the deposition model is to parameters within it.
 - (iii) The main aim of this thesis is to (a) develop an agile and robust computational method for turbomachinery applications that captures relevant wet steam effects and enables turbine performance comparison for various operating points and turbine designs (trend capturing), (b) compare calculated predictions with published turbine measurements and high-fidelity CFD results, and (c) provide a definitive answer to the importance of wake chopping for turbine design.

The methods presented in this thesis are integrated with the throughflow code, *SLEQ*, developed by John Denton, which calculates the flow field on the meridional plane (flow axisymmetry assumption) for a set of streamsurfaces. Since a full LP turbine calculation can be performed in a matter of minutes, it is hoped that the methods presented in this thesis will be incorporated in the standard turbine design workflow.

1.4 Structure of the Thesis

Chapter 2 provides a more in-depth review of existing theoretical and experimental methods aimed at understanding wetness and minimising wetness loss. Chapter 3 presents a stochastic method of modelling wake chopping implemented within a widely-used throughflow framework, accompanied by a comprehensive sensitivity analysis. This is followed by a droplet deposition model introduced in chapter 4, which incorporates both inertial and turbulent diffusion contributions. Sensitivity study and implications of wake chopping to deposition rates are also reported in chapter 4. Chapter 5 compares model performance to experimental measurements for a four-stage LP turbine. Finally, chapter 6 discusses the main conclusions and provides suggestions for future research.

Chapter 2

Literature review

2.1 Overview

The foundations of condensation research stem from the 18th century and Fahrenheit's observations of non-equilibrium freezing and liquid water subcooling [43]. However, the systematic investigation of non-equilibrium condensation only started in the late 19th century, when Helmholtz investigated fogging of steam escaping from a pipe [155]. There, he extended Lord Kelvin's equation for the equilibrium pressure over a curved surface, $p_s(T_l, r)$, giving an expression that determines the size of droplets in equilibrium with the surrounding steam. This is known as the Kelvin-Helmholtz equation and it is one of the core expressions in the study of condensation:

$$p_s(T_l, r) = p_s(T_l) \exp\left(\frac{2\sigma}{\rho_l R T_l r}\right). \quad (2.1)$$

Subscripts l and s refer to liquid phase and saturation conditions, respectively, R is the specific gas constant and σ is the surface tension. However, the theory does not provide a mechanism by which such droplets are formed since small droplets are unstable and easily evaporate.

One such mechanism is heterogeneous nucleation – the formation of droplets via condensation on existing surfaces or impurities (e.g., a dust particle), and it was erroneously believed to be the only condensation mechanism [2, 3]. Wilson's experiments (rapid decompression of air saturated with steam in an expansion chamber, [168]), however, conclusively proved the existence of another mechanism where droplets form without the presence of foreign nuclei – named homogeneous nucleation. Sudden expansion brought the mixture to a supersaturated, subcooled state, and thus allowed the droplets to spontaneously form. In his honour, the line of maximum subcooling in the Mollier diagram is named after him [92].

Homogeneous nucleation is expected to be the primary driver of condensation in turbines due to the high expansion rates present within, while the heterogeneous contribution can largely be neglected [137, 10]. Thus, the focus of the following literature review will be on homogeneous nucleation.

2.2 Nucleation and droplet growth

2.2.1 Nucleation

The condensation process is typically separated into nucleation and droplet growth. Nucleation accounts for the initial formation of liquid droplets and is covered by the classical nucleation theory, while droplet growth deals with the subsequent accumulation of molecules by the formed droplets. Classical nucleation theory has been explained in detail by [93, 94] and [10], so only a brief overview will be given here.

Following on the Helmholtz's research, Gibbs outlined the existence of meta-stable, supersaturated steam state, setting the foundations of nucleation theory. Here, the difference between the steam temperature and the saturation temperature for the given steam pressure is called subcooling, ΔT , expressed as:

$$\Delta T = T_g - T_s(p). \quad (2.2)$$

Isothermal compression of steam past the saturation pressure, p_s , increases its Gibbs free energy above the value for the liquid at the same conditions. Gibbs free energy increase can be expressed in differential form as:

$$df = vdp - sdT, \quad (2.3)$$

where v and s are specific volume and entropy respectively. Using the ideal gas relation, eq. 2.3 can be integrated along an isothermal path to a pressure p :

$$\Delta f = RT \ln \left(\frac{p}{p_s} \right) = RT \ln(S), \quad (2.4)$$

showing the increase in Gibbs free energy in terms of the supersaturation ratio, S . The net change is a combination of Δf decrease due to the bulk liquid formation (proportional to the droplet volume) and an increase due to free surface formation (proportional to the droplet surface area), and can be written as:

$$\Delta F = 4r^2\pi\sigma - \frac{4}{3}r^3\pi\rho_l RT \ln(S). \quad (2.5)$$

The surface term is dominant for small droplets and increases ΔF , forming an energy barrier to nucleation and enabling steam to remain in non-equilibrium. Figure 2.1 shows the change in Gibbs free energy of droplet formation for a range of subcooling values. It can be seen that each curve has a unique maximum, after which condensation becomes favourable energy-wise. The radius at that point is called the critical radius and can be obtained by finding the maximum of eq. 2.5:

$$r_* = \frac{2\sigma}{\rho_l RT_g \ln(S)} \approx \frac{2\sigma T_s}{\rho_l h_{lg} \Delta T}, \quad (2.6)$$

where subscripts l and g refer to liquid and gaseous variables respectively. The use of the Clausius-Clapeyron relation enables the critical radius to be expressed in terms of subcooling and latent heat of vaporisation, h_{lg} . The derivation of eq. 2.6 assumes steam to behave like a perfect gas with a constant R , as well as σ and ρ_l to be only a function of temperature. Surface tension σ can be estimated with an acceptable degree of accuracy using flat-film relations and droplet temperature can be assumed equal to saturation temperature [10].

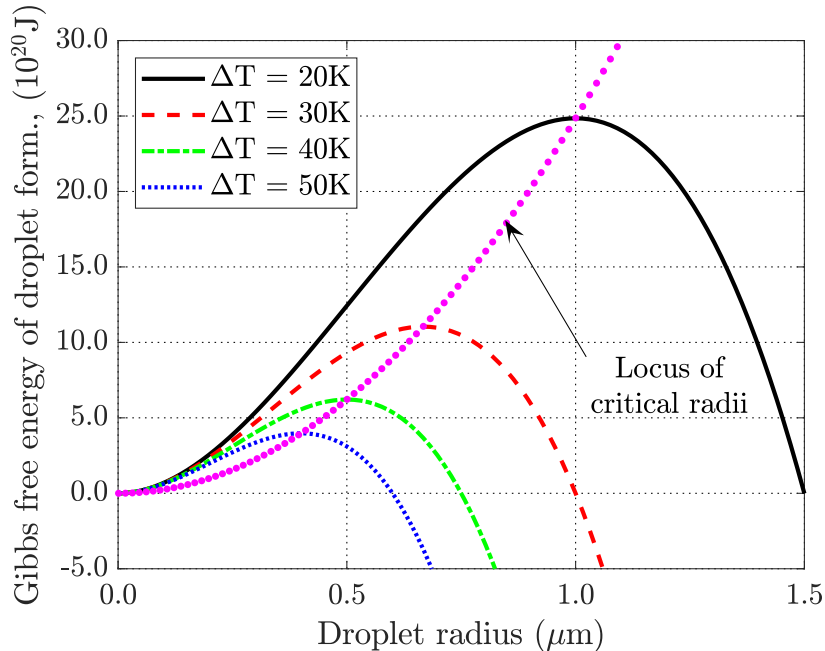


Fig. 2.1 The Gibbs free energy of droplet formation and the critical droplet radii.

A number of authors [154, 44, 15, 187, 48] extended Gibbs' work by estimating molecular fluxes to and from droplet embryos using kinetic theory, thus determining the nucleation rate:

$$J = q_c \frac{\rho_g^2}{\rho_l} \sqrt{\frac{2\sigma}{\pi m_m^3}} \exp\left(-\frac{4\pi r_*^2 \sigma}{3kT_g}\right). \quad (2.7)$$

Here, J is the classical nucleation rate of critically sized clusters, expressed per unit volume, m_m is the mass of a single molecule, and k is the Boltzmann's constant. Condensation coefficient q_c represents the proportion of incident molecules that stick to a condensing droplet (as opposed to rebounding). It is generally agreed that q_c for water is close to unity [96, 125, 50], but it is expected to be significantly lower for small droplets. Furthermore, condensation and evaporation coefficients are assumed to be equal, which is not necessarily true for a non-equilibrium process.

The classical nucleation rate shows reasonable agreement with experiments, but has been under substantial theoretical criticism. Equation 2.7 relies on the assumption that droplets and the surrounding steam have the same temperature T_g . In reality, large subcooling is needed to drive the heat transfer between embryos and the surrounding steam, leading to an order of magnitude (or two) higher deposition rates than what experimental measurements suggest [10]. Non-isothermal correction was introduced by Kantrowitz [81, 45], considering the influence of inelastic rebounding of steam molecules from growing clusters, thus raising their temperature. The correction can be expressed as:

$$J_{n.i.} = \frac{J_i}{1 + \phi_K}, \quad (2.8)$$

where ϕ_K is:

$$\phi_K = 2q_c \frac{(\gamma - 1)}{(\gamma + 1)} \frac{h_{lg}}{rT_g} \left(\frac{h_{lg}}{rT_g} - \frac{1}{2} \right). \quad (2.9)$$

The use of Kantrowitz's correction factor, ϕ_K , decreases the dependence of nucleation rate on the condensation coefficient, reducing the error introduced by setting $q_c = 1$.

While classical nucleation theory is widely considered to give good agreement with measurements, still, a number of uncertainties remain [145]. Since realistic values of surface tension are not known, questions have been raised about the validity of using flat film relations to determine surface tension of a cluster containing only several molecules, effectively assigning bulk properties to a small number of molecules. A number of studies aimed to provide a surface tension correction factor [39, 82, 152, 84, 150], with disappointing results – failing to agree even on the sign of the correction. Due to the sensitivity of J to surface tension, this problem still needs to be resolved for a satisfactory nucleation theory to emerge [10]. Furthermore, [90] argued that the classical nucleation theory does not correctly account for the vibrational and rotational free energies. However, including these caused an increase in nucleation rate and a reduced agreement with experiments [45, 169, 175]. The

effect of increased degrees of freedom (including a better estimate of the surface energy term) was examined by [39], resulting in a complex set of equations that improved agreement with expansion chamber measurements. However, the indication of mathematical inconsistencies [86] as well as the high associated computational cost make it unsuitable for fast calculation methods.

2.2.2 Droplet growth

The nucleated droplets continue to increase in size as the incident water molecules condense on their surfaces and, as the droplet surpasses the critical radius, nucleation theory is no longer suitable to predict their growth over time. The condensation latent heat release increases the droplet temperature, making them hotter than the surrounding steam. Therefore, droplet growth is primarily governed by the mass flux to, and energy flux from the droplet. Historically, this was modelled in two ways, based on the Knudsen number, Kn, [83]:

$$\text{Kn} = \frac{\lambda_g}{2r}. \quad (2.10)$$

Here, λ_g is the mean-free-path (MFP) of steam molecules, expressed as [59]:

$$\lambda_g = \frac{1.5\mu_g \sqrt{RT_g}}{p}. \quad (2.11)$$

Droplets substantially larger than the molecular MFP ($\text{Kn} \ll 1$) are considered to be in the continuum regime, and are thus modelled using continuum mechanics principles. On the other hand, small droplets whose size is comparable to the MFP are described using kinetic theory, and growth is modelled using Hertz-Knudsen model [62]. However, typical turbine flow conditions span a large range of Knudsen numbers,¹ requiring a unified theory that would also cover intermediate Kn values.

The first such model was developed by Langmuir [87], whereby he assumed the existence of a fictional spherical boundary surrounding each droplet. Kinetic theory is assumed to govern the flow within each boundary and continuum mechanics everything outside. The boundary radius is larger than the droplet radius by a factor β of MFP, $r_b = r_l + \beta\lambda_g$. Young [184, 185] developed a growth model based on Langmuir's research and reported $\beta = 0.75$ gives the best agreement with experiments.

The energy conservation for a single spherical droplet can be written as:

¹In a typical turbine MFP is $\sim 10^{-7}$ while droplet diameters are usually between 10^{-9} and 10^{-6} .

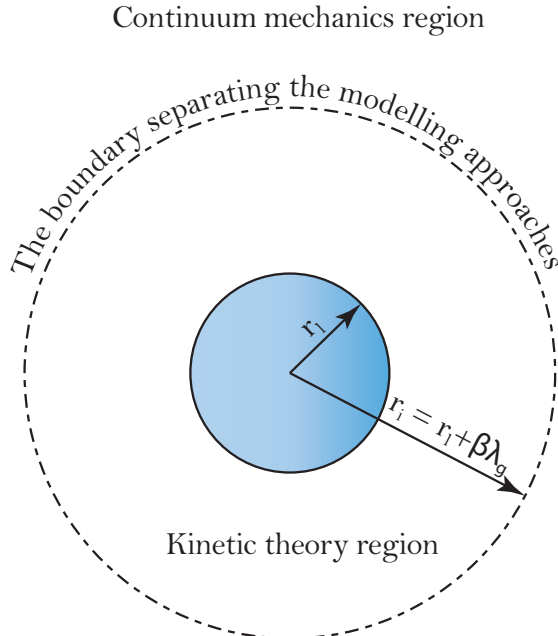


Fig. 2.2 Langmuir's droplet growth model.

$$h_{lg} \frac{dm_l}{dt} = mc_{pl} \frac{dT_l}{dt} + 4r^2 \pi \alpha_{ht} (T_l - T_g), \quad (2.12)$$

where $c_{p,l}$ is the heat capacity of liquid and α_{ht} is the heat transfer coefficient, showing that the latent heat released due to condensation adjusts the temperature of the droplet while a part of it is conducted to the surrounding steam due to the finite temperature difference. Unless the steam is subject to extremely rapid change of state, the dT_l/dt term is low and can be neglected. Equation 2.12 can now be written as a droplet growth rate:

$$\frac{dr}{dt} \approx \frac{\alpha_{ht}}{h_{lg} \rho_l} (T_l - T_g). \quad (2.13)$$

Gyarmathy [54] proposed the expression for α_{ht} over the entire range of Kn (from free molecular on one end to the continuum regime on the other end of the Kn spectrum) as:

$$\alpha_{ht} = \frac{k_g}{r} \left(1 + 3.78 \frac{\text{Kn}}{\text{Pr}} \right)^{-1}. \quad (2.14)$$

Here k_g is the thermal conductivity and Pr is the Prandtl number of steam, defined as the ratio of momentum diffusivity to thermal diffusivity:

$$\text{Pr} = \frac{c_{p,g} \mu_g}{k_g}, \quad (2.15)$$

where $c_{p,g}$ and μ_g are the heat capacity and the dynamic viscosity of steam, respectively. Furthermore, Gyarmathy [54] expressed droplet temperature in eq. 2.13 in terms of steam subcooling as:

$$T_l - T_g = \left(1 - \frac{r_*}{r}\right) [T_s(p) - T_g]. \quad (2.16)$$

This equation, however, assumes that the non-equilibrium steam pressure is the same as its equilibrium counterpart, which is not strictly correct. Further to these considerations, Schrage [133] argued that vapour velocity towards the droplet needs to be included in the analysis of droplet growth to satisfy the conservation of radial momentum. Young [184] also noticed that most growth models perform poorly when modelling condensation at pressures lower than 0.1 bar, suggesting this might be due to the assumed equal condensation and evaporation coefficients. This was also supported by [115]. Young proposed an improvement to the Gyarmathy's model as:

$$\alpha_{ht} = \frac{k_g}{r} \left[\frac{1}{1 + 2\beta Kn} + 3.78(1 - v) \frac{Kn}{Pr_g} \right]^{-1}, \quad (2.17)$$

keeping the structure of the droplet growth formulation the same as in eq. 2.13. Coefficient v was introduced to improve agreement with low pressure nozzle experiments by allowing for the difference between evaporation and condensation coefficients as:

$$v = \frac{RT_s}{h_{lg}} \left[\psi - \frac{1}{2} - \frac{2 - q_c}{2q_c} \left(\frac{\gamma + 1}{2\gamma} \right) \frac{c_{pl}T_s}{h_{lg}} \right]. \quad (2.18)$$

There is, however, no empirical evidence suggesting the difference between condensation and evaporation coefficients, thus the coefficient included in Young's growth model can be considered as an empirical correction. Furthermore, kinetic theory calculations [52] indicate that the Schrage effect has barely any impact on the energy transfer between phases and, thus, droplet growth rate.

2.2.3 Experimental measurements and validation

The validation of nucleation and droplet growth theories primarily relies on condensing nozzle flow measurements. Nozzles provide steady, near 1D flow that, while being much simpler than turbine flow, replicates expansion rates, the Mach number, and subcooling conditions observed in operating turbines.

Condensing nozzle flows

In the early days of condensation research, it was only possible to measure *condensation shock* (pressure jump in the Wilson zone caused by the condensation latent heat release) in the de Laval nozzles (e.g., [178]). However, using only pressure distribution data was insufficient to validate nucleation and growth theories, so in the 1960s Walters developed light extinction probes which measured the attenuation of monochromatic light passing through wet steam populated with monodispersed or polydispersed droplet spectra. Light extinction measurements recorded for a number of wavelengths can be inverted using Mie theory (a process ridden with mathematical difficulties [158]) to obtain information on droplet sizes.

In his review, Young [184] reported more than a hundred nozzle condensation experiments available in the literature, with fifteen containing droplet size data. However, a large number of those contain incomplete data or the data was collected using faulty techniques (e.g., the use of sliding nozzles designed in [58] was shown to adversely affect nucleation and, hence, pressure measurements [184]).

Moore et al. [100] experimented with expansion of pure steam in five nozzles at very low pressures (Wilson point pressure around 0.1 bar) and recorded pressure traverse and Sauter mean diameter with excellent accuracy [157]. The nozzles had a range of throat widths and divergence angles, producing the range of expansion rates typically found in steam turbines (460 s^{-1} to 3160 s^{-1}). The authors compared measurements with 1D calculations based on the theory given in the previous sections, showing very good agreement.

A large number of low pressure tests was performed by Moses and Stein [103], whose nozzle was smaller than that of Moore et al. resulting in higher expansion rates (6500 s^{-1} to 10000 s^{-1}). In many of them, however, the Wilson zone temperature fell below 0°C , making it difficult to discern whether subcooled liquid or ice was formed. The reported comparison of measurements with 1D calculations showed very good agreement (comparable to findings in [100]).

Other notable nozzle expansion tests can be found in [16, 17, 57, 13] for intermediate pressures (Wilson point pressure between 0.15 bar and 0.65 bar) and in [58, 56, 153] for high pressures (Wilson point pressure between 6 bar and 37 bar)

Starzmann et al. [146] presented a comprehensive review of the main nucleation, droplet growth, and equation of state models, and compared them to the selected measurements for Mystery, Moore et al. and Moses and Stein nozzles. Several uncertainties remaining in the theories resulted in the lack of a clear consensus regarding the best modelling approach (and modelling parameters), however, several models reliably captured the relevant effects. The results confirmed the importance of non-isothermal correction and Young's growth law, reducing the nucleation and increasing growth rates compared to classical nucleation

theory and Gyarmathy's growth law. They also showed lower nucleation rate and higher droplet growth rate than what classical nucleation theory and Gyarmathy's growth law would suggest, with better agreement when non-isothermal correction and Young's growth law were applied – confirming their importance. Modelling droplet size spectra using monodispersed model overestimated droplet sizes by more than 20%, showing the need for the use of e.g., momentum method to model the droplet size spectra.

2.3 Other drivers of condensation in turbines

On-site optical measurements conducted in the late 1980s on operational turbines (e.g., work done by [159] and [183, 186]) revealed droplet size distributions that are much broader and with larger average diameters than those observed in steady flow experiments (see fig. 2.3), as reviewed in section 2.2.3. This indicated the presence of mechanisms that strongly influence nucleation in turbines but are not replicated in the nozzle and steady cascade experiments. Possible explanations include: (i) nucleation in blade-wake vortices [47], (ii) heterogeneous nucleation triggered by steam impurities [149], and (iii) unsteady wake segmentation due to rotor-stator interaction [59].

Nucleation in blade-wake vortices According to [47], temperature fluctuations caused by eddies shedding from blade trailing edges are responsible for widening of the nucleation

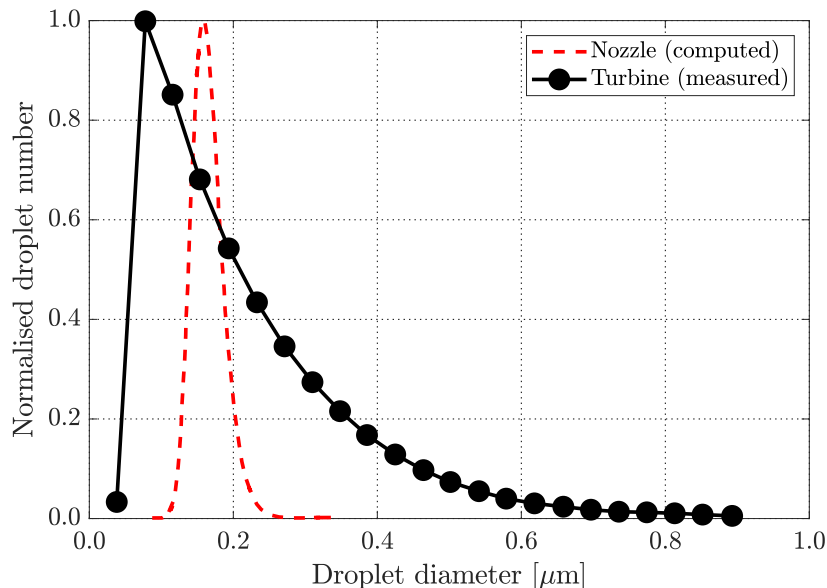


Fig. 2.3 Droplet size spectrum comparison between nozzles and turbines, reproduced from [186].

zone and broadening of the droplet size spectrum. However, two nozzle experiments by [100] – with and without turbulent eddy inducing mesh at the test section inlet – had a negligible difference between measurements, suggesting that the mesh had no influence on the results. Numerical work by [176] showed nucleation occurring in the turbulent blade wakes, supporting the claim by [53] that true turbulence superimposes a low amplitude, high frequency oscillation onto the large temperature fluctuations caused by rotor-stator interaction.

Heterogeneous nucleation Heterogeneously formed droplets due to the impurities in the steam provide surface for further condensation and can delay or even suppress homogeneous nucleation [7]. [149] attempted to explain the widening of the droplet size spectrum in turbines to be a consequence of heterogeneous nucleation. Experimental measurements of the effect of steam impurities on nucleation in a steam cascade were performed by [5, 20] using three different types of steam: steam generated using town supply water, extremely pure steam, and steam dosed with various concentrations of ammonia. It was found that for same degree of inlet superheat and overall pressure ratios, measured pressure distributions were identical for all types of steam, demonstrating that the presence of impurities did not affect the overall nucleation behaviour. Similarly, [116–118] reported that the presence of impurities does not significantly change the results and that the nucleation and droplet size spectra in steam turbines can be adequately captured by assuming homogeneous nucleation as the dominant mechanism.

Unsteady blade row interaction Large scale temperature fluctuations in multistage turbines were first reported by [170], measuring total temperature oscillations at the outlet comparable to a blade row temperature drop. The fluctuations of that magnitude could not be produced by turbulence alone. Gyarmathy and Spengler [59] proposed a theory whereby the unsteady segmentation of blade wakes is responsible for the observed phenomenon. Several authors ([6, 53, 116, 118]) have confirmed it as a primary cause of droplet spectrum widening, thus a more detailed review is given in the following section.

2.3.1 Wake chopping

Steam passing through a blade row experiences different levels of dissipation depending on its proximity to blade surfaces, with free stream flow expanding almost isentropically and near-wall flow experiencing high levels of viscous dissipation and thus forming wakes, as illustrated in fig. 2.4. The wake regions (orange) have a higher entropy production and a higher temperature than the core flow (reduced subcooling), thereby postponing

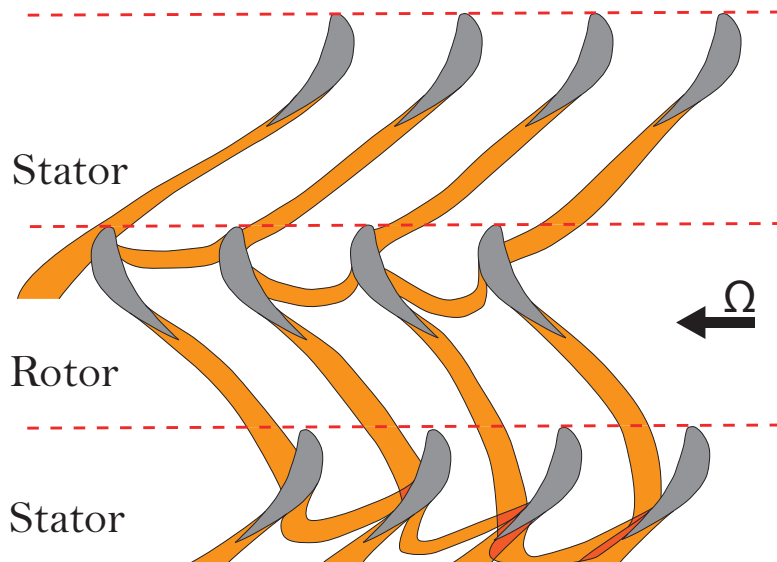


Fig. 2.4 Illustration of unsteady blade wake segmentation by subsequent blade rows, leading to complex flow patterns downstream.

the nucleation. Upon leaving the blade row, wakes are periodically segmented by the relative motion of subsequent blade rows and distorted by the circumferentially variable flow acceleration within blade passages, creating complex temperature patterns in the downstream blade passages and widening the nucleation zone. This process is known as unsteady wake segmentation, or *wake chopping*. Since nucleation is spread over more than one stage, it may occur at locations with very different expansion rates (e.g., blade throat vs. inter-row gap), resulting in a broad range of nucleation rates and, consequently, a much wider size distribution than would occur in a steady condensing flow.

Unsteady wake segmentation was first recorded by [140], who introduced dye in the core of the flow upstream of a rotor and observed it being segmented by the blade leading edges. Similarly, hot-wire anemometer readings downstream of a first stage rotor of a four stage compressor recorded oscillations caused by rotor wakes, as well as smaller oscillations originating from upstream stator wakes. Placing the anemometer downstream of subsequent rotor blades recorded increasingly complex fluctuation patterns coming from an increased number of upstream blade rows, suggesting the segmentation of wakes.

Wood [170] reported temperature fluctuations in a 500 MW multistage steam turbine. He collected total temperature and mass flow rate downstream of the last three blade rows using a high-frequency response hot-wire anemometer and estimated the root-mean-square (RMS) temperature fluctuations to be between 6% and 8.2%. Filtering the data behind the last blade row at the frequency of the final rotor enabled Wood to isolate the contribution

coming from the last blade row. RMS temperature fluctuations coming from the upstream rotor were between 1.6% and 2%, implying that the overall measured variations are primarily caused by the effects further upstream. The fluctuation measurements in condensing flow experiments are, however, difficult to interpret since the condensation tends to revert flow back to equilibrium.

The measured temperature fluctuations are comparable to a temperature drop within a stage, signifying that the nucleation zone in condensing steam turbines is spread over a broad axial range (and, hence, broad range of expansion rates), widening the generated droplet size spectrum, as previously seen in fig. 2.3. Gyarmathy and Spengler [59] attempted to model these fluctuations for a single-phase flow, while addressing the importance of the same phenomenon for the condensing flows. The principal idea is that, as steam passes through a multistage machine, the loss experienced by individual fluid parcel is a function of the path it took through the machine. Depending on the proximity to the solid surfaces, the flow will experience different levels of dissipation, with free stream flow expanding almost isentropically and near-wall flow experiencing high levels of viscous dissipation and thus forming wakes. They assumed that the pressure of all fluid parcels downstream of any turbine stage is nearly uniform while their specific entropies and, hence, static temperatures will be significantly different, resulting in a broad range of thermodynamic conditions at the same axial location. Each blade row was assigned a pitchwise loss profile and pitchwise entry position for each steam parcel was assumed to be random, with the condition that the time-averaged value of loss across all parcels has to agree with the overall turbine loss distribution. Gyarmathy and Spengler performed calculations with and without heat exchange between steam parcels and reported better match to the measurements by [170] when heat exchange was excluded.

Bakhtar and Heaton [6] applied the same method to a condensing flow in a model four stage turbine and compared results with measurements by [139]. Measurements were done for two inlet temperatures, with the first one sufficiently high to inhibit nucleation (dry test) and the other, lower one, allowed nucleation to occur in the turbine (wet test, $\sim 10\%$ outlet wetness). Dry test temperature and pressure measurements in each blade row passage were used to determine average loss through the turbine. The calculations were performed for 10 000 random steam pathlines through the machine at approximately mid-span, using two artificial loss coefficient profiles. Nucleation characteristic in the wet case was approximated by assessing the nucleation rate near the leading and trailing edges, using a tabular method developed by [9]. If the flow was not substantially nucleating close to the LE, it was assumed to remain in a subcooled state as it continued to expand in the blade passage. If there was significant subcooling at the TE, the flow was allowed to nucleate in the inter-row

gap. The wet test wake chopping calculation showed a broad droplet size spectrum ($0.1 \mu\text{m} < d_l < 1.1 \mu\text{m}$), qualitatively resembling measurements by [186] (shown in fig. 2.3), which could not be reproduced using a 1D calculation. These results strongly suggested that the wake chopping model can improve agreement with turbine measurements, even when using artificial wake profiles.

The model was further refined by Guha and Young [53], using dry streamline curvature calculations to determine the pressure trajectory through a six-stage LP turbine. Wake chopping was then performed at mid-span by tracking 10000 random pathlines in the Lagrangian frame of reference for two artificial wake profiles (resulting in 8% loss per blade row), using linear axial pressure variation between leading and trailing edges. While radial mixing between streamlines was neglected, wake decay was modelled as the decay of gradients in stagnation enthalpy, and the associated temporal constant, τ_w , was estimated at $\tau_w = 5\Delta t_{ls}$, where Δt_{ls} is the transit time in the last stage stator. Six stages allowed for larger variation within blade rows, causing large temperature fluctuations and spreading the nucleation zone over two stages. The calculated droplet size spectrum was much broader, skewed, and with a larger mean diameter than what 1D calculations would suggest, thereby matching the empirical measurements more closely (Sauter mean diameter). Droplet size spectra were shown to be very sensitive to wake decay rate and pitchwise loss profile, changing between unimodal and bimodal distributions as the parameters were varied, while being fairly insensitive to the streamwise loss distribution. The results overall show a very strong influence of wake chopping on the formation and growth of water droplets in multistage turbines. The model, however, suffers from the lack of pitchwise pressure variation which is likely to have a substantial effect on the results since the characteristics of the nucleated droplets strongly depend on the local expansion rate.

Petr and Kolovratnik [116] investigated the influence of wake chopping in a full-size four stage LP turbine. They extended the work done by [53] by adding linear pressure variation across the pitch (albeit without explaining how the variation was estimated), labelling it as a 2D method. Mid-span pressure distribution was estimated using a throughflow calculation, with no wake dissipation allowance. Condensing steam calculations were performed as either steady or unsteady (wake chopping, 5000 randomly generated steam paths), with 1D (axial) and 2D (axial and pitchwise) expansion rate variation. Surprisingly, all calculated spectra show very little difference, apart from the steady 1D case, which resulted in a typical narrow distribution but with a much larger Sauter mean diameter than what other calculations suggested. The authors unfortunately did not provide an explanation for this. On the other hand, agreement with light extinction measurements was very good. To avoid the complex mathematical procedure of inverting the extinction measurements into a droplet spectrum,

Petr and Kolovratnik transformed the calculated spectra into corresponding light extinction for a range of wavelengths of light using Mie theory. The closest match was achieved when including pitchwise pressure variation in the wake chopping calculation, suggesting the importance of 2D effects.

Following on their previous paper, Petr and Kolovratnik examined the influence of impurities (i.e., heterogeneous nucleation) in the context of wake chopping [117], concluding that the widening of the droplet spectrum is, indeed, primarily driven by wake chopping and that the heterogeneous nucleation does not play a significant role in the shape of the droplet spectrum.

Using the work by [53] and [116] as the basis, Hughes [68] developed a deterministic approach to wake chopping. Each blade row was assigned a user-specified number of trajectories and deterministic wake chopping was performed by assigning each trajectory outlet from blade row n to every trajectory inlet at blade row $n + 1$. Naturally, the number of tracked steam trajectories (and, thus, memory requirements) in this model exponentially increased with the number of turbine stages as the number of possible combinations increased, requiring the use of artificial averaging every n blade rows. Pressure distribution throughout the turbine was determined using throughflow calculations and pitchwise loss variation was estimated using a Gaussian function. The model included allowance for wake mixing, and pitchwise pressure variation was based on linear interpolation of pressure profiles for each blade row, which were provided as input (either from measurements or high-fidelity calculations). This enabled the author to study the effect of changing the blade shapes (by adjusting the pressure profiles) on the nucleation zone. The results were compared to the RANS calculations, showing reassuring similarity. Wake chopping calculations successfully captured the axial spread of the nucleation zone, somewhat overpredicting its length compared to the CFD calculations. However, no clear reason for it is given.

2.4 Droplet deposition

2.4.1 Inertial deposition modelling

In his comprehensive work, Gyarmathy [54] presented a simple deposition model for turbomachinery applications, whereby deposition was divided into leading edge and blade surface contributions. Leading edge deposition was approximated by calculating collection efficiency of a cylinder in a uniform flow and the blade surfaces were approximated using a parabolas mimicking steam pathlines (to avoid false deposition). Surface deposition was then determined by estimating droplet trajectories (using numerical integration) in the steam flow

field, assuming Stokes drag force to be dominant. However, the method does not include the effect of blade row rotation. The calculation estimated the *limiting pathline position* (i.e., determining pitchwise position from which a droplet tangentially touches the trailing edge). All trajectories from pitchwise positions “lower” than the limiting value, thus, intersect with the pressure side surface. Those droplets are assumed to be perfectly captured by the existing liquid film on the blade, without any splashing or rebounding. More on this method will be given in chapter 4.

Since Stokes’ drag law is not very accurate for large droplets, Crane [25] modified Gyarmathy’s model and integration scheme, showing that droplets with diameter smaller than $0.5\text{ }\mu\text{m}$ result in negligible leading edge deposition rates in LP steam turbines. Blade pressure sides were shown to account for the majority of deposited droplets, leading to the conclusion that droplets larger than $0.5\text{ }\mu\text{m}$ contribute the majority of the deposited liquid mass.

Young and Yau [182] expanded Gyarmathy’s model, using Denton’s throughflow [34] and time-marching blade-to-blade codes [32] to determine the turbine flow field for a range of operating conditions. The calculations were performed on the last stage of a 500 MW LP, and an unspecified HP turbine stage, for a range of droplet sizes. The deposition rates were found to be sensitive to the resolution of the blade geometry and nearby flow field. Deposition rates in HP and LP turbine stages were found to be comparable for the identical droplet sizes and were shown to be strongly affected by the blade geometry (blade angles and chord length). Moreover, the authors suggest that the Coriolis acceleration in the rotating blade rows is unlikely to change the deposition rates by more than 20%. Gyarmathy’s model underpredicted deposition of smaller droplets and resulted in an unrealistic, uniform deposition distribution along the blade pressure side. However, the total deposition mass flow rate was estimated surprisingly well.

2.4.2 Turbulent deposition modelling

The deposition of droplets in a turbulent flow field is governed by complex mechanisms. Early researchers believed that particles are deposited on vertical walls only by turbulent diffusion. However, the seminal paper by Friedlander and Johnstone [49] reported deposition rates which varied by almost four orders of magnitude before levelling off at much higher values than what turbulent theory suggested. This can be seen in fig. 2.5, which shows dimensionless particle deposition rate measurements as a function of particle size for a fully developed pipe flow (and confirmed by a number of measurements [89, 136, 163, 135, 49]), summarised by [181].

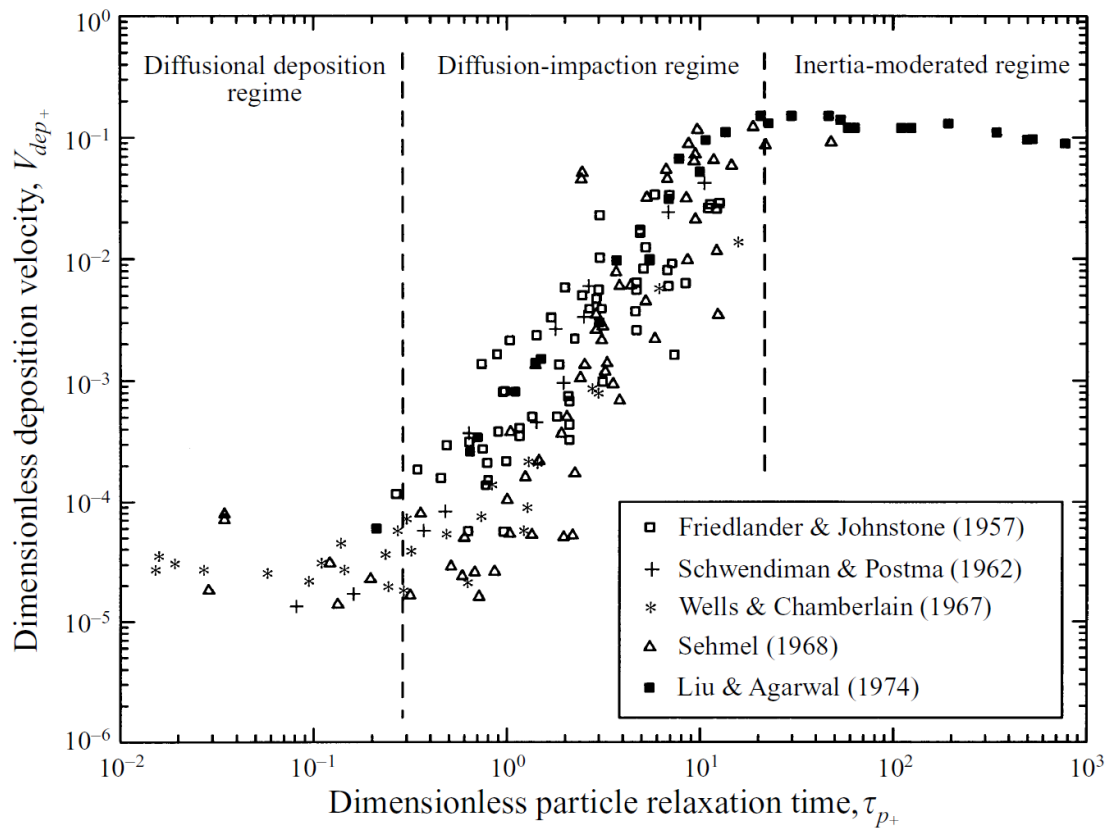


Fig. 2.5 A summary of experimental particle deposition measurements for fully developed, turbulent, vertical pipe flow, shown in [181].

Here, dimensionless deposition velocity, V_{dep+} , is defined as:

$$V_{dep+} = \frac{J_w}{\bar{\rho}_{l,v} u_*}, \quad (2.19)$$

where J_w is the deposition rate (number of droplets deposited on unit area in unit time), $\bar{\rho}_{l,v}$ is the mean particle density (mass of droplets per unit volume), and u_* is the friction velocity ($u_*^2 = \text{wall shear stress} / \text{steam density}$). Dimensionless particle relaxation time is expressed as:

$$\tau_{p+} = \frac{\tau_p u_*^2}{v_g}, \quad (2.20)$$

where τ_p is the droplet inertial relaxation time (function of droplet diameter), and v_g is the kinematic viscosity of steam. A more detailed breakdown of these terms is given in chapter 4.

Based on the droplet size parameter, turbulent deposition can be roughly divided into three distinct regimes: (i) diffusional deposition regime, (ii) diffusion-impaction regime, and (iii) inertial-moderated regime.

Diffusional deposition regime, ($\tau_{p+} < 0.1$)

In this regime, droplets are transported through the boundary layer by a combination of turbulent eddy diffusion (turbulent version of Fick's law) and Brownian motion, whereby turbulent diffusion enables droplet migration in the core of the flow and Brownian motion helps droplets cross the viscous sub-layer (thin, almost laminar layer that provides most of the resistance to deposition) adjacent to the blade surfaces [181]. For small droplets, V_{dep+} is monotonically decreasing with τ_{p+} and is a function of Schmidt number, which is defined as a ratio of momentum diffusivity of steam and droplet mass diffusivity ($Sc = v_g/D_d$).

Eddy diffusion-impaction regime, ($0.1 < \tau_{p+} < 10$)

Diffusion-impaction regime is characteristic by the rapid increase in V_{dep+} with τ_{p+} (several orders of magnitude), caused by the interaction between intermediate sized particles (significant inertia) and the steam turbulent eddies [181]. This mechanism is still not understood well enough. Friedlander and Johnstone [49] proposed a “free-flight” (also known as “stop-distance”) model, where gradient diffusion transports droplets to “one stop-distance” away from the wall. From that point, the droplets coast through the viscous sublayer as a response to an impulse from a large eddy in the buffer layer (a comprehensive review of free-flight model variations can be found in [110]). However, the model suffers from the assumption

that droplets acquire a velocity component towards the wall that is similar in magnitude to friction velocity, u_* . RMS of velocity fluctuations in the region close to the wall (one to ten stop-distances away) is much lower than u_* , and [30] showed this model results in two orders of magnitude lower deposition rate than measured. Alternative methods have been extensively discussed in literature [177, 26, 171]. Modern approach to diffusion-impaction regime modelling depends on the inclusion of forces such as turbophoresis and thermophoresis to capture the rapid rise in deposition rates since, nowadays, turbophoresis is considered to be the primary driver of deposition rate increase in steam turbines [177]. More on those forces will be given in the following sections and in chapter 4.

Inertial-moderated regime, ($10 < \tau_{p+}$)

Diffusion is assumed to have a negligible effect in the inertial-moderated regime, as large eddies provide the droplets with enough momentum to reach the blade surface. Larger droplets are progressively less sensitive to eddy fluctuations (orthogonal to the blade surfaces) due to their high inertia, causing a decrease in deposition rates with an increase in τ_{p+} .

Early deposition models [111, 127] primarily relied on turbulent diffusion and showed good agreement since they were confined to low droplet sizes ($\tau_{p+} < 1$). The first attempt at modelling all three regimes was done by Wood [171], who also included the effect of surface roughness and showed it had a modest effect for $\tau_{p+} > 1$ (these findings were confirmed in [177]). Several authors [177, 25] realised the large uncertainty associated with friction velocity, which is very sensitive to boundary layer conditions and laminar-to-turbulent transition location [27], and have used simple boundary layer solvers to improve the predictions.

Young and Leeming [181] developed a deposition model formally based on particle mass and momentum conservation equations, and applied it to turbulent pipe flow. The equations are expressed in the Eulerian frame of reference and are Reynolds averaged, leading to several turbulence correlations. The two most important ones are turbulent diffusion flux – caused by a concentration gradient, and turbophoresis. Turbophoretic force (first proposed by [21, 124]) accelerates droplets towards the wall (down the gradient of RMS fluctuating velocity), creating a convective drift of droplets. The turbophoretic term naturally emerges when averaging particle momentum equation, as shown in [181, 138]. As seen in fig. 2.6, turbophoresis plays a minor role when it comes to small particles since their inertia cannot maintain the necessary drift velocity against the viscous drag slowing it down. Similarly, large droplets with high inertia are decreasingly sensitive to turbulent fluctuations and, thus, turbophoresis. However, intermediate sized droplets struggle to follow turbulent eddies in

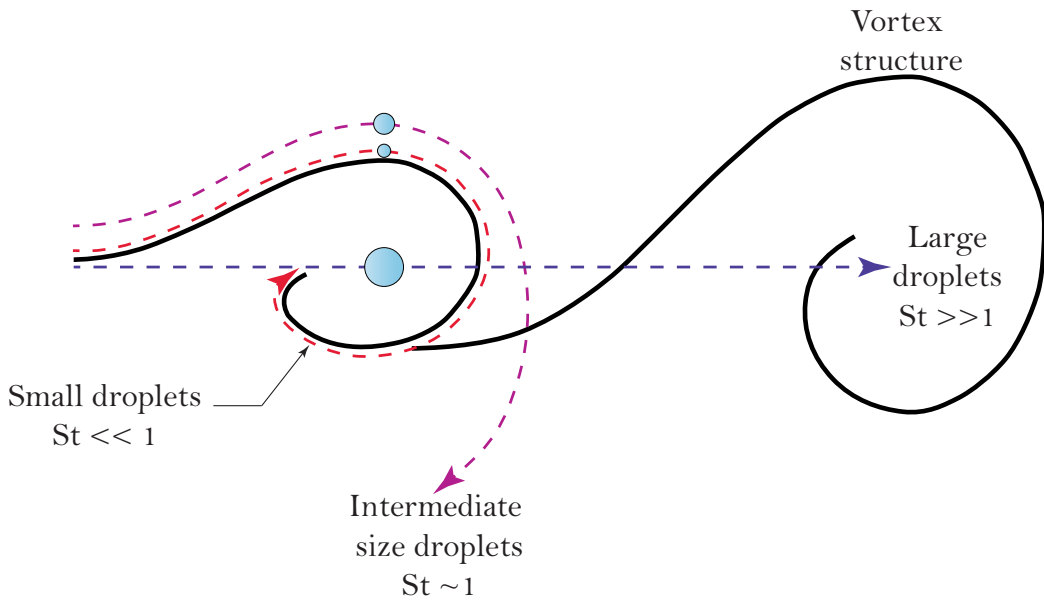


Fig. 2.6 Impact of turbophoresis on different droplet sizes.

the buffer layer and are impelled towards the wall (droplets are unable to return since RMS velocity fluctuations are lower in the sub-layer).

The theory by Young and Leeming [181] also included the Saffman lift force (initially proposed in [128, 129]). Droplets are assumed to acquire a spin due to the presence of velocity gradients in their immediate surroundings, resulting in a higher pressure on the lower velocity side and, hence, generating lift. The authors reported a complex balance between diffusion, turbophoresis, and Saffman lift force, and suggested that the lift force plays an important role in the inertia-moderated regime. Gravitational force was, however, reported as negligible compared to the other effects.

Guha [51] expanded the work by [181] and added effects of thermophoresis and electrophoresis. Thermophoretic force on a droplet is generated due to the presence of local temperature gradients, formulated by Talbot [151] (a good overview can be found in [61]). Since the molecules in the higher temperature region have higher kinetic energy, molecular bombardment of the droplet surface results in a net force in the downward direction of the temperature gradient. This effect was reported to be important in cooled gas turbines, where temperature gradients near the blades are high, thus driving deposition rates. However, tem-

perature gradients are much lower in steam turbines, making thermophoresis less impactful. Moreover, blade wakes are hotter than the core of the flow (see section 2.3.1), thus inhibiting deposition.

Electrophoretic force causes a drift of charged particles in an electric field and can be estimated using the “method of images” [106]. While this effect is important in gas turbines, it is less relevant in the context of steam turbines.

Wu and Young [173] examined deposition in a duct, a curved duct, and a steam cascade turbulent flow using a 2D Eulerian method. The results showed a complex interaction between depositional modes as their influence changed with local curvature. The curvature played a great role on deposition rates as droplets coasted outwards, increasing droplet concentration on the outer side of the bend, thus increasing turbulent deposition rates even for very small droplets ($\tau_{p+} = 0.64$).

Slater et al. [138] performed deposition calculations that included both inertial and turbulent diffusion effects in a 2D turbulent channel, and a gas turbine cascade. The authors decomposed the particle flux into convective and diffusive contributions which helps clarify the different roles of depositional mechanisms. Most importantly, the results demonstrated the interaction between inertia driven deposition (streamline curvature), diffusion, and turbophoresis. Particles were shown to drift into the boundary layer due to streamline curvature, increasing their local concentration. The added diffusional effect (favourable particle concentration) enhanced inertial particle flux to the buffer layer, whereby particles were further aided by turbophoresis and deposited on the nearby surfaces. The combined effects resulted in a larger deposition rate than what the sum of individual contributions suggested.

2.4.3 Deposition measurements

A big problem of deposition research is the general lack of accurate deposition rate measurements. The majority of published experimental data was collected for fully-developed turbulent flows in simple geometries such as pipes [89, 136, 163, 135, 49], ducts [181, 174], and annular flows [61]. Deposition measurements in turbines are rare and usually performed with particle sizes relevant for gas turbines [27].

Parker et al. [112, 111] studied deposition of uranium particles ($0.01 \mu\text{m} < d < 1 \mu\text{m}$) suspended in air in a turbine cascade. The conditions were selected so that inertial deposition contribution could be kept at a minimum, allowing for turbulent deposition rates to be determined by fluorometric analysis of individual metal-foil collector strips. Deposition rates were recorded for several droplet sizes and inlet turbulence levels, while Reynolds and Schmidt numbers were kept comparable to LP turbines. The measurements showed

negligible pressure side and small suction side deposition rates (less than 0.1% of particle mass flow rate). However, the inertial relaxation time for used particle sizes was very low, corresponding to minimal deposition rates associated with the diffusional regime.

Based on these findings, [126, 109] examined how blade heating can reduce deposition, using the same methodology and rig as Parker et al. Heat flux of 600 W m^{-2} applied to the blade surfaces generated a thermophoretic force that significantly reduced deposition rates (30 – 90% reduction) along both pressure and suction sides. The experiment was performed for $0.05 \mu\text{m}$ and $0.25 \mu\text{m}$ droplets, showing larger deposition reduction for larger droplets, indicating the variation in thermophoretic force with droplet diameter. Moreover, the authors recognised the influence of evaporation on water droplets next to heated blades.

Young et al. [183] reported detailed radial profiles of coarse water flow in the final stages of two 500 MW LP turbines (identified only as “A” and “B”). Traverses upstream and downstream of the last stage recorded measurements of droplets and casing film flow, thus enabling the comparison of coarse water flow rate entering and leaving the stage. The deposition rate was evaluated by calculating the difference between outlet and inlet coarse water mass flow rates, assuming that fog agglomeration and condensation onto blade surfaces played a negligible role. Radially integrated coarse water (coarse water fraction) in turbine “A” was around 2.5% of total water (suspended droplets and blade films) at the stage inlet and 4.1% at the outlet. It was reported that around 3% of suspended droplets entering the stage get deposited. Turbine “B” operated with a higher back pressure and stage inlet and outlet coarse water fractions were recorded as 1.7% and 3.1% respectively, with 2.1% of all droplets deposited in the stage.

2.5 Wetness loss mechanisms in steam turbines

One of the drawbacks of crossing the saturation line to maximise power output is the increased energy dissipation due to the formation of liquid phase in the steam flow. It is collectively referred to as *wetness loss* and consists of the irreversibility in the wetness formation and the effect wetness has on downstream flow dynamics. Modern steam turbines operate with many stages under wet conditions (often in nuclear power plants the entire LP turbine operates with wet steam), with wetness loss ranging between 1% and 5% of overall power output [143]. Baumann was the first to recognise the importance of wetness losses on turbine performance [14], and examining their magnitude became the goal of many authors. Despite the complex nature of wetness losses, he proposed a simple empirical rule whereby the efficiency changes by one percent for each one percent variation in wetness. Understanding of wetness and, thus, related losses was improved by the comprehensive work by Gyarmathy [54]. Many

researchers tried providing theoretical estimates, indicating that wetness loss is a function of wetness fraction and droplet size, and is proportional to aerodynamic losses [101]. However, turbine measurements showed that wetness loss does not increase proportionally to the wetness fraction but is concentrated in the stage where nucleation occurs [137]. It is currently accepted (e.g., [120, 119, 144]) that wetness loss primarily consist of (i) thermodynamic relaxation loss (irreversible heat transfer between droplets and steam during non-equilibrium condensation), (ii) kinematic relaxation loss (the drag due to the friction between the droplets and the steam), (iii) braking loss caused by coarse water droplets, and (iv) centrifuging loss (centrifuging liquid films on the rotor blades towards the casing).

Thermodynamic relaxation loss Rapid expansion in turbines leads steam into a non-equilibrium, subcooled state, triggering homogeneous nucleation when critical subcooling is reached. Growing droplets quickly reach a temperature close to the saturation temperature [55], which is higher than the surrounding steam temperature. Heat released by the condensation process is irreversibly transferred from droplets to the surrounding steam, bringing the flow to near equilibrium conditions (relaxation process) and increasing entropy of the mixture. This process occurs in the initial region of the wet-steam expansion (around 3-4% wetness, labelled as “the Wilson zone” in [63]) and the majority of the relaxation loss is agglomerated here. As nucleated droplets grow further downstream, relaxation loss increase is significantly reduced due to the low subcooling, except in the case where rapid expansion causes a secondary nucleation event. As shown in [179, 180], entropy production due to the thermal non-equilibrium effects per unit volume, \dot{S}_{th} , can be expressed as:

$$\dot{S}_{th} \simeq \dot{m}_l \frac{h_{lg}\Delta T}{T_s^2} \frac{Dy}{Dt} \simeq \dot{m}_l \frac{(1-y)c_{pg}}{T_s^2} \frac{\Delta T^2}{\tau_T}, \quad (2.21)$$

where y is wetness fraction, h_{lg} is the specific latent heat of condensation, \dot{m}_l mass transfer rate per unit volume c_{pg} is the isobaric specific heat capacity of steam, T_s is the saturation temperature, and τ_T is the thermal relaxation time.

Kinematic relaxation loss Nucleated droplets migrate with the surrounding steam as it passes through the machine. However, large density difference between the two phases causes droplets to acquire velocity slip and deviate from steam pathlines. The kinematic relaxation loss is, thus, caused by the friction between liquid droplets and the surrounding steam, leading to the momentum transfer responsible for additional dissipation. Entropy

production per unit volume was given in [148, 144] as:

$$\dot{S}_{kin} = \frac{N}{T_m} \mathbf{F}_D (\mathbf{v}_g - \mathbf{v}_l). \quad (2.22)$$

\mathbf{F}_D is the drag force acting on a single droplet, N is the number of droplets per unit volume, T_m is the mean temperature of the phases, and $(\mathbf{v}_g - \mathbf{v}_l)$ is the velocity slip. Kinematic relaxation loss is considered to be negligible for small droplets ($d_i < 0.1 \mu\text{m}$) which can closely follow steam pathlines. However, intermediate droplets ($0.1 \mu\text{m} < d_i < 1 \mu\text{m}$), and especially coarse water droplets, acquire a substantial slip and generate loss. A more detailed analysis of velocity slip is provided in chapter 4.

Braking and centrifuging loss As droplets develop velocity slip and deviate from surrounding steam pathlines, a portion of them impinge and deposit on the surrounding blades. Incident droplet momentum transfer onto rotor blades, caused by the different velocity triangles (resistant effect), reduces the overall turbine output and is known as braking or impact loss [119]. Water collected on blades forms rivulets and liquid films which migrate and are broken off by aerodynamic forces at the trailing edges, producing significantly larger coarse water droplets. Furthermore, liquid films on the rotor blades are centrifuged towards the tip region of the blades, thus inducing the centrifuging loss.

Coarse water droplets are considered to be around two orders of magnitude larger than homogeneously nucleated ones. Crane [27] reported droplets in the range of $10 \mu\text{m} < d_i < 100 \mu\text{m}$, Gyarmathy et al. [54] estimated the mean diameter to be around $140 \mu\text{m}$, while measurements by Moore et al. [98] reported droplets up to $300 \mu\text{m}$. Consequently, they fail to accelerate fast enough to reach steam velocity (acquire large velocity slip) and deposit in the following blade rows, significantly contributing to the total braking loss. Additionally, droplet impaction causes local pressure jumps above the yield stress of the blade material [122], resulting in blade erosion, reduction in performance and blade life span (see, e.g., [99, 121]). Hence, estimation of braking loss is highly dependent on their concentration in the flow [144].

There is a general agreement in the literature that thermodynamic relaxation loss is the primary contributor to wetness loss. Starzman et al. [144] performed CFD calculations of a model three-stage LP steam turbine operating at 9% outlet wetness and included thermodynamic and kinematic non-equilibrium conditions, while braking loss was estimated in a separate numerical calculation. The calculations showed the dominant impact of thermodynamic relaxation loss, accounting for more than 90% of wetness loss (and $\sim 1.5\%$ of

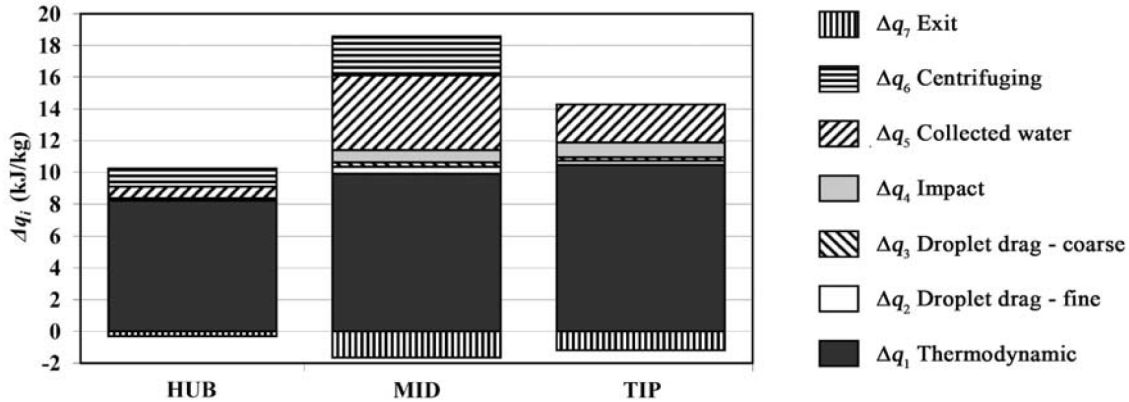


Fig. 2.7 Wetness loss breakdown for a 1000 MW nuclear LP turbine by Petr and Kolovratnik [120].

total power output of the three stages). Kinematic and braking loss were shown to be a function of droplet diameter, with braking loss approximately twice as large as kinematic relaxation loss. Due to the higher expansion rates in a model turbine, recorded droplet sizes are smaller than in full scale turbines. Hence, the contribution of kinematic and braking losses to overall wetness loss is likely to be larger in full scale turbines. Blade erosion is, however, successfully treated nowadays by water extraction and surface hardening of blades [148].

Similarly, Petr and Kolovratnik [120] performed a computational analysis of wetness loss contributors in a 210 MW fossil-fired, and a 1000 MW nuclear LP steam turbine. The model included contribution from (i) thermodynamic relaxation loss (Δq_1), (ii) kinematic relaxation loss of small (homogeneously nucleated) droplets (Δq_2), (iii) kinematic relaxation loss of large (coarse water) droplets (Δq_3), (iv) braking loss (Δq_4), (v) collected water loss (Δq_5), (vi) centrifuging loss (Δq_6), and (vii) exit energy loss (Δq_7). Calculations were performed using a statistical wake chopping model (outlined in section 2.3.1) for approximately 10000 random pathlines through the machine and the loss breakdown for three span fractions is given in fig. 2.7. Calculated thermodynamic relaxation loss was the reported as dominant wetness loss contributor while kinematic relaxation of both nucleated and coarse water droplets did not show a significant impact. Similarly, droplet deposition (braking loss) was shown to play a minor role, whereas spinning of the resulting liquid films substantially increased wetness loss.

The results in fig. 2.7 were obtained considering only homogeneous nucleation (pure steam), potentially reducing the depositional and liquid film loss contributions. Petr and Kolovratnik [119] expanded the previous study by introducing a low concentration of NaCl

as a chemical impurity, triggering both heterogeneous and homogeneous nucleation (labelled as binary nucleation). Nucleation was modelled using the theory of binary nucleation based on the capillary approximation by [108]. The calculations in a 1000 MW nuclear LP steam turbine, however, showed small difference between the binary and unary nucleation results (9% lower wetness loss and 3.6% lower Sauter mean diameter when modelling binary nucleation), indicating that turbine condensation can be predicted with sufficient accuracy when modelling only homogeneous nucleation.

2.6 Summary

This chapter demonstrated that nucleation and droplet growth are well understood and can be predicted with reasonable accuracy in steady flow conditions. However, the complex interactions between blade rows in steam turbines give rise to a plethora of new physical effects (wake chopping, velocity slip, etc.) that have a strong influence on the condensation process, change the shape of the droplet size spectrum, and give rise to a large number of loss terms. These can be predicted using high-fidelity CFD calculations which are too detailed, expensive, and time consuming for the industrial early-stage turbine design process. Therefore, there is a strong need for a rapid computational method that incorporates relevant effects and can predict turbine performance trends over a broad range of operating conditions.

Chapter 3

Unsteady wake segmentation

3.1 Introduction

As discussed in the previous chapter, the majority of authors agree that the root cause of droplet spectrum widening in steam turbines is unsteady wake segmentation (wake chopping). However, current research does not provide answers what impact does wake chopping have on turbine performance (i.e., droplet size spectra become wider but how does that affect turbine performance) or how sensitive the established wake chopping models are.

A fast and robust calculation method based on the streamline equilibrium approach that includes a stochastic wake model is presented in this chapter. The aim is to provides answers to the questions above by (i) designing a repeating stage turbine model (decoupling the influence of geometry on the droplet spectra), (ii) performing a comprehensive sensitivity study of the predominantly used wake chopping model to main parameters, (iii) examining how inlet conditions affect droplet spectra, and (iv) determining how do changes in droplet sizes affect turbine losses, therefore answering *if* and *why* wake chopping is important for turbine designers.

3.2 Streamline equilibrium description of the flow field

A streamline equilibrium (SLEQ) calculation procedure for turbine analysis and design was developed by Denton [34] and has been widely used in the turbine industry due to its capability of handling supersonic flow regions. The procedure is based on the streamline curvature method, on the assumption of axisymmetric flow – implying no circumferential variation in the velocity field or fluid properties. The flow field is represented through a set of radially distributed meridional streamlines (surfaces of revolution) set at equal mass

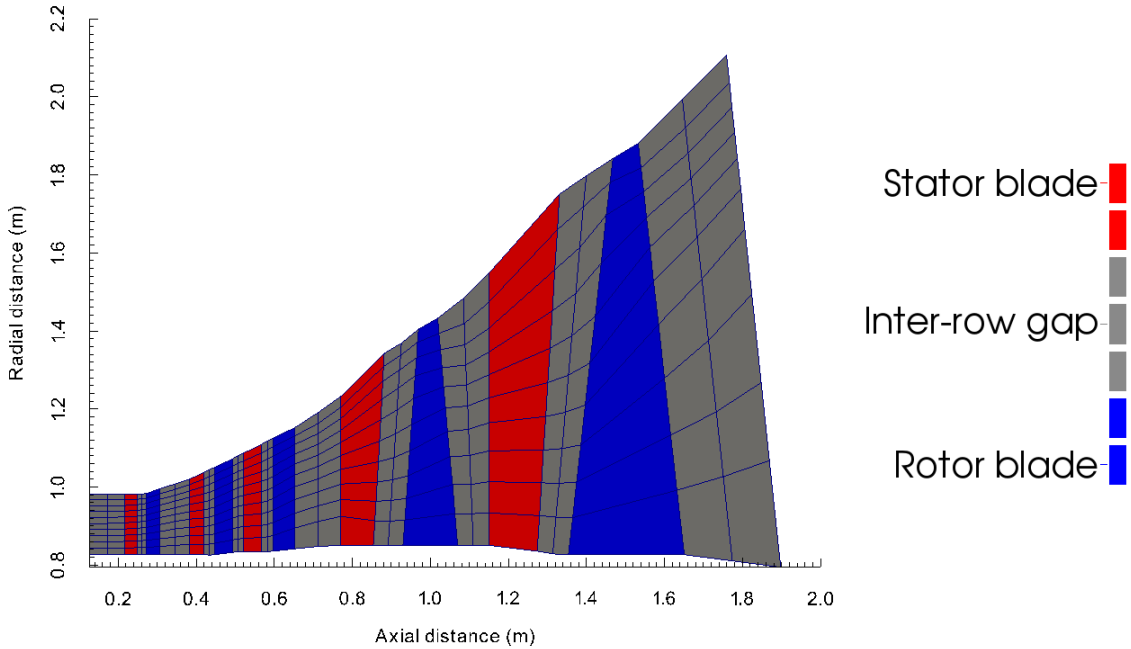


Fig. 3.1 Example of the computational grid of streamlines and quasi-orthogonals on the meridional plane.

flow intervals. The method is described in detail in [34] and is briefly outlined below for completeness.

The governing equations are defined on a set of lines approximately perpendicular to the streamsurfaces called quasi-orthogonals (QO), creating a coarse computational grid, as shown in fig. 3.1. The streamline equilibrium procedure solves the flow equations along each streamline, (at the intersections with the QOs) in terms of meridional streamline curvature.

Fluid acceleration in the QO direction at point P is balanced by the pressure gradient and the blade force component in the q direction. With reference to fig. 3.2, this equilibrium is expressed by:

$$-\frac{v_\theta^2}{r} \sin(\phi + \alpha) + \frac{v_m^2}{r_c} \sin \alpha + v_m \frac{\partial v_m}{\partial m} \cos \alpha = -\frac{1}{\rho} \frac{\partial p}{\partial q} + \frac{F_q}{\rho}, \quad (3.1)$$

where v_m and v_θ are meridional and circumferential velocity components of the steam flow, F_q is the blade force component in the q direction, and r_c is the local curvature radius. The three terms on the left hand side of eq. 3.1 represent the centripetal acceleration due to the swirl velocity, centripetal acceleration from streamline curvature and acceleration along the streamline. The pressure gradient can be expressed in terms of stagnation enthalpy and entropy by applying the second law of thermodynamics:

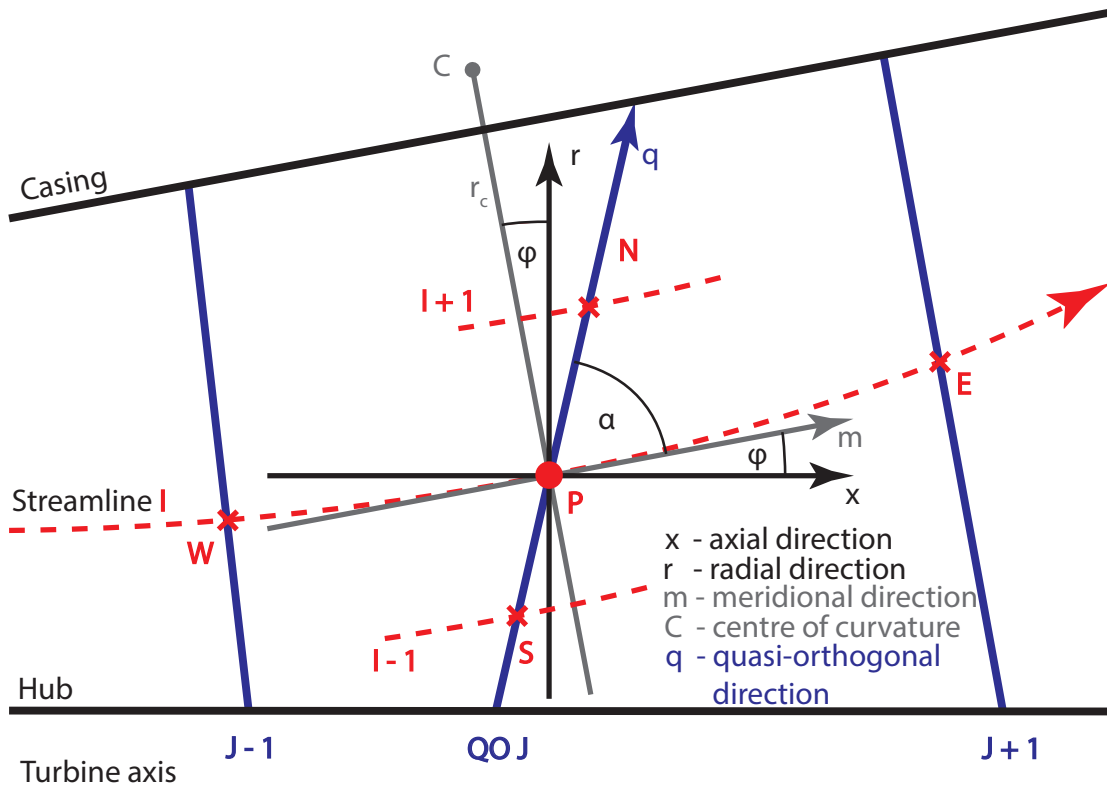


Fig. 3.2 Coordinate systems associated with a fluid parcel in streamline equilibrium.

$$-\frac{1}{\rho} \frac{\partial p}{\partial q} = T \frac{\partial s}{\partial q} - \frac{\partial h_0}{\partial q} + \frac{1}{2} \left(\frac{\partial(v_m^2)}{\partial q} + \frac{\partial(v_\theta^2)}{\partial q} \right). \quad (3.2)$$

Merging eq. 3.2 with eq. 3.1, while keeping in mind that $\sin(\alpha + \phi)$ can be written as $\partial r / \partial q$ (see fig. 3.2), leads to the core expression of the throughflow calculation:

$$\frac{1}{2} \frac{\partial(v_m^2)}{\partial q} = \underbrace{\frac{\partial h_0}{\partial q} - T \frac{\partial s}{\partial q} - \frac{F_q}{\rho} - \frac{1}{2r^2} \frac{\partial}{\partial q}(r^2 v_\theta^2)}_{\text{Radial equilibrium}} + \underbrace{v_m \frac{\partial v_m}{\partial m} \cos \alpha + \frac{v_m^2}{r_c} \sin \alpha}_{\text{Streamline curvature}}. \quad (3.3)$$

The terms in eq. 3.3 can be divided into radial equilibrium and streamline curvature contributions. Radial equilibrium terms – from left to right – are work done by the blade, aerodynamic losses, blade loading, and change in angular momentum, while the streamline curvature terms are acceleration in the streamline direction, and centripetal force due to local turbine radius.

Turbulent mixing of fluid properties (enthalpy, entropy, and angular momentum) between streamlines is coarsely modelled to prevent the accumulation of high entropy flow in the

streamlines close to the end walls (hub and casing). This is achieved by making the flow at the intersection between QO I and streamline J originate partially from the streamlines above and below ($J \pm 1$) at the QO $I - 1$. Even though this model gives a more realistic prediction than the models without streamline interactions, it can lead to reverse flow regions and, in extreme cases, calculation failure.

The SLEQ code can be used in *analysis* or *design* mode, and the calculation procedure is depicted in fig. 3.3. Analysis mode requires the specification of the turbine annulus geometry, QOs, as well as blade intermediate and trailing edge (TE) angles. This fully defines the stage enthalpy and angular momentum distributions, enabling the calculation of the velocity distribution and blade leading edge angles. The analysis mode can also be used for off-design performance prediction, assuming all blade angles are known.

In the design mode, turbine annulus, QOs, and blade loading in the form of angular momentum distribution along the blade need to be provided and are used to determine the velocity distribution, while the leading edge (LE) and trailing edge angles are varied in order to achieve the desired loading.

The meridional velocity distribution is determined based on eq. 3.3 where blade row stagnation enthalpy (h_0) is calculated from the Euler work equation along a streamline:

$$\Delta h_0 = \Delta(\Omega r v_\theta), \quad (3.4)$$

where Δ represents the change in properties from the starting to the end point, Ω is the angular velocity of the blade row, r is the local radius and v_θ is the local circumferential velocity, thus relating the change in stagnation enthalpy to the change in angular momentum (rv_θ). Therefore, in non-rotating blade rows ($\Omega = 0$) stagnation enthalpy will be constant along the streamline, while in rotating blade rows rothalpy ($I = h_0 - \Omega r v_\theta$) will be constant along the streamline. A detailed derivation of the Euler work equation can be found in any standard textbook on turbomachinery, e.g., Dixon and Hall [40].

Entropy generation is estimated based on the profile, secondary, tip leakage, and wetness loss. Profile loss is defined in line with the work from Balje and Binsley [11], with a scaling factor of 1.135 to improve the agreement with cascade data. Secondary loss is based on the work by Dunham [41], with a scaling factor of 0.75, also to improve agreement. Tip leakage loss is based on a simple analytical theory by Denton [37]. Otherwise, it can be defined through a loss coefficient provided by the user. Thermodynamic relaxation loss is implemented using Young's model [179, 180], previously shown in section 2.5. Flow properties in the ducts are calculated using the conservation equations along each streamline and fluid properties are determined using the IAPWS-IF97 equation of state.

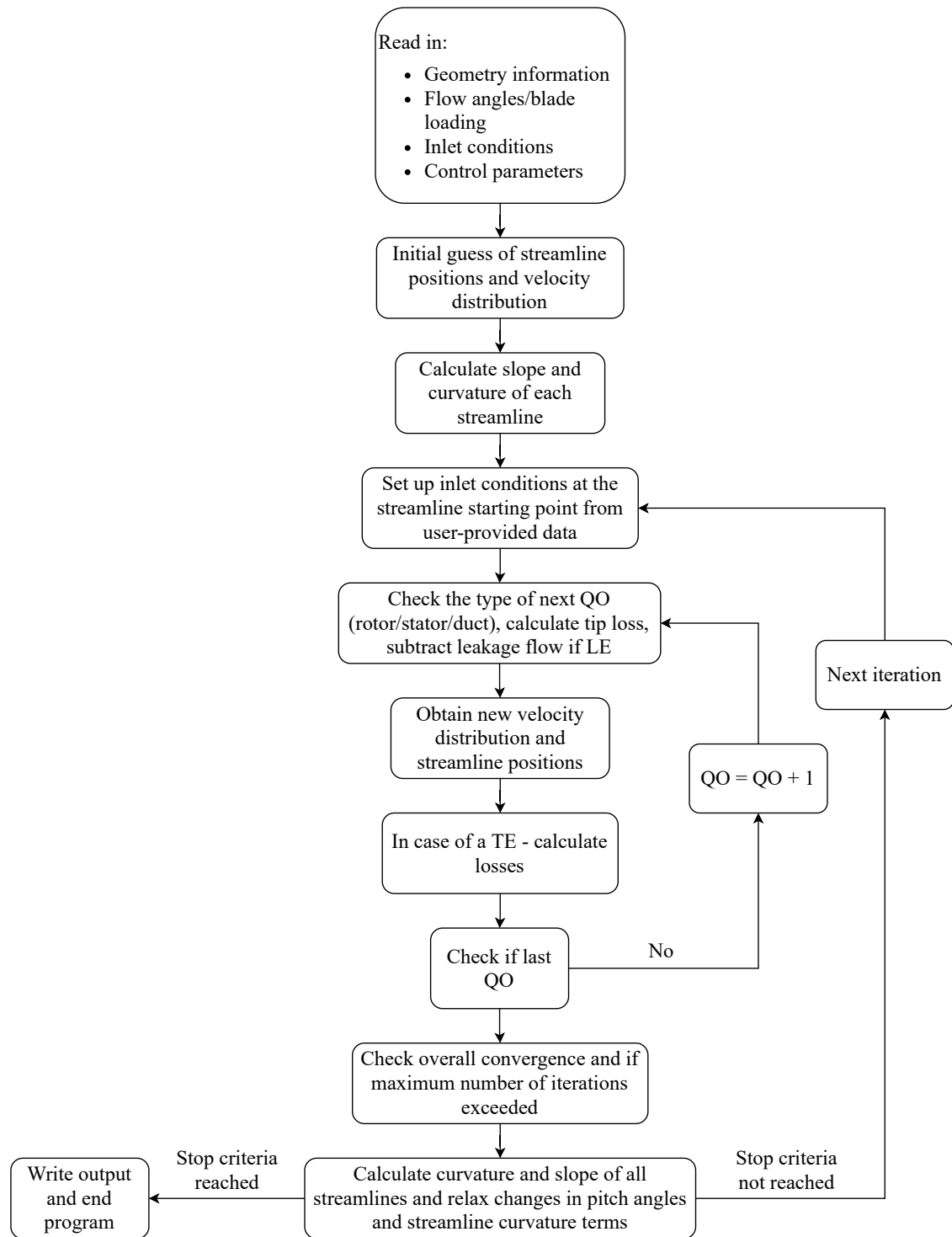


Fig. 3.3 SLEQ code flow chart.

Equation 3.3 is solved in an iterative fashion, where an initial guess of the streamline shapes is used to estimate the curvature terms. Based on the known radial equilibrium terms, a meridional velocity distribution along a streamline is obtained and the process is repeated along all streamlines. The new velocity distribution is used to determine the mass flow through the QO, expressed as an integral between two vertically neighbouring intersection points along a QO:

$$\dot{m}_{PN} = \int_P^N 2r\pi\rho v_m \sin \alpha (1-b) dq, \quad (3.5)$$

where the factor ($0 < b < 1$) accounts for blade thickness. The positions of streamline-QO intersections are then adjusted in order to achieve equal mass flow between all streamlines. The new streamline shape (inclination and curvature) is determined through a parabolic curve fit between the current point P and its east and west neighbouring points on the same streamline. The streamline curvature terms can then be updated and the process is repeated.

To improve the stability of the procedure, the updated solution needs to be introduced gradually. Unlike conventional under-relaxation of radial equilibrium terms, Denton [34] proposed that the pitch angle and the streamline curvature terms (which do not change significantly) should be damped, causing faster convergence and simplified mathematical treatment of the terms.

Another element that impacts the stability of calculations is the mesh aspect ratio, A . Work done by Wilkinson [165] showed that the optimal under-relaxation factor is inversely proportional to A^2 , leading to a high number of iterations needed for aspect ratios larger than 10. The streamline equilibrium method requires QOs to be placed at blade LE and TE, while intermediate QOs in the blade passage are rarely placed within high aspect blade rows since densely populated QOs lead to very low relaxation values and prolonged CPU time.

Due to this constraint on the number of QOs in the blade passage, the blade force in eq. 3.3 and blade thickness in eq. 3.5 are neglected. Denton [34] clarified that at least five QOs are needed to evaluate those terms, while in practice it is rarely possible to place more than one QO in the passage (aspect ratio constraint). However, the impact of blade force and blade thickness on the overall solution is negligible, thus justifying this simplification.

3.2.1 Supersonic/transonic flow treatment

The treatment of transonic and supersonic flow regimes used to pose a large difficulty on the throughflow methods due to the exceedingly high sensitivity of the velocity distribution to the mass flow rate. There are two velocity fields – subsonic and supersonic – that satisfy the desired mass flow rate and there is no way of knowing a priori which one is the correct solution. The first proposed treatment was outlined in [34], stating that these problems can

be avoided by finding the location of the throat QO. The solution can then be assigned as supersonic downstream and subsonic upstream of that QO. However, due to the aspect ratio restrictions, it is impossible to follow the same procedure in high aspect turbine blades.

Given that the throat is mostly located close to a trailing edge, the choking point can be assumed to be located between the penultimate QO and the TE QO. Using eq. 3.3, the value of relative Mach number is examined to determine where it reaches sonic or supersonic value ($M_{rel} \geq 1$). For all streamsurface-QO intersections where supersonic conditions occur, the mass flow per unit blade height is checked against the mass flow that can be passed at choking conditions. Velocity and density at the QO upstream of the throat are taken as the sonic values based on the conditions prior to the blade row, while at the TE QO they are determined from the local flow properties. The blade outlet angle (β_{TE}) is now different from its subsonic value provided as input due to the streamsurface deviation at the supersonic trailing edge and can be determined from the mass conservation equation, as defined in [36], using the opening-to-pitch ratio (O/P):

$$\cos \beta_{TE} = \frac{O}{P} \cdot \frac{(\rho w)^*}{(\rho w)_{TE}}, \quad (3.6)$$

where the (*) represents the values at sonic conditions. Equation 3.6 is then used with the estimate of the blade exit Mach number to iteratively adjust the blade exit angle, thus ensuring that the mass conservation equation is satisfied between the LE and TE. The mass flow of the choked streamtube remains constant for constant upstream conditions, therefore all streamtubes need to reach $M_{rel} \geq 1$ to achieve the complete choking of a blade row.

3.2.2 Strengths and limitations of the streamline equilibrium method

The first idea of S1 (blade-to-blade) and S2 (hub-to-tip, core of the streamline equilibrium method) calculations was introduced by Wu [172] and was the predominant method for years because of the limitations imposed by the lack of computational power. Nevertheless, even with the present 3D CFD methods, SLEQ remains the primary tool of any turbine designer due to its robustness, speed, and versatility. A typical LP steam turbine setup can be calculated in under a minute, using ideal gas properties, on an average desktop computer.¹ The accuracy of the streamline equilibrium models, according to Denton [34], mainly depends on the quality of the information provided to the calculation and not on the level of modelling detail. The flow field and performance predictions are sensitive to blade exit angles and aerodynamic entropy increase, whose values can be determined from existing correlations or directly provided by the user.

¹Tested on cases with 33 QOs and 11 streamlines, using a single i5 or i7 processor (15 W).

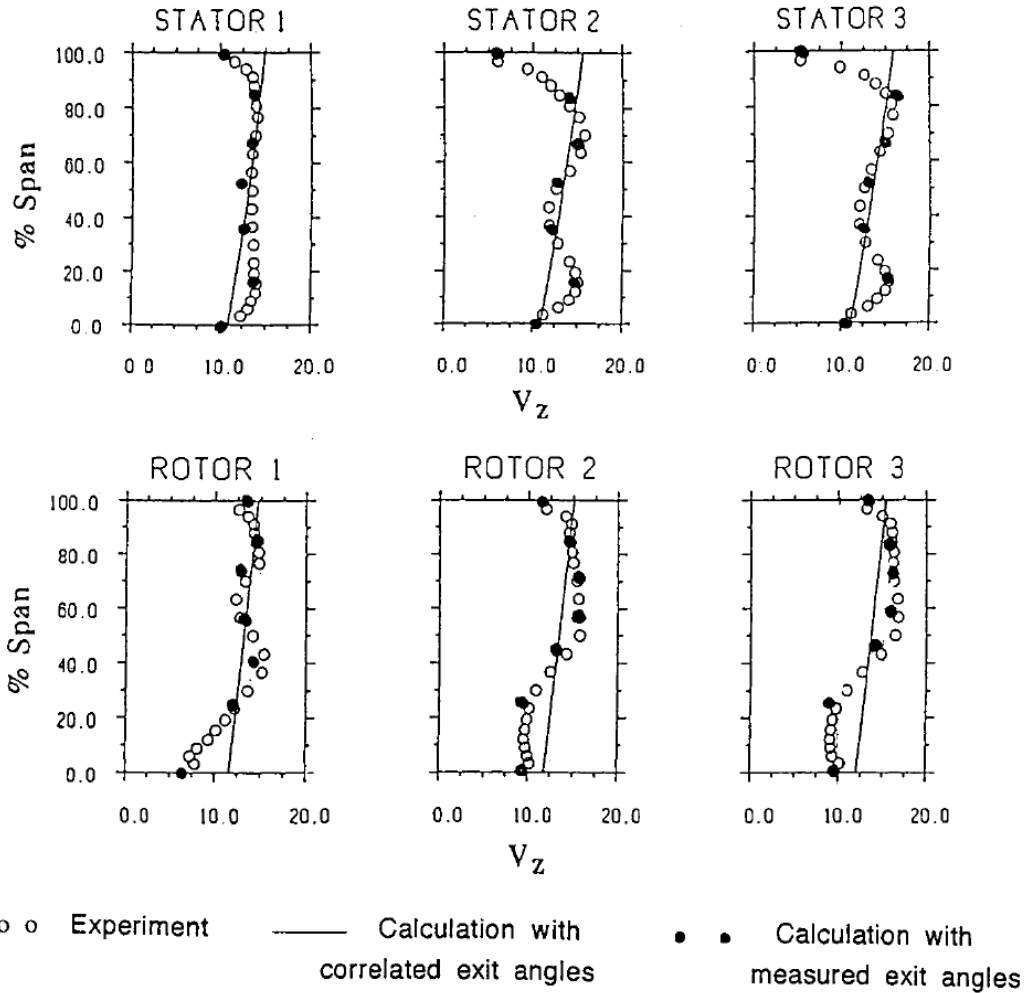


Fig. 3.4 Axial velocity profile comparison, extracted from Denton and Dawes [33].

Denton and Dawes [33] presented a comparison of streamline equilibrium axial velocity profiles (when using measured blade exit angles vs. built-in correlations) to experimental data, shown in fig. 3.4. Excellent predictions can be expected with experimental input (or 3D CFD), even while using correlations for aerodynamic entropy loss. However, this amounts to *ex-post* calibration of the model and does not paint an accurate picture of the throughflow method performance. The use of built-in correlations for both the blade exit angles and entropy reduces the quality of the output, resulting in approximately $\pm 2\%$ variation in predicted turbine efficiency [66]. While still capable of capturing general trends, SLEQ fails to predict the details of the velocity distributions. Thus, it is easy to conclude that the most accurate performance predictions for turbine design can be made when using experimental data from a similar design or 3D CFD data. SLEQ, however, was never intended as a CFD alternative. It was developed as a tool for rapid successive calculations, enabling turbine performance trend

predictions over a broad range of operating conditions and relative comparison of turbine designs (i.e., how the performance compares between two designs). Implementing the work of Young [179], SLEQ also provides information on wetness, which is not usually included with other methods (e.g., 3D CFD) due to a high computational overhead.

But SLEQ is not a tool to predict the performance of a turbine in the absolute sense since it is, in the end, an approximative method that does not capture the fine details (e.g., shock waves, boundary layers, blade sweep). Furthermore, the information on wetness is considered difficult to interpret due to high modelling uncertainty and the lack of understanding how to implement these findings into blade designs. To produce a complete design, SLEQ needs to be coupled with another method – usually involves S1 time marching for blade-to-blade design or full 3D CFD for last stage blades design.

3.2.3 Real gas properties of steam

Inclusion of condensation effects is likely to substantially increase computational cost, hence the evaluation of gas properties must be done in an efficient but accurate way. This is achieved following the method by Hill et al. [64] where a wide-ranging Helmholtz representation of stable and meta-stable equilibrium thermodynamic properties is used. The equation is expressed in the shape of a truncated Taylor series and the terms are stored in a table for quick evaluation, making this approach accurate and sufficiently fast to be used with iterative methods. The Taylor series is evaluated at several user-defined points before the start of the main calculation (as a form of pre-processing) and the accurate steam properties (within the experimental uncertainty measure) are stored in two tables. The first table contains information needed to find gas temperature (T_g) from gas enthalpy (h_g) and entropy (s_g):

$$T_g(h_g, s_g), \frac{\partial T_g}{\partial h_g}, \frac{\partial T_g}{\partial s_g}, p_g(h_g, s_g), \frac{\partial p_g}{\partial h_g}, \frac{\partial p_g}{\partial s_g}, \rho_g(h_g, s_g), \frac{\partial \rho_g}{\partial h_g}, \frac{\partial \rho_g}{\partial s_g}. \quad (3.7)$$

The second table contains information needed to find the equilibrium wetness fraction and pressure from equilibrium enthalpy and entropy:

$$p_{eq}(h_{eq}, s_{eq}), \frac{\partial p_{eq}}{\partial h_{eq}}, \frac{\partial p_{eq}}{\partial s_{eq}}, y_{eq}(h_{eq}, s_{eq}), \frac{\partial y_{eq}}{\partial h_{eq}}, \frac{\partial y_{eq}}{\partial s_{eq}}. \quad (3.8)$$

The information on the thermodynamic properties of water comes from the IAPWS Industrial Formulation (IF97) [70], which is the international standard. IAPWS formulations are also used for the viscosity [72], thermal conductivity [73], and surface tension of water [71].

The error introduced due to the discrete nature of lookup tables was examined by Chandler [23] by comparing the nozzle condensation results using a 20×20 table versus a direct

calculation method. The analysis revealed that the difference between two methods was negligible ($< 0.003\%$). Since the required computational time was shown to be insensitive to the size of the lookup table, 400×400 tables were used for all calculations presented in this work. The impact of real gas effects and condensation shocks on computational time was investigated by Hill et al. [64], where a marginal increase in calculation time was reported when real gas effects were included without condensation shocks. However, the addition of condensation shocks would almost double the required time to convergence. Since condensation shocks are an important generator of loss (thermodynamic relaxation loss), they are included in this work.

3.3 Condensation and droplet growth modelling

As described in the previous section, streamline equilibrium method can easily deal with the turbine flow field but does not provide any information on the condensation itself. Thus, it is coupled with steamLag: a Lagrangian two-phase solver that determines nucleation and droplet growth along a pre-defined pathline. SteamLag methodology for capturing the non-equilibrium condensation effects and wet steam flow has been developed by Young [186] and is briefly introduced here.

Through the condensation process, equilibrium (dry or meta-stable) steam turns into wet steam: a mixture of vapour (at pressure p , temperature T_g , and density ρ_g) and a large number of uniformly dispersed spherical water droplets. Droplets have a distinct diameter, creating a continuous function of droplet sizes which is modelled using N discrete droplet groups. The number of groups is chosen in a way to reduce the memory requirements and computational time while preserving the overall shape and features of the droplet size distribution. The space between the droplets is assumed to be sufficiently large that any interaction between the droplets can be neglected. Moreover, the effect of droplets on the surrounding steam flow is assumed to be small enough to be neglected, leading to a one-way vapour-liquid coupling. Since the droplets are considered to be uniformly distributed, it allows for the simplification of all equations by expressing them per unit mass of mixture.

Due to their small size, nucleated droplets are assumed to follow the steam flow without any velocity slip.² Droplet properties are considered to be uniform and are evaluated at the saturation temperature associated with the local steam pressure.

Each droplet group consists of n_i droplets with the radius r_i , having mass m_i . Droplet size groups individually contribute to the wetness fraction y (per unit mass mixture) as:

²This assumption will be relaxed in chapter 4 to investigate depositional processes.

$$y = \sum_{i=1}^N y_i = \sum_{i=1}^N n_i m_i = \sum_{i=1}^N n_i \cdot \frac{4}{3} r_i^3 \pi \rho_l, \quad (3.9)$$

where the ρ_l is the density of water. The mixture volume, V , is occupied by the volume of liquid water, V_l , and the volume of steam, V_g . Dividing it with the mass of the mixture, the expression for mixture density, ρ , is found:

$$\frac{1}{\rho} = \sum_{i=1}^N \frac{V_{l,i}}{m_{l,i}} \frac{m_{l,i}}{m} + \frac{V_g}{m_g} \frac{m_g}{m} = \sum_{i=1}^N \frac{y_i}{\rho_l} + \frac{1-y}{\rho_g} \approx \frac{1-y}{\rho_g}. \quad (3.10)$$

Since the volume occupied by water is considerably smaller than the volume of steam, the mixture density can be approximated by $(1-y)/\rho_g$ as shown in eq. 3.10. Now the equations for enthalpy, entropy and specific internal energy of the mixture can be written in terms of wetness fraction:

$$h = \sum_{i=1}^N y_i h_i + (1-y) h_g, \quad (3.11)$$

$$s = \sum_{i=1}^N y_i s_i + (1-y) s_g, \quad (3.12)$$

$$e = \sum_{i=1}^N y_i e_i + (1-y) e_g. \quad (3.13)$$

Steam and droplet enthalpies can be expressed as $h_g = e_g + p/\rho_g$ and $h_i = e_i + p/\rho_l$. The pressure p here is the partial pressure of vapour and, considering the partial pressure of droplets to be negligible, it can be treated as stagnation pressure.

The conservation equations for inviscid, thermally non-conducting flow of the wet steam mixture take the shape equal to their single phase flow counterparts, however using mixture properties (eqs. 3.11 to 3.13) as transported properties:

$$\frac{\partial \rho}{\partial t} + \nabla \cdot (\rho \mathbf{v}) = 0, \quad (3.14)$$

$$\frac{D\mathbf{v}}{Dt} + \frac{\nabla p}{\rho} = 0, \quad (3.15)$$

$$\frac{\partial(\rho e_0)}{\partial t} + \nabla \cdot (\rho \mathbf{v} h_0) = 0. \quad (3.16)$$

The conservation eqs. 3.14 – 3.16 are expressed in the Lagrangian sense, following a steam parcel along a pathline, where D/Dt stands for the material derivative $D/Dt = \partial/\partial t + (\mathbf{v} \cdot \nabla)$. They can be used to express the thermodynamic form of the energy equation:

$$\frac{Dh}{Dt} - \frac{1}{\rho} \frac{Dp}{dt} = 0. \quad (3.17)$$

Identical expression can be obtained by treating the fluid particle as a closed thermodynamic system.

It is important to point out that, unlike in the single phase, adiabatic, inviscid flow, eq. 3.17 does not imply no entropy production. Irreversibilities caused by various aerodynamic effects (profile loss, shock waves, etc.) are introduced in the form of entropy increase along the streamline to the right hand side of the eq. 3.17:

$$\frac{Dh}{Dt} - \frac{1}{\rho} \frac{Dp}{dt} = T_g \frac{Ds_{aero}}{Dt}. \quad (3.18)$$

The energy transport equation between i -th droplet group and the surrounding steam, when assuming no droplet velocity slip, was derived by Jackson and Davidson [77]:

$$(h_g - h_i) \frac{Dm_i}{Dt} = 4r_i^2 \pi \alpha_i (T_i - T_g) + m_i \frac{Dh_i}{Dt}. \quad (3.19)$$

α_i is the surface heat transfer coefficient, defined by Gyarmathy [101] as:

$$\alpha_i = \frac{k_g}{r_i [1 + 3.78(1 - v_y) \text{Kn}_i / \text{Pr}_g]}, \quad (3.20)$$

where k_g is the thermal conductivity of vapour, $(1 - v_y)$ is the Young's correction factor proposed in [184] and shown previously in eq. 2.18. Pr_g is the vapour Prandtl number and Kn_i is the Knudsen number ($\text{Kn}_i = \lambda_g / 2r_i$) of the i -th droplet group. The mean free path of vapour (λ_g) was defined by Gyarmathy [54] as:

$$\lambda_g = \frac{1.5 \mu_g \sqrt{RT_g}}{p}, \quad (3.21)$$

where μ_g is the vapour dynamic viscosity.

Droplet nucleation and growth equations were defined in section 2.2 and are used to determine the new wetness fraction while assuming constant subcooling across the timestep. The droplets and the surrounding steam are not in equilibrium since the droplets are at saturation temperature and steam expanded into the supersaturated state. The difference in temperature between the two phases is expressed through subcooling. Subcooling, ΔT , is a measure of how much the temperature of a substance differs from the saturation temper-

ature corresponding to the local pressure, in this case defining how much lower the vapor temperature is compared to the local saturation temperature:

$$\Delta T = T_g - T_S(p). \quad (3.22)$$

Standard thermodynamic expression for the imperfect vapour is:

$$dh_g = c_{p,g}dT_g + \left(1 - \frac{\alpha_g T_g}{\rho_g}\right) dp, \quad (3.23)$$

where α_g is the coefficient of steam expansion at constant pressure:

$$\alpha_g = -\frac{1}{\rho_g} \left(\frac{\partial \rho_g}{\partial T_g}\right)_p. \quad (3.24)$$

Combining the eqs. 3.18 and 3.23 (with mixture properties substituted inside), while keeping in mind the definition of subcooling, leads to the expression for the change in vapour subcooling over the integration time step in terms of wetness fraction and pressure change:

$$\frac{D(\Delta T)}{Dt} = \frac{DT_S(p)}{Dt} - \frac{1}{c_{p,g}} \left\{ \sum_{i=1}^N \frac{D}{Dt} [y_i(h_g - h_i)] + \left(\frac{\alpha_g T_g - y}{\rho_g}\right) \frac{Dp}{Dt} + T_g \frac{Ds_{aero}}{Dt} \right\}. \quad (3.25)$$

The non-equilibrium phase change process will cause an increase in entropy, which is modelled as:

$$\frac{Ds_{th}}{Dt} = \frac{\Delta T}{T_g T_S} \left[\underbrace{\left(h_{lg} - c_{p,g} \Delta T \right) \frac{Dy}{Dt}}_{\text{Irreversible heat transfer}} - y \underbrace{\left(c_{p,l} \frac{DT_S}{Dt} - \frac{1}{\rho_l} \frac{Dp}{Dt} \right)}_{\text{Liquid mass entropy change}} \right]. \quad (3.26)$$

Equation 3.26 was derived using Young's definition of the irreversible heat transfer and the change in entropy of the liquid droplets. The second term comes from rearranging the thermodynamic form of the energy equation.

The calculations are performed in the Lagrangian framework, following the vapour parcels (integrating the eq. 3.19 along each streamline) one by one from turbine inlet to outlet. This increases the accuracy (compared to Eulerian methods) in the Wilson zone region, where the flow is very sensitive. The calculation procedure requires information on pressure and aerodynamic entropy increase, Δs_{aero} , specified as a function of time along each streamline. They are usually provided by coupling the calculation with a general flow solver (e.g. SLEQ) but can be also provided directly by the user. Notice that the nucleation and droplet growth calculation procedures are written in the thermodynamic form, hence not requiring any

information on the velocity field, and allowing the calculation to be executed independently of the flow solver. The method allows for dynamic change of the integration time step, enabling local refinement in regions with large gradients. The main interval is segmented into a number of sub-steps, and the pressure and entropy across each are determined using four-point Lagrangian interpolation. The integration scheme relies on the predictor-corrector iterations, where the predictor step uses steam properties from the integration starting point, and the calculated wetness is used to estimate the steam properties at the end of the integration step, using eq. 3.18. In the corrector step, the mean value of steam properties across the integration step is used to update the wetness prediction. According to [186], around four to five steps are usually needed to reach convergence, but even one step is enough to produce an estimate sufficiently accurate for practical purposes. The calculated thermodynamic entropy increase and wetness fraction are then propagated back to the flow calculation (e.g., SLEQ) to improve the flow field prediction, and the process is repeated until a stop-criterion is reached.

3.4 Unsteady wake segmentation modelling

The majority of wake chopping models described in section 2.3.1 follow a stochastic approach to capture the unsteady nature of the underlying physical process. This model follows a similar approach, tracking a large number of fluid parcels as they pass through a representation of the turbine flow field.

The model was developed as an extension to the SLEQ code, following the mathematical procedures outlined in section 2.3, and it neglects radial wake deformations and radial mixing between different streamlines. It uses a prescribed circumferential polytropic efficiency distribution for each blade row to capture the variation in loss generation across the pitch as the efficiency decreases with proximity to the blade surfaces. Circumferentially and time averaged entropy increase in each blade passage calculated by SLEQ is converted into averaged polytropic efficiency:

$$\bar{\eta} = \frac{dh}{dh_{is}} = \frac{\Delta h_{is} - T_2 \Delta s_{aero}}{\Delta h_{is}}, \quad (3.27)$$

based on a sufficiently small time step, where T_2 is the temperature at the end of the time step. Experimentally obtained efficiency distributions across the pitch can be provided by the user but they are rarely available. Hughes [68] compared a CFD-generated³ pitchwise time-averaged loss distribution to a Gaussian function, and reported a very close match

³Eulerian 3D calculations of viscous two-phase flow using an unsteady RANS solver, applied to a turbine cascade.

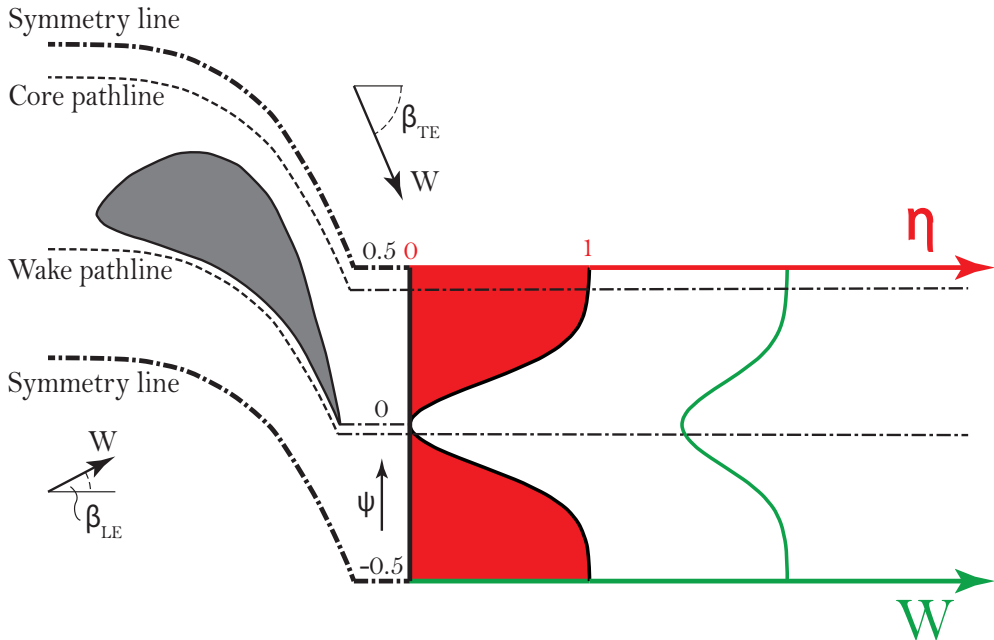


Fig. 3.5 Schematic of polytropic efficiency assignment to individual pathlines across the pitch.

between the two. While wakes in turbines are not perfectly symmetric, this suggests that they can be described with sufficient accuracy using simple mathematical functions. Hence, $\bar{\eta}$ is then used to construct a mathematical representation of the efficiency profile (approximative wake shapes) across the pitch $\eta(\psi)$, where ψ is a non-dimensional mass flow function.

The polytropic efficiency profile $\eta(\psi)$ represents a time-averaged efficiency distribution across the pitch and is defined at the inlet of each blade row. Each steam parcel is assigned a random value of ψ at each LE, as shown in fig. 3.5, thereby defining its dissipation as it passes through the machine. A full description of the wake profiles is provided later in section 3.4.3 and appendix B.

Direct mixing between individual pathlines is not considered in this model. However, wakes do not persist but are slowly diffused. They are influenced by molecular and turbulent diffusion, leading to erosion of gradients in specific rothalpy of the flow, implying that – given enough time – all steam parcels would reach the same, mass-flow-weighted average value of specific rothalpy, \tilde{I}_∞ . The time averaged energy equation approximating this physical

behaviour was given by Guha and Young [53] as:

$$\bar{\rho} \frac{d}{dt} \left[\tilde{h}_0 - 0.5(\Omega \wedge r)^2 \right] \approx \frac{\partial \bar{p}}{\partial t} + \nabla \cdot \left[\frac{k + k_t}{c_p} \nabla \bar{h}_0 \right], \quad (3.28)$$

where the overbar stands for Reynolds-time averaged mean (e.g., $\bar{\rho}$) and the tilde for Favre density-weighted, time-averaged mean values (e.g., \tilde{h}_0), while k and k_t represent thermal and turbulent heat conductivity, respectively.

Since the oscillations in the pressure field as well as the magnitude and variation in turbulent heat conductivity are too computationally expensive to be determined,⁴ eq. 3.28 is approximated by an exponential decay model, assuming all pressure fields are steady with respect to both stationary and rotating blade rows:

$$\frac{dI}{dt} = -\frac{I - \tilde{I}_\infty}{\tau_w}, \quad (3.29)$$

where I_∞ is the average specific rothalpy and τ_w is the time constant associated with the erosion of gradients (wake decay). The case when $\tau_w = 0$ gives instantaneous equilibration of gradients, where wakes are averaged out as soon as they form, and $\tau_w \rightarrow \infty$ represents infinitely slow wake decay where wakes unchangingly persist in the flow. A simple wake decay analysis given in [53] estimated the wake decay temporal constant as:

$$\tau_w = 5\Delta t_{ls}, \quad (3.30)$$

where Δt_{ls} is the transit time in the last stage stator. Integrating eq. 3.29 and removing “~” for convenience now gives:

$$I - I_\infty = (I_{LE} - I_\infty) \exp \left(-\frac{t}{\tau_w} \right), \quad (3.31)$$

where I_{LE} is the rothalpy at the blade leading edge and t is the time as observed by the fluid parcel. Equation 3.31 is used to model the erosion of gradients, cooling down the high-entropy, hot wakes, and heating up the colder core of the flow.

Mass flow averaged mean rothalpy values, used for wake decay, can be quickly determined by performing a single non-equilibrium calculation (e.g., using the steamLag code defined in section 3.3) on each streamsurface, applying the averaged polytropic efficiency $\bar{\eta}$ for each blade row.

⁴Obtaining a reasonable estimate would require an unsteady 3D RANS/LES calculation.

Steam expansion in a wake chopping calculation yields different values of thermodynamic flow properties along each pathline, caused by different polytropic efficiencies, resulting in a different number and size of nucleated droplets. Directly storing all that information is costly (and unnecessary), and can be avoided by efficient programming, whereby information on only two pathlines is stored. One is the current wake chopping pathline being calculated (*sandbox* pathline), containing information on flow properties and droplet spectrum for the currently calculated steam parcel. Once the parcel reaches the exit, the flow results are aggregated onto a *running-average pathline* which contains contributions (mass flow weighted average) from all pathlines calculated so far. The *sandbox* pathline is then cleared out for the next steam parcel calculation and the process repeats itself until a convergence criterion is reached.

Each nucleation event generates a new droplet group, which can result in a vast number of groups – especially when the aggregation of many thousands of pathlines is considered. This difficulty is overcome by modifying the droplet spectrum “pruning” method, developed by [186]. This entails dividing the (continuous) droplet size space into fixed-width bins, whereby all droplet size groups whose diameter falls within the bin are combined into a single group. The mass is conserved by converting each group into contributing liquid mass which is added to the bin. The droplet groups generated in each pathline calculation are automatically added to the running-average droplet size spectrum, which is now expressed in terms of liquid mass in each bin (each bin is associated with the mean diameter on the range it covers).

3.4.1 Model integration with a flow solver

A routine called *chopCode*, based on the wake chopping model described in the previous section, was integrated with the SLEQ throughflow code. It was, however, programmed as a “black box” that can be attached to any flow solver that provides the right input variables, or on its own (user input required). The routine requires information on the turbine flow field (axial time-averaged pressure and efficiency distributions), and returns improved predictions of wetness, droplet spectra and thermodynamic relaxation loss (see full information list in table 3.1). Numerical experimentation revealed that equilibrium SLEQ calculations provide a sufficiently accurate initial guess of the flow field for the wake chopping calculation (more on this is given in ch. 5). The wake decay model depends on the values coming from a single expansion (single pathline) calculation using circumferentially averaged pressure and polytropic efficiency, defining the values towards which all subsequent pathlines are relaxed.

The wake chopping calculation starts at this point and typically requires approximately 10000 random pathlines to converge. Finally, around 300 subsequent non-equilibrium SLEQ

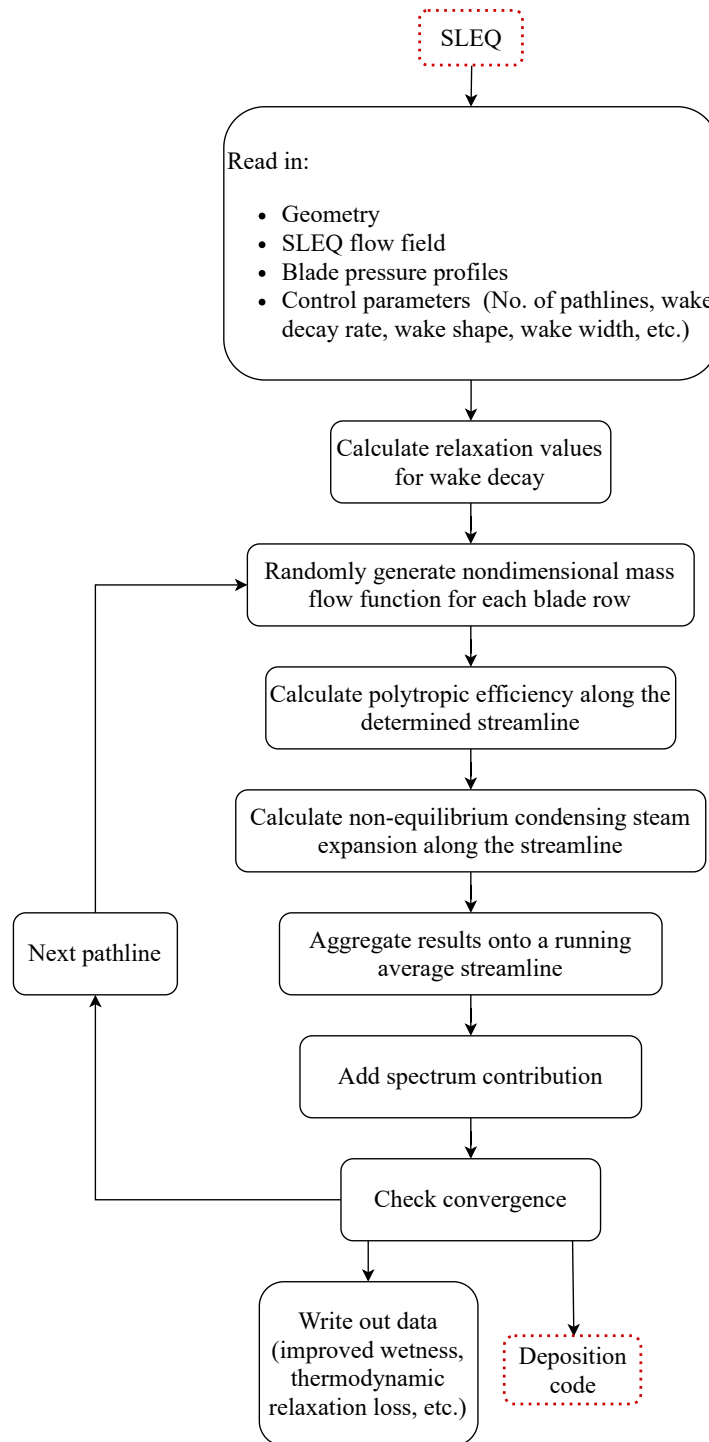


Fig. 3.6 ChopCode flow chart.

iterations are required to update the flow field, as the wake-chopping improvements have only a minor impact on the main flow variables. The computational procedure is outlined in fig. 3.6.

The information on pressure variation within a blade passage cannot be extracted from SLEQ due to low grid resolution. Considering its effect on the condensation zone, it needs to be provided by the user – usually from CFD calculations or experimental measurements, as a generic non-dimensional blade pressure profile (pressure and suction side distributions). The profile is uniformly scaled to ensure that the net pressure (and, thus, the resulting torque) matches the net pressure coming from the flow solver. SLEQ net pressure is determined from the modified Euler equation, using flow turning (change in angular momentum), as:

$$\Delta p = \rho P \frac{v_{x,LE}}{\Delta t_{avg}} (\tan \beta_{LE} - \tan \beta_{TE}). \quad (3.32)$$

Table 3.1 ChopCode input data

Input	Details	Source
Geometry	$I, J, x(J, I), r(J, I), IND(J)$	SLEQ
Inlet conditions	p_{in}, T_{in}, s_{in}	SLEQ
Flow field	$t(J, I), v_x(J, I), p(J, I), \beta(J, I)$	SLEQ
Average polytropic efficiency	$\bar{\eta}$	SLEQ
Pitchwise efficiency distribution	$\eta(\psi)$ for each blade passage	External
Pressure distribution (passage)	$p(t, \psi)$ for each blade passage	External
Wake width	σ_w	External
Wake decay rate	τ_w	External

3.4.2 Random-walk wake-chopping model

Dimensionless mass flow function ψ , used to randomly prescribe the pitchwise position of an i -th steam parcel at a blade row inlet, is an independent and identically distributed (i. i. d.) random variable, uniformly distributed on the $[-1/2, 1/2]$ range:

$$\psi_i \sim U \left[-\frac{1}{2}, \frac{1}{2} \right]. \quad (3.33)$$

The polytropic efficiency profiles are then constructed as a function of ψ in a way that reflects the progressive efficiency decrease with proximity to the solid surfaces (wake region).

The $\eta(\psi_i)$ distributions are assumed to be symmetric around zero, whereby $\psi = \pm 0.5$ corresponds to the core of the flow (both sides of the blade) and $\psi = 0$ indicates blade surface. The consistency between different wake profiles is ensured by matching their mean efficiency and variance.

In this work, four functions (wake shapes) are selected: truncated Gaussian, linear (triangular wake), quadratic, and step function (square wake). Gaussian function (G) is a natural choice for an empirical distribution of any physical occurrence and serves as the baseline function. Linear function (L) is chosen as the extreme case of the Gaussian, where the decay is exactly linear and positive as ψ moves away from zero. A quadratic function (Q) is also an extreme version of the Gaussian which eliminates all the convexity at the tails, and imposes that efficiency decays at an increasing rate as ψ moves away from zero. Finally, the step function (S) imposes that efficiency is a positive constant number (flat line) close to $\psi = 0$, and zero everywhere else; representing another extreme case.

The parameters of each of the four functions $\eta_k(\psi)$, $k \in \{G, L, Q, S\}$ are chosen such that:

1. Expected value of $\eta_k(\psi)$ is equal to the empirically measured average blade row efficiency, $\bar{\eta}$
2. Standard deviation of $\xi_k(\psi)$ is proportional to the empirically measured wake width σ_w , specifically so that when the efficiency loss function $\xi_k(\psi)$ is the Gaussian function (defined below) with parameters $\mu_G = 0$ and $\sigma_G = \sigma_w$, the resulting standard deviation of efficiency loss should be the same for each of the subsequent three functions.

Accurate empirical values of blade row efficiencies and wake widths are rarely available and, while $\bar{\eta}$ can be estimated with throughflow calculations, σ_w cannot be determined with any level of certainty without going into more complex (and costly/time consuming) calculations. It is, however, assumed that wake width is sufficiently narrow that $\eta(\pm 0.5) \approx 1$, and the sensitivity of droplet size spectra to a range of wake widths is examined later in section 3.17 .

3.4.3 Gaussian wake profile

Defining pitchwise loss distribution as:

$$\xi(\psi) = 1 - \eta(\psi), \quad (3.34)$$

the standard expression for the Gaussian function can be written as:

$$\xi_G(\psi) = \bar{\xi} \frac{1}{\sqrt{2\pi}\sigma_G} \cdot \exp\left(-\frac{1}{2} \frac{(\psi - \mu_G)^2}{\sigma_G^2}\right). \quad (3.35)$$

The maximal loss is experienced by parcels in immediate proximity of the blade surfaces, located at $\psi = 0$, thus requiring the function to be centred around the same value. The variance of the loss $\xi_G(\psi)$ is made proportional to the wake width σ_w by setting the Gaussian parameter σ_G to equal the wake width:

$$\mu_G = 0, \quad \sigma_G = \sigma_w. \quad (3.36)$$

Thus, we have:

$$\xi_G(\psi) = \bar{\xi} \frac{1}{\sqrt{2\pi}\sigma_w} \cdot \exp\left(-\frac{1}{2} \frac{\psi^2}{\sigma_w^2}\right). \quad (3.37)$$

Since parameters $\bar{\xi}$ and σ_w are externally imposed, this function is fully characterised for any ψ . The variance can now be expressed as:

$$Var[\xi_G(\psi)] \equiv \sigma_{\xi}^2 = \bar{\xi}^2 \left(\frac{1}{2\sigma_w\sqrt{\pi}} - 1 \right). \quad (3.38)$$

An example Gaussian wake profile, defined with loss $\bar{\xi} = 0.1$, corresponding polytropic efficiency $\bar{\eta} = 0.9$ and wake width $\sigma_w = 0.04$ blade passage width, scaled with the expected value of loss is shown in fig. 3.7.

As mentioned before, the Gaussian variance in eq. 3.38, which is proportional to the wake width σ_w , will be used to parametrise the remaining three functions. The parameters of the three remaining functions will be found by imposing that:

$$\mathbb{E}[\xi(\psi)] = \bar{\xi}, \quad (3.39)$$

$$Var[\xi(\psi)] = Var[\xi_G(\psi)] = \bar{\xi}^2 \left(\frac{1}{2\sigma_w\sqrt{\pi}} - 1 \right). \quad (3.40)$$

Full derivation of the remaining wake functional forms can be found in appendix B and only the final expressions are given in Table 3.2. Comparison of wake functional forms is graphically shown for $\bar{\eta} = 90\%$ and $\sigma_w = 0.04$ in fig. 3.8a. The influence of wake asymmetry on predicted droplet spectra is examined by extending the linear (triangular) wake shape by specifying the asymmetry ratio, r , defined as a ratio of pressure and suction side wake widths.

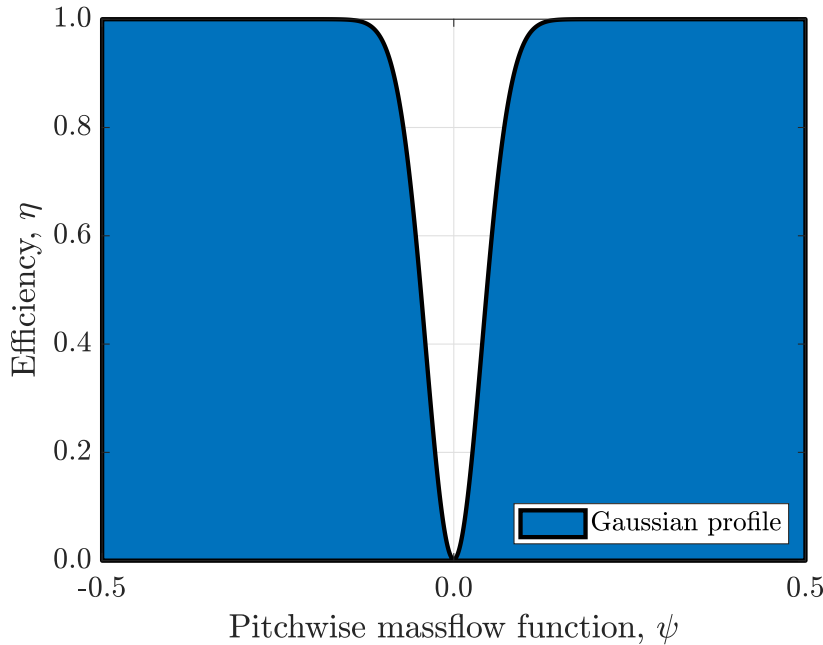
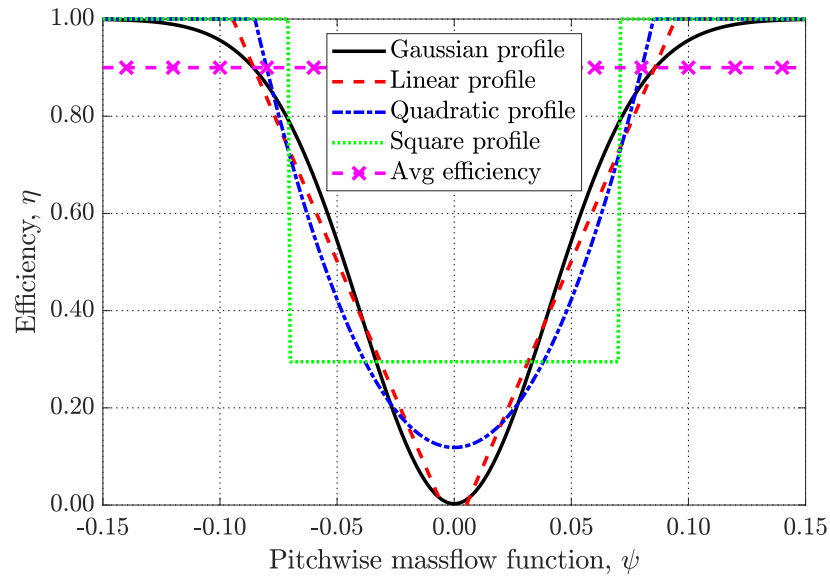


Fig. 3.7 Schematic of wake representation across the pitch, $\bar{\eta} = 90\%$, $\sigma_w = 0.04$.

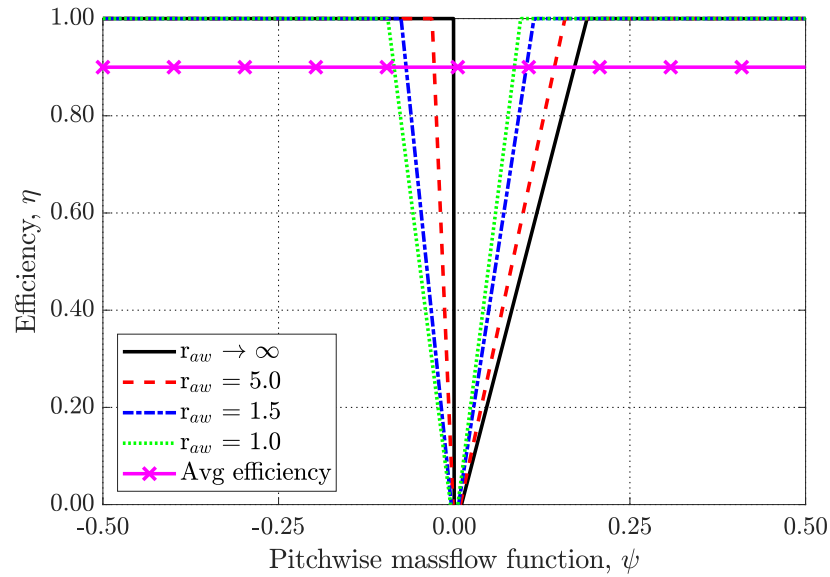
Wakes can thus be defined anywhere on the range from solely pressure side wakes ($r \rightarrow \infty$) to solely suction side wakes ($r \rightarrow -\infty$), as seen in fig. 3.8b. Having defined the polytropic efficiency paths through a single blade row, the calculation can be easily extended to cover multiple blade passages (and inter-row gaps by assuming $\eta(\psi) = 1$), forming a statistical random walk process.

Table 3.2 Wake shape definitions

Profile description	$\xi_k(\psi)$, $k \in \{G, L, Q, S, A\}$
Gaussian	$\xi_G(\psi) = \bar{\xi} \frac{1}{\sqrt{2\pi}\sigma_w} \cdot \exp\left(-\frac{1}{2} \frac{\psi^2}{\sigma_w^2}\right)$
Linear	$\xi_L(\psi) = \bar{\xi} \frac{3}{4\sqrt{\pi}\sigma_w} \left(1 - \frac{3 \psi }{4\sqrt{\pi}\sigma_w}\right)$, for $ \psi \leq \frac{4\sqrt{\pi}\sigma_w}{3}$
Quadratic	$\xi_Q(\psi) = \bar{\xi} \left(\frac{5}{8\sqrt{\pi}\sigma_w} - \frac{16}{9} \left(\frac{5}{8\sqrt{\pi}\sigma_w} \right)^3 \psi^2 \right)$, for $ \psi \leq \frac{\sigma_w\sqrt{\pi}}{30}$
Step (square)	$\xi_S(\psi) = \begin{cases} \bar{\xi} \cdot \frac{1}{2\sigma_w\sqrt{\pi}} & \psi \leq \sigma_w\sqrt{\pi} \\ 0 & \text{otherwise.} \end{cases}$
Asymmetric linear	$\xi_A(\psi) = \begin{cases} \bar{\xi} \cdot \frac{3}{4\sqrt{\pi}\sigma_w} \left[1 - \frac{3(1+r) \psi }{8\sqrt{\pi}\sigma_w}\right] & -\frac{8\sigma_w\sqrt{\pi}}{3(1+r)} \leq \psi \leq 0 \\ \bar{\xi} \cdot \frac{3}{4\sqrt{\pi}\sigma_w} \left[1 - \frac{3(1+r) \psi }{r \cdot 8\sqrt{\pi}\sigma_w}\right] & 0 \leq \psi \leq r \cdot \frac{8\sigma_w\sqrt{\pi}}{3(1+r)} \end{cases}$



(a) Detail of the blade wake profiles.



(b) Asymmetric wake profiles for a range of asymmetry ratios.

Fig. 3.8 Artificial blade wake profiles, $\bar{\eta} = 90\%$ and $\sigma_w = 0.04$.

3.5 Test case – repeating stage turbine design

This parametric study of wake chopping is intended as a guide, determining how sensitive the droplet size spectrum and associated losses are to model parameters. The current body of knowledge suggests that small changes in model assumptions can, in some cases, result in significant differences in the resulting spectrum (e.g., bimodality, shape, and width of the spectrum), i.e., when modelling only axial expansion rate variation, where expansion rate is defined as:

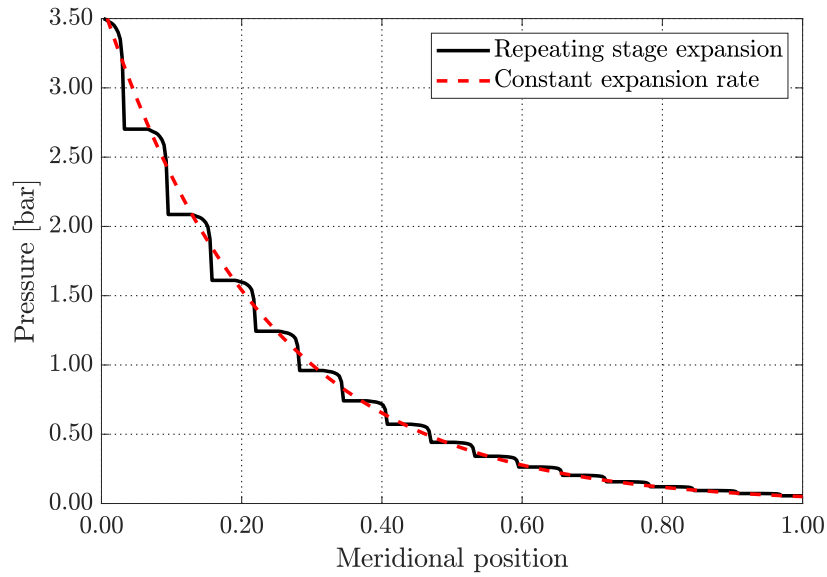
$$\dot{p} = \frac{D[\ln(p)]}{Dt}. \quad (3.41)$$

The inherent complexity of turbine flow fields is exacerbated by having different blade row geometries at each stage, changing the Wilson zone conditions depending on the blade row at which the condensation occurs. Hence, small changes in e.g., wake decay rate or inlet temperature can shift the nucleation zone to a region of completely different expansion rates, demonstrating a sensitivity to both model parameters and inlet conditions (as reported by [53] and [116]).

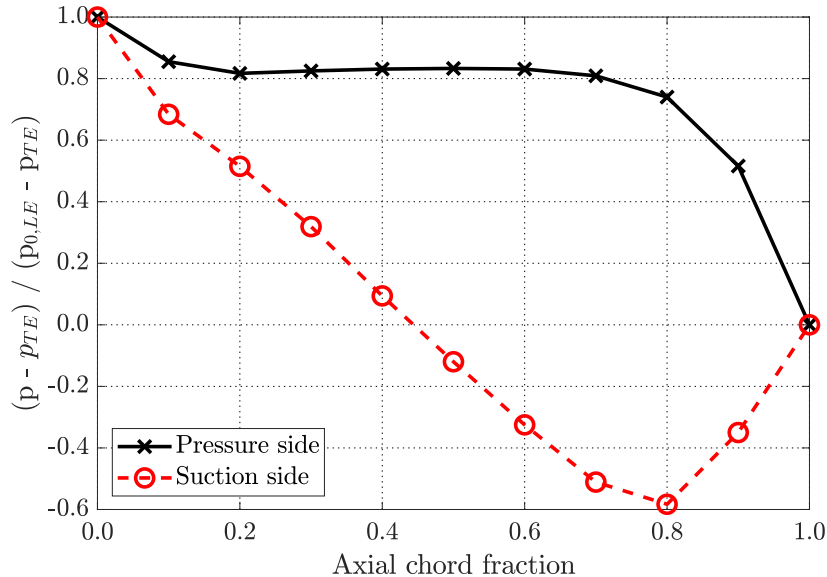
Such complexity also means it is incredibly difficult to determine the exact contribution of turbine geometry characteristics versus variation in modelling assumptions to changes in droplet size spectrum. Thus, in the spirit of statistical regression analysis⁵, the test case for measuring the isolated effect of modelling assumptions on the droplet size spectrum was designed as a hypothetical eight stage repeating-stage design. This design enables the decoupling (or, at least, limiting the influence) of geometrical characteristics of individual blade rows from the effects of modelling parameters on the results. Eight stages were chosen specifically for representativeness, since the aim is to show the cumulative effect of varying model assumptions on the resulting droplet size spectrum for a “model” turbine that could be encountered in practice. Moreover, the flow has enough time in the machine to revert to equilibrium, hence allowing for the model assumption effects to be completely reflected in the droplet spectrum.

Calculations were performed in one dimension, following a meridional representation of the mid-streamsurface, using a typical axial pressure distribution with a pressure ratio of 0.6 per stage, extracted from Hughes [68] and shown in fig. 3.9a. Suction and pressure side pressure distributions shown in fig. 3.9b are based on CFD results by Hughes [68] and scaled according to blade loading using eq. 3.32. Circumferential pressure distribution is assessed

⁵The regression parameters reflect the sensitivity of the outcome variable (droplet size spectrum) to perturbations of a single independent variable (modelling assumptions or geometry) while holding all else constant.



(a) Centreline axial pressure distribution for a constant and a variable expansion rate.



(b) Blade pressure profile based on CFD results in [68].

Fig. 3.9 Pressure distributions in the repeating-stage model turbine.

using a simple, linear variation between blade pressure and suction sides. This allows for the cross-passage (pitchwise) pressure and expansion rate variations to be taken into account and their effect to be investigated.

3.5.1 Convergence

As with any numerical calculation, convergence plays a major role in the overall validity of results, outlining the error remaining in the solution. The calculation will tend towards $\bar{\xi}$ with the increase in sample size,⁶ and in the limiting case where sample size N tends to infinity:

$$\frac{1}{N} \sum_{i=1}^N \xi(\psi_i) = \bar{\xi}. \quad (3.42)$$

Therefore, it becomes a question of how large the sample size N needs to be for the desired accuracy level.

The convergence was tested using 100 000 iterations on wetness fraction and thermodynamic relaxation loss as variables that get passed back to the streamline equilibrium routine. The solution becomes stable after $\sim 10\,000$ pathlines, as can be seen in fig. 3.10a. Wetness fraction converges very quickly, after 200 pathlines, while relaxation loss (whose amplitude of values is much larger than for wetness) requires a higher number of iterations to reach a converged solution due to the low frequency of the error term (seen in the detail of fig. 3.10a).

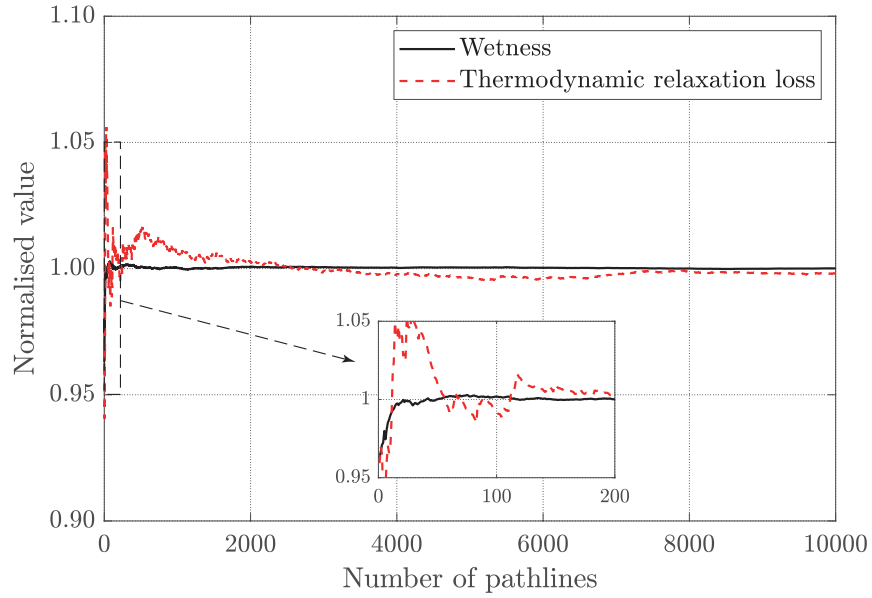
Droplet size spectrum converges quite quickly, as seen in fig. 3.10b and the general shape of the spectrum is already captured after 1000 calculations. However, the finer details require longer to converge, as was previously seen in the thermodynamic relaxation loss, reaching a converged solution usually in less than 10 000 pathline calculations.

3.6 Sensitivity to modelling assumptions

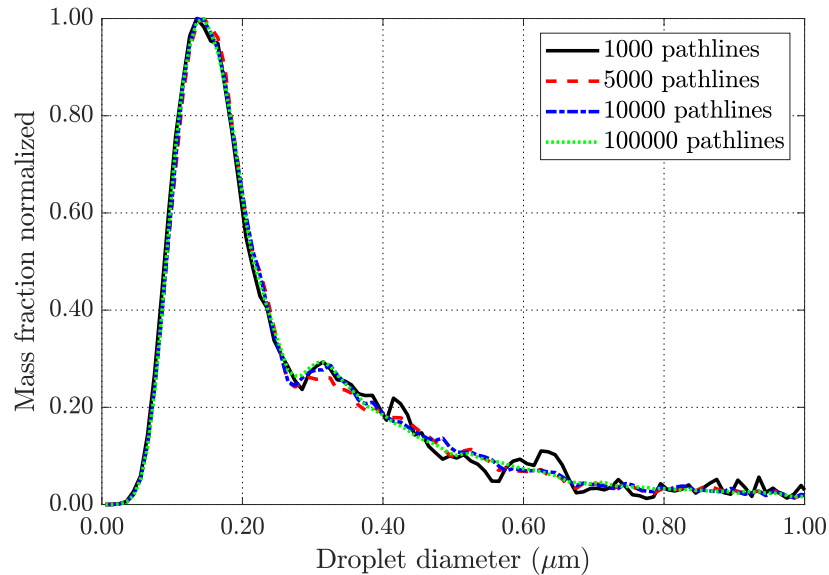
3.6.1 Fixed expansion rate

Static temperature of the steam (and the corresponding level of subcooling) throughout the machine determines the location of the condensation zone and its axial length, as defined in more detail by Guha and Young [53], and can be influenced through three interconnected mechanisms that happen simultaneously: expansion rate, dissipation, and phase change.

⁶A sample consists of a single steam parcel expansion from turbine inlet to outlet.



(a) Wetness and thermodynamic relaxation loss convergence, normalized with the final converged value.



(b) Droplet size spectrum convergence, normalized with peak value.

Fig. 3.10 Wake chopping convergence over a range of pathline calculations.

While expansion in blade passages increases subcooling, viscous dissipation and the latent heat release due to phase change decrease it. The sensitivity study of wake chopping assumptions in steam turbines starts from those three mechanisms. The influence of wake shape is examined in a wake chopping calculation with persisting wakes ($\tau_w \rightarrow \infty$) and fixed expansion rate ($\dot{p} = D(\ln p)/Dt = -1000$) throughout the machine. Viscous dissipation, characterising the tendency of the flow to smoothen out gradients and revert to equilibrium when no external forces are present, is included through two parameters: (i) wake decay time constant representing molecular and turbulent mixing and (ii) wake shape representing viscous loss distribution across the pitch. Therefore, a calculation with persisting wakes removes the dissipative contribution from wake decay and isolates the impact of wake shape on subcooling and, consequently, spreads the Wilson zone to a much wider axial region. Finally, steam parcels nucleating at significantly different axial locations are affected by local geometrical features that define the expansion rate, whose influence is removed through the assignment of constant \dot{p} on the entire domain, separating the influence of wake shape on droplet size spectrum. The droplet size spectra at the turbine outlet are shown in fig. 3.11 for each of the four wake profiles, while keeping all other parameters constant ($\bar{\eta} = 0.9$ and $\sigma_w = 0.04$).

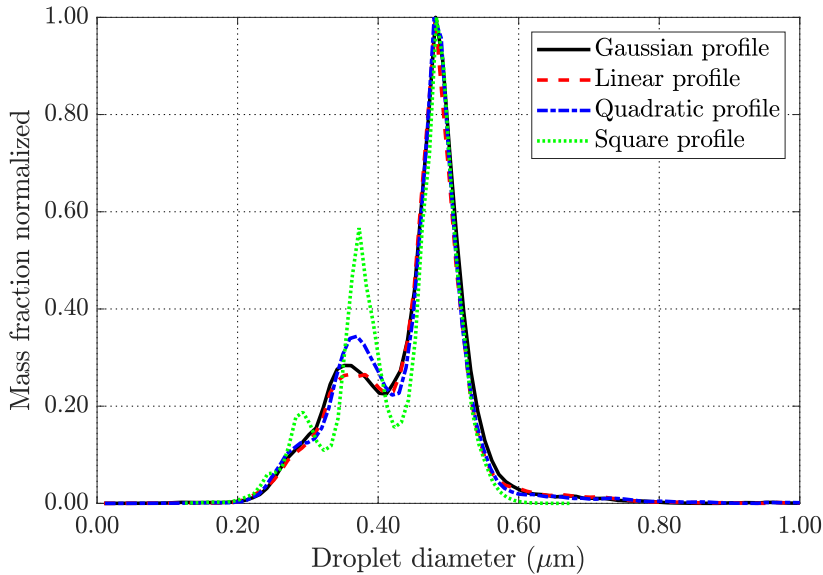


Fig. 3.11 Wake shape influence assuming a fixed expansion rate and no wake decay ($\tau_w \rightarrow \infty$).

Some differences in the detailed shape of the size distributions are observed which in this case come from different dissipation histories experienced by the fluid particles, expansion rates being the same in all cases. These differences originate from the variability in axial locations of Wilson points for individual parcels, changing the available (remaining) time

in the machine for droplets to grow. It should be noted, however, that the differences are quite modest given the sizeable variations in wake shape, and are only significant for the discontinuous, square wake profile. Note that the wake widths have been scaled such that the standard deviation of fluctuations is the same for each profile. Moreover, the discrepancies are much less pronounced when wake mixing and variable expansion rate are taken into account (see section 3.6.3).

3.6.2 1D expansion rate

As discussed in the previous section, temperature fluctuations caused by unsteady wake segmentation widen the nucleation zone but it is the flow conditions within the zone that determine the size of formed droplets and, ultimately, shape of the droplet size spectrum. Those conditions can have a substantial effect on the downstream flow field. E.g., in case of nucleation in the inter-row gap, the generated number of (large) droplets might not be sufficient to maintain the flow near equilibrium conditions in the following blade rows, possibly resulting in a second nucleation event.

Introduction of axial \dot{p} variation changes the expansion rate throughout the blade passage, affecting the modelled condensation process. The width of the Wilson zone sets the limit on expansion rate variation – the wider it is, the larger the number of unique Wilson point conditions a steam parcel can experience. The maximum theoretical width can be easily established by identifying the pathline loss extrema, assuming negligible mixing ($\tau_w \rightarrow \infty$, implies constant subcooling in the inter-row gaps). The pathline that always passes through the core of the flow, expanding almost isentropically, is the coldest and is the first to reach critical subcooling (fastest subcooling increase), thus defining the upstream Wilson zone edge. Conversely, the steam parcel that always passes right next to the blade surfaces and experiences maximum possible loss also has the highest possible temperature and the slowest subcooling rise. It is the last to nucleate and, therefore, defines the downstream Wilson zone edge.

Naturally, wake relaxation (proportional to $(I - I_\infty)$) heats up the coldest pathlines and cools down the hottest ones, decreasing the condensation zone width. However, even when applying realistic wake decay, fig. 3.12 still shows the Wilson zone spread over approximately two stages, indicating a broad range of expansion rates contained within. Since all other pathlines nucleate somewhere between the limiting two, the expansion rate variation broadens the droplet spectrum and makes it less sensitive to inlet superheat (compared to fixed \dot{p} case or a steady calculation, whereby all steam parcels nucleate experiencing the same expansion rate, generating a narrow spectrum).

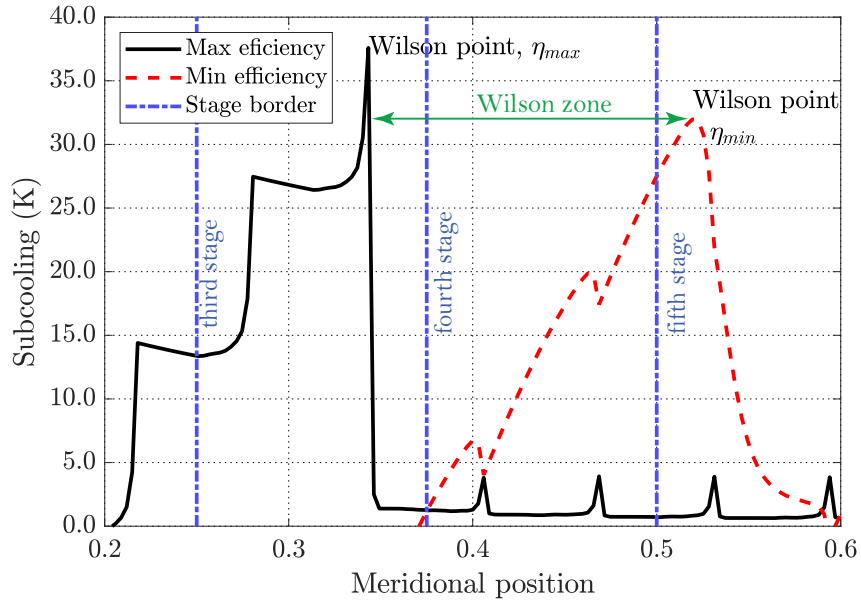


Fig. 3.12 Wilson zone length, determined by the steam parcel that passes exclusively through the core of the flow vs. parcel that passes exclusively through the wakes. While the position of η_{max} Wilson point is fixed, η_{min} location depends on the value of τ_w and wake shape, thus changing the Wilson zone length. Here, $\tau_w = 5\Delta t_{ls}$.

Wake decay rate

The high entropy wakes are assumed to mix out with time constant τ_w , as defined in eq. 3.29, which can be estimated from simple physical modelling or from CFD, but cannot easily be determined with any precision. As a result, it is very difficult to correctly predict the Wilson zone width and, thus, the \dot{p} range that condensing steam parcels experience. Since the generated droplet spectra and thermodynamic relaxation losses are influenced by the local expansion rates, the model sensitivity to τ_w is examined on 1D \dot{p} and 2D \dot{p} variation cases.

Figure 3.13 shows droplet size spectra for a τ_w range ($0 < \tau_w \leq 50\Delta t_{ls}$), using the axial pressure distribution (1D \dot{p}) previously shown in fig. 3.9a. The wake decay range covers more than an order of magnitude offset from the τ_w proposed in eq. 3.30. From the initial observations it is clear that the inclusion of wake chopping widens the droplet size spectrum. This is consistent with the established findings in the literature.⁷ The first peak, located at $d \approx 0.1\mu\text{m}$, is shared by all calculations. The no wake chopping calculation ($\tau_w \rightarrow 0$), functionally equivalent to instantaneous dissipation of gradients, implies that all steam parcels expand along a path with the mean polytropic efficiency ($\bar{\eta}$), generating a singular peak in the distribution. For wake chopping calculations, it corresponds to the most probable thermodynamic history of steam parcels passing through the machine (i.e. unconditional

⁷More details can be found in section 2.3

value of mean polytropic efficiency through the machine, $\mathbb{E}[\eta_{t,i}]$). Hence, seeing that all calculations have a large fraction of liquid mass associated with that diameter serves as another indicator of calculation convergence. The small difference in the first peak diameter is caused by wake decay which slightly changes the Wilson point axial position for those pathlines. However, the second peak position changes significantly and non-monotonically

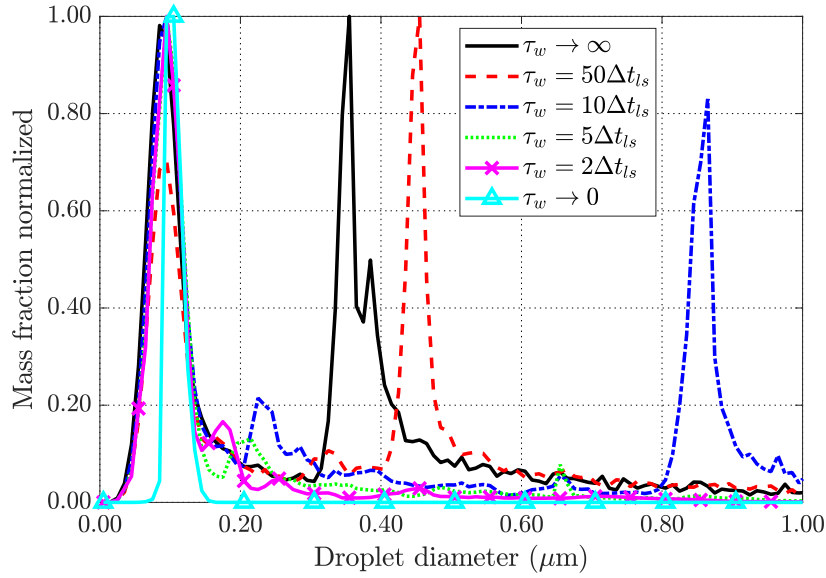


Fig. 3.13 Droplet spectrum sensitivity to wake decay, assuming a 1D \dot{p} variation.

on the range of wake decay rates. Deviation of the Wilson point location for individual pathlines (caused by different rates of flow mixing) changes the number of steam parcels nucleating at locations with significantly different expansion rates (e.g., gap between blade rows). Since the liquid mass scales with d^3 , even a small increase in the number of large nucleated droplets causes the appearance of a substantial spike in the droplet size distribution (e.g., for $\tau_w = 10\Delta t_{ls}$, second peak forms at $d \approx 0.85\mu\text{m}$). The results point that the value of τ_w might reasonably be estimated to within a factor of 5 ($2 < \tau_w/\Delta t_{ls} < 10$).

Repeating the calculations, this time including the pitchwise pressure variation, expands on these findings. Droplet spectra, presented in fig. 3.14, show that the sensitivity to τ_w is much less pronounced when pitchwise pressure variations are taken into account. The spectra are much wider than for the steady calculation, strongly skewed, and with a larger mean diameter. Qualitatively, they closely resemble the optical measurements on real turbines (shown previously in fig. 2.3) due to the increased variability of \dot{p} in the condensation zone. Steam parcels that reach the critical level of subcooling at the same axial location result in differently sized droplets owing to different pitchwise positions. A more detailed analysis of the pressure (and, thus, expansion rate) variation is given further below.

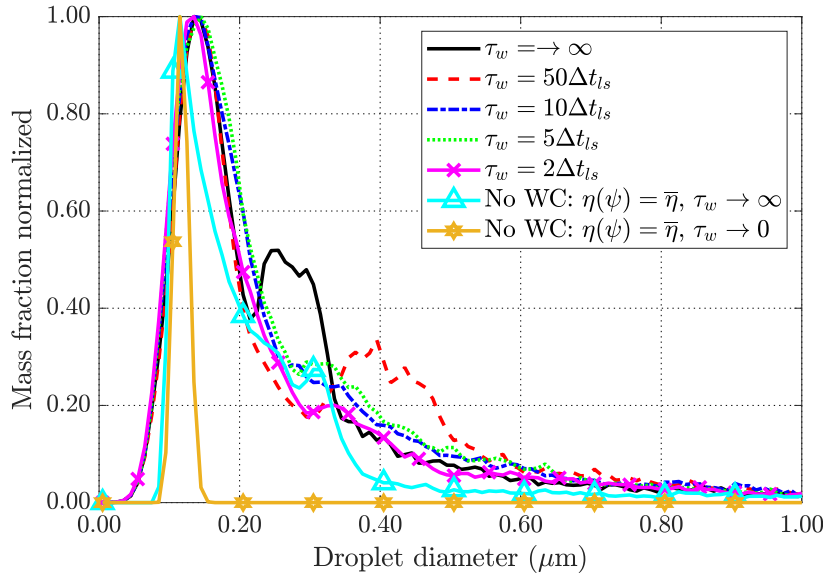


Fig. 3.14 Droplet spectrum sensitivity to wake decay, assuming a 2D \dot{p} variation.

3.6.3 2D expansion rate

Pitchwise pressure variation

The previous section showed that the local diversity of expansion rates (\dot{p}) has a dominant effect on the droplet size spectrum shape (large \dot{p} results in a large number of small droplets, while small \dot{p} gives rise to a small number of large droplets). This relationship can be explained using a simple example: following pathlines with the most probable loss history through the machine (i.e., largest number of pathlines that start to condense at the same axial location). As each steam parcel expands, it experiences dissipation according to the prescribed polytropic efficiency, defining the axial location of the Wilson point. The \dot{p} at this point determines the characteristics of nucleated droplets. In the case of an axial expansion rate variation, all parcels nucleate with the same \dot{p} , generating droplets of same size. Introduction of pitchwise pressure variation ensures that all of those steam parcels condense while experiencing different \dot{p} , depending on their relative pitchwise position, therefore widening the spectrum.

Figure 3.15 shows how the droplet size spectrum changes with the increase in \dot{p} modelling complexity: 0D, 1D, and 2D \dot{p} variation. For the 0D case, a constant expansion rate of $\dot{p} = -1000$ was applied, while the 1D pressure variation corresponds to the mid-passage distribution shown previously in fig. 3.9a. 2D effects were added using linear interpolation of suction and pressure side pressure curves (previously shown in fig. 3.9b) based on the parcel pitchwise position. The underlying spectrum shape for the 2D case is similar to that

for 1D, but the additional pitchwise variations increase the range of expansion rate in the nucleation zone, causing further widening of the spectrum. By contrast, expansion with a constant \dot{p} generates a narrow distribution with a very different shape,⁸ making it very sensitive to inlet superheat. In this case, wake chopping varies the axial location of nucleation (thereby changing the remaining time available for droplets to grow) but the final droplet size is determined chiefly by the number of nucleated droplets and, hence, by \dot{p} in the Wilson zone.

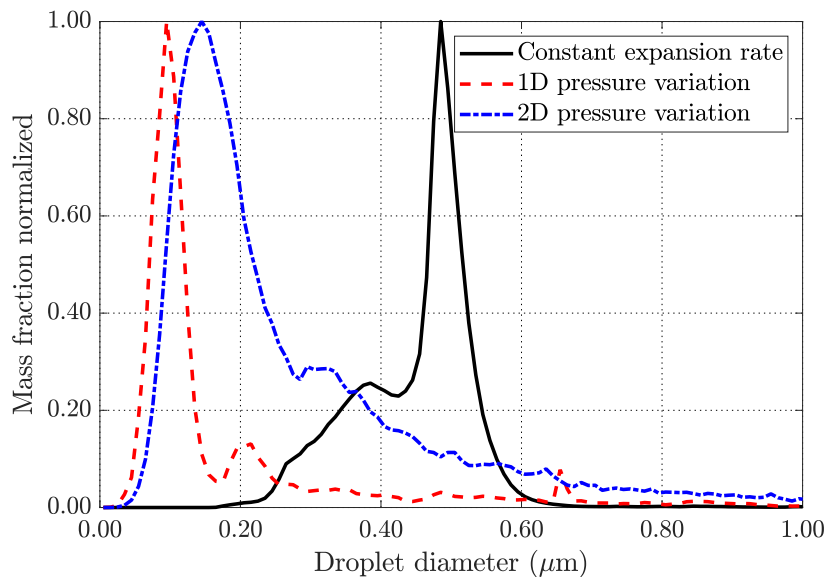


Fig. 3.15 Impact of 1D and 2D \dot{p} variation on droplet size spectrum for a fixed wake decay rate ($\tau_w = 5\Delta t_{ls}$).

Wake shape revisited

The influence of wake shape on the droplet size spectrum is tested again, this time including both axial and pitchwise pressure variation, and wake decay. The limited impact of wake shape variation on droplet size in a constant \dot{p} scenario is further diminished by accounting for wake mixing and 2D expansion rate variation. Despite the difference in wake profile description, the droplet size spectra are very much alike, as seen in fig. 3.16. Droplets with different thermodynamic histories, due to a random pitchwise position in each blade row, reach their Wilson points at different axial locations, spreading the nucleation zone. This

⁸Larger mean diameter is the consequence of the condensation occurring in the gap between blade rows where pressure is almost constant ($\dot{p} \approx 0$), resulting in a smaller number of large droplets. A small change in inlet conditions would shift the Wilson point to a different axial location (different \dot{p}) and the resulting spectrum would drastically change (larger number of smaller droplets).

diffuses the effect of wake discontinuities (e.g., square wake) making the droplet spectrum prediction more robust.

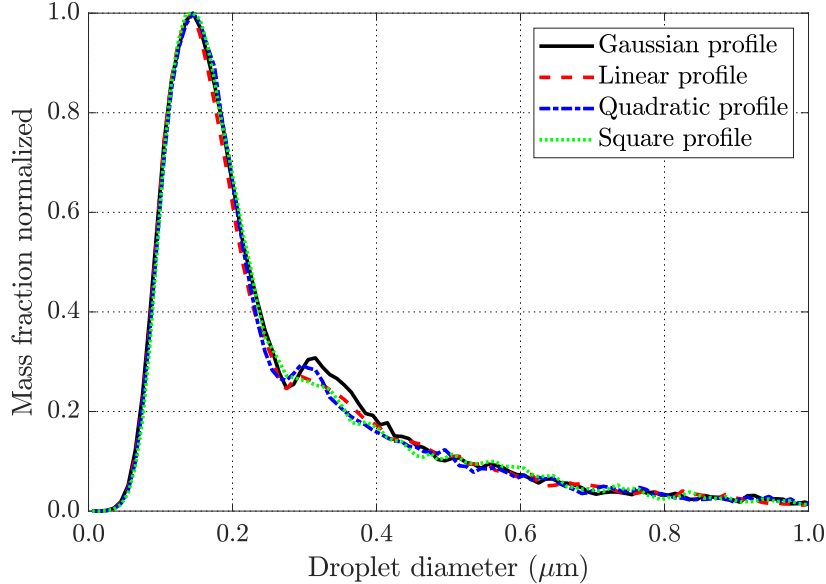


Fig. 3.16 Wake shape influence assuming 2D \dot{p} variation and wake decay ($\tau_w = 5\Delta t_{ls}$).

Wake width

As discussed in section 3.4.2, wake width represents one of the uncertainty factors in this model. Experimental results on full blade wakes are rarely accessible and, even then, there are processing differences in how the wake boundary is defined.⁹ The relation between the measure of wake width, σ_w , and the standard deviation of wake functional form σ_k can be defined as:

$$\sigma_k = f(\sigma_w), k \in \{G, L, Q, S\} \quad (3.43)$$

where the form of function f is unknown, leading to a second source of uncertainty in this model. However, it is clear from eq. 3.43 that these two sources of uncertainty are observationally equivalent in this model. Therefore, a wide interval of wake widths has been selected ($0.04 \leq \sigma_w \leq 0.16$), enabling the joint study of model sensitivity to both uncertainty sources, as shown in fig. 3.17.

Thin wakes imply that most of the steam flow passes through the core, experiencing almost no dissipation and nucleating in a very narrow region (i.e., most probable pathline history). The generated droplets are seen as the primary peak in fig. 3.17. Since the maximal

⁹Loss is continuously distributed across the pitch and hence requires a measure to define a discrete boundary where the wake ends and core flow begins.

dissipation is higher for narrow wakes (to keep mean loss the same), small fraction of the flow that experiences it ends up nucleating further downstream, making the Wilson zone broader than for wide wakes. Conversely, wider wakes mean larger proportion of the flow experiences some loss, making nucleation more evenly distributed throughout the Wilson zone. However, the droplet spectra in fig. 3.17 are mostly invariant over a reasonable range of wake widths, showing only a slight thinning of the global peak and thickening of the edges of the distribution as the wakes widen and isentropic core becomes narrower.

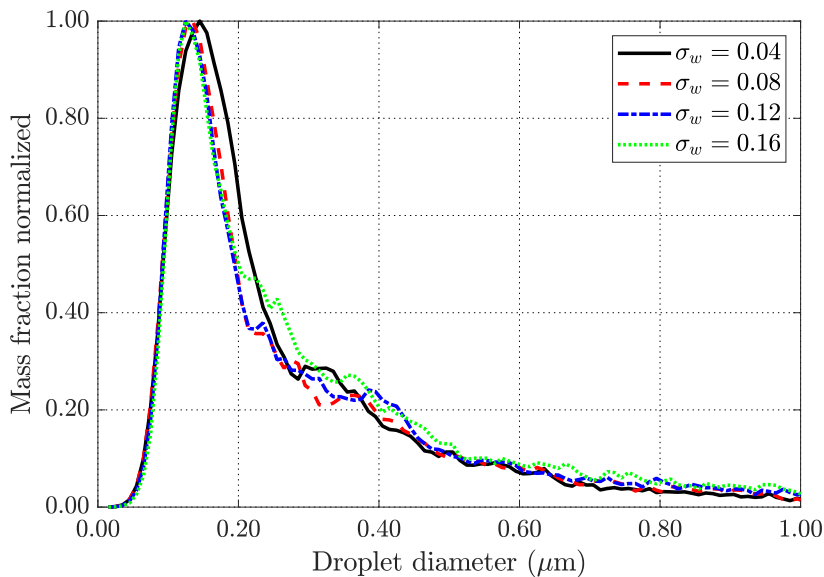


Fig. 3.17 Wake width influence assuming 2D \dot{p} variation, Gaussian wake profile, and wake decay ($\tau_w = 5\Delta t_{ls}$).

Influence of wake asymmetry

The impact of wake asymmetry on predicted droplet spectra was tested for several asymmetry ratios, (r = pressure side wake width/suction side wake width), and the results are shown for a 40% larger wake ($r = 1.4$ and $r = 1/1.4$) and for a limiting case where one wake is infinitely thin ($r \rightarrow \infty$ and $r \rightarrow -\infty$). The predicted spectra are almost the same across all cases, with a small change in the secondary peak at $d \simeq 0.3 \mu\text{m}$ caused by a distortion of the nucleation zone in the wake regions for the limiting r values. In case of a, e.g., infinitely thin pressure side wake, steam parcels passing close to the blade pressure side will nucleate earlier as they now experience less dissipation and, conversely, the effect of suction side wake reaches further away from the surface, postponing the nucleation (core flow width is constant across all cases). This change in the near-wall regions changes the axial location

of the Wilson point for a small number of steam parcels (and, hence, expansion rate at the Wilson points), causing the observed variation in the spectrum.

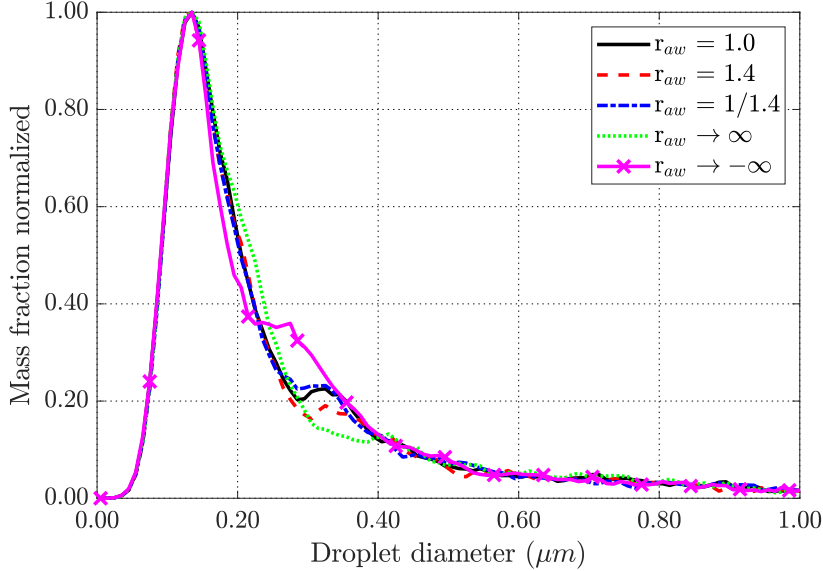


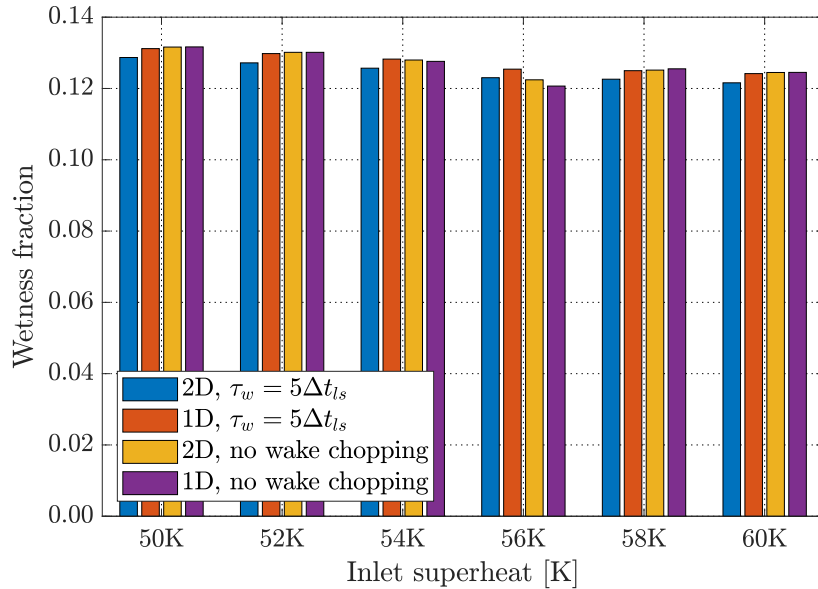
Fig. 3.18 Influence of wake asymmetry assuming 2D \dot{p} variation and wake decay ($\tau_w = 5\Delta t_{ls}$, $\sigma_w = 0.04$).

3.6.4 Wetness and thermodynamic relaxation loss sensitivity

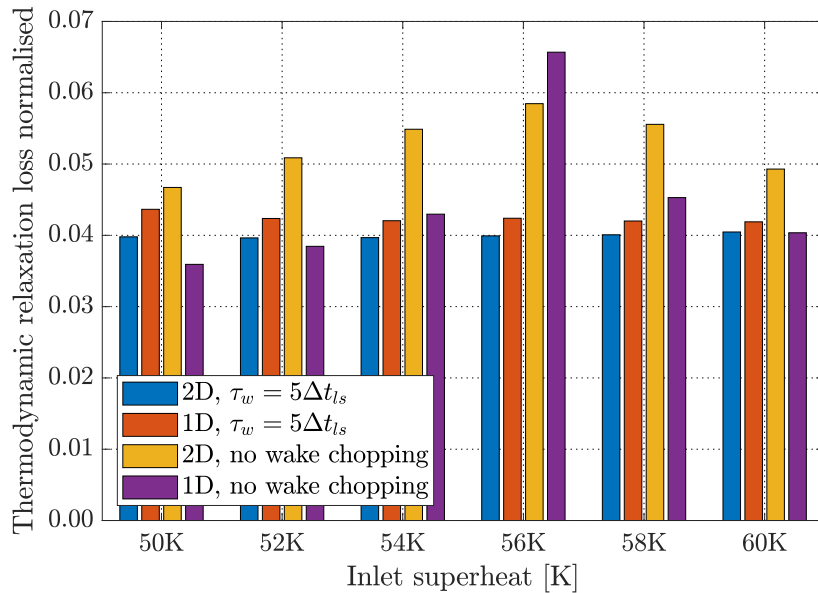
Previous sections demonstrated the importance of modelling wake chopping when attempting to predict droplet spectra in steam turbines. Since a number of other phenomena (e.g., losses, droplet deposition) are directly influenced by the shape of the spectrum, it is important to determine their sensitivity and distinguish physical behaviour from modelling limitations (especially across a number of operating conditions).

Figure 3.19a shows the difference in outlet wetness fraction depending on the included effects, and for a range of inlet superheat temperatures, which shift the axial location of nucleation. The impact of the different modelling assumptions on outlet wetness fraction is relatively small. This is to be expected because the equilibrium wetness is determined by the pressure and entropy.

However, wake chopping has a more pronounced impact on the relaxation loss (defined as the component of entropy generation due to irreversible phase change) shown in fig. 3.19b. Note that the entropy changes have been normalised by the specific gas constant, making the values comparable to a fractional stagnation pressure loss. Axial pressure variation with no wake chopping causes each nucleation event to be confined to a singular expansion rate, generating a narrow droplet spectrum. This makes the thermodynamic



(a) The impact of wake chopping on outlet wetness.



(b) The impact of wake chopping on thermodynamic relaxation loss.

Fig. 3.19 The impact of wake chopping on outlet wetness and thermodynamic relaxation loss for a range of inlet superheat values.

relaxation loss sensitive to the axial location of the Wilson point and, thereby, dependent on the inlet temperature. By increasing the inlet temperature, nucleation moves from the blade passage to the inter-blade gap where pressure is almost constant ($\dot{p} \approx 0$). This occurs for an inlet superheat of 56K and leads to lower outlet wetness because the flow does not reach equilibrium. For a two-dimensional pressure field, however, the nucleation events are spread over a range of expansion rates at approximately the same axial location of the Wilson point, thus broadening the droplet size spectrum even in the absence of wake chopping.¹⁰ Consequently, the relaxation loss becomes considerably less sensitive to inlet temperature. Inclusion of wake chopping spreads the nucleation over a broad axial zone that may span two blade rows, hence further reducing the sensitivity to inlet superheat. Thus, as shown in fig. 3.19b, the relaxation loss for the 2D wake-chopping model is more or less independent of inlet superheat.

¹⁰For the 56 K inlet superheat case, nucleation occurred close to the blade trailing edge, where there is still a small circumferential pressure gradient, leading to the observed difference between the 1D and 2D no wake chopping peaks. If nucleation occurred in the passage, where there is no pitchwise \dot{p} variation, loss values would have been the same.

3.7 Conclusions

A non-equilibrium wet-steam wake-chopping model has been presented, suitable for incorporation into streamline curvature or other throughflow calculation methods. The model follows a similar approach to previously published work by other authors, but also includes a study of the sensitivity of results to the key modelling parameters. Pitchwise variations in pressure and (inertial) deposition are included, as well. The main conclusions are:

- (i) The predicted droplet spectra are more or less insensitive to the wake shape and wake asymmetry, provided both mean loss and standard deviation (i.e., the effective wake width) are held constant. Previous studies show a dependence on the wake shape because the effective width was not held constant and cross-passage pressure variations were not included.
- (ii) Inclusion of pitchwise pressure variation also renders the results less sensitive to other modelling parameters (notably the wake decay rate) by spreading nucleation over a broader range of expansion rates. Predicted droplet spectra and relaxation losses become less sensitive to inlet temperature for similar reasons.
- (iii) In keeping with previous work and optical measurements, droplet spectra are predicted to be much broader as a result of wake chopping. This has a significant impact on the inertial deposition rate and is likely to have an even more pronounced effect on turbulent deposition, which is known to vary strongly with Stokes number.

Chapter 4

Droplet deposition modelling

4.1 Introduction

Typical low pressure (LP) turbine nucleation results in a large number of polydispersed droplets that grow and migrate with the surrounding steam flow, reaching outlet Sauter mean diameters often between $0.1 \mu\text{m}$ and $1 \mu\text{m}$. However, the droplets are not capable of perfectly following the steam due to their large density difference. In an accelerating or curved flow, they develop velocity slip – a difference between droplet and steam velocity – with large droplets deviating more than small ones. Some of the droplet trajectories intersect the surrounding surfaces, depositing on turbine blades and casing, forming liquid films and, subsequently, breaking off as coarse water droplets at the trailing edge. Although these secondary droplets are typically ~ 2 orders of magnitude larger, their concentration is very low and so they carry only a small fraction of total liquid mass [182].

The droplet deposition model in this chapter is developed as an extension to the streamline equilibrium calculations. The first part treats inertial deposition and outlines the calculation procedure for three-dimensional droplet trajectories based on a coarse flow field representation. The second part deals with deposition due to other effects based on empirical deposition models, which require estimates of the local blade-surface friction coefficients (these are not directly available from the streamline curvature method). To assess the impact of these estimates, CFD calculations have been undertaken for White's cascade experiment [164]. Finally, the impact of wake chopping on deposition rates is examined.

4.2 Inertial deposition

The inertial deposition model is based on 3D tracking of water droplets as they migrate with the surrounding steam flow and recording their final locations. Droplets are assumed to be uniformly distributed in the circumferential direction, and sufficiently far apart for their interaction to be considered negligible, while their shape is assumed to be perfectly spherical as they move throughout the turbine. Inertial deposition of spherical droplets in turbines was first described by Gyarmathy [54] and the model was further refined in [182, 167, 95]. The model described in this section was developed following similar principles, whereby individual droplets – representing their respective droplet size bin – are tracked through the turbine flow field. Streamline curvature calculations are used to provide a coarse 2D flow field as a set of radially distributed streamsurfaces. Whilst this 2D representation of the flow clearly diminishes the accuracy, it is worth remembering that the primary goal is to enable rapid comparison of turbine designs and global deposition trends over a range of operating conditions.

Droplet size spectra are generated by either steady throughflow or wake chopping calculations. Individual droplets representing their respective size bins are released from each blade row inlet and tracked through the passage, maintaining constant diameter. While the assumption of constant diameter within a passage neglects the effect of droplet growth on deposition, it is limited to a single passage at a time since droplet spectra at each leading edge (LE) come from a calculation that includes droplet growth.

The model is built around the assumption that inertia has the dominant effect on droplet motion while the influence of gravitational and other smaller forces can be neglected. Applying Newton's second law in the Lagrangian frame of reference, water droplet motion can be written as:

$$\mathbf{F}_D = m_l \mathbf{a}_l = \frac{\rho_l d^3 \pi}{6} \frac{D\mathbf{v}_l}{Dt_l}, \quad (4.1)$$

where \mathbf{F}_D is the resulting external force on a droplet¹, \mathbf{a}_l and \mathbf{v}_l are droplet acceleration and velocity vectors, d is the droplet diameter and ρ_l is the density of water. $D/Dt_l = \partial/\partial t_l + \mathbf{v}_l \cdot \nabla$ is the derivative with respect to time in the droplet frame of reference.

The drag force is related to the drag coefficient, C_D , through:

$$\mathbf{F}_D = \frac{\rho_g d^2 \pi}{8} |\mathbf{v}_g - \mathbf{v}_l| (\mathbf{v}_g - \mathbf{v}_l) C_D, \quad (4.2)$$

where ρ_g is vapour density and $\Delta\mathbf{v} = \mathbf{v}_g - \mathbf{v}_l$ is the slip velocity.

¹In this case, the resulting force comprises solely of steady state viscous drag.

For most cases, slip velocities are sufficiently small for the drag to obey Stokes law, $C_D = 24/\text{Re}_s$, where Re_s is the droplet slip Reynolds number, defined as:

$$\text{Re}_s = \frac{\rho_g d |\mathbf{v}_g - \mathbf{v}_l|}{\mu_g}. \quad (4.3)$$

For larger slip velocities, a correction may be applied to C_D , such that:

$$C_D = \frac{24}{\text{Re}_s} \cdot \Phi_D(\text{Re}_s)^{-1}. \quad (4.4)$$

Expressions for $\Phi_D(\text{Re}_s)$ are given in the appendix C with a brief discussion. Combining eqs. 4.1 – 4.4 gives:

$$\frac{D\mathbf{v}_l}{Dt_l} = \frac{18\mu_g}{\rho_l d^2} \Phi_D(\text{Re})^{-1} (\mathbf{v}_g - \mathbf{v}_l) = \frac{\mathbf{v}_g - \mathbf{v}_l}{\tau_d}, \quad (4.5)$$

from which the inertial relaxation time, τ_d , is:

$$\tau_d = \frac{\rho_l d^2}{18\mu_g} \Phi_D(\text{Re}). \quad (4.6)$$

Accounting for the non-continuum effects (see discussion in the appendix D) leads to the following form for the relaxation time

$$\tau_d = \frac{\rho_l d^2}{18\mu_g} [\Phi_D(\text{Re}) + 2.7\text{Kn}]. \quad (4.7)$$

Note, however, that the Knudsen correction is only significant for very small droplets which, in any case, have negligible slip.

Equation 4.5 can be written in terms of velocity slip, $\Delta\mathbf{v} = \mathbf{v}_g - \mathbf{v}_l$, as:

$$\frac{D}{Dt_l}(\Delta\mathbf{v}) + \frac{\Delta\mathbf{v}}{\tau_d} = \frac{D\mathbf{v}_g}{Dt_l}. \quad (4.8)$$

This is integrated under the assumption [182] that τ_d and $D\mathbf{v}_g/Dt_l$ stay approximately constant over a time step² Δt_l , giving:

$$\Delta\mathbf{v}_2 = \Delta\mathbf{v}_1 \beta + \bar{\tau}_d (1 - \beta) \left[\frac{D\mathbf{v}_g}{Dt_l} \right], \quad \beta = \exp \left(-\frac{\Delta t_l}{\bar{\tau}_d} \right), \quad (4.9)$$

²As denoted in eq. 4.9 by overbar and square brackets.

where, indices 1 and 2 denote values at the beginning and the end of the time step respectively. This (semi-)analytical integration removes the numerical stiffness and avoids the need for excessively short time steps. A numerical scheme is nonetheless required to take account of changing gas-phase acceleration and the rotating frame of reference.

4.2.1 Coordinate system definition and coordinate transformations

Droplet tracking is performed by integrating eq. 4.9 in the droplet's frame of reference as it passes through the machine, and the choice of coordinates determines the complexity of final equations. Cartesian coordinates, while appealing due to the constant orientation of base vectors, complicate the expression for velocity slip and make the analysis unnecessarily complex. Since turbines are rotational machines with a single axis of rotation, a cylindrical coordinate system is applied, resulting in a simpler set of equations. The droplet position in cylindrical coordinates, shown in fig. 4.1, is defined through its axial location, z , radial distance from the axis, r , and the angle $\theta = \angle(\mathbf{P}, \mathbf{r})$ formed by the radial axis and a reference plane \mathbf{P} , defined by the origin point and two vectors as $\mathbf{P} = r_0 + s\mathbf{p} + w\mathbf{z}$, $(s, w) \in \mathbb{R}$.

Local coordinate system is attached to the droplet and is defined by unit vectors \mathbf{e}_r , \mathbf{e}_θ and \mathbf{e}_z . The relationship between Cartesian and cylindrical coordinates is as follows:

$$\mathbf{e}_r = \mathbf{e}_x \cos \theta + \mathbf{e}_y \sin \theta, \quad (4.10)$$

$$\mathbf{e}_\theta = -\mathbf{e}_x \sin \theta + \mathbf{e}_y \cos \theta, \quad (4.11)$$

$$\mathbf{e}_z = \mathbf{e}_z. \quad (4.12)$$

The orientation of base vectors does not change with z or r , but only with a change in θ , which rotates them around the z axis. With that in mind, time derivatives of base vectors can be written as:

$$\frac{d\mathbf{e}_r}{dt_l} = \dot{\theta}\mathbf{e}_\theta = \frac{v_{l,\theta}}{r}\mathbf{e}_\theta, \quad (4.13)$$

$$\frac{d\mathbf{e}_\theta}{dt_l} = -\dot{\theta}\mathbf{e}_r = -\frac{v_{l,\theta}}{r}\mathbf{e}_r, \quad (4.14)$$

$$\frac{d\mathbf{e}_z}{dt_l} = 0. \quad (4.15)$$

The steam velocity vector can now be expressed in terms of cylindrical base vectors:

$$\mathbf{v}_g = v_{g,r}\mathbf{e}_r + v_{g,\theta}\mathbf{e}_\theta + v_{g,z}\mathbf{e}_z. \quad (4.16)$$

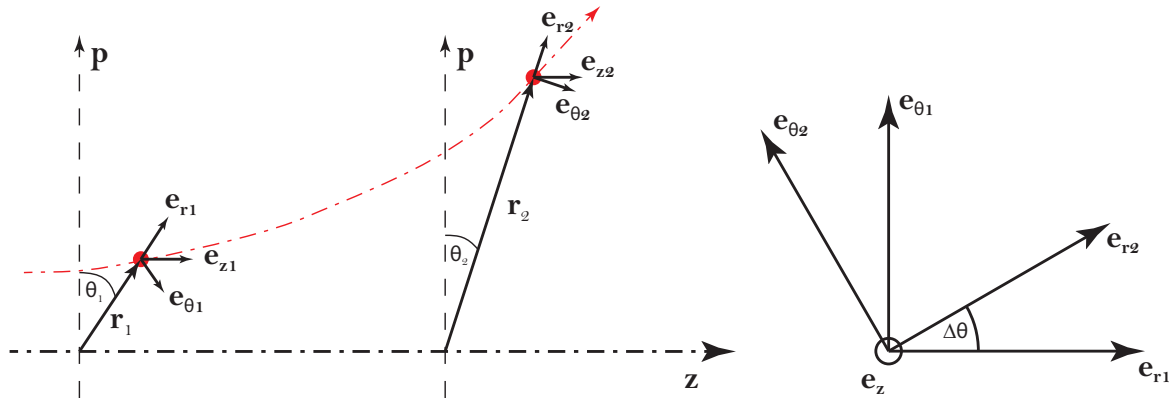


Fig. 4.1 Base vector rotation in the cylindrical coordinate system.

Relative velocity components, w , in cylindrical coordinates can be related to their absolute velocity counterparts as:

$$w_r = v_r, \quad (4.17)$$

$$w_\theta = v_\theta - \Omega r, \quad (4.18)$$

$$w_z = v_z. \quad (4.19)$$

Angular velocity vector with magnitude Ω [rad s^{-1}] is aligned with the z axis, and r is the radial distance from the same axis. Equations 4.17 – 4.19 are valid for both gaseous and liquid phase and, in this particular case, slip velocity is the same in both relative and absolute frame of reference, $\Delta\mathbf{v} = \Delta\mathbf{w}$.

Knowing the derivatives of base vectors, steam acceleration³ is obtained by differentiating eq. 4.16 with respect to time:

$$\begin{aligned} \mathbf{a}_g &= \frac{d\mathbf{v}_g}{dt} = \dot{v}_{g,r}\mathbf{e}_r + v_{g,r}\dot{\mathbf{e}}_r + \dot{v}_{g,\theta}\dot{\theta}\mathbf{e}_\theta + v_{g,\theta}\ddot{\theta}\mathbf{e}_\theta + v_{g,\theta}\dot{\theta}\dot{\mathbf{e}}_\theta + \dot{v}_{g,z}\mathbf{e}_z + v_{g,z}\dot{\mathbf{e}}_z \quad (4.20) \\ &= a_{g,r}\mathbf{e}_r + a_{g,\theta}\mathbf{e}_\theta + a_{g,z}\mathbf{e}_z, \\ a_{g,r} &= \frac{dv_{g,r}}{dt_l} - \frac{v_{g,\theta}v_{l,\theta}}{r}, \\ a_{g,\theta} &= \frac{dv_{g,\theta}}{dt_l} + \frac{v_{g,r}v_{l,\theta}}{r}, \\ a_{g,z} &= \frac{dv_{g,z}}{dt_l}. \end{aligned}$$

³Keep in mind that steam acceleration equation is derived in the droplet frame of reference.

Substituting eqs. 4.17 – 4.19 and 4.20 into eq. 4.9, we obtain the set of droplet velocity slip equations in cylindrical coordinates:

$$\Delta w_{r2} \mathbf{e}_{r2} = \beta \Delta w_{r1} \mathbf{e}_{r1} + \bar{\tau}_d (1 - \beta) \bar{a}_{g,r} \bar{\mathbf{e}}_r, \quad (4.21)$$

$$\Delta w_{\theta 2} \mathbf{e}_{\theta 2} = \beta \Delta w_{\theta 1} \mathbf{e}_{\theta 1} + \bar{\tau}_d (1 - \beta) \bar{a}_{g,\theta} \bar{\mathbf{e}}_\theta, \quad (4.22)$$

$$\Delta w_{z2} \mathbf{e}_{z2} = \beta \Delta w_{z1} \mathbf{e}_{z1} + \bar{\tau}_d (1 - \beta) \bar{a}_{g,z} \bar{\mathbf{e}}_z. \quad (4.23)$$

The final term on the right-hand side features overbar values which stand for time step averaging. Notice, however, how the left-hand side terms are written in terms of base vectors at the end of the time step. Referring to fig. 4.1, base vectors rotate around z axis across the time step by $\Delta\theta = \theta_2 - \theta_1$ angle. Hence, they can be expressed in terms of initial base vectors and rotation across the time step:

$$\mathbf{e}_{r2} = \cos(\Delta\theta) \mathbf{e}_{r1} + \sin(\Delta\theta) \mathbf{e}_{\theta 1}, \quad (4.24)$$

$$\mathbf{e}_{\theta 2} = -\sin(\Delta\theta) \mathbf{e}_{r1} + \cos(\Delta\theta) \mathbf{e}_{\theta 1},$$

$$\mathbf{e}_{z2} = \mathbf{e}_{z1}.$$

Substituting that into eqs. 4.21 – 4.23 and separating terms according to their direction, eqs. 4.21 – 4.23 can be written in terms of base vectors at the start of the time step:

$$\Delta w_{r2} \cos(\Delta\theta) \mathbf{e}_{r1} - \Delta w_{\theta 2} \sin(\Delta\theta) \mathbf{e}_{r1} = \beta \Delta w_{r1} \mathbf{e}_{r1} + \bar{\tau}_d (1 - \beta) \bar{a}_{g,r} \bar{\mathbf{e}}_r, \quad (4.25)$$

$$\Delta w_{r2} \sin(\Delta\theta) \mathbf{e}_{\theta 1} + \Delta w_{\theta 2} \cos(\Delta\theta) \mathbf{e}_{\theta 1} = \beta \Delta w_{\theta 1} \mathbf{e}_{\theta 1} + \bar{\tau}_d (1 - \beta) \bar{a}_{g,\theta} \bar{\mathbf{e}}_\theta, \quad (4.26)$$

$$\Delta w_{z2} \mathbf{e}_{z2} = \beta \Delta w_{z1} \mathbf{e}_{z1} + \bar{\tau}_d (1 - \beta) \bar{a}_{g,z} \bar{\mathbf{e}}_z. \quad (4.27)$$

Components of the time averaged base vectors, $\bar{\mathbf{e}}$, can be estimated as the mean of start and end orientations, $\bar{\mathbf{e}} = 0.5(\bar{a}\mathbf{e}_1 + \bar{a}\mathbf{e}_2)$:

$$\bar{\mathbf{e}}_r = \frac{1}{2} (\mathbf{e}_{r1} + \mathbf{e}_{r2}), \quad (4.28)$$

$$\bar{\mathbf{e}}_\theta = \frac{1}{2} (\mathbf{e}_{\theta 1} + \mathbf{e}_{\theta 2}), \quad (4.29)$$

$$\bar{\mathbf{e}}_z = \mathbf{e}_{z1} = \mathbf{e}_{z2}. \quad (4.30)$$

Substituting them into eqs. 4.25 – 4.27, the problem is expressed in terms of base vectors at the beginning of the time step. It can be formulated as $\mathbf{A} \cdot \mathbf{x} = \mathbf{b}$, where \mathbf{A} is the coordinate transformation matrix,⁴ \mathbf{x} is the velocity slip vector at the end of the time step and right

⁴Matrix formulation of eq. 4.24.

hand side vector, \mathbf{b} , contains all other variables with known values. Hence, the problem is reduced to finding the inverse of matrix \mathbf{A} . Finally, the velocity slip can be written in terms of variables at the start of the time step, in matrix form, as:

$$\begin{bmatrix} \Delta w_{r2} \\ \Delta w_{\theta 2} \\ \Delta w_{z2} \end{bmatrix} = \begin{bmatrix} \cos(\Delta\theta) & \sin(\Delta\theta) & 0 \\ -\sin(\Delta\theta) & \cos(\Delta\theta) & 0 \\ 0 & 0 & 1 \end{bmatrix} \begin{bmatrix} b_r \\ b_\theta \\ b_z \end{bmatrix}, \quad (4.31)$$

$$\begin{bmatrix} b_r \\ b_\theta \\ b_z \end{bmatrix} = \begin{bmatrix} \beta \Delta w_{r1} + 0.5 \bar{\tau}_d (1-\beta) \{ \bar{a}_{g,r} [1 + \cos(\Delta\theta)] - \bar{a}_{g,\theta} \sin(\Delta\theta) \} \\ \beta \Delta w_{\theta 1} + 0.5 \bar{\tau}_d (1-\beta) \{ \bar{a}_{g,\theta} [1 + \cos(\Delta\theta)] + \bar{a}_{g,r} \sin(\Delta\theta) \} \\ \beta \Delta w_{z1} + \bar{\tau}_d (1-\beta) \bar{a}_{g,z} \end{bmatrix}. \quad (4.32)$$

4.2.2 Leading edge collection efficiency

Inertial deposition on turbine blades can be assumed to occur predominantly on the pressure side surface and leading edge, while suction side contribution can usually be neglected [54]. The leading edge contribution is estimated by approximating the geometry as a cylinder in a uniform parallel incompressible flow [54]. The fraction of droplets deposited is given by:

$$F_{LE} = \eta_c \frac{d_{LE}}{P}, \quad (4.33)$$

where η_c is the collection efficiency and P is the blade pitch. Since the analytical solution for droplet trajectories in such a field is not known, several authors have performed numerical calculations to determine LE deposition rates ([54], [182], [138], [46]), and the reported collection efficiency trends are consistent across all publications.

The Stokes number, a dimensionless number representing a ratio between inertial and viscous drag forces, is defined as:

$$St = \frac{\tau_d}{t_f}, \quad (4.34)$$

where τ_d is the particle relaxation time and t_f is a characteristic time of the steam flow (in this case, residence time in a blade passage). The present work uses the numerical results by [182], shown in fig. 4.2, whereby Stokes numbers for each droplet size group is used to determine the LE collection efficiency and, hence, deposition rates. However, the Stokes numbers for small fog droplets in a turbine flow is low ($St < 10^{-1}$) and it can be safely assumed that LE deposition is negligible. This is supported by [138], where CFD calculations showed imperceptible LE deposition rates for droplets smaller than 5 μm . Nevertheless, LE

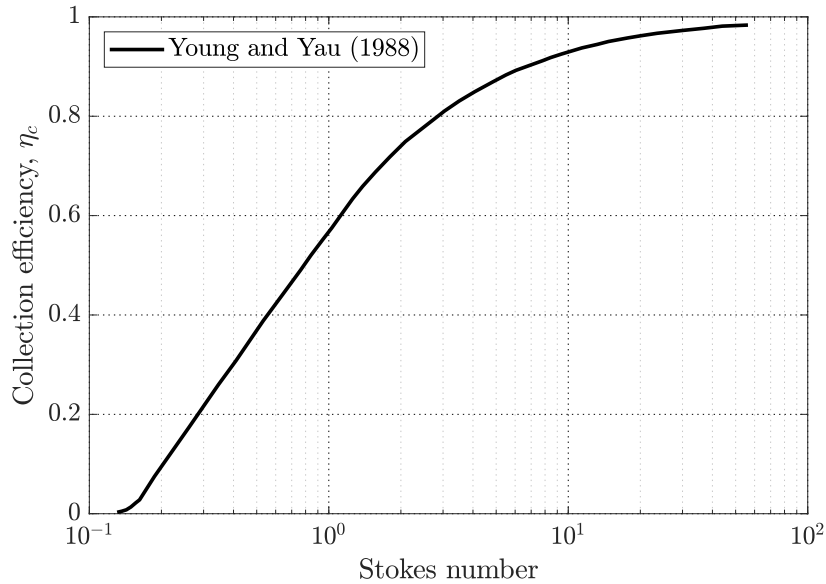


Fig. 4.2 Leading edge collection efficiency based on the droplet Stokes number, calculated in [182].

inertial deposition contribution becomes relevant when larger droplets (e.g., coarse water droplets) are present.

4.2.3 Calculation procedure

Figure 4.3 shows schematically the inertial deposition algorithm, requiring flow field and droplet spectrum information and returning inertial deposition rates either as fractional deposition (percentage of droplets of each size deposited per unit time and per unit mass of mixture) or as liquid mass deposited per unit time and per unit mass of mixture. The flow field information comes from streamline equilibrium calculations (with or without wake chopping), which in general only provide information at blade leading and trailing edges. Hence, steam pathlines are then approximated assuming linear velocity variation, leading to quadratic trajectories. Leading edge deposition is accounted for through eq. 4.33 while, following Gyarmathy's original approach [54], blades are reduced to infinitely thin quadratic shapes (pseudo-blades) matching steam pathlines to prevent false deposition. Turbine angular velocity is set to zero for stators and blade gaps, ensuring correct calculation of relative velocity components in eq. 4.18.

Individual droplets representing their respective size bins are released from every blade row inlet with no velocity slip. This is a reasonable assumption since particle relaxation times for fog droplets are substantially lower than the transit time in the blade row gaps, thus any velocity differences are eroded before reaching the next blade row. Information

from the previous time step is used as a downstream velocity slip guess and is iteratively corrected (usually needing only a few iterations). Velocity slip and resulting trajectory deviation in all three directions is calculated across a suitably selected small time step using time-step-averaged values. In case a droplet trajectory intersects with any of the blade surfaces, the location is recorded and associated liquid mass is deposited. Droplet splashing and rebounding is ignored based on Gyarmathy's argument [54] that small droplets impacting a wetted surface at an oblique angle get perfectly deposited. While the evidence supporting this claim is not sufficiently large, inertial deposition rates shown in this chapter can be considered as upper limiting values.

The above procedure is done once for each droplet group and each blade row, generally requiring under a hundred time steps per blade row to produce a sufficiently accurate trajectory.

4.2.4 Analysis of droplet trajectories

The main obstacle to deposition validation efforts is the lack of experimental data, which is notoriously hard to obtain and, in most cases, has very high uncertainty levels. It is, however, possible to test model performance against theoretically expected behaviour for very large and very small droplets. Small droplets with a low value of Stokes number rapidly adjust to any changes in the flow, closely following steam pathlines. Conversely, large droplets ($St \gg 1$) are mostly unaffected by the changes in steam velocity vectors and travel in a straight line, maintaining their initial velocity.

Testing was done on a General Electric five-stage LP turbine, described in [85, 68]. Figure 4.4a shows the true blade shape of the final stage stator and the steam streamlines are approximated as a linear combination of blade PS and SS surface geometries over a range of pitchwise positions. The droplets are released from the blade inlet with steam axial velocity and 0° incidence angle. On the other hand, fig. 4.4b shows a part of the gap between blade rows, labelled as *duct region*, as well as the blade row passage. Here, droplets are released from the duct assuming no velocity slip, and blade geometry is approximated by infinitely thin parabolic blades.

Droplets with the diameter of $0.1\text{ }\mu\text{m}$ have a Stokes number well below unity and closely follow steam pathlines. This is significant because Sauter mean diameters at LP turbine outlets are often in the range $0.2 - 1\text{ }\mu\text{m}$ [8]. Droplets with diameter of $3\text{ }\mu\text{m}$, which are representative of the largest droplets found in the fog-droplet spectrum (e.g., see fig. 3.14), acquire higher velocity slip but are still strongly affected by the changes in steam flow. Finally, the droplets with Stokes number much larger than unity – similar to coarse water droplets – migrate through the passage in a straight line, maintaining their initial velocity.

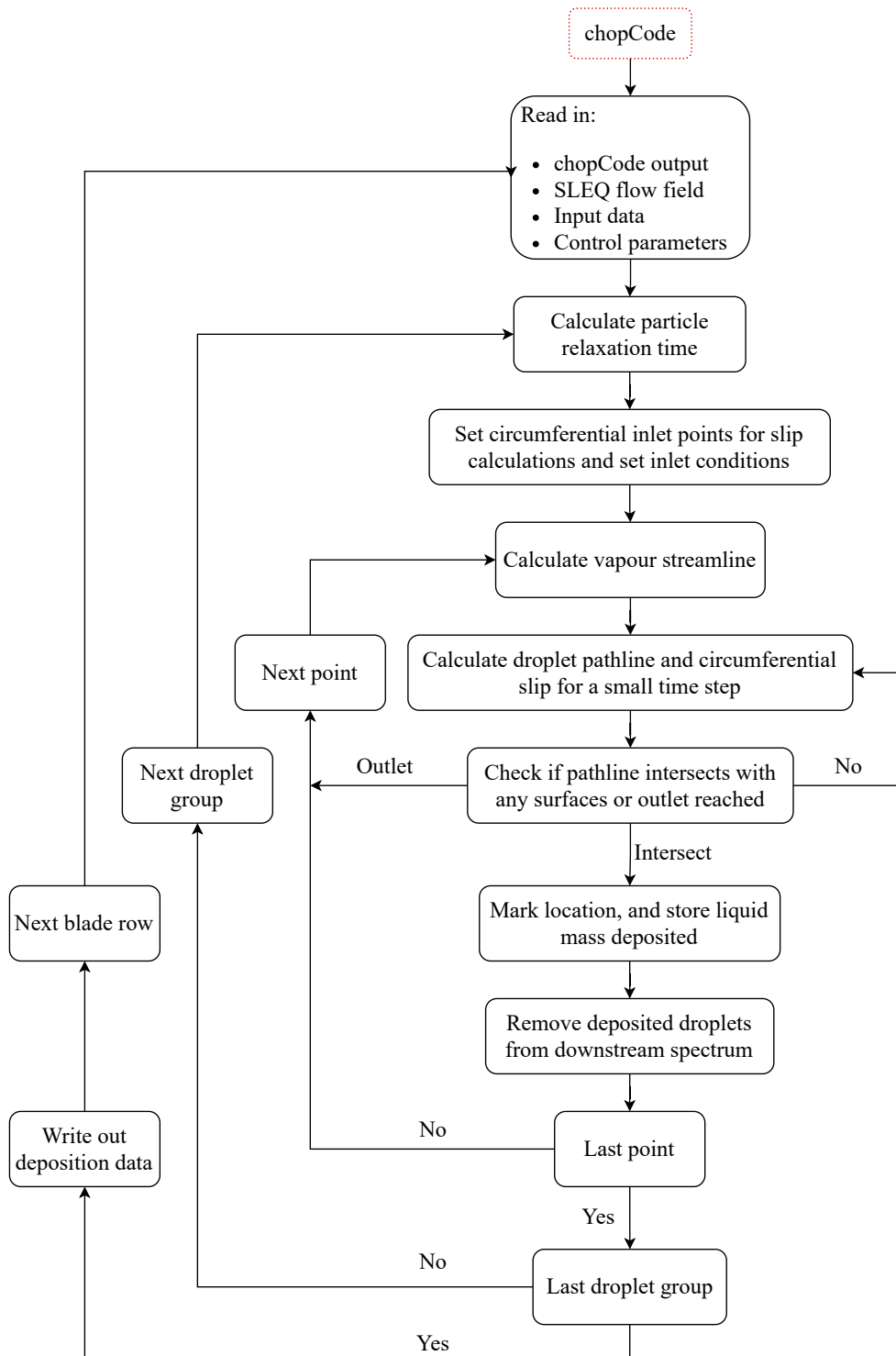


Fig. 4.3 Deposition code flow chart.

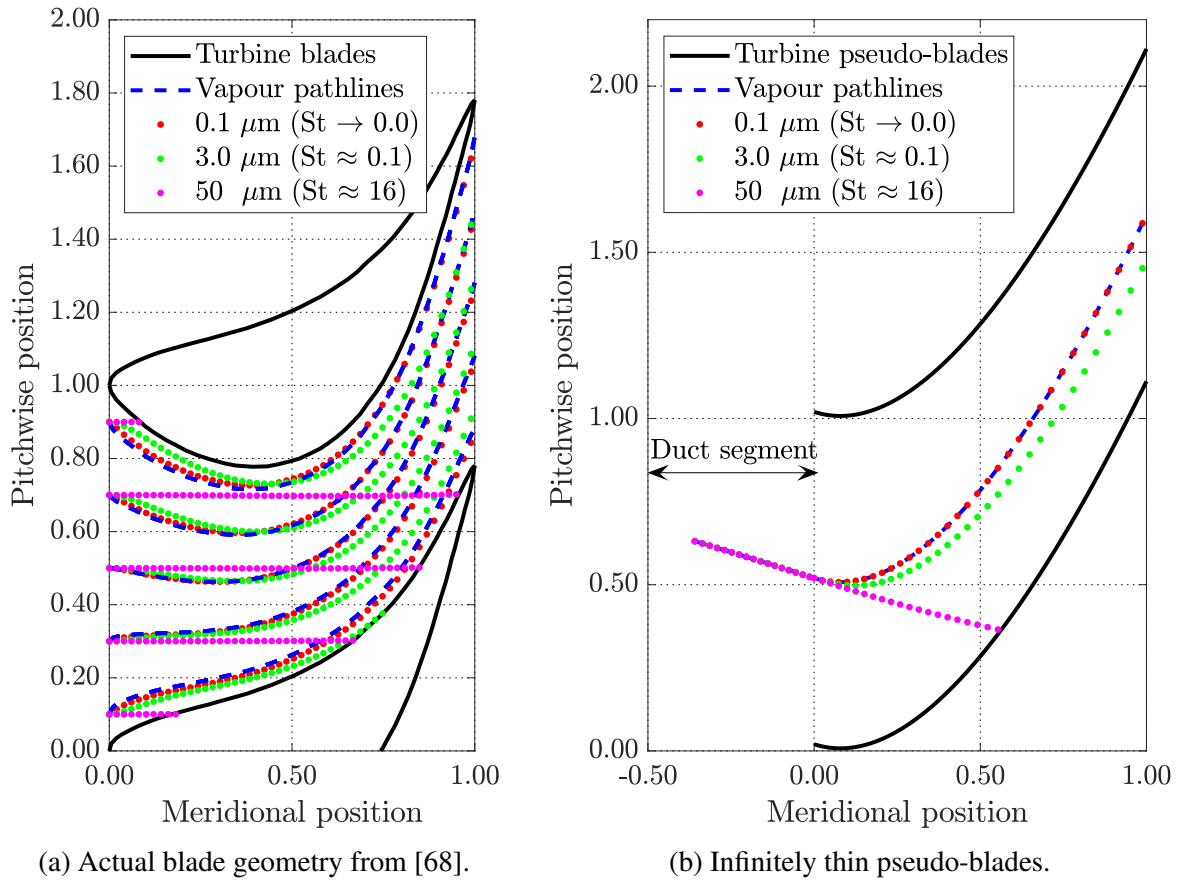


Fig. 4.4 Pitchwise droplet trajectories for a range of droplet sizes (Stokes number).

Cases with no initial droplet velocity slip result in exclusively pressure side deposition, with droplet pathlines at best tangentially touching the suction surface (as is the case in fig. 4.4b). However, different incidence angles coming from changing operating conditions as well as any remaining velocity slip for large droplets causes droplets to deposit on both pressure and suction surfaces (seen close to the upper blade LE in fig. 4.4a) which can be captured even with the thin pseudo-blades.

Breakdown of inertial velocity slip

The low slip for droplet sizes associated with homogeneous nucleation indicates that deposition in steam turbines is driven by pitchwise velocity slip. This assumption is tested by introducing droplets of various sizes at the turbine inlet and recording trajectories as they are centrifuged towards the casing. Figure 4.5 shows the mid-height steam streamline and droplet trajectories, assuming droplets pass through the entire machine without intersecting any of the blade surfaces. Based on the *limiting pathlines*,⁵ it can be said that radial slip is very low for droplets under 5 µm, especially considering that most LP turbines operate with superheated steam at the inlet, reducing the time droplets have to drift towards the walls (from Wilson point until the outlet). Furthermore, nucleated droplets are much smaller than their outlet diameters and overall slip values will be much lower in the earlier stages. Finally, even for pathlines above the limiting one, there is a large probability droplets will impinge on a blade surface (especially in cases with high flow turning) before ever centrifuging sufficiently far to get deposited on the turbine casing, as each passage width is many times smaller than the passage height. Hence, radial drift of primary fog can be neglected, reducing computational time. For the much larger coarse water droplets, radial slip is dominant and must be included in the trajectory calculations.

The results shown in fig. 4.4 and 4.5 demonstrate that the model correctly predicts droplet trajectories for extreme values of Stokes number. This provides confidence that the model is capturing the correct physical behaviour, even though velocity slip might not be fully accurate on the range of intermediate Stokes numbers.

4.3 Turbulent deposition

As previously discussed in section 2.4, deposition of small droplets onto surrounding surfaces in a turbine flow field is only partly caused by inertia. A range of complex phenomena, such

⁵For each droplet size group there is a pathline that tangentially touches a turbine surface and is called the *limiting pathline*. All droplets released from a "higher" position intersect with a solid surface and are assumed to perfectly deposit on it, determining the overall proportion of deposited droplets.

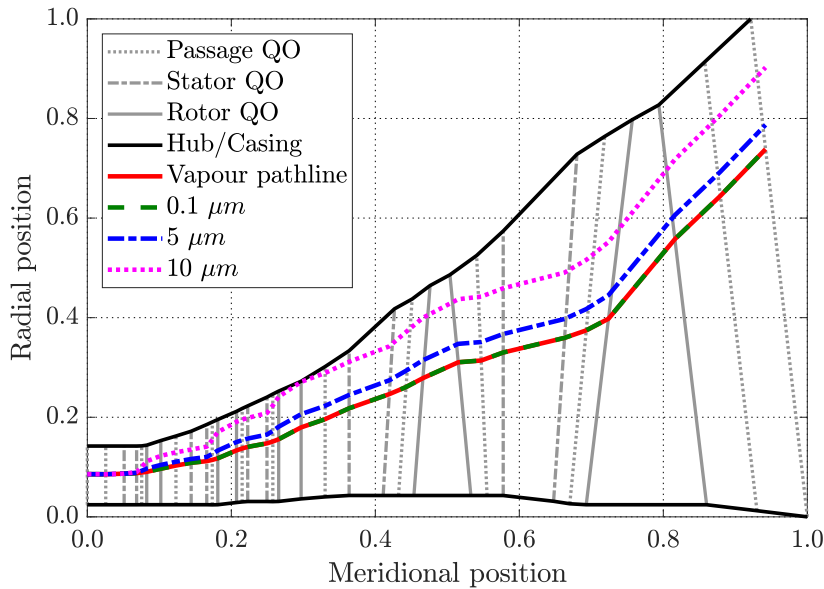


Fig. 4.5 Meridional trajectories for droplets of different sizes.

as turbophoresis and thermophoresis, affects velocity slip and causes a larger proportion of droplets to coast to the nearby walls. Their contribution to the total deposition rate is governed by the fine details in the flow field, especially turbulence in the regions close to a wall,⁶ which is very difficult to predict even in a single phase flow. This problem is further complicated by the tendency of water droplets to slip relative to vapour streamlines and turbulent eddies, establishing their own turbulent flow field [174].

One of the largest obstacles to turbine deposition research is the scarcity of experimental data since accurate deposition measurements are very hard to obtain. Moreover, measurements of deposition rates are mostly done on simple geometries (straight pipe: [135], [163], [136], [89], annular flow: [61], curved duct: [174]) and have high uncertainty levels.

A number of authors (see section 2.4.2) have attempted to address the problem of turbulent deposition of fog droplets. The standard modelling approach relies on high-fidelity numerical simulations to capture fine flow features (e.g., turbulent fluctuations in the boundary layer region) that drive the turbulent deposition rates, such as LES or DNS calculations. While those are effective methods for deposition research, they are not suitable for the industrial setting, especially when trying to model multiple turbine stages.

Coarse-grid turbine calculations using the streamline equilibrium method do not provide enough information to explicitly model turbulent deposition contributions. They often yield only leading and trailing edge flow properties, with no data on the flow within the blade

⁶Near-wall turbulence tends to be anisotropic and non-homogeneous, adding another layer of complexity to the problem; [174]

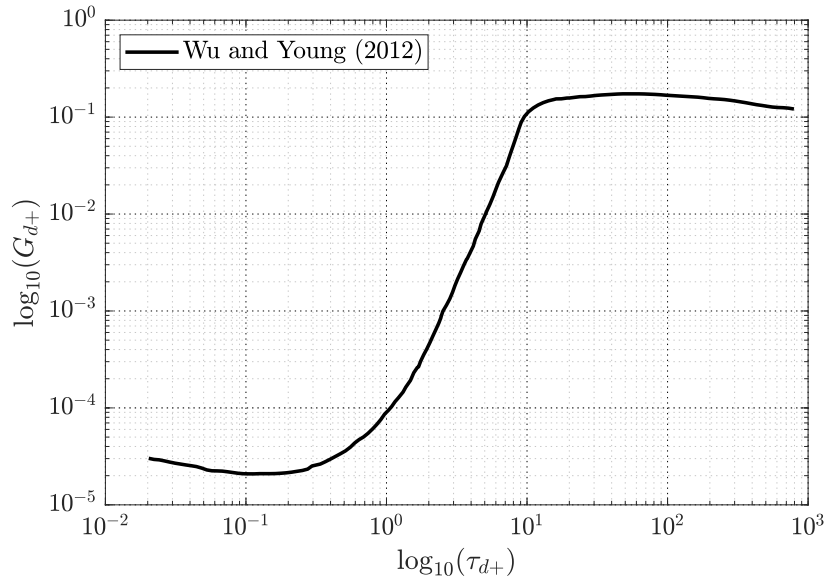


Fig. 4.6 Turbulent deposition curve extracted from Wu and Young [174].

passage and no turbulence correlations. Approximate methods based on the data available are therefore required.

This work uses empirical data to approximate the deposition rates due to non-inertial effects (primarily turbophoresis) in steam turbines. It is based on the experimental and theoretical data by Wu and Young, [174], who reported deposition rates in a straight duct segment, shown in fig. 4.6. Deposition rates due to inertial and other contributing effects are assumed to be mutually independent and the total deposition rate can be determined by summing up individual contributions. While this assumption is often used in deposition models described in the literature (e.g., [46]), it may not always be accurate. Gas turbine cascade calculations reported in [138], for example, showed complex interaction between the driving forces of deposition, with each mechanism affecting all others and leading to an enhanced deposition rate.

While turbophoresis has the largest effect on fog droplets [46], the influence of thermophoresis in steam turbines is significantly lower due to small pitchwise temperature gradients. Furthermore, thermophoresis decreases deposition in steam turbines since the boundary layers have a higher temperature than the core of the flow. By contrast, in gas turbines, where blades are cooled, thermophoresis increases deposition. This means that omission of thermophoresis not only simplifies the modelling but also reduces the effect of the independence assumption for the steam turbines.

The data in fig. 4.6 is reported as dimensionless deposition rate (mass flow) G_{d+} against dimensionless particle relaxation time τ_{d+} .⁷ Particle relaxation time, shown previously in eq. 4.7, is non-dimensionalized as:

$$\tau_{d+} = \frac{\tau_d u_*^2}{v_g}, \quad (4.35)$$

where v_g is the kinematic viscosity of steam and u_* friction velocity, expressed as:

$$u_* = \sqrt{\frac{\tau_s}{\rho_g}}. \quad (4.36)$$

Here, τ_s is the wall shear stress and ρ_g is the vapour density. On the other hand, deposition rate G_d is non-dimensionalized as:

$$G_{d+} = \frac{G_d}{\bar{\rho}_{l,v} u_*}, \quad (4.37)$$

with $\bar{\rho}_{l,v}$ being the mean particle density (mass of droplets per unit volume). Wall shear stress, proportional to the velocity gradient orthogonal to the solid surface, cannot be directly determined from a streamline equilibrium calculation but can be estimated from empirical relations for the skin friction coefficient C_f , defined as:

$$C_f = \frac{\tau_s}{0.5 \rho_g v_\infty^2}, \quad (4.38)$$

where v_∞ is the free-stream velocity.⁸

There is a substantial body of literature on skin friction coefficient (e.g., [156], [132], [131]), with many empirical relations expressing it as a function of Reynolds number. For laminar boundary layers, Blasius [18] proposed an analytical equation for a flat-plate in zero-gradient flow on both sides as:

$$C_f = \frac{1.328}{\sqrt{\text{Re}}}, \quad (4.39)$$

valid for $\text{Re} < 10^7$. Schlichting [131] proposed the relation for flat-plate turbulent boundary layer as:

$$C_f = [2 \log_{10}(\text{Re}_x) - 0.65]^{-2.3}, \quad (4.40)$$

valid for $5 \cdot 10^5 < \text{Re} < 10^9$. While eqs. 4.39 and 4.40 provide good approximations in many engineering problems, flow around a turbine blade is curved, with a strong favourable

⁷The subscript “+” stands for a dimensionless property, non-dimensionalized using the wall variables from turbulence theory [174].

⁸Blade row outlet velocity is often used as the free-stream velocity.

streamwise pressure gradient (accelerating flow), deviating from the flat plate assumptions. The impact of curvature and flow acceleration on skin friction has been examined by a large number of authors (curvature: [107], [141], [104], [162], [161]; acceleration: [105], [134], [80], [1]), and comprehensive reviews are given in [97] and [113]. Convex surfaces tend to compress turbulence to a thin layer near the wall, resulting in a fast decrease in C_f at the beginning of curvature, with values remaining low over the entire length of the curve [141]. Boundary layers on concave surfaces are significantly more difficult to analyse due to the possibility of longitudinal vortices and are slower to react to curvature changes. However, on average, concave surfaces tend to increase C_f [113]. While the two effects are closely connected and difficult to decouple (avoiding pressure gradients that often accompany surface curvature is a very challenging task), it was shown that pressure gradients have a greater impact on skin friction than curvature effects [113].

Finally, data on turbine blade skin friction is very scarce. Experimental values of C_f for a turbine cascade were reported in [91], [67], and [60], showing boundary layer transition from laminar to turbulent regime at locations between 30% and 60% blade length, bringing the blade average C_f closer to Schlichting's prediction. While the experimental measurement variation of $\approx 10\%$ is considered good in complex geometries like turbine blades, large uncertainties are reported for Mach numbers close to unity, as well as for cases where the pressure side shock wave impinges on the suction side surface.

Due to the lack of a more accurate estimate, flat-plate skin friction coefficient equations are still used in coarse turbine models (e.g., [46]) even though the physical behaviour significantly deviates from the underlying assumptions. And yet, it is still unclear how large the difference between a turbine blade and flat-plate skin friction coefficients is and how does it affect deposition rates. The following section addresses these questions.

4.4 CFD study of turbine blade skin friction coefficient

The influence of realistic turbine flow conditions on skin friction is the main focus of this section, done through a series of numerical flow calculations around a representative geometry. STEAMBLOCK, a Reynolds-averaged Navier Stokes (RANS) solver is used to rigorously model non-equilibrium steam expansion in a turbine cascade, capturing all relevant physical processes that influence tangential stresses on a blade and, hence, skin friction coefficient. It is based on Denton's three-dimensional viscous Euler solver, T-BLOCK, which has been extensively described in the literature ([32], [35], [123]). A brief overview is provided in the next section.

4.4.1 Non-equilibrium two-phase flow solver

STEAMBLOCK was developed as a T-BLOCK extension and includes non-equilibrium wetness (two phase flow) effects using the moment method [24]. Continuity, momentum, and energy conservation equations are defined in cylindrical coordinates (z, θ, r) for a two phase mixture and solved on a structured hexahedral mesh. This includes four additional equations for droplet spectrum moments that enable the calculation of nucleation and droplet growth, coupled with the conservation equations through wetness fraction.

The complete set of equations can be written as:

$$\frac{\partial}{\partial t} \int_V \mathbf{F}_v dV + \int_A \mathbf{F}_s \cdot d\mathbf{A} = \mathbf{S}. \quad (4.41)$$

Equation 4.41 is integrated in a cell with volume V and area A where \mathbf{F}_v , \mathbf{F}_s , and \mathbf{S} are body forces, surface fluxes and source terms, respectively, defined as:

$$\mathbf{F}_v = \begin{pmatrix} \rho \\ \rho v_z \\ \rho v_\theta \\ \rho v_r \\ \rho E \\ \rho \mu_0 \\ \rho \mu_1 \\ \rho \mu_2 \\ \rho \mu_3 \end{pmatrix}, \quad \mathbf{F}_s = \begin{pmatrix} \rho \mathbf{w} \\ \rho v_z \mathbf{w} + p \mathbf{e}_z \\ \rho r v_\theta \mathbf{w} + p \mathbf{e}_\theta \\ \rho v_r \mathbf{w} + p \mathbf{e}_r \\ \rho H \mathbf{w} + p r \omega \hat{\theta} \\ \rho \mu_0 \mathbf{w} \\ \rho \mu_1 \mathbf{w} \\ \rho \mu_2 \mathbf{w} \\ \rho \mu_3 \mathbf{w} \end{pmatrix}, \quad \mathbf{S} = \begin{pmatrix} 0 \\ F_z \\ M_\theta \\ F_r + \int \frac{p + \rho v_\theta^2}{r} dV \\ Q + W_v \\ \int \rho J_* dV \\ \int (\rho G \mu_0 + \rho J_* r_*) dV \\ \int (2\rho G \mu_1 + \rho J_* r_*^2) dV \\ \int (3\rho G \mu_2 + \rho J_* r_*^3) dV \end{pmatrix}, \quad (4.42)$$

where \mathbf{w} is the relative fluid velocity, F_z and F_r are viscous force components in axial and radial directions, and M_θ is the circumferential viscous torque. Viscous forces are evaluated at cell faces and the resultant is applied to the cell centre as a body force. Q and W_v are heat transfer and viscous work done on the control volume, respectively. In the moment equation terms, r_* is the critical radius, J is the nucleation rate and G is the droplet growth rate, all previously defined in section 2.2, while μ_i , $i \in \{0, 1, 2, 3\}$, are the first four moments of the droplet spectrum.

Numerical method

Conserved properties calculated in eq. 4.41 are stored in cell vertices and surface integrals are approximated using a face average⁹ value. Steady-state calculation time stepping (and inner time stepping of the unsteady calculation) begins with the application of eq. 4.41 to each cell in the form:

$$\frac{d\mathbf{F}_v}{dt}V + \mathbf{R}(\mathbf{F}_v) = 0, \quad (4.43)$$

where $\mathbf{R}(\mathbf{F}_v)$ is the residual term, containing all sources and surface fluxes. Cell volume is considered to be invariant in time (no mesh deformation or cell generation/destruction) and can be brought in front of the time derivative. Change in conserved properties along i -th time step, Δt_i , is then calculated using the *scree* scheme [38]:

$$\Delta\mathbf{F}_v = \frac{(2\mathbf{R}_i - \mathbf{R}_{i-1})\Delta t_i}{V}. \quad (4.44)$$

The value of Courant-Friedrich-Levy (CFL) number at each cell is used to determine the time step size Δt_i and the change in conserved properties is then distributed to cell vertices.¹⁰ Numerical stability is improved using the adaptive smoothing method by Jameson et al. [79] based on the local gradients, blending a second and fourth order smoothing. This improves flow stability next to shock waves and prevents oscillations near the Wilson zone. Unsteady calculations are performed using implicit dual time stepping [78].

Turbulence and boundary layer modelling

Turbulence is modelled using the one-equation Spalart-Allmaras model [142], [4], which was shown to have good agreement with both experiments and two-equation $k-\omega$ SST model [147], with Denton's limitation on the effective wall distance [36] to prevent excessive turbulence destruction. Total viscosity, consisting of laminar and turbulent contributions ($\mu = \mu_{lam} + \mu_{tur}$), is used to determine viscous forces and work done on each cell. Heat transfer between cells is modelled assuming Prandtl number is equal to unity, with more details on the viscous and heat transfer terms given in [23].

Boundary layers next to solid surfaces are modelled using wall functions defined by [35], establishing velocity profiles and shear stresses and preventing mass flow orthogonal to the wall surface. The function relies on Reynolds number next to the wall, which determines

⁹Face average is determined as a sum of contributions from individual vertices making the face. Finally, flux value is determined by multiplying the face average with the face vector.

¹⁰In a structured hexahedral mesh, each vertex is a member of eight cells and, therefore, receives one-eighth contribution from each cell when updating its value.

whether the first layer of cells falls in the laminar sub-layer or logarithmic region of the turbulent boundary layer. It is calculated as:

$$\text{Re} = \frac{V\bar{\rho}\bar{u}}{A_w\mu_{lam}}, \quad (4.45)$$

where V is cell volume, A surface area, and overbar stands for face averaged values. Skin friction coefficient, shown previously in eq. 4.38 is expressed as a function of Reynolds number, based on the face distance from the wall, assuming the first cell is located within laminar sub-layer or the logarithmic region of the turbulent boundary layer:

$$C_f = \begin{cases} 2/\text{Re}, & \text{Re} \leq 125 \\ -0.001767 + 0.03177/\ln(\text{Re}) + 0.25614/(\ln(\text{Re}))^2, & \text{Re} > 125 \end{cases} \quad (4.47)$$

where $\text{Re} = \rho Vy/\mu$ and y is the distance from the wall.

Face position within the boundary layer is determined based on the non-dimensional distance from the wall, y_+ :

$$y_+ = \frac{\rho u_* y}{\mu_{lam}}, \quad (4.48)$$

where u_* is friction velocity shown in eq. 4.36. Laminar sub-layer stretches up to $y_+ \approx 11$, followed by a transition into the log-law region. The vertices within the turbulent boundary layer have turbulent viscosity value reduced close to the wall; and if in laminar sub-layer, turbulent viscosity is considered negligible.

4.4.2 White's cascade test case

The solver outlined in the previous section was applied to a steam cascade test case built around a blade geometry previously investigated by White [164]. The blade, shown in fig. 4.7, is a typical turbine geometry, based on the quarter annulus, full size profile of a fifth stage LP turbine stator. The computational domain was constructed around a single blade slice, with a short flow segment leading to the blade and a long downstream section.

Three-dimensional finite volume mesh, shown in fig. 4.8, was built in eight structured H-mesh blocks, with two cell layers along the blade height. Cell height was progressively refined in the near-wall region (see fig. 4.9a and 4.9b) to correctly capture flow gradients. The mesh was built in two resolutions (medium: 22048 cells, fine: 45280 cells) to verify mesh independence of results.

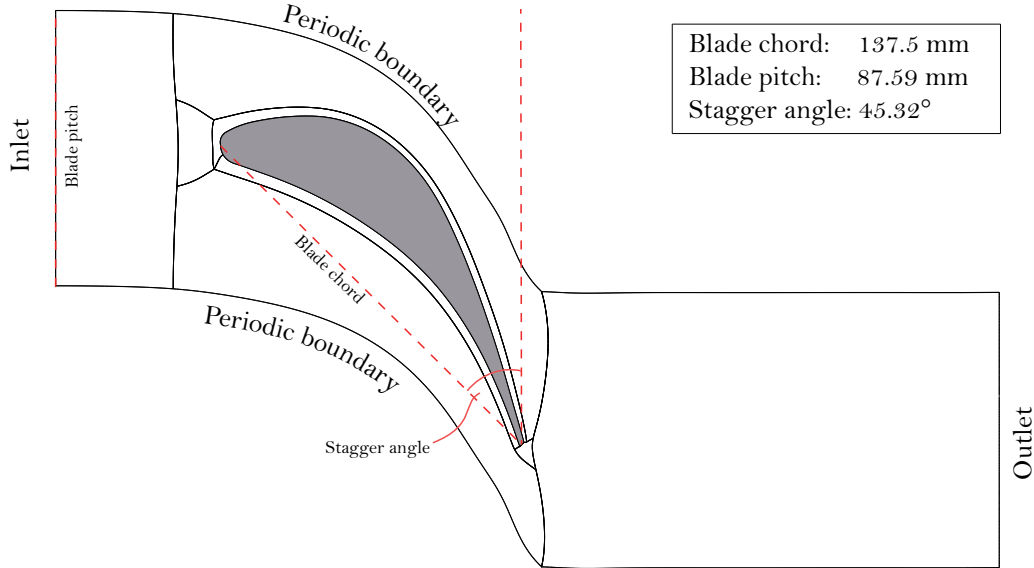


Fig. 4.7 Blade geometry and computational domain.

Stagnation pressure, temperature and flow angle of steam are provided at the inlet and static pressure at the outlet boundary. Periodic boundary condition was applied to circumferential and radial boundaries, making the calculation analogous to a cascade flow around infinitely long blades, avoiding end-wall effects. Finally, blade surfaces were assigned wall boundary conditions with wall functions.

4.4.3 Comparison with experimental measurements

Experimental observations of pressure along the surface of the blade, as reported by [164], are used to validate the numerical results. Two distinct configurations were chosen: one with high inlet superheat, maintaining dry steam conditions throughout the blade row, and one with low superheat, resulting in a spontaneous heterogeneous nucleation event. More details on input data defining these cases are given in table 4.1. Mach number used below stands for average isentropic exit value, based on total-to-static pressure ratio p_{01}/p_2 and isentropic exponent of $\gamma = 1.32$.

High inlet superheat

Numerical results in fig. 4.10 show very good agreement with experimental data. Despite the inlet superheat of 28 K, high expansion rates on the blade suction side increase subcooling enough to trigger homogeneous nucleation, which is subsequently suppressed by the suction side shock. The calculation successfully captures the impingement of the pressure side

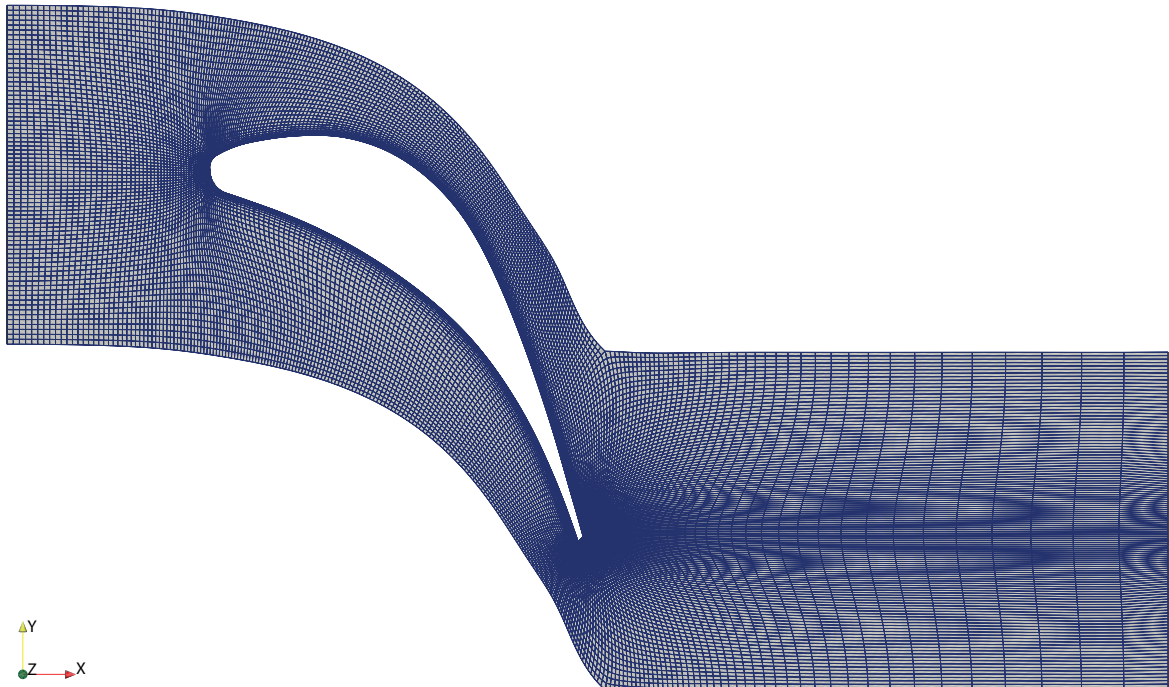
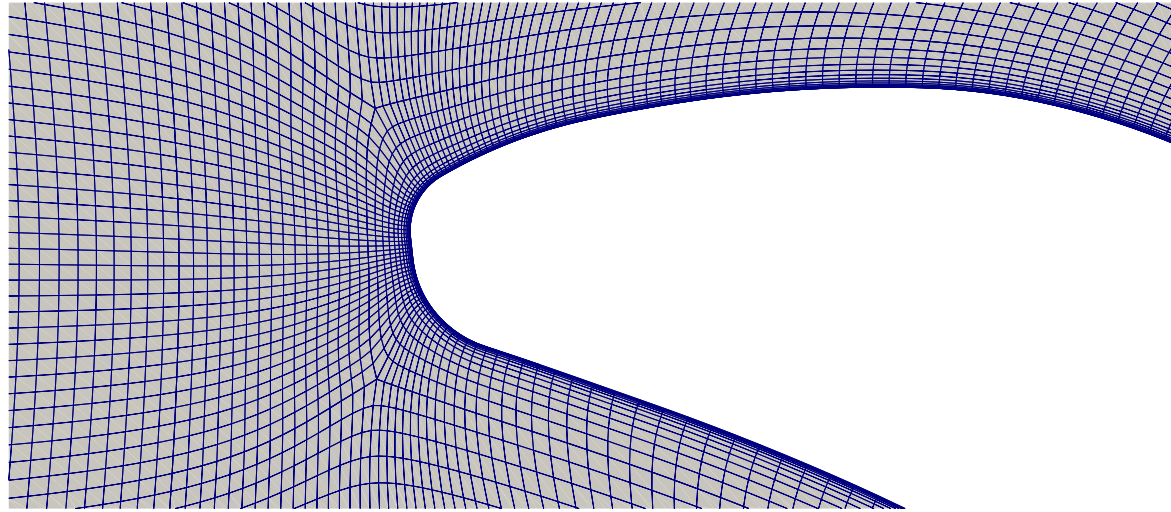


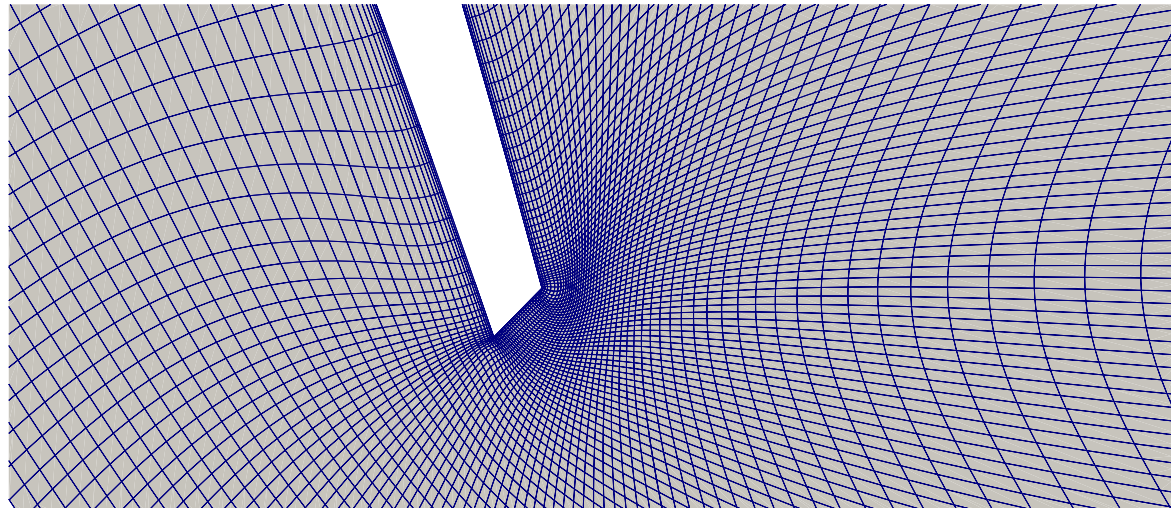
Fig. 4.8 Block structured finite-volume mesh (fine resolution).

Table 4.1 Steam boundary conditions used for the high and low superheat cases.

ID	Inlet			Outlet	
	Stagnation pressure p_{01}	Stagnation temperature T_{01}	Stagnation superheat $T_{01} - T_s(p_{01})$	Mean static pressure p_2	Isentropic Mach No. M_2
L2	40.9 kPa	354 K	4 K	19.4 kPa	1.11
H2	41.9 kPa	378.5 K	28 K	17.7 kPa	1.20



(a) Leading edge mesh detail



(b) Trailing edge mesh detail

Fig. 4.9 Mesh structure in the proximity of the blade. Cells are progressively refined in the wall-normal direction to accurately capture flow gradients, while maintaining reasonable y_+ values ($25 < y_+ < 90$). Nodes are non-uniformly distributed along the blade, creating thin, elongated cells in the region with lower streamwise gradients and reducing overall cell count while retaining the quality of the results.

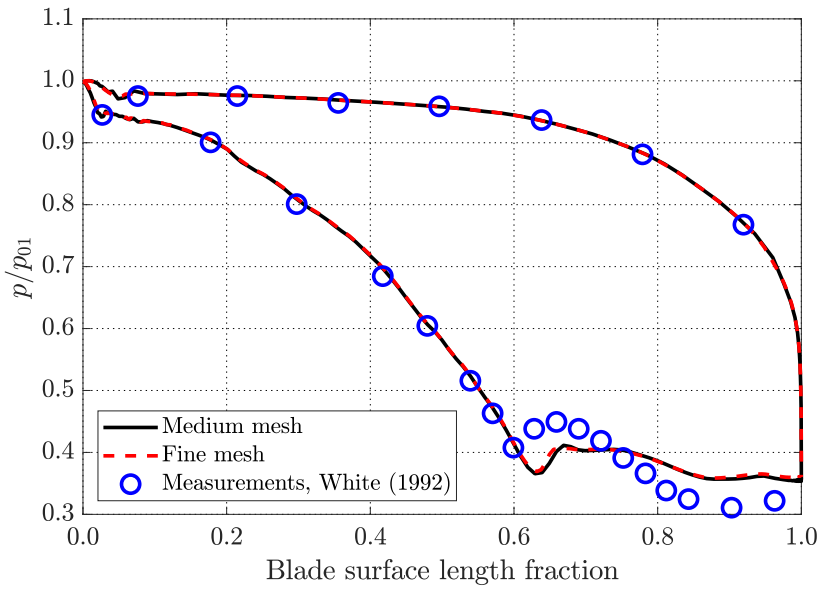


Fig. 4.10 H2 steam cascade case.

shock wave (coming from the trailing edge of the blade above) on the blade suction side, at approximately 65% blade length, albeit with a small difference in the impingement location. A sharp pressure rise, a consequence of the shock wave presence, is captured but is smaller in magnitude and is followed by a slightly gentler pressure decrease than what the experiments show. This is a consequence of numerical smoothing around the shock wave – which presents a discontinuity in the variables, results in sharp gradients that produce oscillatory behaviour of the solution, and needs to be damped to ensure convergence.

Low inlet superheat

Reducing inlet superheat causes a spontaneous nucleation event, with pressure side shock interacting with the condensation shock. The Wilson point occurs at the same location as the shock wave and contributes to the local pressure rise, reducing the impact of numerical smoothing. As a result, the pressure change is sharper and fits the experiments better, as seen in fig. 4.11. Moreover, temperature rise from the shock causes part of the nucleation front to be postponed, occurring further downstream.

In conclusion, both cases demonstrate the capability of STEAMBLOCK solver to reliably predict flow around a blade when dealing with complex flow conditions such as non-equilibrium steam expansion, shock waves, and condensation shocks.

As for the skin friction coefficient, experimental measurements of C_f in turbine blades are rarely available and contain very high uncertainty margins. However, the blade-average C_f , calculated and shown in the following section, qualitatively agrees with experimental

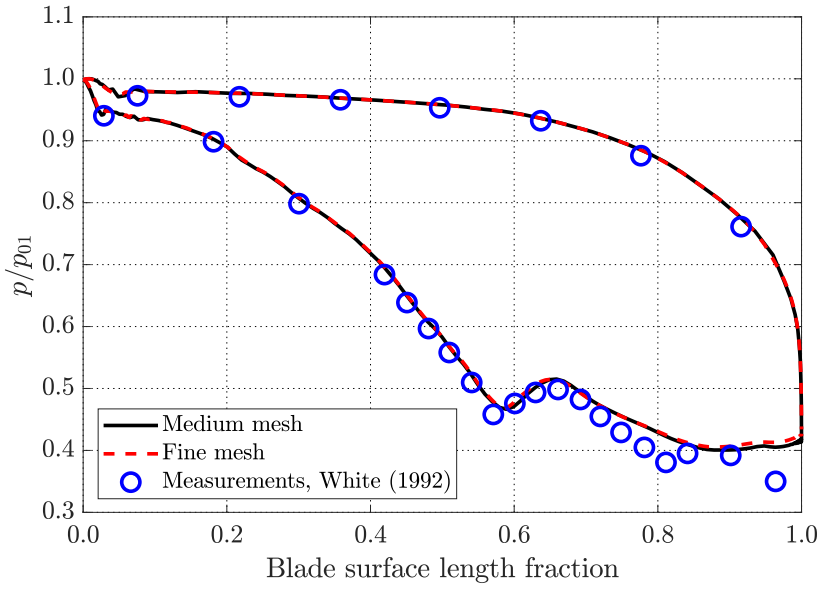


Fig. 4.11 L2 steam cascade case.

findings for a comparable steam cascade reported in [91] over a range of inlet conditions, lending further support to the validation efforts.

4.4.4 Breakdown of factors influencing the skin friction coefficient (C_f)

The skin friction coefficient is calculated along blade length for the H2 case presented above. The blade is roughly divided into pressure (PS) and suction (SS) side surfaces, as shown in fig. 4.12. The surfaces are "unwrapped", starting from pressure side TE to suction side TE, and normalized with their respective lengths. The starting point is set at the blade LE, defining points along the suction side on the positive x-axis and pressure side along the negative x-axis.

Local blade skin friction coefficient

The skin friction coefficient strongly varies along the blade surface, with distinctively different behaviour on PS and SS, as seen in fig. 4.13. The actual stagnation point for this configuration lies slightly on the suction side of the curve, recognisable by the zero value of C_f . The brief region of rapid increase following the stagnation point on both SS and PS comes from the flow acceleration and strong local curvature around the LE. This is followed by the strong progressive increase along the SS as the boundary layer develops, while values remain reasonably low along the majority of the PS, and experiences a sharp increase close to the trailing edge.

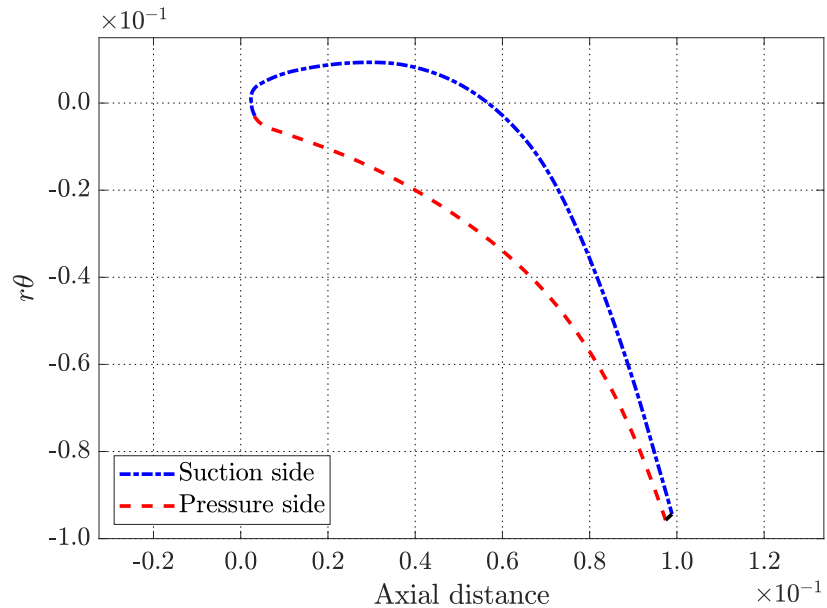


Fig. 4.12 Definition of suction and pressure side surfaces.

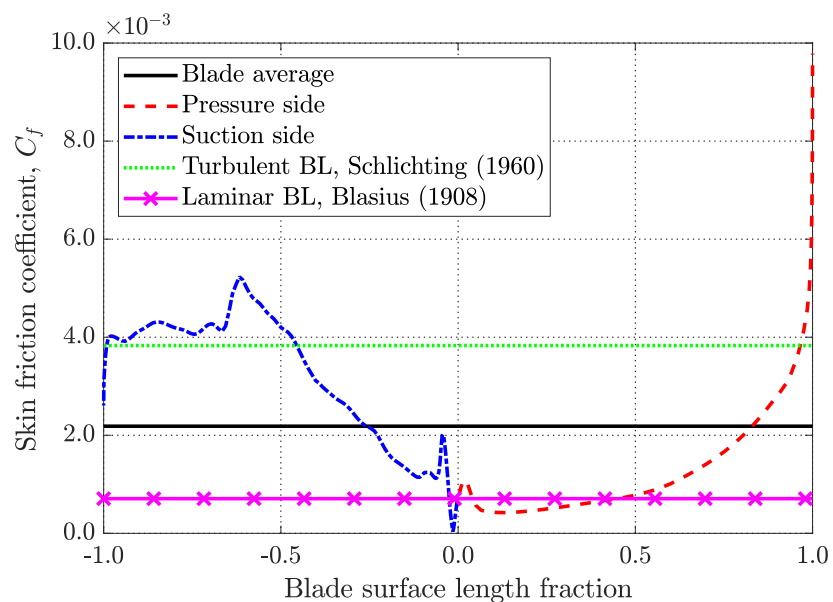


Fig. 4.13 Skin friction coefficient distribution along the blade.

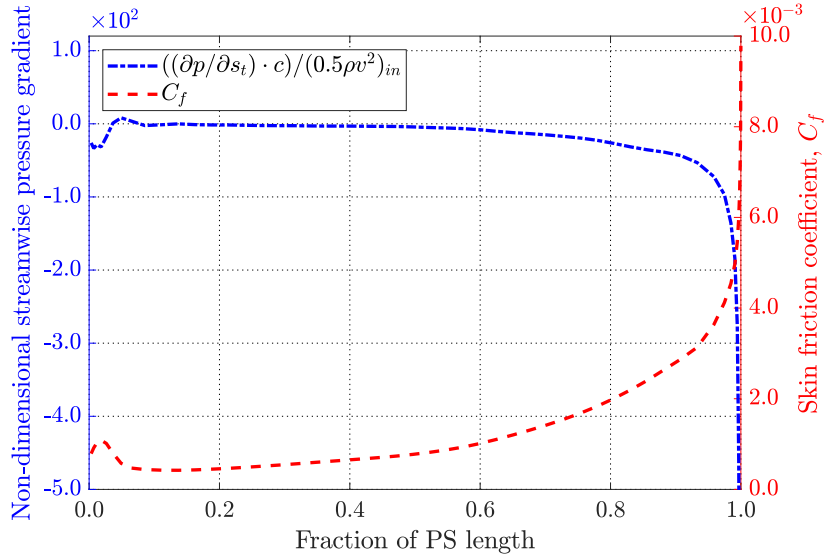


Fig. 4.14 Streamwise pressure gradient and skin friction coefficient along the blade pressure side.

Streamwise pressure gradient ($\partial p / \partial s_t$), assumed to be zero in flat-plate approximations, is strongly present in turbine passages and its influence on blade C_f is examined. Figure 4.14 shows C_f plotted against $\partial p / \partial s_t$ along the blade surface, scaled by inlet dynamic pressure to chord ratio, $(0.5\rho v^2)_{in}/c$. The pressure side distributions show simple trends, with a short region of flow acceleration and deceleration around the LE as the local curvature rapidly changes from convex to concave, followed by a long region of low flow acceleration. The C_f distribution mirrors the pressure gradient, exponentially increasing in the last segment of the blade towards the TE with large curvature radius (i.e., negligible curvature effects) as the flow approaches the PS-TE shock wave. However, the rapid increase is limited to the very end of the blade, keeping the PS-averaged C_f low.

The trends on the SS are more complex, as seen in fig. 4.15. Following the stagnation point ($C_f = 0$), the flow goes through acceleration-deceleration as it passes around the LE. Acceleration progressively increases along the blade, at a higher rate than on the PS, rapidly increasing skin friction. However, impingement (and reflection) of the pressure side shock coming from the TE of the blade above causes a jump in the pressure – seen as a spike at $\approx 65\%$ blade length.¹¹ This is followed by a separation region, with $\partial p / \partial s_t$ oscillating around zero until the flow passes through the SS-TE shock wave, seen as the second jump in $\partial p / \partial s_t$.

Both figures demonstrate a range of complex flow phenomena (strongly accelerating flow, curvature, shock wave interaction, boundary layer separation) that commonly occur in

¹¹Spike width is increased by numerical smoothing, as described in the previous section.

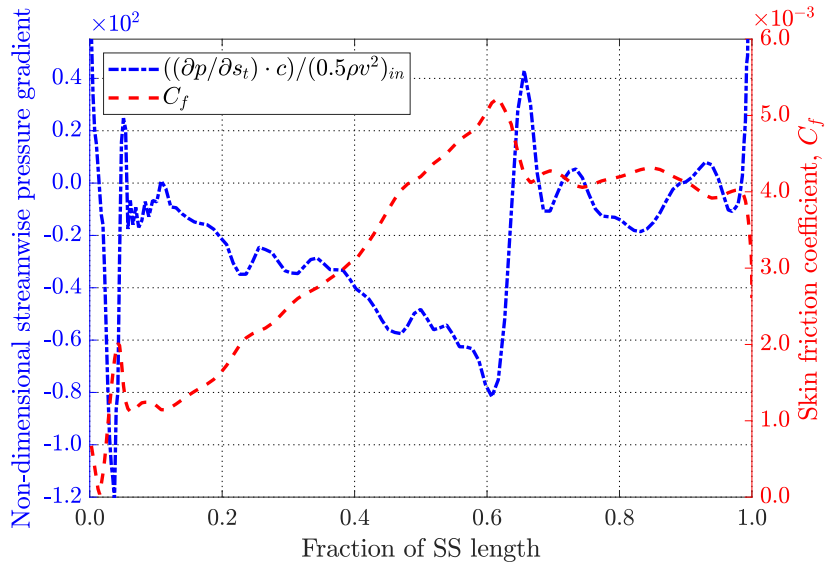


Fig. 4.15 Streamwise pressure gradient and skin friction coefficient along the blade suction side.

turbines and affect the local skin friction coefficient. They are all overlooked when using the flat-plate assumption. The effect this might have on deposition rates is discussed in section 4.5.

The streamwise pressure gradient has the dominant effect on C_f , clearly seen from the middle of the blade onwards where blade curvature is less pronounced. There, $\partial p / \partial s_t$ is almost directly reflected in C_f , following the same global trends (skin friction increase is proportional to local flow acceleration). Curvature affects skin friction in a more subtle way, seen in the region close to the LE where changes in C_f cannot be entirely attributed to flow acceleration. Its impact on skin friction is, however, significantly smaller than $\partial p / \partial s_t$, playing only a minor role in shaping the C_f curve. The occurrence of shock wave impingement and reflection depends on the inlet conditions while the boundary layer separation requires a sufficiently strong incident shock [31]. Hence, it is difficult to know *a priori* how the presence of TE shock waves might interact with the SS boundary layer and, consequently, with local C_f .

Difference between modelling approaches

With the non-inertial deposition model depending directly on blade-average skin friction coefficient, flat-plate estimates are examined on a range of Reynolds numbers typically observed in LP steam turbines and compared to CFD results. Flow Reynolds number is changed by adjusting the inlet steam superheat, maintaining constant total-to-static pressure

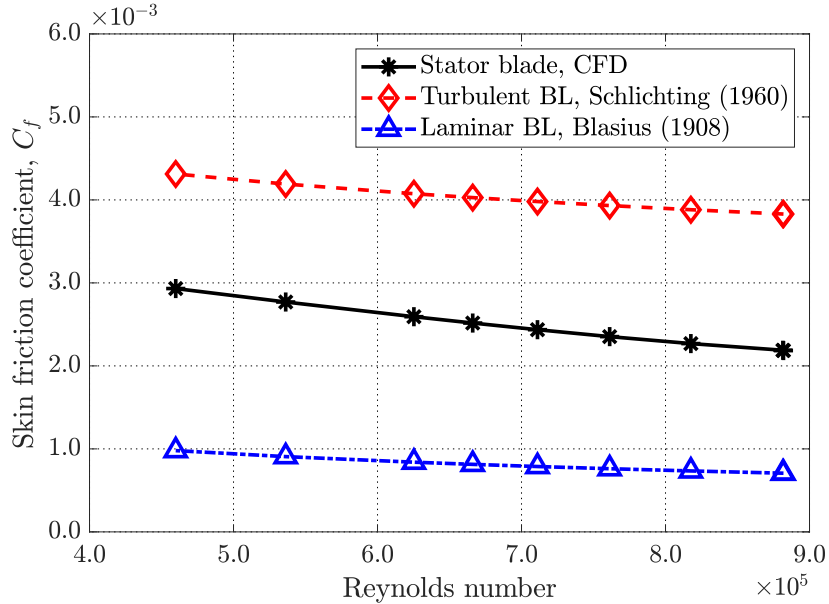


Fig. 4.16 Difference in C_f prediction between Schlichting's flat plate equation and White's turbine cascade CFD calculation.

ratio (p_{01}/p_2) in all calculations. The total drag force in the CFD calculations is determined by integrating the wall shear stress, τ_s , over the blade surface, and non-dimensionalized using outlet flow properties as a reference. Similarly, outlet Reynolds number is used in flat-plate eqs. 4.39 for laminar and 4.40 for turbulent boundary layers. The results are shown in fig. 4.16.

It can be concluded that: (i) the use of Schlichting's equation for droplet deposition in turbines overestimates C_f over the Re range. This is because it assumes the boundary layer to be turbulent over the entire blade. (ii) The converse is true for Blasius' equation; (iii) They overlook all relevant effects (discussed above) that impact both local and blade-averaged skin friction by assuming a zero pressure gradient, flat-plate boundary layer.

Since the blade boundary layer starts as laminar and transitions to turbulent (according to [164], transition for this blade mostly occurs at around 30% blade length) it can be expected that the $C_f(\text{Re})$ curve will fall somewhere in between Blasius' (laminar) and Schlichting's (fully developed turbulent) predictions for most blade geometries. Blade-average CFD results follow the same trend as the approximative equations, albeit with a slightly steeper rate of descent – most likely caused by the shock wave interaction with the suction side surface, decreasing C_f in the final section of the blade.

On the other hand, change in flow inlet incidence angle (applied to the H2 inlet conditions) does not seem to affect blade average C_f significantly, as seen in fig. 4.17. The incident shock wave causes boundary layer separation at a relatively fixed location, preventing a larger

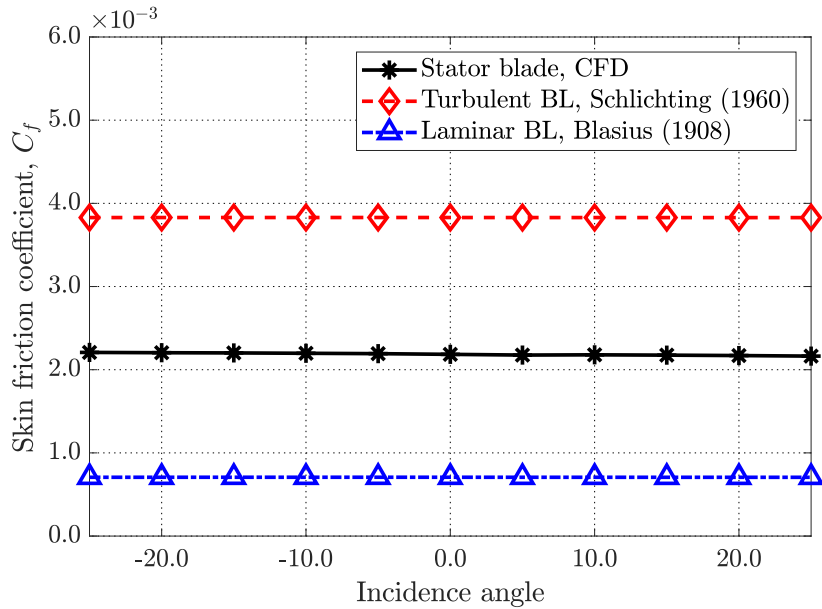


Fig. 4.17 Effect of flow incidence angle on skin friction coefficient.

variation in C_f for this combination of geometry and inlet conditions even when larger angles are considered. However, small incidence angles usually associated with changing operating conditions (e.g., for turbine flexing) are not expected to significantly influence average C_f even when no shock impingement is present.

The difference between Schlichting's equation and CFD results outlines the error magnitude associated with the use of flat-plate assumptions for turbine blade C_f prediction. While performing complex CFD calculations as pre-processing for a coarse deposition calculation would defeat the purpose of the model, available C_f data for similar blade geometries – such as the CFD curve in fig. 4.16 – provides a much better approximation than eq. 4.40. Since the turbulent deposition model described in section 4.3 directly depends on the blade-averaged C_f , the following section investigates how sensitive the deposition is to changes in C_f modelling.

4.5 Impact of skin friction coefficient on droplet deposition

A study of the sensitivity of turbulent deposition to skin friction coefficient has been done on the repeating stage turbine design test case, previously shown in chapter 3. Deposition calculations have been performed on the final stage stator blade row, using the droplet size spectrum generated by wake chopping calculations with decaying wakes (with $\tau_w = 5\Delta t_{ls}$, where Δt_{ls} is the last stage stator transit time) and two-dimensional expansion rate variation,

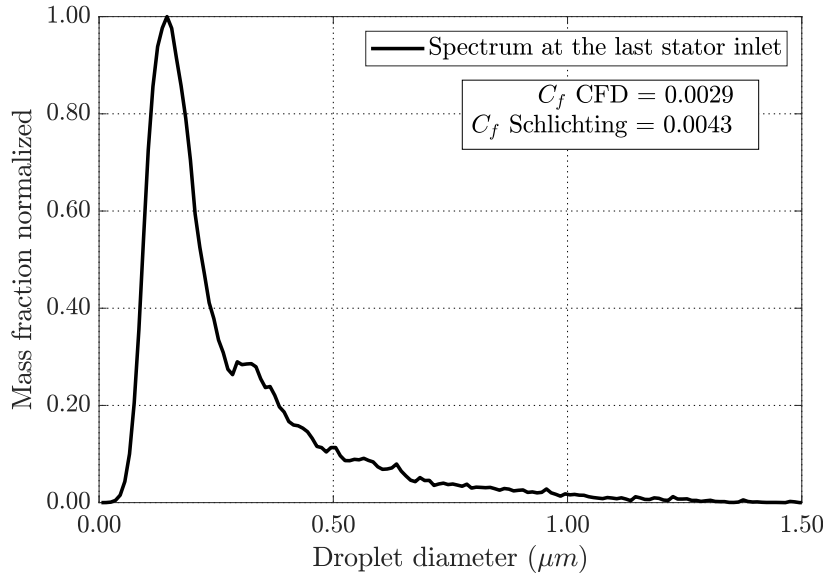


Fig. 4.18 Droplet size spectrum at the last stage stator inlet and estimated skin friction coefficients.

as seen in fig. 4.18. The computational procedure goes through each droplet size bin by tracking droplet motion through the blade row and recording final locations as well as inertial deposition rates for deposited droplets. This is followed by a turbulent deposition calculation, using skin friction coefficients and particle relaxation times to determine deposition rates before moving on to the next droplet size bin. Skin friction coefficients are estimated based on the local Reynolds number using: (i) Schlichting's empirical equation for a flat plate turbulent boundary layer (eq. 4.40), and (ii) linear interpolation of CFD results for White's cascade.

Deposition rates are processed as deposited liquid mass ($\text{kg}_i/\text{kg}_{mix}$), deposited fraction of droplets ($\%_i$), and total fraction of liquid mass deposited (%), for each droplet diameter d_i .

4.5.1 Influence of different models: Schlichting vs. CFD

Figure 4.19 compares fractional deposition rates for the two skin friction models. Since inertial deposition model does not depend on C_f , inertial rates are identical for both calculations, showing rapid increase with diameter as droplets become less able to follow the vapour. In contrast, turbulent fractional deposition rates, while following the same trend in both cases, show large differences, particularly for diameters in the range $0.2 - 0.6 \mu\text{m}$. The overall result, for this case, is that the Schlichting's correlation doubles the turbulent deposition rate relative to the CFD-based values of C_f . The cause behind it can be seen in fig. 4.20. Each dot represents an individual droplet size group within the droplet spectrum and is coloured

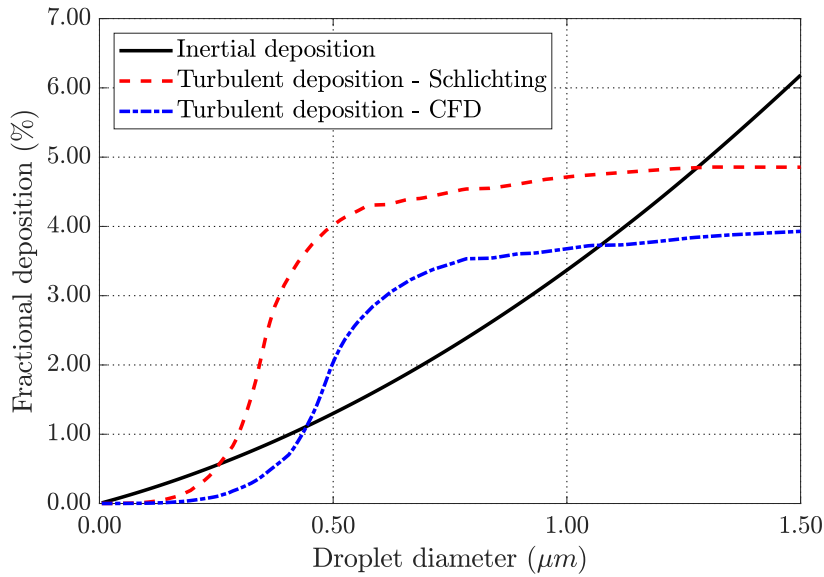


Fig. 4.19 Fractional deposition rate in the last stage stator. Fraction is defined with respect to the inlet liquid mass flow.

based on the associated liquid mass (normalized by the peak value, shown in fig. 4.18). The position of each dot is given by the dimensionless inertial relaxation time, calculated using the CFD result (fig. 4.20a) or Schlichting's flat-plate equation (fig. 4.20b). Higher friction velocity, as a consequence of a larger C_f associated with the flat plate assumption, increases τ_{d+} for droplets of the same diameter. As a result, droplet size bins in fig. 4.20b are shifted to the right from their respective counterparts in fig. 4.20a. The colour red characterises droplet size bins where most of the liquid mass is concentrated (i.e., the majority of droplets have a diameter in that range), which are in this case, located in the diffusion-impaction deposition regime. Hence, a shift to the right strongly increases the dimensionless deposition rate for droplet groups with highest concentration in the flow.

However, fig. 4.21 shows that it is not the droplet size with the highest concentration that dominates the change in deposition rate. Droplets around the small secondary peak in the distribution (e.g., $0.3 - 0.4 \mu\text{m}$), while having a $\sim 66\%$ lower concentration than the $0.145 \mu\text{m}$ droplets (the peak in fig. 4.18), contribute more than eight times the mass per deposited droplet since $m_i \propto d^3$. The largest difference in fractional deposition, seen for sizes between $0.3 - 0.7 \mu\text{m}$ in fig. 4.19, increases fractional deposition for those sizes and boosts the deposited liquid mass contribution from smaller droplets, as seen by the strong rise of the red line in fig. 4.21 over the same range of droplet diameters. For larger droplets, the difference in fractional deposition rates remains almost constant between the two models. However, since the concentration of large droplets in the flow rapidly decreases with diameter, their impact on total deposition rates is diminished.

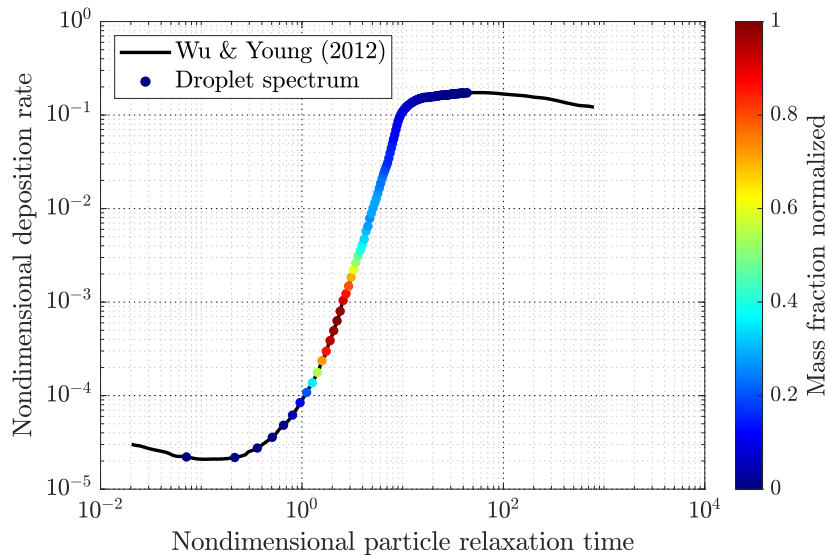
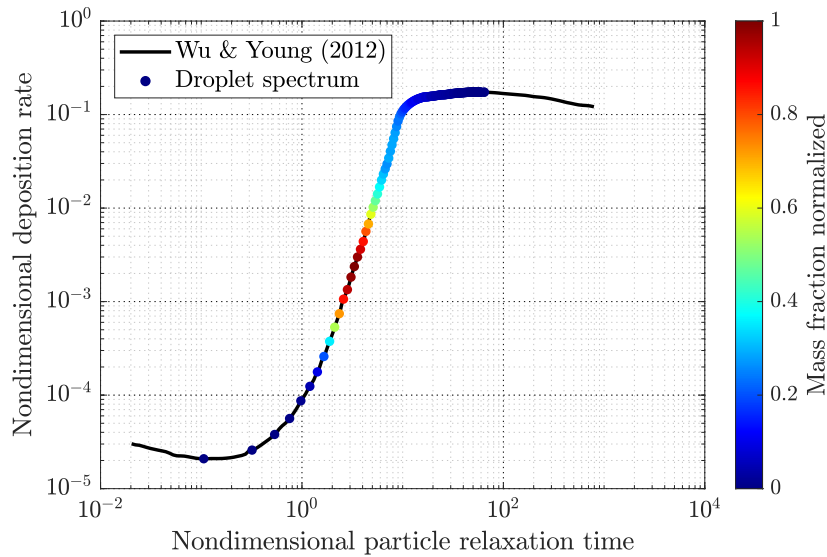
(a) Dimensionless deposition rates using CFD C_f relation.(b) Dimensionless deposition rates using Schlichting's C_f relation.

Fig. 4.20 Change in dimensionless particle relaxation time based on the used $C_f(\text{Re})$ function. Individual droplet size groups are coloured according to the amount of liquid mass contained within (i.e., number of droplets with the same diameter).

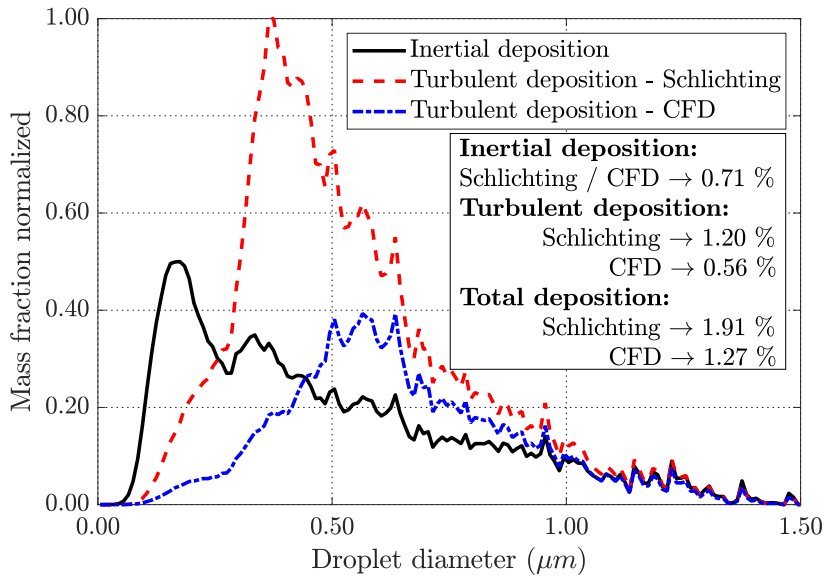


Fig. 4.21 Deposited liquid mass fraction for different C_f models. Normalized with global peak value.

In conclusion, Schlichting's significantly higher skin friction coefficient changes the dominant depositional mechanism. While the inertial deposition model is not a function of C_f , the turbulent deposition model showed significantly higher deposition rates when using Schlichting's formula: $\sim 50\%$ larger C_f results in a $\sim 115\%$ larger turbulent deposition rate and a $\sim 50\%$ larger total deposition rate (expressed as deposited fraction of liquid mass, $\text{kg}_l/\text{kg}_{mix}$), as can be seen in the fig. 4.21, indicating a substantial sensitivity to the choice of C_f model. While the sensitivity magnitude is case specific and depends on flow conditions and proportion of droplets in the diffusion-impaction regime, the difference in depositional mass flow rate should not be ignored. A qualitative comparison of presented deposition results with numerical ([148], [177]) and experimental ([91]) data confirms that a blade-average skin friction coefficient predictions from a similar turbine design represents a significantly better alternative to flat-plate approximations when examining new design options.

4.5.2 Sensitivity to small variations in C_f

The model sensitivity to small variations (such as when using an available C_f as an estimate) is tested by scaling the baseline C_f value,¹² emulating the effect of different blade designs and operating conditions. We see in fig. 4.22 that a $\pm 10\%$ variation in C_f leads to a $\sim \pm 10\%$ change in total deposited fraction of liquid mass. Since inertial deposition rate is not a

¹²Using the CFD calculated blade-average value of C_f for White's steam cascade.

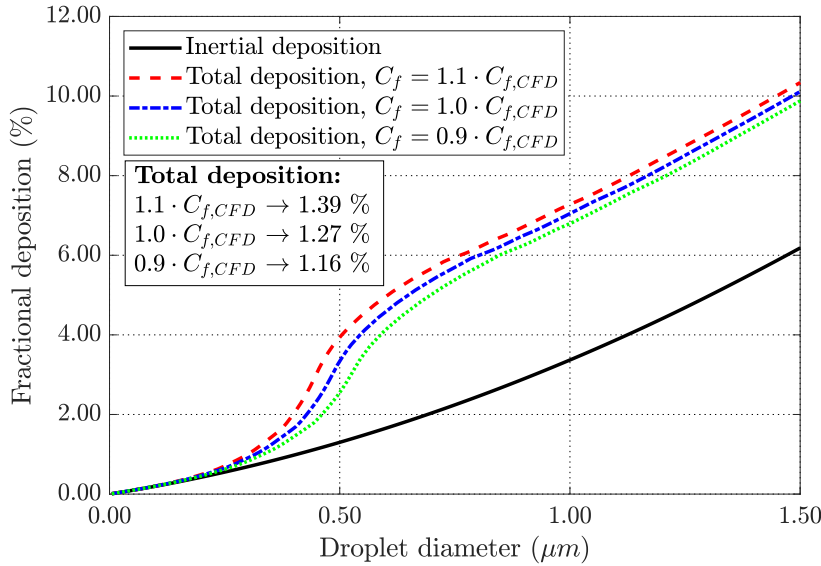


Fig. 4.22 Total deposition variation.

function of C_f and is comparable in magnitude to turbulent deposition rates, it dampens the sensitivity of total deposition rates to changes in C_f .

This sensitivity analysis was expanded to cover a broader range of skin friction coefficient variation. Given the approximate linearity in fig. 4.23, we see that 1% error change in C_f is associated with a $\sim 1\%$ change in total deposition rates for a C_f variation range of $\pm 25\%$. For C_f values lower than the 75% of the reference value, the error in deposition rates tends to decrease, caused by the larger proportion of fixed inertial deposition rate in the total deposition rate. The opposite is true for overestimated C_f values, driving the deposition error further up.

Existing numerical and CFD data on turbine and compressor blade skin friction coefficients points to a difference range of $\pm 20\%$, outlining the expected error range of deposition rates when using skin friction coefficient from a similar blade geometry.

4.6 Importance of droplet spectrum accuracy

Having determined the sensitivity of the model to skin friction coefficient for a single case, the aim is to examine the effect of wake chopping on droplet deposition. Figure 4.24a shows droplet size spectra released from the inlet of the last stage stator, as generated by throughflow calculations: (i) with or without wake chopping, and (ii) with one-dimensional or two-dimensional expansion rate variation. All other parameters have been kept constant (wake decay rate, τ_w , is equal to $5\Delta t_{ls}$, and wake width, σ_w , is kept at 0.04, with Δt_{ls} being

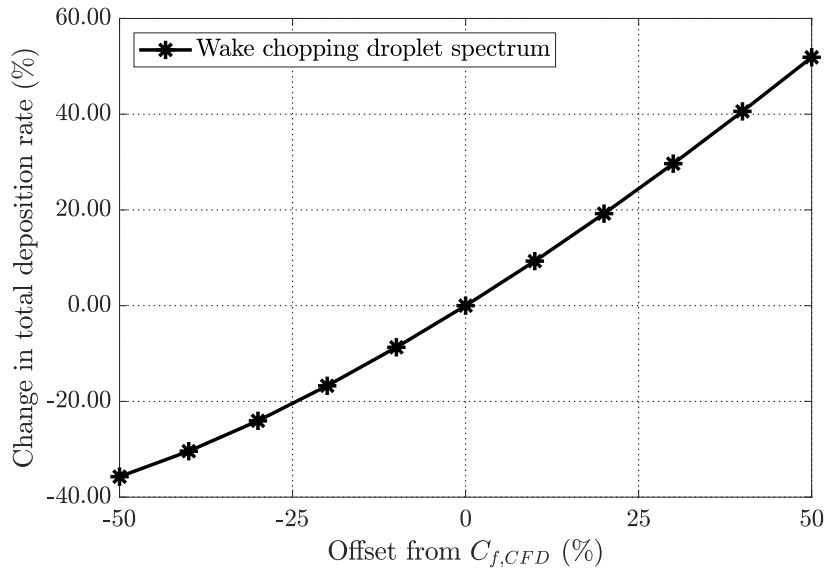


Fig. 4.23 Change in total deposition rates with C_f variation.

the transit time in the last stage stator) and the values in each figure are normalized by individual maxima. One-dimensional expansion rate calculations with no wake chopping typically generate a narrow droplet size spectrum, while the addition of pitchwise \dot{p} variation postpones the nucleation for a portion of the steam, resulting in a substantially wider spectrum which is very sensitive to changes in inlet conditions. Similarly, pitchwise pressure variations expand the already widened droplet spectrum when including the effects of wake chopping. Although the mass fraction of droplets larger than $1.0\text{ }\mu\text{m}$ is very small, the much higher deposition rates for larger droplets mean they contribute significantly to the mass deposited.

4.6.1 Effect of wake chopping and expansion rate variation

The deposited liquid mass fraction due to the inertial velocity slip and scaled by the global peak is shown in fig. 4.24b. The rapid decrease in liquid mass with diameter after the peak in the droplet spectrum results in a much milder decrease when looking at inertial deposition. Since larger droplets contain more liquid mass and take longer to adjust to surrounding flow changes, a larger proportion of them end up impinging on the surrounding surfaces, which significantly contributes to overall deposition mass flow. The opposite is true for small droplets: even though their concentration in the flow is large, deposition rates are low and each droplet does not contribute a lot of liquid mass. Sharp jumps in the droplet size spectrum also occur in the inertially deposited spectrum. However, peaks associated with small diameters are reduced while peaks associated with larger droplets are amplified in the inertially deposited spectrum, due to the higher droplet mass and relaxation time. This is

easiest to see in the spectrum for the wake chopping calculation with axial \dot{p} variation. The global peak ($d \approx 0.1 \mu\text{m}$) contains approximately ten times the liquid mass of the $d \approx 0.2 \mu\text{m}$ and $d \approx 0.65 \mu\text{m}$ peaks, but $0.65 \mu\text{m}$ droplets deposit almost the same amount of liquid mass as the $0.1 \mu\text{m}$ ones.

Turbulent deposition, shown in fig. 4.25a, paints a similar picture. Due to the rapid increase in deposition rates for droplet diameters that fall under the diffusion-impaction regime, turbulent deposition rates are very sensitive to the accuracy of droplet size spectrum in this range. Droplet spectrum predicted by a steady (no wake chopping) calculation with axial \dot{p} variation, with the largest inertial deposition of $d \approx 0.1 \mu\text{m}$ droplets, results in very low turbulent deposition rates. Even if the finer details of the spectrum were lost for this range of droplet sizes, it wouldn't affect turbulent deposition rates because of the inherently small rates in the diffusion regime. On the other hand, the widening of the droplet size spectrum due to wake chopping rapidly increases deposition rates for droplets in the diffusion-impaction regime. What are usually considered as fine details in the droplet size spectrum (e.g., $d \approx 0.65 \mu\text{m}$ peak in the *wake chopping, 1D \dot{p} distribution*, fig. 4.24a) get strongly amplified and suddenly become large contributors to deposition rates.

Figure 4.25b, shows that the impact of wake chopping is not limited to shape of the droplet size spectrum and thermodynamic relaxation loss but also affects processes downstream of the Wilson point, leading to a ~ 6 times larger total deposition rate. Pitchwise pressure variation also plays a large role in the nucleation and deposition processes. Even when wake chopping is not included (i.e., polytropic efficiency is constant across the pitch $\eta(\psi) = \bar{\eta}$) pitchwise expansion rate variation provides enough diversity to widen the spectrum and increase the deposition rates by ~ 4 times.

4.6.2 Effect of wake decay rate

Wake decay rate, τ_w , was shown to have a moderate impact on the droplet size spectrum over the entire range of values,¹³ slightly adjusting the number of droplets in each size group and, for large τ_w , inducing the formation of a secondary peak in the size distribution. Variation in liquid mass per size bin, observed as a fuzziness in the size distribution for larger droplets, is amplified by the depositional mechanisms, resulting in stronger variation in deposition rates, seen in fig. 4.26. Moreover, the presence of a strong secondary peak enhances deposition rates, as seen for $\tau_w = 50\Delta t_{ls}$ at $d \approx 0.45 \mu\text{m}$. However, deposition rates can also decrease when having a secondary peak. $\tau_w \rightarrow \infty$ has a secondary peak that consists of small droplets and a thinner tail of the spectrum (equilibrium wetness is the same for all cases). As a result,

¹³ $\tau_w \rightarrow 0$ meaning instantaneous return to equilibrium, and $\tau_w \rightarrow \infty$ meaning infinitesimally slow wake decay.

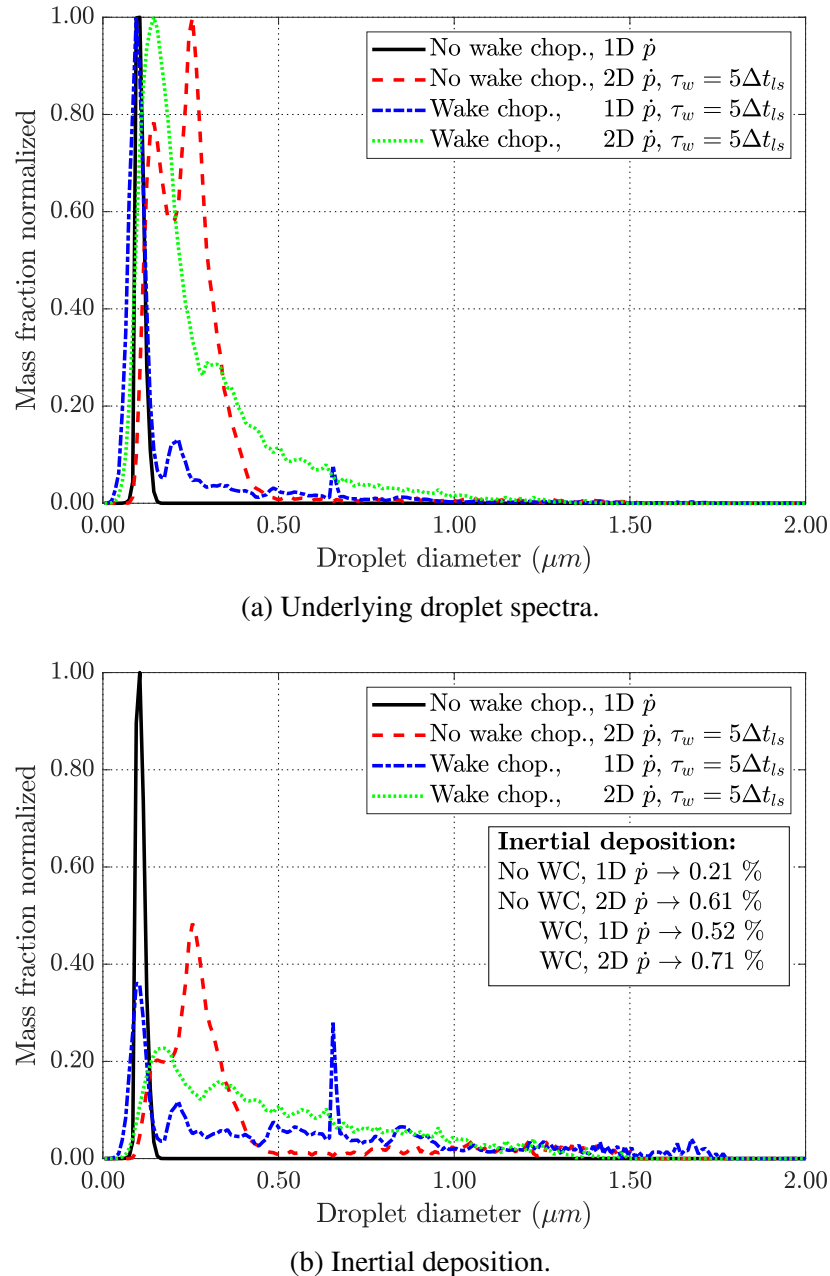
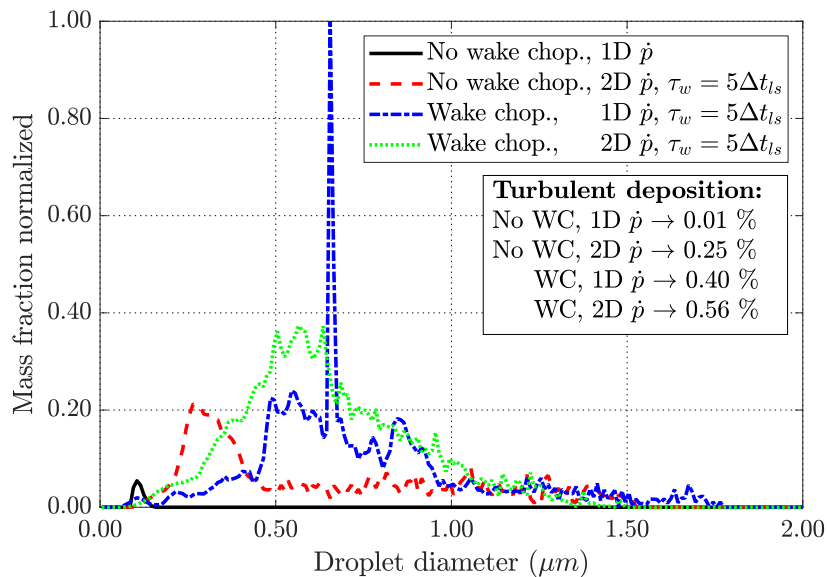
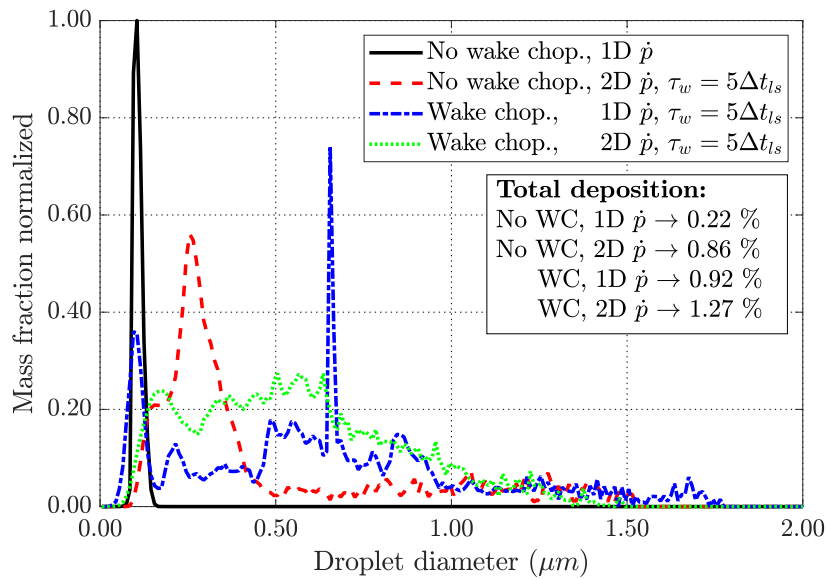


Fig. 4.24 Effect of wake chopping and pressure variation on deposition rates – part 1.



(a) Turbulent deposition.

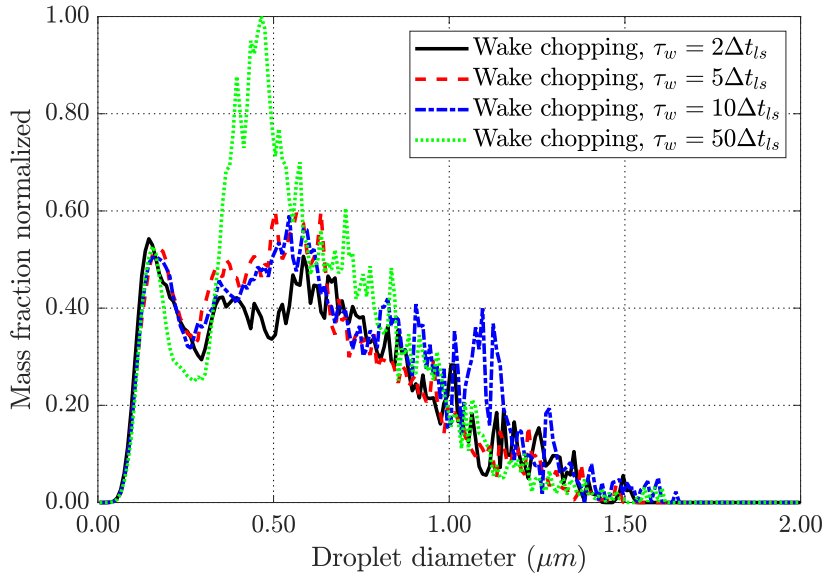


(b) Total deposition.

Fig. 4.25 Effect of wake chopping and pressure variation on deposition rates – part 2.

Table 4.2 Fraction of total liquid mass deposited for a range of wake decay rates.

Wake decay rate (τ_w)	0	$2\Delta t_{ls}$	$5\Delta t_{ls}$	$10\Delta t_{ls}$	$50\Delta t_{ls}$	∞
Inertial deposition	0.21%	0.68%	0.71%	0.77%	0.78%	0.69%
Turbulent deposition	0.01%	0.53%	0.56%	0.63%	0.70%	0.49%
Total	0.22%	1.22%	1.27%	1.40%	1.48%	1.18%

Fig. 4.26 Impact of wake decay rate on total deposition rates(2D \dot{p} variation case).

a larger proportion of the droplets is in the diffusion regime with low deposition rates. Table 4.2 shows that there is less than a 10% change in deposition rates when doubling the rate at which the wakes are eroded, indicating a reasonably small sensitivity to τ_w .

4.6.3 Effect of wake width

Increasing the wake width changes the distribution of loss across the blade pitch, slightly changing the conditions within the Wilson zone. Consequently, fine details in the droplet size spectrum change as well, resulting in marginally fewer small droplets (narrower global peak) and more larger droplets when increasing wake width. This change is amplified in the total deposition rates in fig. 4.27, showing larger deposition rates of small droplets for narrower wakes and, vice versa, larger deposition rates of large droplets for wider wakes. Nevertheless, all curves follow the same general trend.

The total fraction of deposited droplets in table 4.3 shows a progressively higher deposition rate with widening of the wakes, due to the larger proportion of large droplets. However, considering the six times increase in wake width over the range of tested val-

Table 4.3 Fraction of total liquid mass deposited for a range of wake widths.

Wake width (σ_w)	0.02	0.04	0.06	0.08	0.10	0.12
Inertial deposition	0.71%	0.71%	0.73%	0.76%	0.78%	0.80%
Turbulent deposition	0.56%	0.56%	0.61%	0.65%	0.62%	0.70%
Total	1.27%	1.27%	1.33%	1.40%	1.40%	1.49%

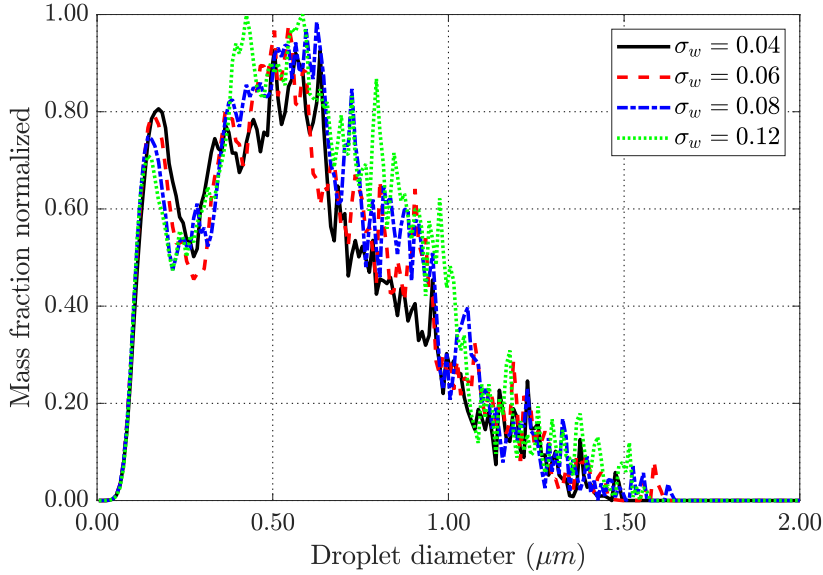


Fig. 4.27 Impact of wake width on total deposition.

ues, a total increase of $\sim 17\%$ is very small. For a range of values expected in a turbine ($0.02 \leq \sigma_w \leq 0.06$), the increase is under 5%. Compared to the introduced modelling errors defined in the previous sections, it can be concluded that deposition is insensitive to wake width variation.

4.6.4 Effect of wake asymmetry

Starting from having a thick wake on the pressure side (PS) and an infinitely thin one on the suction side (SS), continuing over the possible range of wake thicknesses on both PS and SS, and ending with the other extrema of having a thick SS and infinitely thin PS wake, droplet deposition is mostly insensitive to wake asymmetry. Over the entire range of wake asymmetry, defined through r_w (the ratio of wake and base widths), deposition rates change by just 2.5%, as seen in table 4.4. The cause of insensitivity lies in the impact of wake asymmetry on the droplet size spectrum. The deviation from wake symmetry, while keeping mean and standard deviation of loss constant across all cases, results in an axial shift of the Wilson point for a small range of possible pathline histories. This shift is not sufficiently large,

Table 4.4 Fraction of total liquid mass deposited for a range of wake asymmetry ratios.

(r_{aw})	$-\infty$	1/2.0	1/1.4	1/1.1	1.0	1.1	1.4	2.0	∞
Inertial	0.70%	0.70%	0.67%	0.70%	0.68%	0.70%	0.67%	0.70%	0.67%
Turbulent	0.53%	0.53%	0.52%	0.53%	0.52%	0.53%	0.51%	0.53%	0.53%
Total	1.22%	1.22%	1.19%	1.22%	1.20%	1.22%	1.19%	1.22%	1.20%

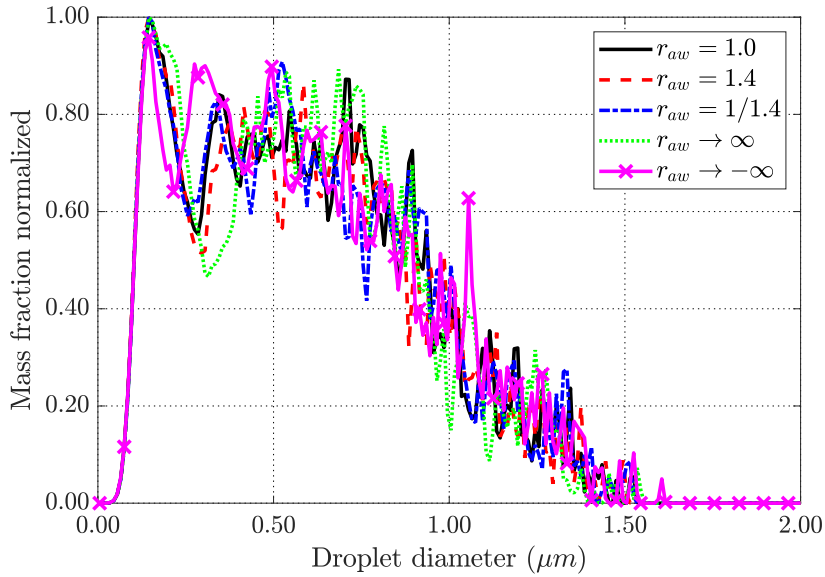


Fig. 4.28 Impact of wake asymmetry ratio on total deposition.

for example, to push affected Wilson points to the inter-stage gap and generate significantly different droplet size groups. The change in droplet size spectrum is primarily focused on smaller droplets that form the secondary peak, as seen for $d \approx 0.3 \mu\text{m}$ in fig. 4.28, making deposition rates insensitive to wake asymmetry.

4.7 Conclusions

This chapter presented a deposition model consisting of: (i) three-dimensional droplet tracking based on inertial velocity slip, and (ii) a method for estimating deposition rates due to non-inertial effects (primarily turbophoresis as the dominant driver of deposition in steam turbines). The inertial velocity slip model gives the correct limiting behaviour for very large and very small droplets, and gives qualitatively good agreement with CFD calculations for other sizes [148]. Flat-plate estimates of skin friction coefficient, a key element of the turbulent deposition model, were compared with the detailed CFD simulation for a steam cascade, showing a large difference in values. This comes primarily from large streamwise pressure gradients present in the flow, as well as the laminar boundary layer in the first section of the blade which reduces the blade-average C_f . A sensitivity study of the deposition model was performed and the main conclusions are as follows:

- (i) Flat-plate $C_f(\text{Re})$ equations for turbulent boundary layer probably overestimate skin friction coefficient by almost a factor of two for $400\,000 \leq \text{Re} \leq 900\,000$, increasing deposition rates by $\sim 50\%$. Due to the general lack of data, they are still considered the best approximative method. Skin friction coefficient comparison between different blade designs and operating points shows that a much better prediction ($\pm 20\%$ error margin) can be made by using a known blade-average C_f from a similar blade design.
- (ii) The turbulent deposition is very sensitive to the choice of skin friction coefficient model, resulting in a $\sim 120\%$ larger deposition rate when using the flat-plate C_f . Over-predicted C_f increases the dimensionless particle relaxation time, greatly increasing the deposition rates. However, the level of sensitivity depends on the combination of droplet sizes and flow conditions (i.e., if the dominant droplet sizes do not fall in the region with rapid change in deposition rates, sensitivity is strongly reduced). On the other hand, inertial deposition does not depend on skin friction, thereby reducing the overall sensitivity. Using a C_f from a similar turbine design brings down the sensitivity of total deposition rates, resulting in a $\sim \pm 1\%$ change in deposition rates for every $\pm 1\%$ error in the C_f estimate. It is important to notice, however, that this model is largely a simplification of reality because of the lack of any flow information within the blade passage and, hence, is not capable of capturing the increase in turbulent deposition rates caused by the increased droplet concentration near the walls as a result of inertial velocity slip. Nevertheless, a qualitative comparison with experimental data shows that the overall deposition trends are captured and this model can be used to qualitatively compare and assess different turbine designs and operating conditions, which was the intended purpose of this work.

- (iii) Wake chopping increases deposition almost six-fold relative to calculations without wake chopping. Pitchwise expansion rate variation plays a large role in broadening the droplet spectrum and driving the deposition rates even without modelling blade wakes, and should therefore be included in the calculations. The impact of each droplet size group on the deposited liquid mass fraction depends on the fine balance between: (i) concentration of droplets with size d_i in the flow, (ii) fraction of droplets that get deposited, and (iii) droplet diameter (i.e., liquid mass that each droplet contributes), demonstrating the importance of capturing the droplet size spectrum as accurately as possible.
- (iv) Deposition rates are more sensitive to variation in wake chopping parameters, changing total deposition rates by approximately $\pm 10\%$ over the range of wake decay rates and wake widths. Wake asymmetry results in less than 2.5% change in deposition rates which, when compared to the other modelling errors, can be considered negligible.

Finally, as shown in the previous chapter, it is the variation in flow conditions caused by a combination of wake chopping and two-dimensional expansion rate variation that results in a robust droplet size spectrum (i.e., the spectrum becomes fairly insensitive to small perturbations in inlet conditions and modelling parameters). The spectrum is ~ 20 times wider than the steady throughflow calculations would suggest, with liquid mass distributed over the entire spectrum (unlike 1D wake chopping cases where most of the mass is concentrated in one or more peaks). It is the fine resolution of the droplet size spectrum over the entire range of droplet sizes that governs deposition rates, which is impossible to capture without the inclusion of wake chopping and pitchwise expansion rate variation. Only by including these effects in the throughflow calculations can we ever hope to be able to rapidly optimize turbine design based on wetness-related turbine losses. These findings not only confirm the importance of wake chopping but also answer *why modelling it is important* for domain experts in both academia and industry.

Chapter 5

Comparison with experiments

5.1 Introduction

In this chapter, the methods discussed in ch. 3 and ch. 4 are integrated with Denton's throughflow code (*SLEQ*) [34] to form a routine called *sleqWake*. *SleqWake*'s performance is first compared with other fast computational methods and the code convergence is discussed. This is followed by a four-stage turbine validation case, whereby published experimental measurements [85] and CFD calculation results [22] for a broad range of inlet conditions are compared to *sleqWake*'s predictions. The comparisons are done for flow, performance, and wetness parameters and the implications for predictive industrial applications are discussed.

5.2 Unified streamline equilibrium model

The full turbine geometry calculation goes as follows: A single throughflow calculation is used to generate a coarse meridional-plane estimate of the flow field (determining streamline shapes and flow information at their intersections with quasi-orthogonals (QOs)) without taking into consideration any of the inherent unsteady or 3D effects. In an initial predictor step, steam properties can be determined using either equilibrium or non-equilibrium methods, slightly changing the calculated flow angles and the aerodynamic loss prediction. Unlike the equilibrium mode, where wetness fraction can be easily calculated, wetness formation in a non-equilibrium calculation depends on the local expansion rate, requiring *SteamLag* calculations for each blade row. The generated pressures and polytropic efficiencies for each streamsurface are passed to the wake chopping routine which takes into consideration pitchwise flow variation and models unsteady wake segmentation by performing a Markov-chain process (described in more detail in section 3.4). This returns an improved prediction

of the droplet size spectra, thermodynamic relaxation loss, and wetness, which are used in the corrector step to improve the flow field in a second throughflow calculation. Converged flow field information and droplet size spectra ahead of each blade row are passed to the droplet deposition routine which is called for each streamsurface. The deposition routine sequentially sweeps through individual blade rows, and the deposited liquid mass associated with each droplet size bin is subtracted from the following blade row spectrum.

5.2.1 Convergence and comparison with other methods

The model is based on iterative corrections of the throughflow-generated flow field which can be performed any desired number of times. However, often only one corrective step is sufficient to reach a converged solution. Using the five-stage General Electric model turbine from section 4.2.4 as an example, throughflow calculations using: (i) equilibrium steam (steady flow), (ii) non-equilibrium steam (steady flow), (iii) non-equilibrium steam with deterministic wake chopping (developed by Hughes [68]) and (iv) non-equilibrium steam with stochastic wake chopping with n corrective iterations ($n \in 1, 2, 6$) were performed.

Figure 5.1a shows that all non-equilibrium calculations predict the Wilson points at approximately the same location, close to the third stage rotor trailing edge. However, steady calculations are very sensitive to local expansion rate at the Wilson point. With nucleation occurring in the duct region for the steady-flow case, the Sauter mean diameter (d_{32}) is much larger than that predicted with wake chopping calculations, as seen in fig. 5.1b. Deterministic and stochastic wake chopping show close agreement with each other for averaged flow properties. The differences in predicted Sauter mean diameter, d_{32} , come from the different approach to wake decay modelling.¹ This creates a small difference in the loss distribution within the Wilson zone, slightly changing the size distribution. Similarly, spanwise outlet wetness distribution shows close agreement between the wake chopping models, as seen in fig. 5.1c.

The results shown in fig. 5.1 indicate that the sleqWake calculation reaches a sufficiently converged solution after only one predictor corrector step. While the results are comparable between stochastic and deterministic approaches, stochastic is computationally more efficient. A deterministic calculation with wake averaging after three blade rows requires around 20Gb of RAM and ~ 6 h of computational time on a single CPU, while stochastic code requires ~ 100 Mb RAM and ~ 30 min to converge on a single CPU.

¹Hughes [68] proposed a mixing length-based wake decay, combined with circumferential averaging after n blade rows (n is user prescribed, resulting in small discontinuities). Conversely, the stochastic wake chopping model described in 3.4 gradually erodes wakes, as defined by eq. 3.31.

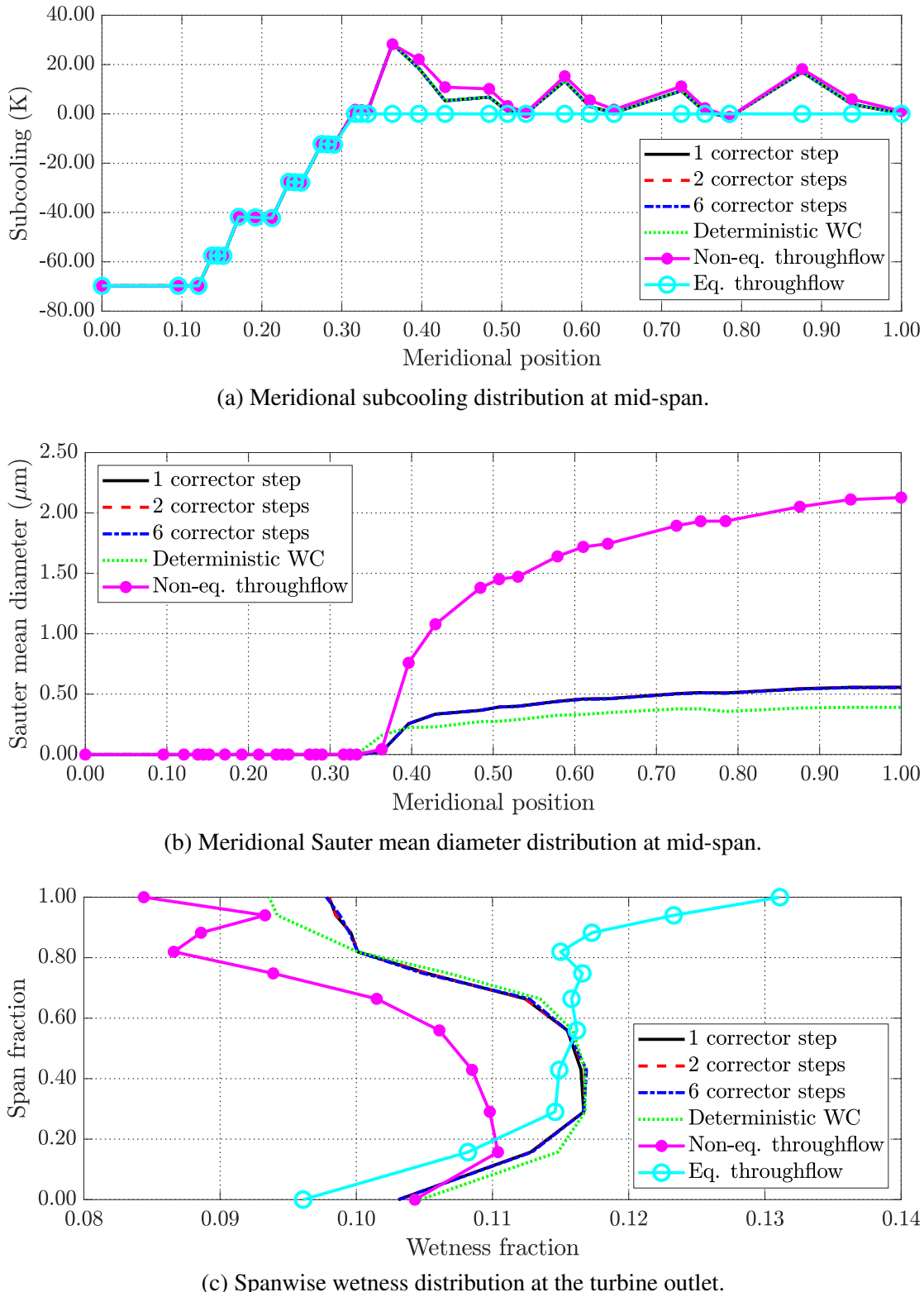


Fig. 5.1 Convergence of sleqWake calculations with the number of corrector calculations and comparison with other methods.

5.3 Validation case – four-stage LP turbine

5.3.1 Turbine measurements

The unified code was validated by comparison with measurements on an approximately one-third scale model of the double-flow General Electric (GE) LP turbine module, provided by GE and described in more detail by Chandler et al. [22], with four stages and a split-shaft configuration. The first two stages are mounted on the front and the last two on the rear shaft, enabling individual power measurements using separate water brakes. While the diffuser, casing and blading shapes are different, the overall layout and geometrical features are similar to the rig described by Kreitmeier et al. [85], with the scaled right-flow side shown schematically in fig. 5.2. A brief overview of the experimental measurements is given below and more details can be found in [85, 22].

As described in [22], inlet conditions were measured downstream of a perforated disk (providing uniform flow) using a set of rakes while the inlet mass flow rate was determined with a calibrated nozzle. Steam is extracted at two locations: in the passage upstream and downstream of the penultimate stage, labelled in fig. 5.2 as A2 and A1. Extracted mass flow showed a non-monotonic variation with inlet temperature (0.06 and 0.09 kg s^{-1} respectively) and its effects are considered negligible. Static pressure was measured in the diffuser and between each blade row along the hub and casing. Flow angle and light extinction measurements were collected on planes located downstream of the front, penultimate, and final stages, and labelled as 42, 52, and 62 in fig. 5.2. The light extinction probes measured two wavelengths of light (red and blue), at approximately 70% span for plane 42 and mid-span for plane 52. While this is theoretically sufficient to determine the Sauter mean diameter and wetness fraction [22], more wavelengths are needed to resolve the shape of the droplet spectrum. The measurable range of the method is limited to droplets larger than $0.1 \mu\text{m}$, whereas predicted droplet spectra (e.g., fig. 3.16) contain a considerable number of smaller droplets, thus introducing a degree of uncertainty.

The measurements were performed for a range of total inlet temperatures ($152.5^\circ\text{C} \leq \theta_{01} \leq 260.3^\circ\text{C}$), maintaining constant inlet total and outlet static pressures ($p_{01}/p_{out} \approx 27$), resulting in outlet wetness between approximately 6% and 14%.

CFD results reported in [22]

Chandler et al. performed steady-state condensing-steam CFD calculations in the same turbine, using a mixing-plane interface between blade rows. However, neglecting unsteady effects limits the temperature fluctuations within blade rows and reduces the width of the

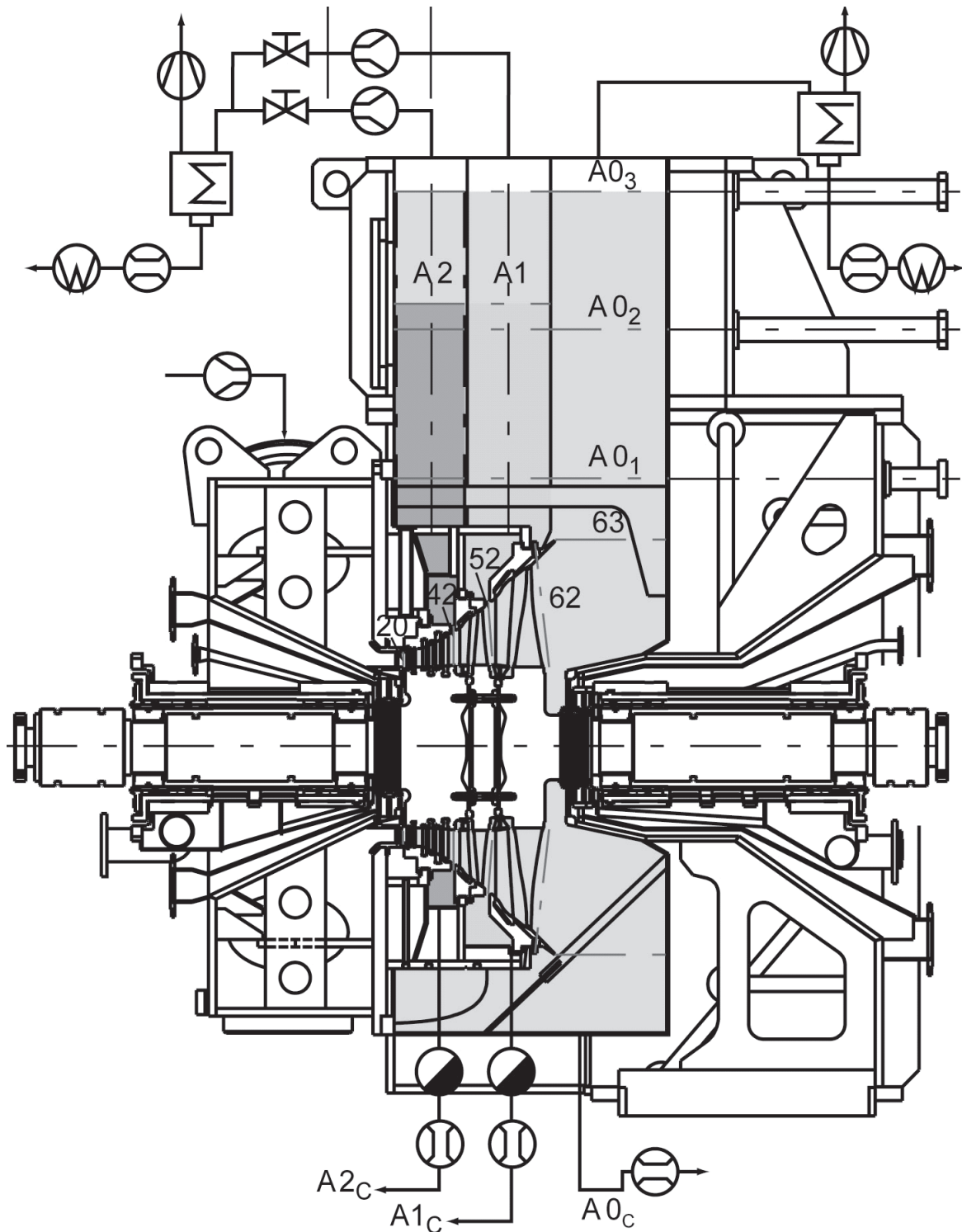


Fig. 5.2 Experimental test rig schematic with control surfaces (CS). A_1 and A_2 are the steam extraction locations at the casing upstream of the penultimate and final stage. A_{0c} , A_{1c} , and A_{2c} are the coarse water drains in the exhaust and extractors. Traverse planes are labelled 42, 52, and 62. Adapted from [22].

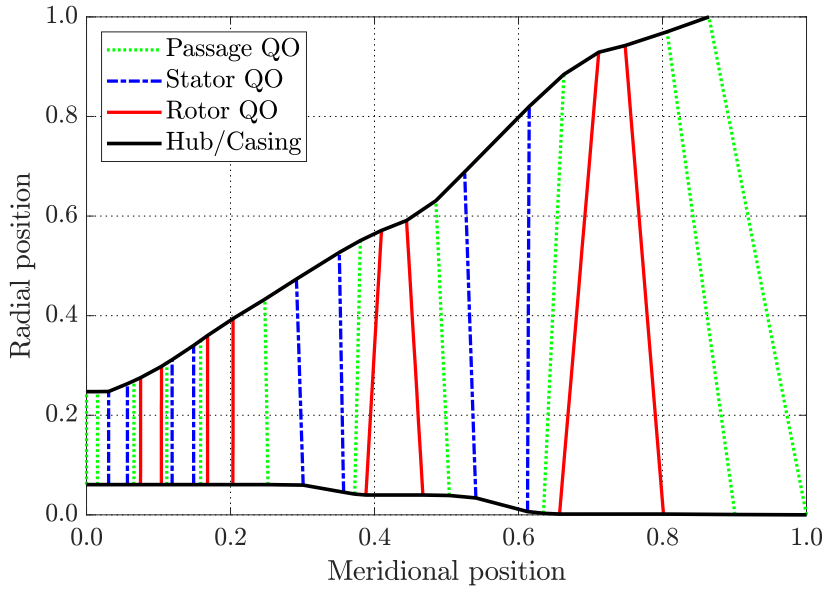


Fig. 5.3 Throughflow calculation computational grid.

predicted Wilson zone. This effect is further amplified by the use of mixing planes which artificially increase mixing, and is expected to increase the sensitivity of predicted droplet spectra and thermodynamic relaxation loss to inlet temperature variations (see sections 2.3.1 and 3.6.4 for more information).

5.3.2 Turbine calculations

The turbine geometry was represented with 11 streamsurfaces and 27 quasi-orthogonals, as shown in fig. 5.3, with the flow field properties determined at each intersection. The calculations use built-in loss correlations and not the (more accurate) user-specified loss coefficients for this turbine. Similarly, polytropic efficiencies needed for the wake chopping calculations come directly from the throughflow calculation and are not adjusted using measured or CFD data.

Pressure profiles for each blade, needed for pitchwise pressure variation, were extracted from CFD calculations by Chandler et al. [22] at three spanwise locations ($\sim 10\%$, 50% , and 90% span) for the first three stages, and five for the final stage ($\sim 10\%$, 30% , 50% , 70% , and 90% span). Pressure pathlines through the passage are determined along 16 uniformly distributed virtual points placed in each blade row by pitchwise linear interpolation of pressure profiles, based on the current random value of the dimensionless mass flow function ψ . Wake width parameters for each blade, σ_w , were extracted from CFD results as

the standard deviation of polytropic efficiency across the pitch. Wake decay time scale, τ_w , was kept at $5\Delta t_{ls}$, where Δt_{ls} is the transit time in the last stage stator, as derived in [53].

The flow field results shown in the following sections could be further improved by providing measured flow angles and loss coefficients. Denton and Hirsch [65] cite a number of papers claiming superior accuracy when scaling loss correlations with measured data, essentially *ex-post* calibrating the model (as previously demonstrated in fig. 3.4). However, the goal is to assess model performance using default parameters (since model training data is often not available in practice) without fine-tuning it to the already known solutions.

Due to the coarseness of the computational grid, there are no points corresponding directly to the probe locations. Hence, all values presented in this chapter are linearly interpolated from the closest two QOs. Since the probes are located in the passages between blade rows where gradients are low, this approach is unlikely to introduce a significant error.

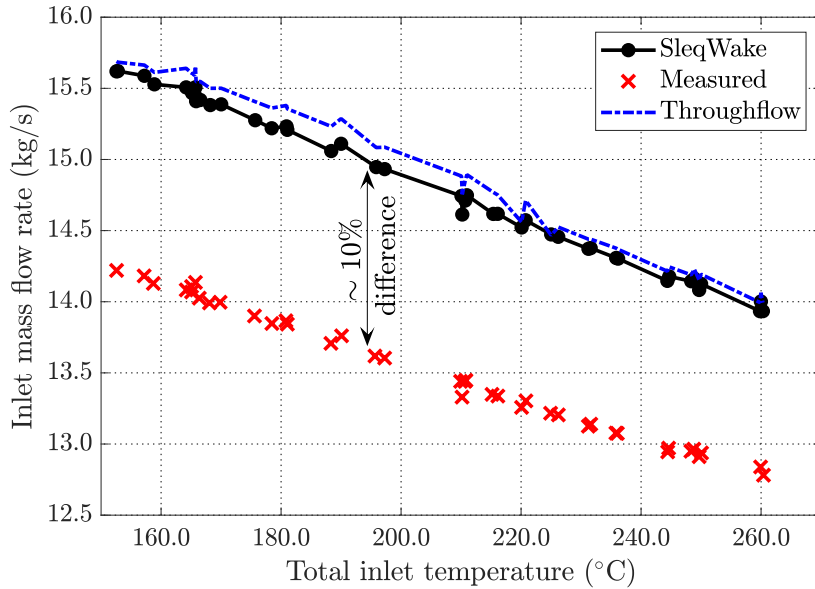
5.3.3 Inlet mass flow rate

Comparison of measured and computed inlet mass flow rates shows that throughflow calculations consistently over-predict \dot{m} by $\sim 10\%$, seen in fig. 5.4a, which is within the known margin of error for throughflow calculations [66]. Computed mass flow rate is primarily influenced by the computed span-wise distribution of exit flow angles and, in much smaller measure, by estimated loss. Hence, the error in computing those values is directly reflected in the mass flow rate prediction. The analysis of eq. 3.3 in [65] shows that a 1° error in exit flow angle results in up to $\sim 5\%$ change in \dot{m} while the typical accuracy of exit flow angles at mid-span falls within $\pm 2^\circ$ (the accuracy close to the end-walls falls dramatically due to secondary flow effects).

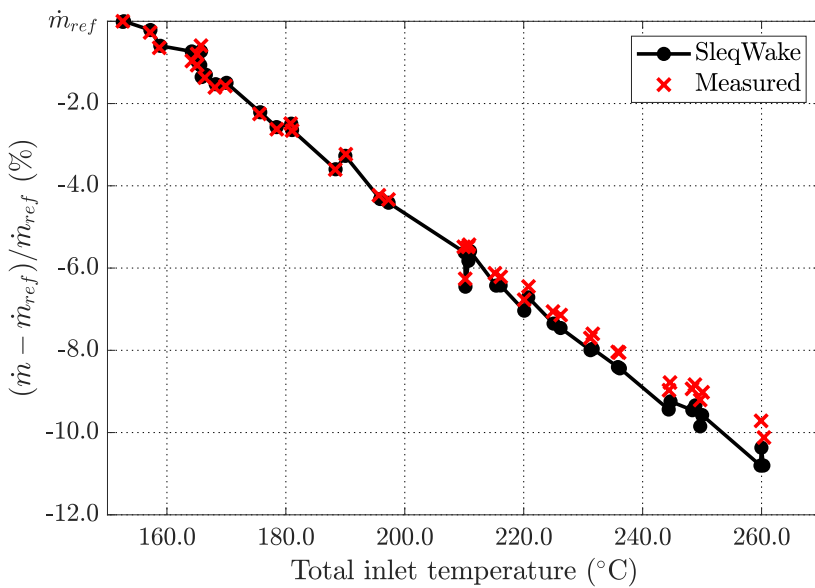
Hence, improved loss estimates only marginally improve the mass flow rate compared to the equilibrium calculation in the absolute sense. However, change of predicted loss with inlet temperature (discussed further in section 5.3.5) finely tunes \dot{m} . The trend comparison in fig. 5.4b, expressed as a fraction of \dot{m} for the lowest inlet temperature case, shows excellent agreement with measurements, accurately capturing even the minute details in the distribution.

5.3.4 Pressure probes

The measurements include static pressure readings along the hub and casing for a range of inlet total temperatures, with probes placed between blade rows. Figures 5.5 – 5.7 compare measurements with sleqWake and equilibrium-steam throughflow calculations for only three positions: upstream, downstream, and between stator and rotor of the penultimate stage. The



(a) Inlet mass flow rate variation with inlet total temperature.



(b) Inlet mass flow rate trends, shown as a fraction of the lowest inlet total temperature mass flow rate.

Fig. 5.4 Measured and calculated inlet mass flow rates for a range of inlet total temperatures.

migration of the nucleation zone through the penultimate stage is observed over the reported range of inlet temperatures. Comparison of all probe positions with calculations is given in the appendix F.

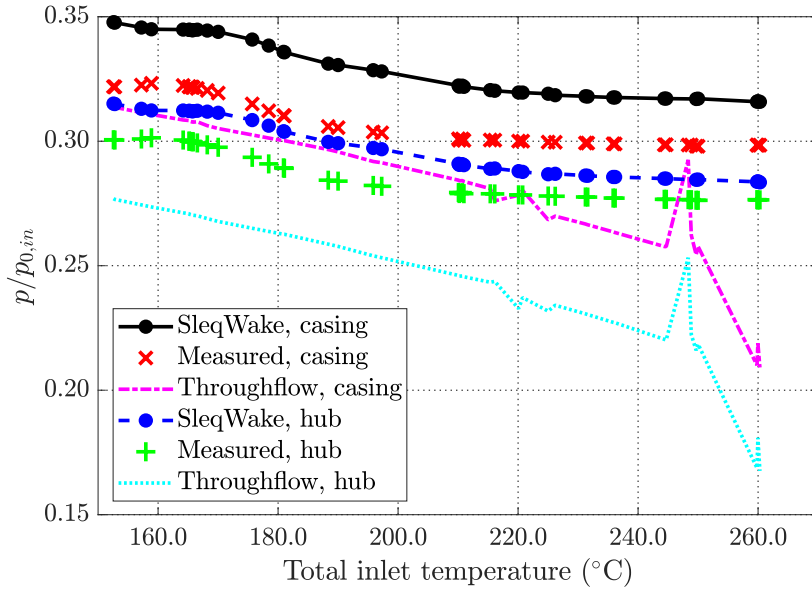
The predicted pressure in all figures shows an offset from the measured data. This is known to be caused by the inherent reduction in accuracy of the throughflow method in the near-wall regions [66]. Exit flow angle deviation significantly increases close to the walls due to the secondary flow which is strongly dependent on the blade profile and cannot be estimated with any degree of accuracy using correlations.²

Figure 5.5 compares the measured and computed static pressure upstream of the penultimate stage both in absolute terms and as trend progressions against total inlet temperature. Even though there is an offset between measured and calculated pressure in fig. 5.5a, the trends are captured remarkably well. The steam at this location is dry for θ_{01} between 260 °C and 220 °C and the calculated pressure increase follows measurements. However, below 220 °C the wake chopping model starts recording first steam parcels nucleating in the passage upstream of the penultimate stage. While they are still rare, their presence is reflected in the calculated pressure and their number increases with further temperature drop. This can be observed as the divergence between calculated and measured trends between 220 °C and 190 °C, as the measurements still record dry conditions. The stronger measured pressure rise from 190 °C comes as the Wilson zone reaches the probe location and moves further upstream. From this point the trends are converging as the Wilson zone moves within the passage and the majority of pathlines nucleate there. The trends start slowly diverging again as the model begins recording nucleation in the upstream rotor ahead of what the measurements suggest.

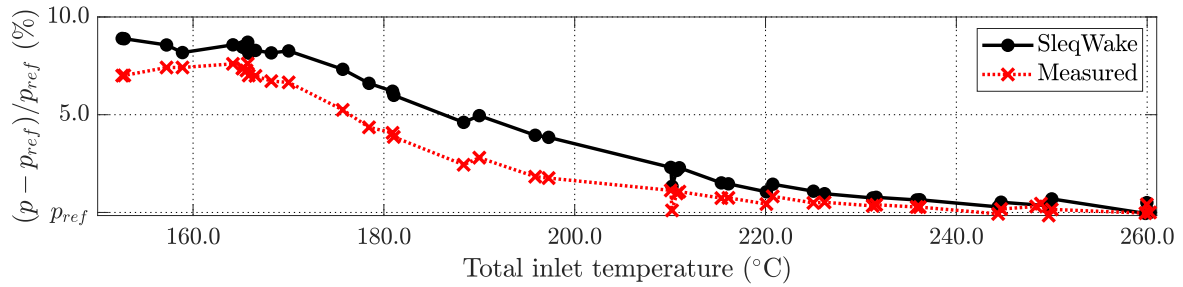
Similar behaviour is observed at the following probe location, one blade row downstream, in fig. 5.6. The initial trend deviation between 260 °C and 245 °C is again caused by the model capturing a small number of droplets nucleating in the passage between rows sooner than what the experiments suggest. This is followed by an increase in pressure (with matching trends) as both calculations and measurements record the Wilson zone moving upstream through the passage (230 – 195 °C). The calculations predict an earlier pressure levelling off in fig. 5.6c, at 195 °C, as a larger fraction of the flow nucleates in the upstream stator. This difference is, however, quickly reduced as the turbine nucleation zone moves to the stator.

The probe placed downstream of the penultimate stage records wet steam over the entire range of inlet temperatures, shown in fig. 5.7. The Wilson zone is located right at the inter-

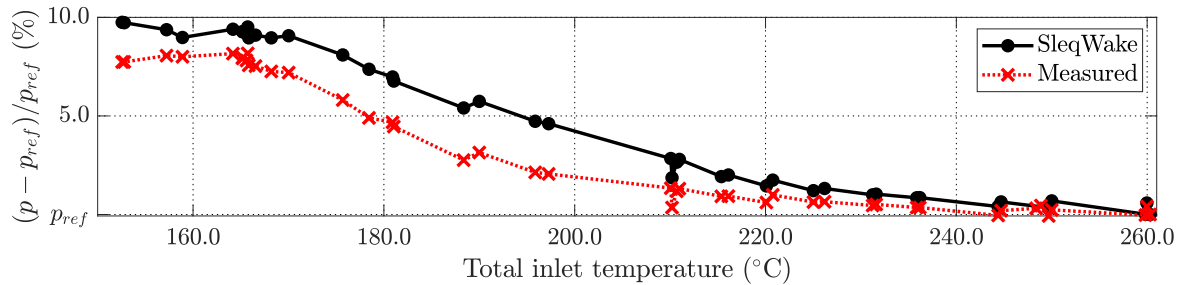
²Bardon et al. [66] proposed a correlation based on the application of secondary flow theory to a range of cascades. Even though it does not show good agreement with turbine measurements, it is the only correlation available [12] and, hence, widely used.



(a) Static pressure at the hub and casing upstream of the penultimate stage, normalized with inlet total pressure.

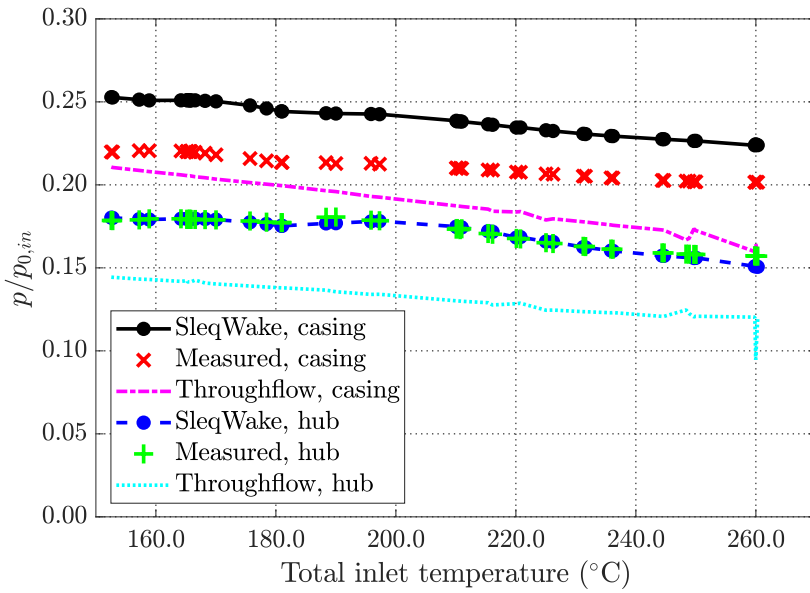


(b) Static pressure at the casing upstream of the penultimate stage for a range of inlet total temperatures. Each curve is scaled by its static pressure for the highest temperature case, p_{ref} , respectively.

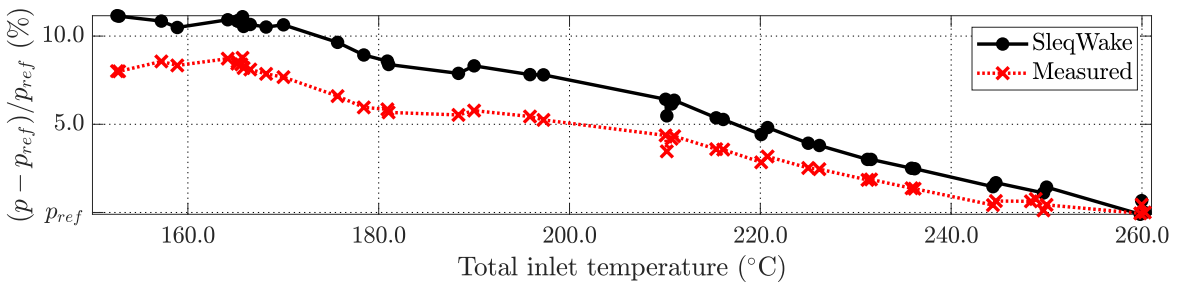


(c) Static pressure at the hub upstream of the penultimate stage for a range of inlet total temperatures. Each curve is scaled by its static pressure for the highest temperature case, p_{ref} , respectively.

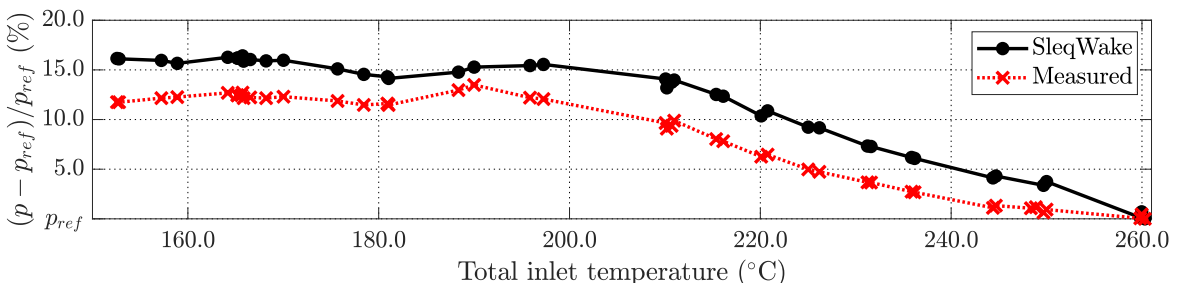
Fig. 5.5 Pressure variation with inlet total temperature, upstream of the penultimate stage.



(a) Static pressure at the hub and casing between the penultimate stage stator and rotor, normalized with inlet total pressure.



(b) Static pressure at the casing between the stator and rotor of the penultimate stage for a range of inlet total temperatures. Each curve is scaled by its static pressure for the highest temperature case, p_{ref} , respectively.



(c) Static pressure at the hub between the stator and rotor of the penultimate stage for a range of inlet total temperatures. Each curve is scaled by its static pressure for the highest temperature case, p_{ref} , respectively.

Fig. 5.6 Pressure variation with inlet total temperature, between the penultimate stage stator and rotor.

stage passage for the highest inlet temperature cases ($\sim 260 - 240^\circ\text{C}$) and continues moving upstream, reaching the previously discussed pressure probes.

Sharper measured pressure changes in figs. 5.5 – 5.7 suggest that the nucleation zone is limited to a shorter axial distance than what the wake chopping model would suggest. Shorter Wilson zone is inherently more sensitive to inlet temperature variations, which "slide" it axially and change the expansion rate range within. Guha and Young's [53] suggestion of wake decay time constant of $\tau_w = 5\Delta t_{ls}$ seems to under-predict the mixing out of wakes, producing a longer, "axially smeared" Wilson zone, and resulting in a lower sensitivity to inlet temperature variation.

It is important to point out the presence of distinct local minima in the pressure measurements, notably at 245°C , 220°C , 185°C , and 155°C . These inlet temperatures result in the Wilson zone primarily occupying a passage between blade rows, resulting in much larger droplets. These points are directly reflected in the light extinction measurements, shown later in fig. 5.12. Calculations successfully capture all of those flow features at all probe locations, albeit with a reduced amplitude, implying that the majority of nucleation occurs within the same region as in the experiments and only the edges of the nucleation zone are smeared.³ Conversely, equilibrium calculations fail to capture any of these effects, indicating the importance of non-equilibrium effects and nucleation zone conditions on the downstream flow field.

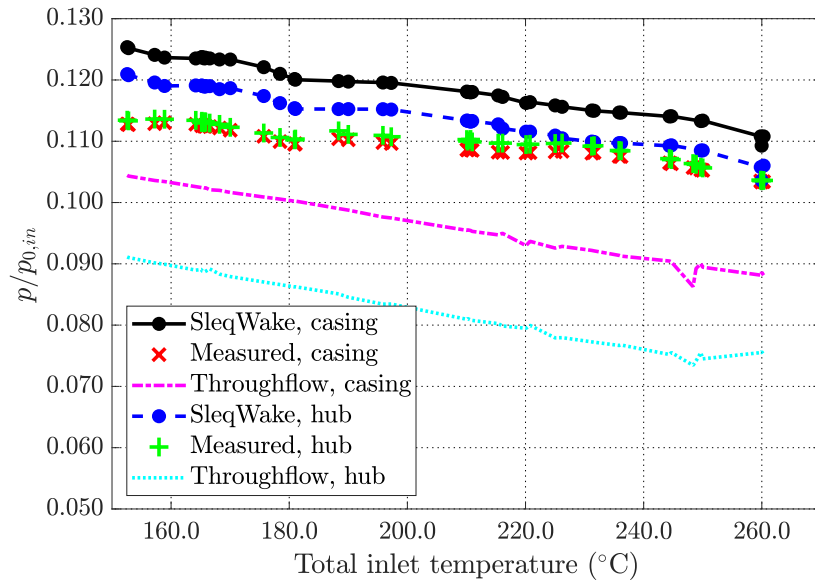
5.3.5 Turbine performance

Following the notation from [22], turbine total-to-static efficiency, η_{TS} , can be expressed as

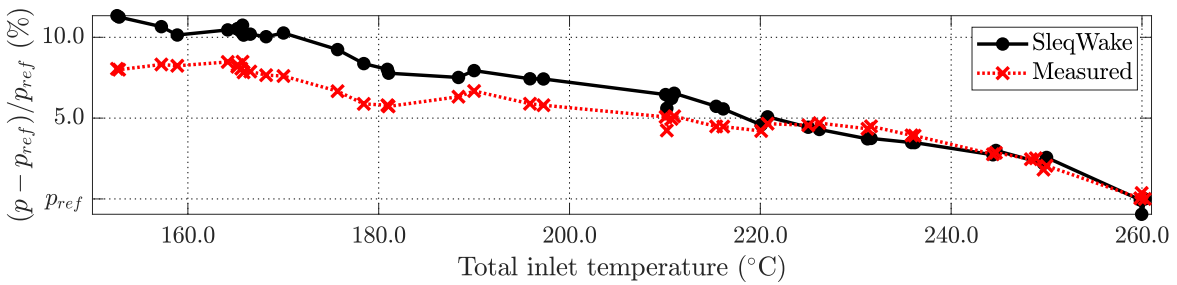
$$\eta_{TS} = \frac{P_{FS} + P_{RS}}{\dot{m}(h_0 - h'_E) - \dot{m}_{A1}(h'_{A1} - h'_E) - \dot{m}_{A2}(h'_{A2} - h'_E)}, \quad (5.1)$$

where P_{FS} and P_{RS} are the power output at the front shaft (first two stages) and rear shaft (last two stages) respectively, h_0 is the total enthalpy at the turbine inlet, and h'_E is the isentropic enthalpy at the exit, calculated using the static pressure at the final QO and mass-averaged over the span. h'_{A2} and h'_{A1} are the isentropic enthalpies of extracted steam at extraction slots A2 and A1 respectively (see fig. 5.2), and are evaluated using the static pressure at the casing. \dot{m} , \dot{m}_{A2} and \dot{m}_{A1} are steam mass flow rates at the inlet and extraction slots A2 and A1 respectively.

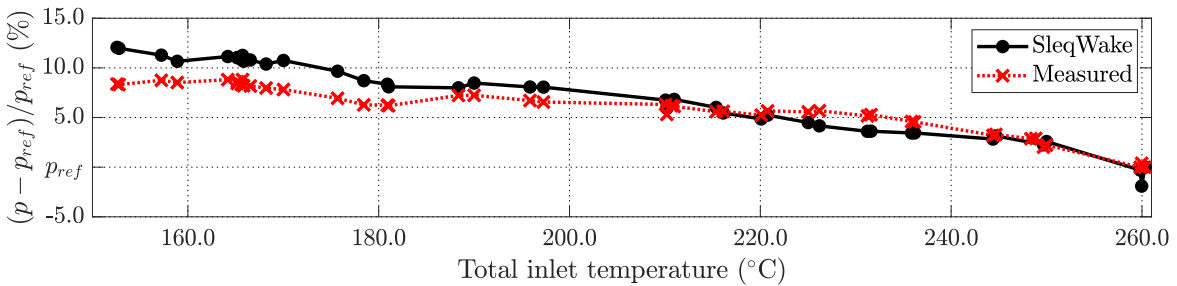
³The (axial) Wilson zone edge regions consist of very early or very late nucleating pathlines, corresponding to increasingly rare thermodynamic histories (e.g., steam parcel that ends up in the wake of every blade row. It heats more than the rest of the flow and will nucleate significantly later, but has a very low probability of occurring.) and, thus, lower impact on the overall flow conditions. Effectively, it acts as a diffusion term, smearing out gradients in the solution.



(a) Static pressure at the hub and casing downstream of the penultimate stage, normalized with inlet total pressure.



(b) Static pressure at the casing downstream of the penultimate stage for a range of inlet total temperatures. Each curve is scaled by its static pressure for the highest temperature case, p_{ref} , respectively.



(c) Static pressure at the hub downstream of the penultimate stage for a range of inlet total temperatures. Each curve is scaled by its static pressure for the highest temperature case, p_{ref} , respectively.

Fig. 5.7 Pressure variation with inlet total temperature, downstream of the penultimate stage.

Ensuring consistency with η_{TS} , thermodynamic wetness loss, ξ_{wet} , was defined in [22] as:

$$\xi_{wet} = \frac{P_{wet}}{\dot{m}(h_0 - h'_E) - \dot{m}_{A1}(h'_{A1} - h'_E) - \dot{m}_{A2}(h'_{A2} - h'_E)}, \quad (5.2)$$

where, P_{wet} is the lost power due to the thermodynamic wetness loss, and is expressed as:

$$P_{wet} = (\dot{m} - \dot{m}_{A1} - \dot{m}_{A2}) T_E (s_{th,FS} + s_{th,PS} + s_{th,LS}) + \dot{m}_{A1} T_{A1} (s_{th,FS} + s_{th,PS}) + \dot{m}_{A2} T_{A2} s_{th,FS}. \quad (5.3)$$

Here, $s_{th,FS}$, $s_{th,PS}$, and $s_{th,LS}$ are the specific entropy increases due to the heat transfer between droplets and steam for front, penultimate, and last stage respectively. T_E , T_{A2} , and T_{A1} are the thermodynamic saturation temperatures at the exit, A2, and A1, determined based on the pressures used in eq. 5.1.

Figure 5.8 compares calculated total-to-static isentropic efficiencies with measurements, and thermodynamic wetness loss with CFD results from [22]. Each η_{TS} curve is presented as a difference ($\eta_{TS} - \eta_{ref}$) from its reference case at the highest inlet θ_{01} , whereas wetness loss is shown as the difference from the lowest computed value for each curve ($\xi_{wet} - \xi_{ref}$). According to [22], the standard uncertainty of efficiency measurements is $\sim 0.4\%$, which mostly consists of systematic error, while random error is sufficiently small to observe trend changes caused by non-equilibrium effects. The systematic error effect is, however, significantly reduced when observing trend changes.

Turbine efficiency and wetness loss

The overall efficiency trend is surprisingly well captured, considering that the typical through-flow efficiency error margin when using loss correlations is $\sim \pm 2\%$ [66]. Calculated results contain the majority of the fine features present in the measured distributions. The measurement oscillation between 260°C and 240°C is attributed to higher measurement error at temperatures that are close to the maximum feasible one for this turbine [22]. Conversely, the jumps and drops in efficiency between 180°C and 160°C are caused by the overall sensitivity to the nucleation zone location. Within this temperature range, primary nucleation occurs within the second stage and, depending whether the generated number of droplets is sufficient to keep the flow close to equilibrium, a secondary nucleation event is very likely. Moreover, in case the secondary nucleation occurs in the passage, resulting loss will be further increased. Hence, a combination of the primary nucleation zone location and the presence of a secondary nucleation zone (flow conditions within both zones) are the most

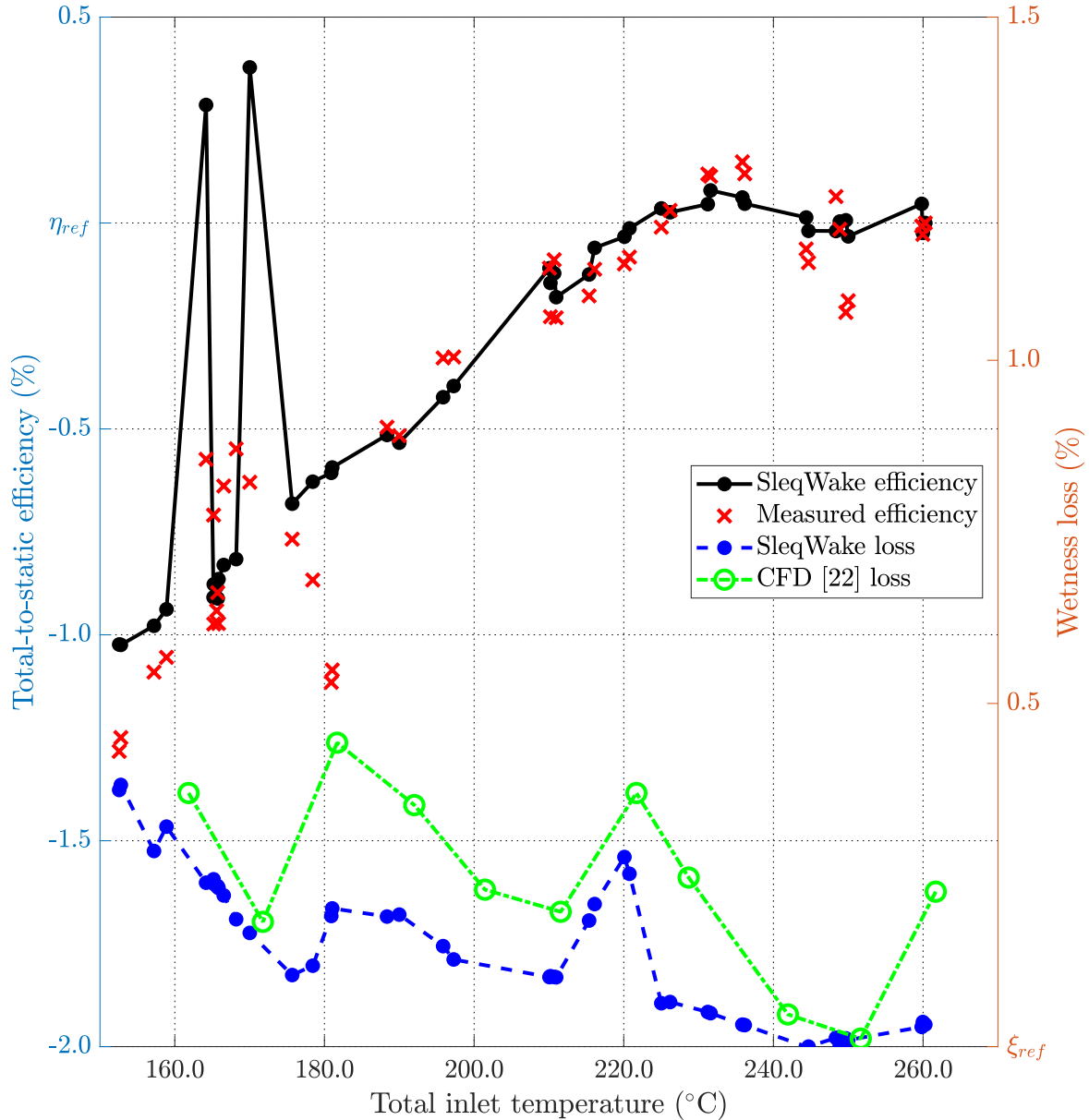


Fig. 5.8 Comparison of wake chopping results to measured total-to-static efficiency and CFD wetness loss prediction. η_{ref} is the efficiency for the highest inlet superheat case, while ξ_{ref} is the lowest computed wetness loss value.

likely cause for the efficiency oscillation. This behaviour can be seen in the meridional plots shown later in section 5.3.9.

The presence of two η peaks at 165 °C and 170 °C is captured by the wake chopping calculation but the magnitude is overestimated due to lower total loss prediction. However, the efficiency drop at 180 °C is not recorded by the calculations. This is a direct consequence of wake decay temporal constant (τ_w) over-prediction, resulting in an axially longer Wilson zone (often spanning more than one stage). The increased length reduces sensitivity of the generated droplet size spectra and thermodynamic wetness loss to small changes in inlet temperature since the range of expansion rates within does not change as much as for the shorter zone.⁴ Thus, passage nucleation predicted by wake chopping takes a smaller proportion of the overall nucleation zone length.

The same smoothing effect can be observed in the wetness loss distribution. The overall trend shows the migration of nucleation zone upstream with decreasing inlet temperature, with individual peaks at 220 °C, 180 °C and 160 °C corresponding to dominant passage nucleation (same trend can be observed in the light extinction measurements shown in fig. 5.12). Wake chopping model does a very good job at predicting those trends but shows a milder increase than what CFD suggests due to the wider nucleation zone. The rapid increase in wetness loss, associated with dominant passage nucleation, is damped by the spread of the nucleation zone to the surrounding blade rows. The sensitivity is not as noticeable for high inlet superheat cases since the nucleation occurs close to the final stage and the calculated Wilson zone is cut short by the turbine exit. The difference between wake chopping and CFD wetness loss is further exacerbated by the use of steady calculation with mixing planes. Circumferential averaging of properties after each blade row artificially amplifies flow mixing, thereby shortening the nucleation zone and making the loss more sensitive to inlet temperature variations.

Turbine specific work output

Specific work output is split into contributions from front (containing the first two) and rear shaft (containing the last two stages), and shown in fig. 5.9. All curves are using specific work output for the highest inlet temperature w_{ref} as a reference. The calculations are showing remarkable agreement with the experiments, especially in the 260 °C to 210 °C region. At

⁴A simple analogy might be beneficial for understanding why shorter Wilson zone is more sensitive to θ_{01} variation. For example, imagine the expansion rate variation in a turbine as a 1D array of letters: [A, B, C, D, E, F, G, H]. Now, define the measured Wilson zone to be three letters long [A, B, (C, D, E), F, G, H] and the predicted (wake chopping) zone to be five letters long [A, B, (C, D, E, F, G), H]. It is clear that moving the zone by a single letter has a substantially larger impact on the conditions within the shorter one (only two old letters remain versus four old letters in the computed one).

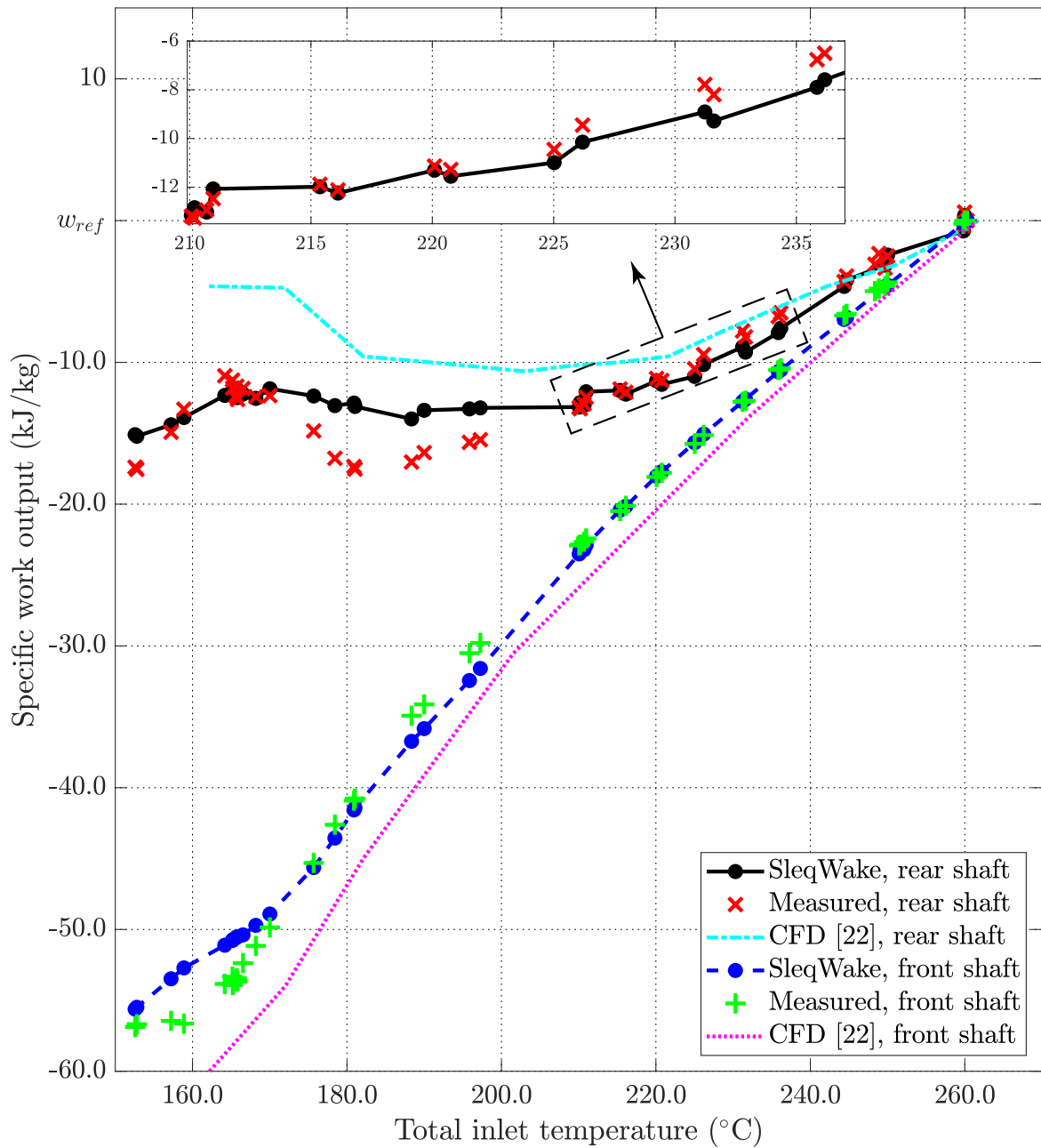


Fig. 5.9 Comparison of wake chopping, measured, and CFD specific work output.

high inlet superheat, the calculated Wilson zone is cut shorter by the turbine outlet, thereby increasing the sensitivity to inlet temperature variation but reducing the variability of the parameters within the zone and narrowing the calculated droplet size spectrum. The increase in the rear shaft work output between 180 °C and 165 °C (and a decrease in the rear shaft output) is a consequence of nucleation zone changing blade rows, moving from the rear to the front shaft and, thus, moving the thermodynamic wetness loss upstream. The peak represents the temperature at which the entire nucleation zone moved to the rear shaft.

The transition is also captured by the calculations. The longer Wilson zone recorded by the wake chopping model starts transitioning to the front shaft ~20 °C earlier than what experiments suggest, slowly increasing the rear shaft work and decreasing front shaft work output. The faster rise starts ~10 °C earlier, as more and more of steam parcels start nucleating upstream. Consequently, the jump recorded by the experiments is smeared over a wider range of temperatures. The same smoothing effect of the longer Wilson zone was also recorded earlier, when comparing pressure trends in section 5.3.4.

5.3.6 Wetness and subcooling

Figure 5.10 compares calculated subcooling and wetness fraction over a range of inlet temperatures using (i) sleqWake running-average,⁵ (ii) steady non-equilibrium throughflow, and (iii) CFD calculations. The data was sampled at two locations: upstream (fig. 5.10a) and downstream (fig. 5.10b) of the penultimate stage. Droplet size spectra and Sauter mean diameters were sampled at the same locations and will be discussed in the following sections.

The upstream probe (fig. 5.10a) records dry steam for high inlet superheat cases, and the Wilson point reaches the probe location at 190 °C for CFD and sleqWake. Further temperature decrease moves the nucleation zone further upstream, showing rapidly decreasing subcooling levels at the probe location as the nucleation latent heat release brings the flow closer to equilibrium. The wetness levels are in good agreement until 175 °C, which is the point where the CFD calculation predicts the end of the nucleation zone moving upstream and the flow at the probe location reverting to equilibrium. Higher subcooling and lower wetness in the 175 °C to 160 °C range confirms that the wake chopping model indeed spreads the nucleation zone over a longer axial range than in reality, with the flow reaching equilibrium at 160 °C.

Steady throughflow calculation shows a delay of approximately 15 °C in reaching the Wilson zone. This offset is reflected in the wetness fraction, reaching agreement with sleqWake and CFD only at 155 °C as all the calculations predict the flow at the probe location to reach (near) equilibrium.

⁵The results of each stochastic pathline calculation are weighted and aggregated onto a *running-average pathline*, as previously introduced in section 3.4),

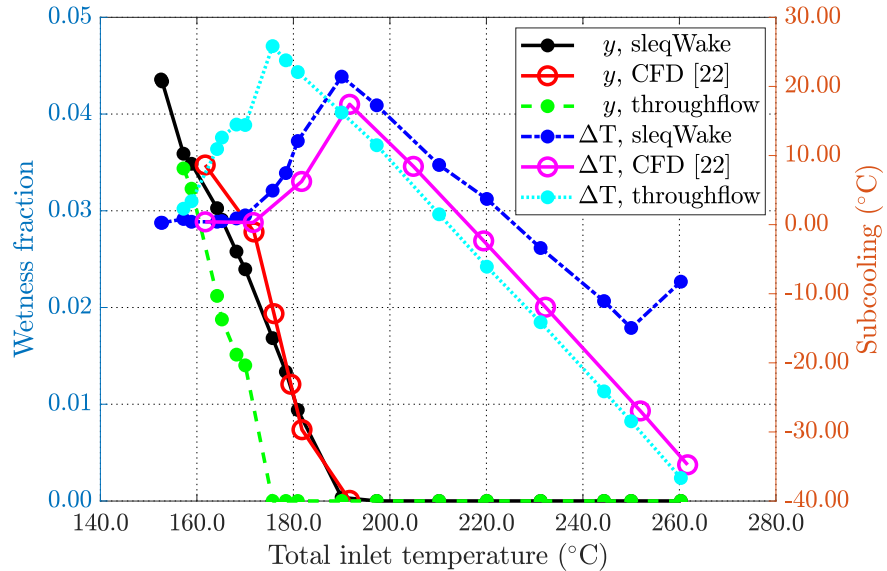
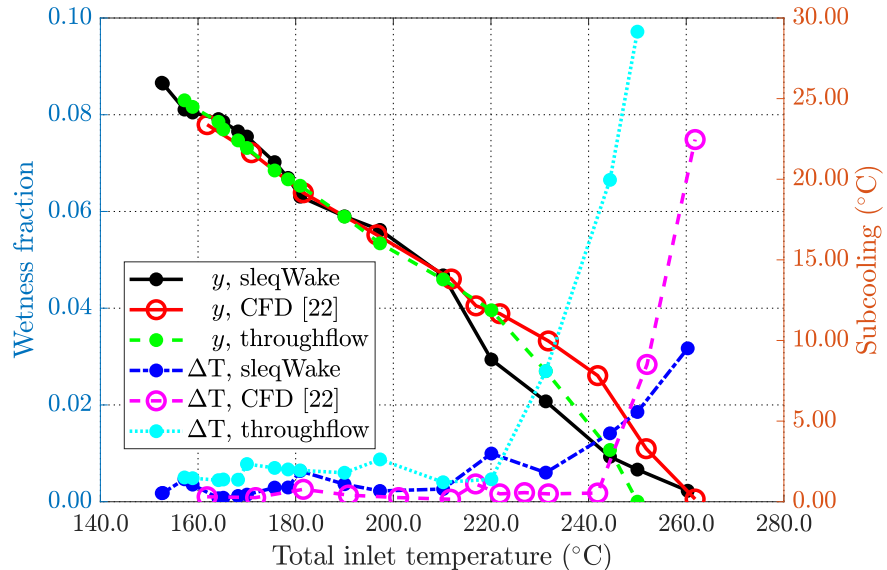
(a) Wetness and subcooling upstream of the penultimate stage at $\sim 70\%$ span.(b) Wetness and subcooling downstream of the penultimate stage at $\sim 50\%$ span.

Fig. 5.10 Comparison of wetness and subcooling between wake chopping throughflow (sleqWake), non-equilibrium steady throughflow, and CFD results. All calculations are performed using non-equilibrium steam.

The downstream probe location records the nucleation zone from the highest superheat case, as seen in fig. 5.10b. High subcooling from the CFD calculation suggests it is the very beginning of the nucleation zone, with flow reverting back to near-equilibrium at 240 °C. SlepWake, however, shows already a presence of wetness at highest inlet superheat, bringing the average subcooling down, indicating that the nucleation zone already started upstream of the probe. The flow also requires almost ~30 °C lower inlet temperature for the nucleation zone to completely move upstream, which can be seen by the difference in subcooling and reduced wetness fraction between 260 °C and 210 °C.

Increased subcooling at 220 °C, 180 °C, and 155 °C point to substantial nucleation in the passages upstream, which is supported by the light extinction measurements. The large droplets are insufficient for the flow to rapidly revert to equilibrium, resulting in subcooling peaks even a full stage later which are captured by both CFD and slepWake (recorded by this probe as the peak at 180 °C).

The Wilson point in steady throughflow calculation is confined to a single axial point and, hence is very sensitive to the inlet superheat (previously seen in section 3.6). The temperature at which the nucleation starts at the probe location is under-predicted by ~15 °C, as was the case with the probe upstream, resulting in a lower wetness fraction than CFD would predict for the same temperature. Moreover, the lack of pitchwise variation makes it unable to properly resolve the influence of upstream nucleation on the downstream flow field, thereby not properly capturing the subcooling trends.

5.3.7 Sauter mean diameter

Figure 5.11 shows computed Sauter mean diameter (defined as $d_{32} = V_p/A_p$), where V_p is the droplet volume and A_p is droplet surface area. The computed results were compared with CFD results upstream (fig. 5.11a) and downstream (fig. 5.11b) of the penultimate stage.

Both figs. 5.11a and 5.11b show remarkable agreement between wake chopping and CFD results. Calculated d_{32} in fig. 5.11a shows that the first steam parcels start nucleating already at 210 °C, which is ~20 °C earlier than the CFD prediction. As the nucleation zone migrates to the passage, the agreement with CFD becomes excellent, capturing the range of temperatures at which the passage nucleation is dominant, as well as the transition to the upstream blade row and its effect on generated droplets.

The trends downstream of the penultimate stage, seen in fig. 5.11a, are in very good agreement. The calculations accurately replicate the variation suggested by the CFD, capturing peaks as the nucleation zone moves through upstream blade rows. The position of the peaks is consistent with the results shown in the previous sections. Initial lower d_{32} between 260 °C and 230 °C is a consequence of the wider computed nucleation zone which already

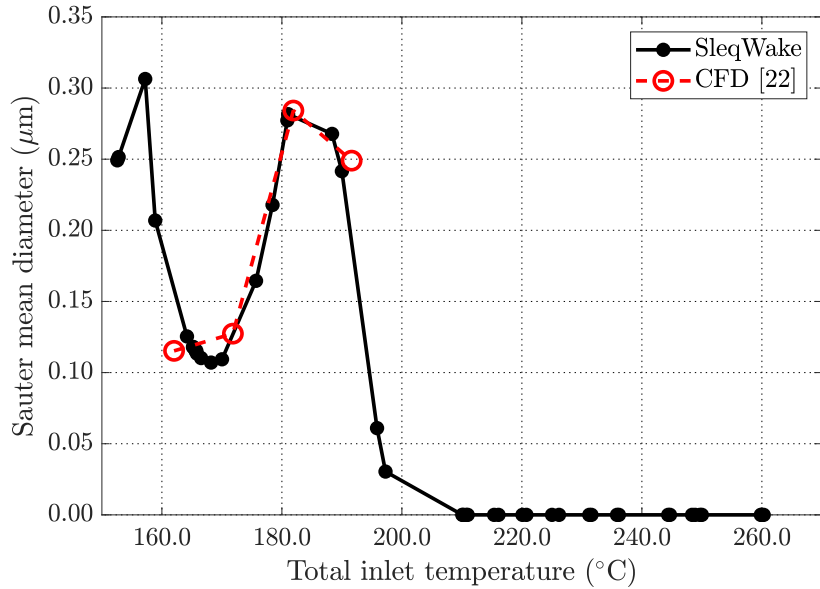
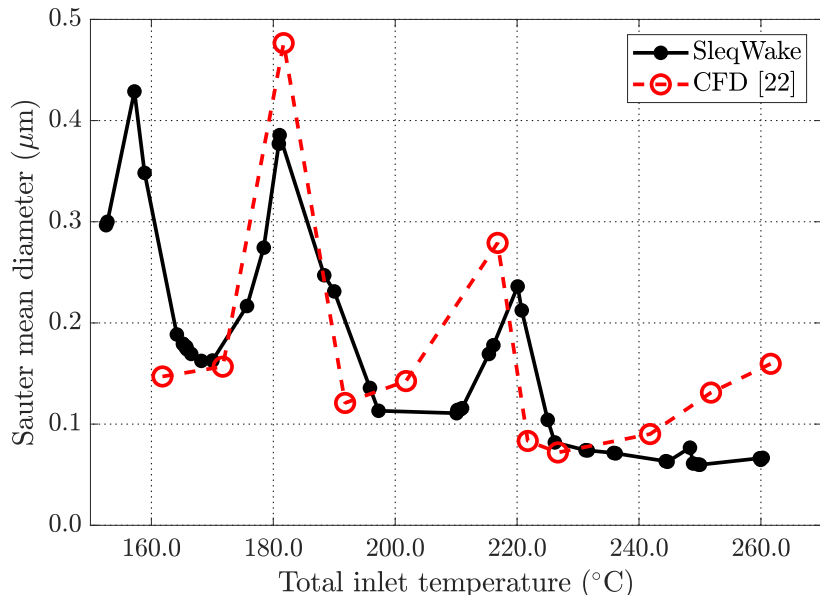
(a) Sauter mean diameter upstream of the penultimate stage at $\sim 70\%$ span.(b) Sauter mean diameter downstream of the penultimate stage at $\sim 50\%$ span.

Fig. 5.11 Sauter mean diameter comparison between CFD and wake-chopping calculations.

takes a portion of the upstream blade row, bringing down the d_{32} at the probe location. The same reason is behind consistently lower peak d_{32} values than CFD suggests at the same temperature, as the wider nucleation zone reduce the proportion of droplets nucleating in the passage.

5.3.8 Light extinction measurements

Light transmittance for polydispersed spectra

The probes located upstream and downstream of the penultimate stage recorded transmittance (I/I_0), the ratio between sampled (I) and reference light intensity (I_0), caused by the light scattering on droplets for two wavelengths, corresponding to blue and red light. Turbidity g can be expressed as a function of transmittance as:

$$g = \frac{1}{l} \ln \left(\frac{I_0}{I} \right), \quad (5.4)$$

where l is the distance travelled by the light beam. The reduction of light intensity of a beam of monochromatic light of wavelength λ for a polydispersed spectrum of transparent spherical droplets comes from the Bouguer-Lambert and Beer law [69, 130]:

$$\frac{1}{l} \ln \left(\frac{I_{0\lambda}}{I_\lambda} \right) = \int_{d_{min}}^{d_{max}} \frac{\pi}{4} d^2 N_v E_\lambda dd, \quad (5.5)$$

where d is the droplet diameter, d_{min} and d_{max} are the limits of the droplet size spectrum, $N_v(d)$ the number of d -sized droplets per unit volume, and l is the distance travelled by the light beam. $E_\lambda(m_r, \alpha_s)$ is the Mie theory extinction coefficient and it varies with the properties of the medium (refraction index m_r) and droplet size parameter $\alpha_s = d\pi/\lambda$ [69]. It is defined for transparent particles as the ratio of total light flux scattered by a particle and the light flux geometrically incident on the particle. E_λ can be obtained from the tabulated results given in [114] or by using a numerical algorithm (see, e.g., [19]), as a unique function of the droplet size parameter.

Equation 5.5 is a Fredholm integral of the first kind where the distribution of droplet sizes $N_v(d)$ is unknown and the kernel function $E_\lambda(m_r, \alpha_s)$ is represented by a complicated series, making the exact solution impossible to find [158]. Furthermore, the approximative methods that depend on numerical inversion require more light wavelengths than the two available for this set of measurements. Therefore, calculated droplet size spectra are transformed into corresponding light extinctions and are directly compared with the measurements.

Equation 5.5 can be discretized [8] as a summation of contributions from n different droplet size bins for each of the wavelengths used as:

$$\ln \left(\frac{I_{0\lambda}}{I_\lambda} \right) = \frac{\pi l}{4} \sum_{i=1}^n d_i^2 N_{v,i} E_{\lambda,i}. \quad (5.6)$$

Here, $N_{v,i}$ is the probable number of droplets of size $d_1 < d_i < d_2$ per unit volume [160]:

$$N_{v,i} = C_n \int_{d_1}^{d_2} N_r(d) dd, \quad (5.7)$$

where C_n is the concentration factor. Droplet size spectra generated by the wake chopping model are already divided into a number of discrete bins of fixed width, each with corresponding liquid mass fraction (as described in chapter 3), and can easily be converted to $N_{v,i}$ by multiplying the liquid mass fraction with the mixture density.

Comparison with measurements

Comparison of light extinction trends in fig. 5.12 shows that the calculations correctly capture the migration of the nucleation zone with the change in inlet temperatures. The results for the upstream probe, shown in fig. 5.12a, show dry steam conditions ($I/I_0 \approx 1$) for $\theta_{01} < 200^\circ\text{C}$, when the first droplets start nucleating at the probe location. Transmittance rapidly decreases with further temperature decrease, indicating a growing presence of larger droplets. The range of droplet sizes in this turbine and the two wavelengths used give droplet size parameters α_s in the 0.2-15 range, resulting in the extinction coefficient variation of around four orders of magnitude on that range, as shown in fig. 5.13. Therefore, larger droplets generated in the passage nucleation significantly decrease transmittance. A local minimum is reached near 180°C when the largest proportion of the flow nucleates in the passage. This is followed by a transmittance increase as the nucleation zone moves in the upstream rotor row, generating smaller droplets. This is repeated in the next stage upstream, giving another minimum at $\theta_{01} \simeq 155^\circ\text{C}$. The overall transmittance trend is progressively decreasing with a decrease in temperature as earlier nucleation allows droplets more time to grow until they reach the extinction probe.

The calculations show a remarkable agreement with the measurements, accurately recording the start of nucleation and the changes in droplet size spectra as the nucleation zone moves between blade rows. The calculations show an almost exact match with the red light measurements over the entire range of temperatures. Similarly, agreement with the blue light measurements is very good but slightly under-predicts transmittance from 170°C even though red measurements are almost a perfect match on that range. This indicates a somewhat over-predicted proportion of smaller droplets (left side of the calculated droplet size distribution). Since α_s decreases with an increase in wavelength for the same droplet

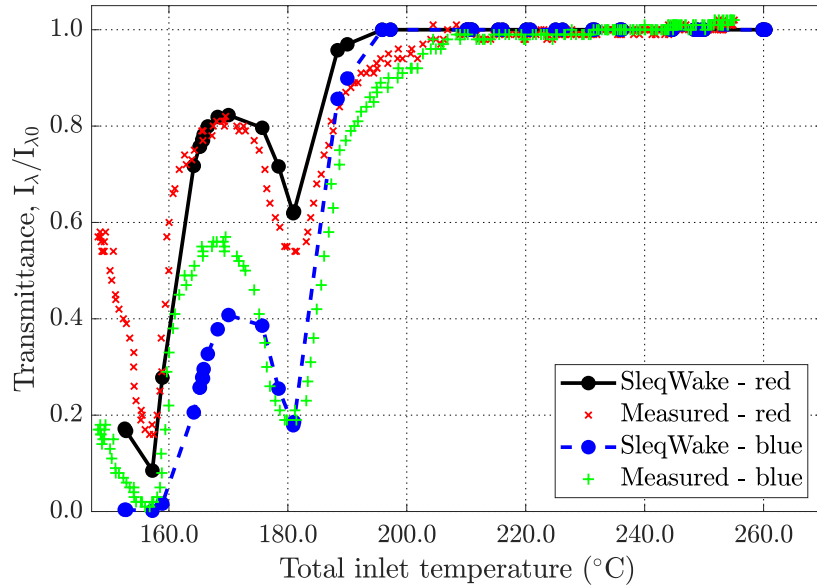
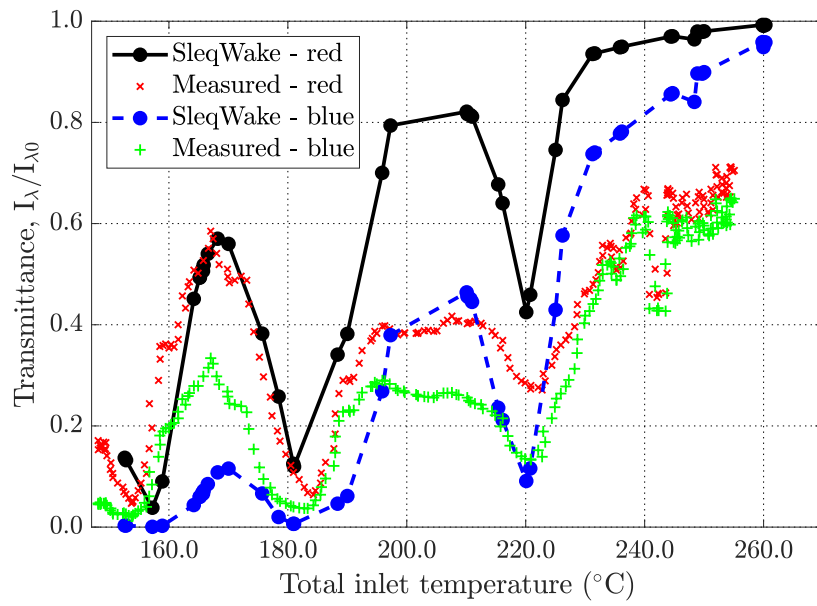
(a) Light extinction upstream of the penultimate stage at $\sim 70\%$ span.(b) Light extinction downstream of the penultimate stage at $\sim 50\%$ span.

Fig. 5.12 Comparison of wake chopping and measured light extinction upstream and downstream of the penultimate stage.

diameter, smaller droplets (resulting in negligibly small extinction coefficient for red light) can end up affecting blue light transmittance as the extinction coefficient suddenly increases as seen in fig. 5.13. However, comparison with more wavelengths would be needed to pinpoint the exact source of difference.

The downstream probe (fig. 5.12b) shows a more complex interaction. Measurements show a low transmittance level from the highest superheat case and the small difference between red and blue light suggests that only large droplets (whose extinction coefficients are less sensitive to λ) are present at the measurement location, corresponding to narrow passage nucleation zone. Temperature decrease moves the nucleation to the rotor, widening the droplet spectrum – indicated by the diverging red and blue light measurements. The upstream passages are reached at 220 °C, 180 °C, and 155 °C, which is in agreement with previously shown results.

The calculations accurately capture the measured trends, reaching local minima and maxima at the same inlet temperatures as the experiments. Significantly higher transmittance for the high inlet superheat cases (and difference between red and blue transmittances) confirms that the computed Wilson zone is much wider than what experiments suggest. Part of the nucleation zone is already stretched upstream of the measurement location, into the rotor blade row, generating smaller droplets than the ones produced in the passage. As the nucleation zone migrates, the difference with the measurements decreases, reaching very good agreement as the zone moves upstream of the probe location. The computed blue light extinction ends up lower than measured for temperatures where red shows good agreement, indicating more liquid mass associated with the smaller droplets. Wider computed nucleation zone changes the ratio of passage to blade row nucleation over the entire Wilson zone length, leading to this difference.

The difference in the level of agreement between upstream and downstream extinction probe is due to the wake chopping model definition. The random walk performed by the wake chopping model defined in chapter 3 increases the number of possible thermodynamic pathline histories with each subsequent blade row, widening the axial zone in which individual pathlines nucleate. Earlier nucleation due to lower inlet superheat, thus, results in a narrower Wilson zone prediction and improves agreement with measurements.

Wake decay temporal constant, defining the rate of wake erosion, can be fine-tuned to reduce the Wilson zone width and a better estimate can be obtained from CFD results. However, the wake chopping model is a coarse 2D model which cannot replicate the level of flow variation in an actual turbine, and thus would result in a much narrower droplet size spectrum if nucleation were confined to the same axial region. The over-predicted nucleation zone, while smoothing variation in flow field properties by making them less sensitive to

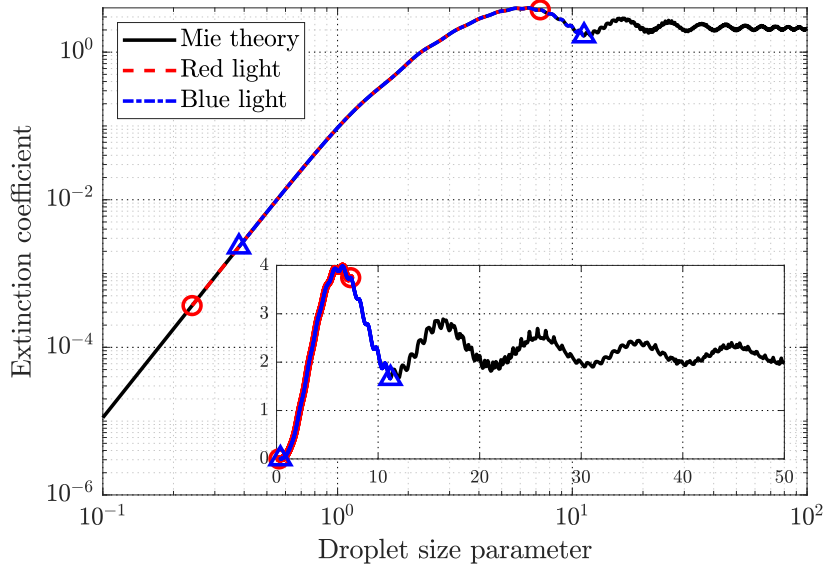


Fig. 5.13 Mie curve of extinction coefficients for a range of droplet size parameters. Red and blue lines show the range of extinction coefficients for a typical droplet spectrum, for red and blue wavelength of light. The markers indicate the smallest and the largest droplet size in the spectrum.

inlet temperature variation, benefits from having a somewhat slower erosion of wakes. It covers a larger range of expansion rates, widening the droplet size spectrum and improving agreement with extinction measurements.

5.3.9 Nucleation zone migration between blade rows

Based on the observed light extinction and specific work output measurements, the nucleation zone is expected to move from the penultimate to the second stage (hence, changing shafts) for inlet temperatures between 200 °C and 170 °C. Figure 5.14 shows the meridional distributions of wetness, d_{32} , and subcooling, collected at mid-span. The values are running averages of all pathline calculations, and are plotted across the second stage rotor and penultimate stage stator and rotor for a range of inlet total temperatures, θ_{01} , that capture this transition.

Nucleation zone is located in the inter-stage passage for $\theta_{01} = 181$ °C and this is captured really well by calculations (see light extinction measurements in fig. 5.12). However, calculated specific work output at that temperature (see fig. 5.9) shows the largest deviation from the measurements which is caused by the early onset of nucleation in the calculations.

Calculated condensation at the passage starts much earlier, at around 200 °C, as seen by the presence of droplets in the passage in fig. 5.14b. The wetness is, however, close to zero and subcooling is not affected as the number of droplets is too low to revert the flow to

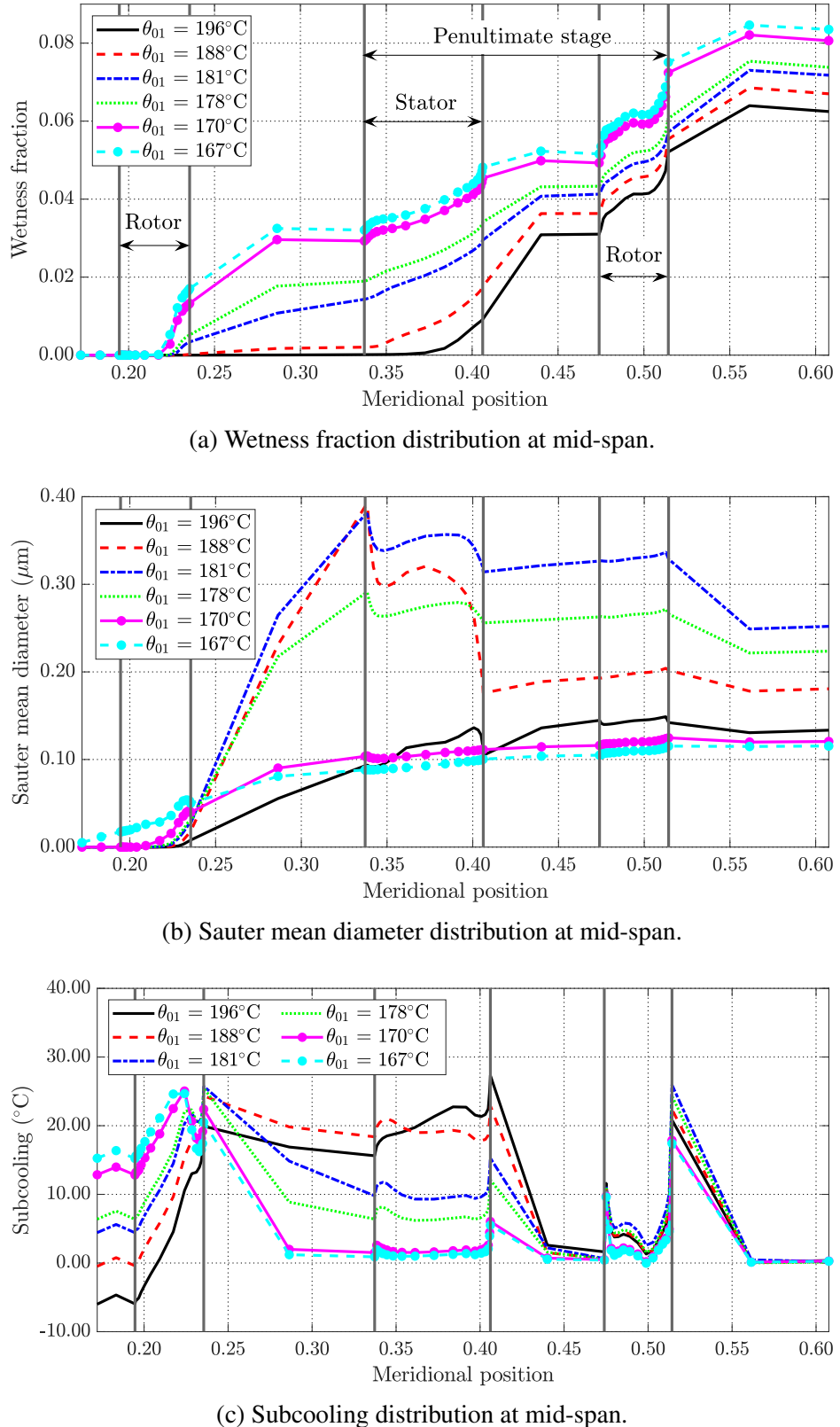


Fig. 5.14 Meridional distributions of running-average properties calculated using sleqWake, capturing the migration of the condensation zone upstream.

equilibrium, as seen in figs. 5.14a and 5.14c. This is caused by the rare, extremely efficient steam parcels that took the most efficient path through the machine (experienced minimum loss and, thus, cooled down the fastest).

Very large droplets start to appear at 188 °C, corresponding to passage nucleation. However, wetness and subcooling again show that just the edges of the nucleation zone are in the passage while the majority of steam nucleates in the penultimate stage stator, rapidly decreasing d_{32} . Only at 181 °C does the bulk of steam pathlines nucleate in the passage, as seen by the substantial decrease in subcooling and increase in wetness fraction.

At 170 °C, the majority of pathlines nucleate at the second stage rotor, resulting in much smaller d_{32} . It is around this temperature that experiments show that the entire condensation zone moved upstream, to the second stage rotor (it can be observed as a local maximum in rear shaft work output), and the agreement between calculated and measured work outputs. The calculations, however, still capture some passage nucleation, observed as a marked rise in d_{32} .

Finally, at 167 °C the start of the nucleation zone already moved to the second stage passage between stator and rotor (see d_{32} increase in that region while corresponding wetness fraction is negligible) while the end was still located in the inter-stage passage (still a substantial d_{32} increase in the first half of the passage). At the same time, the measurements show that the nucleation zone has completely moved from the passage and is located in the blade row (local maximum in the work output and a local maximum in light extinction measurements for both probes). This confirms that the predicted Wilson zone is significantly wider than the measured one, and is the primary reason for reduced sensitivity of other parameters (previously shown in pressure, specific work output, and efficiency distributions) over the tested range of total inlet temperatures. Furthermore, widened nucleation zone changes the proportion of steam nucleating in the blade row versus the passage between blade rows, and affects the light extinction measurements (as discussed in the previous section). These findings strongly suggest that the wake decay rate in real turbines is significantly higher than the one used in this model, limiting the nucleation zone to a shorter axial region (mechanism previously discussed in fig. 3.12). However, reduction of the wake decay rate in the current model significantly restricts the range of expansion rates within the nucleation zone (only modelling \dot{p} variation in 2D), indicating that this limitation cannot be overcome in the current model. Further improvement requires the implementation of radial expansion rate variation (a computationally cheap model would be e.g., a linear variation between blade pressure profiles at different span fractions, based on a secondary generated random number), thus sufficiently expanding the \dot{p} variation in the Wilson zone to research more realistic wake decay rates without compromising the predictive capabilities of the method.

5.4 Conclusions

This chapter demonstrated the capabilities of sleqWake, an improved throughflow routine, by comparing calculation results with experimental measurements and CFD calculations of a model four-stage LP turbine. The calculations were performed without fine-tuning, and the agreement with measurements can be improved by providing more accurate loss coefficients and wake decay rate estimates. The main conclusions are:

- (i) The calculation routine requires only one corrective throughflow calculation to reach a converged solution since the improved wetness loss contributes only a small percentage of the total loss.
- (ii) Inlet mass flow rate and hub/casing pressure suffer from the use of generic loss correlations and are not largely corrected by the inclusion of improved wetness loss. However, the variation of wetness loss with inlet temperature determines the fine features of the distributions and the calculations have shown to be capable of picking up even the minute changes caused by the non-equilibrium effects. Turbine performance is predicted very well, with calculations capturing the effects of nucleation zone moving from the rear to the front shaft and the loss variation caused by the difference between passage and blade row nucleation.
- (iii) Equilibrium calculations fail to capture the change in trends with inlet temperature, pointing to the importance of non-equilibrium effects when resolving the flow field of a condensing steam turbine. Furthermore, passage condensation (generating large droplets) was shown to have a significant effect on downstream flow field and, thus, needs to be accurately resolved to obtain meaningful trends.
- (iv) The inability of axisymmetric calculations (even when modelling non-equilibrium steam) to capture correct trends indicates the importance of 3D effects on the overall turbine flow field. A simple wake chopping model with pitchwise pressure variation significantly improves agreement, while remaining computationally light, alleviating the need for high-fidelity CFD calculations during the early design phase.
- (v) Wake decay rate was shown to have a significant impact on performance predictions. Turbine measurements indicate faster mixing of wakes and a larger variation of expansion rates, resulting in an axially shorter Wilson zone than what the calculations suggest and making it more sensitive to inlet temperature. Since the wake chopping model cannot replicate the broad range of conditions within the real nucleation zone without introducing a radial loss and expansion rate variation, it benefits from an over-predicted nucleation zone length. Even though the over-prediction dampens the sensitivity to temperature variations, it broadens the range of expansion rates, thus mimicking the conditions within a real Wilson zone and improving the droplet spectrum agreement.

Introduction of faster wake mixing would make the calculation more sensitive to inlet temperature variation but the droplet spectrum would be significantly narrower and the calculation would reduce the accuracy of the effects of Wilson zone migration.

- (vi) Even with the generic loss correlations and wake decay rate, the `sleqWake` routine accurately captures the trends over a broad range of inlet temperatures and gives confidence that it can be used as a design tool within the industrial setting.

Chapter 6

Conclusions and future work

6.1 Concluding remarks

6.1.1 Summary

The aim of this project was two-fold. In the first instance, the objective was to develop a non-equilibrium wet-steam throughflow calculation method, which includes the major loss-generating two-phase phenomena. The second goal was to determine how machine geometry, operating conditions, and model assumptions influence the overall magnitude of losses and their distribution between the different phenomena, by performing a comprehensive sensitivity study. The main objectives have been accomplished by (i) implementing a stochastic wake-chopping method within an existing streamline curvature flow solver, (ii) developing a droplet deposition model that includes inertial and turbulent diffusion modes of deposition, (iii) performing a flow sensitivity study (relevant flow properties, e.g., droplet size spectrum, thermodynamic relaxation loss, subcooling, wetness fraction) to key modelling parameters, and (iv) validating the model performance against experimental measurements provided by General Electric over a broad range of turbine operating conditions.

The findings in this thesis extend the understanding of wake chopping and its relevance to steam flow in condensing turbines by comparing experimental measurements with a range of calculations using a steady/wake-chopping approach with an equilibrium/non-equilibrium steam condensation model. The sensitivity study illuminates the strengths and weaknesses of a widely used wake chopping model and clarified which flow features are caused by physical effects and which are caused by modelling limitations. Furthermore, the implications are extended to deposition rates and thermodynamic relaxation loss.

6.1.2 Unsteady wake segmentation

A stochastic wake chopping model was presented and examined in chapter 3, modelling unsteady wake segmentation effects based on the flow field representation (pressure and efficiency distributions on a set of streamsurfaces, calculated using a throughflow code). The model uses a pitchwise polytropic efficiency distribution for each blade row to model the range of thermodynamic variations a steam particle might experience. Individual steam paths through the machine are calculated using a random walk process, with each blade row pitchwise position considered independent of its flow history. Usually, less than 10000 pathline calculations are needed to reach convergence, requiring around 20 minutes on a single CPU and 100Mb RAM for a five-stage turbine calculation.

Modelling the expansion rate variation within blade rows requires pressure profiles (pressure and suction side distributions) to be provided for each blade row since the generated droplet size spectra are known to be sensitive to expansion rates and throughflow codes cannot resolve these in sufficient detail. The pressure distribution experienced by a steam parcel is determined by linear interpolation of the profiles provided, based on its random pitchwise position at each blade row inlet. Pitchwise polytropic efficiency distribution was expressed as a: (i) square (step function), (ii) triangle (linear), (iii) quadratic, and a (iv) Gaussian profile, whereby high efficiency represents near-isentropic expansion in the core of the flow and lower efficiency models viscous dissipation close to the walls. The profiles were expressed in a way to keep the mean value of loss and its standard deviation constant for all profiles. The effect of wake asymmetry was tested by introducing an asymmetry parameter to the linear profile, enabling the examination of wakes anywhere between [100% SS & 0% PS wakes] and [0% SS & 100% PS wakes]. Wake decay was modelled by allowing for pitchwise mixing out of wakes while ignoring radial mixing, and it was tested on the whole spectrum of wake decay temporal constants ($\tau_w = 0$ standing for instantaneous equilibration and $\tau_w \rightarrow \infty$ implying persisting wakes), with a focus on τ_w values close to the “realistic value” estimated by [53]. The model sensitivity study was performed on a five-stage repeating-stage turbine and the main conclusions are:

- (i) Wake chopping was shown to predict a much broader droplet spectra (~ 20 times wider than in steady calculations), in line with previous work and optical measurements. This has a significant impact on deposition rates, which are known to vary strongly with Stokes number.
- (ii) Droplet spectra were shown to be fairly insensitive to wake profile shape, provided the mean and standard deviation of loss are kept constant. The variation shown in previous studies primarily comes from the lack of pitchwise expansion rate variation (\dot{p}) and not keeping the standard deviation of loss constant between different wake shapes.

Similarly, sensitivity to wake decay rates reported in the literature (changing from unimodal to bimodal distribution, with most liquid mass concentrated at the peaks) was also shown to be due to 1D (axial) \dot{p} (neglecting pitchwise and radial variations) and not a flow feature. Pitchwise variations significantly increase the range of expansion rates within the nucleation zone, thus making the spectrum largely insensitive to wake decay rates. The variation in wetness fraction and thermodynamic relaxation loss with inlet temperature is very low due to the same reasons.

- (iii) Pitchwise pressure variation has the largest impact on the predicted droplet sizes, resulting in a wider droplet spectrum even for steady calculations since the Wilson point is no longer associated with a single expansion rate.

6.1.3 Droplet deposition

A droplet deposition model consisting of inertial and turbulent diffusion modes was presented in chapter 4. The model uses droplet size spectra (droplets are split into droplet bins according to their size) and the basic flow field information to determine deposition rates on blade surfaces in each blade row, with the calculation progressing in a sweeping manner through the machine.

The inertial deposition model is based on 3D velocity slip calculations for spherical droplets uniformly distributed in the pitchwise direction and sufficiently far apart to avoid their interaction, assuming the interaction between droplet inertia and viscous drag as the dominant effect. The much higher density of water makes droplets less capable of following steam pathlines, with a proportion of them impinging on the surrounding surfaces. Blades are approximated using infinitely thin parabolic shapes, matching steam pathlines, to prevent artificial deposition. Droplet trajectories are then estimated by performing a semi-analytical integration of equations of motion over small time steps.

Turbulent diffusional deposition rates are estimated based on the empirical deposition data in fully turbulent pipe flow, as the throughflow calculations do not model the flow field in blade passages. The model depends on the friction velocity estimate, which is often obtained from empirical (flat plate, no streamwise pressure gradient) equations for the skin friction coefficient which are not expected to be very accurate. An estimate of errors involved was obtained by deriving values of C_f from representative CFD calculations.

The model was tested on the last stage stator blade row of a five-stage repeating-stage LP turbine, whereby the flow field was calculated using the throughflow method and droplet size spectra were generated for a range of steady and wake-chopping calculations. The total deposition rate was estimated as the sum of inertial and turbulent deposition rates, neglecting how the interaction between the two mechanisms could alter total deposition rate. Finally,

the sensitivity of deposition rates to wake chopping parameters was tested. The main findings are:

- (i) Flat-plate equations for turbulent boundary layers overestimate the skin friction coefficient (C_f) by approximately a factor of two in the $400\,000 \leq \text{Re} \leq 900\,000$ range. However, they are still considered the best approximative method due to the general lack of measurement data. A better estimate could be made using existing C_f data from similar blade designs or from detailed CFD calculations.
- (ii) Turbulent deposition is sensitive to C_f , resulting in a $\sim 120\%$ higher deposition rate when using flat plate expressions, as it increases particle relaxation time which, in the diffusion-impaction regime, strongly amplifies deposition rates. However, the sensitivity level varies with droplet sizes and flow conditions (i.e., if the dominant droplet sizes fall outside of the diffusion-impaction regime, the sensitivity is greatly reduced). The inertial deposition model was shown to give correct behaviour in the limiting cases (for very large and very small droplets), and qualitatively agrees well with previous studies over the typical range of droplet sizes found in LP turbines.
- (iii) Wake chopping typically increases deposition rates by almost a factor of six, relative to steady calculations, as the droplet size spectrum becomes roughly 20 times wider. Pitchwise pressure variation plays a large role in droplet spectrum widening (even in steady calculations), driving the deposition rates up, and should always be modelled. The changes to droplet size spectra due to wake chopping parameter variation are amplified by the deposition model. Nonetheless, overall deposition rates vary by less than 10% over the realistic range of these parameters.

6.1.4 Comparison with turbine measurements

The models presented in chapters 3 and 4 were combined within a throughflow solver and results compared against model LP turbine measurements and CFD calculations in chapter 5. The measurements were kindly provided by General Electric and CFD results were extracted from Chandler et al. [22]. The turbine consists of four stages, with first two and last two stages mounted on separate shafts. Turbine performance and wetness characteristics were calculated over a wide range of inlet temperatures that correspond to outlet wetness between approximately 6% and 14%, hence capturing the migration of the nucleation zone upstream through blade rows and inter-row gaps. The model requires only one corrective throughflow calculation to obtain a converged solution as the improved wetness loss prediction (wake chopping model) contributes only a small fraction of the total loss. The main findings are:

- (i) The wake chopping calculations were shown to pick up detailed changes to the inlet mass low rate caused by the unsteady and non-equilibrium effects, resolving even

minute changes. Turbine performance trends are predicted very well, with wake chopping calculations capturing the effect of the nucleation zone moving upstream from one shaft to the other as well as the thermodynamic relaxation loss variation caused by the nucleation zone moving between blade rows and inter-row gaps.

- (ii) Equilibrium calculations fail to predict the correct trends across the range of inlet temperatures, pointing to the importance of non-equilibrium effects to the overall flow dynamics downstream of the nucleation zone. Moreover, inter-row gap nucleation is shown to have a significant influence on the downstream flow field and, thus, needs to be correctly resolved to obtain meaningful prediction trends.
- (iii) Steady (axisymmetric) calculations fail to correctly resolve trends, even when using non-equilibrium steam, thus pointing to the importance of unsteady, inherently 3D effects (primarily wake chopping and expansion rate variation). A simple wake chopping model improves the wetness formation prediction, accurately predicting nucleation zone moving between blade rows. It shows very good agreement with light extinction measurements, which could not be achieved with narrow and sensitive spectra predicted by the steady calculations.
- (iv) Turbine measurements indicate faster wake mixing, confining the nucleation zone to a shorter axial region than predicted by the wake chopping calculations, making it more sensitive to inlet temperature changes. Since the current wake chopping model cannot replicate the broad range of expansion rates and fluctuations occurring in a real turbine, it benefits from an axially smeared nucleation zone (stretched over a longer axial region due to slower mixing of wakes) as it artificially expands the range of conditions a nucleating steam parcel can encounter, bringing the predicted droplet spectrum closer to measurements. This, however, comes with the unwanted consequence of reduced sensitivity to inlet temperature variation. The results suggest that the wake chopping model might benefit from a simple radial expansion rate variation model (e.g., linear variation between input pressure profiles at different span fractions) that would further increase the expansion rate variation in the nucleation zone, further reduce sensitivity to modelling parameters, and enable faster wake mixing without compromising the results.

6.2 Suggestions for future research

The calculation routine developed in this thesis is capable of modelling a broad range of phenomena but there are multiple simplifications and assumptions that can be improved upon. Furthermore, there are a host of additional flow phenomena that can be modelled without

compromising the agile approach to turbine development that this routine embodies. The suggestions for further developments are as follows.

Extensions to the unified throughflow method

- (i) The range of expansion rates in the nucleation zone was shown to have a large influence on the generated droplet sizes. While the current 2D \dot{p} variation improves the results and reduces sensitivity to both modelling parameters and inlet conditions, it still does not introduce sufficient variability of expansion rates. Hence, the model would benefit from a somewhat more complex expansion rate variation which would bring the nucleation zone conditions closer to the range observed in reality. In turn, this would allow for finer tuning of wake decay rates.
- (ii) The calculated deposition rates allow for a simple liquid film model to be implemented. There are already several models in the literature (e.g., the model developed by Williams and Young [166] to track liquid films caused by water ingestion in jet engines) which could be added without significant CPU overhead. In turn, this would enable the modelling of coarse water formation as the films break-up at the trailing edge, and provide an estimate of centrifuging losses, thus covering all of the major contributors to wetness loss. Breaking and kinematic relaxation losses could be added once the coarse water is modelled, however, they are not expected to strongly influence wetness loss [120].

Modelling improvements

- (i) The presented comparison with measurements suggests that wake mixing is occurring at a faster rate in reality than what the current model (based on the simple analysis in [53] that neglects any wake distortions due to convective effects) predicts. Since the wake mixing rate effectively imposes a limit to the nucleation zone length by eroding static temperature fluctuations, it would be useful to examine the wake mixing mechanisms and develop a more flexible model that could be adjusted based on the local flow parameters.

Validation data

- (i) Literature analysis of depositional processes confirmed the long standing opinion that there is a need for a detailed dataset that could be used to validate and compare performance of deposition models. Currently, models are validated based on comparisons

with vertical pipe flow measurements, although the flow conditions in turbines are significantly different.

- (ii) Moreover, the entire turbomachinery community would benefit from a detailed, accessible turbine dataset, which would include flow, performance, and wetness measurements over a broad range of operating conditions. Developing such a dataset would improve the validation efforts of various research groups and enable quantitative model comparisons on a standardised test case.

Applications of the unified throughflow method

- (i) The model presented in this thesis consistently predicts turbine performance over a range of operating conditions. Considering the low computational cost needed for a single calculation, this methodology enables rapid performance comparison over a range of design parameters, thus opening doors to turbine optimisation based on wetness-related losses.
- (ii) Similarly, this method can be applied to energy storage calculations, for example, to examine how steam extraction (when storing energy) or steam addition (when drawing from storage) affect overall turbine performance, as well as related losses over a range of turbine-flexing and storage parameters.

References

- [1] Abu-Ghannam, B. and Shaw, R. (1980). Natural transition of boundary layers—the effects of turbulence, pressure gradient, and flow history. *Journal of Mechanical Engineering Science*, 22(5):213–228.
- [2] Aitken, J. (1880). On dust, fogs, and clouds. *Transactions of the Royal Scottish Society of Arts, Edinburgh*, 30:34–64.
- [3] Aitken, J. (1881). Dust, fogs, and clouds. *Nature*, 23(591):384–385.
- [4] Allmaras, S. R. and Johnson, F. T. (2012). Modifications and clarifications for the implementation of the spalart-allmaras turbulence model. In *Seventh international conference on computational fluid dynamics (ICCFD7)*, pages 1–11.
- [5] Bakhtar, F., Ebrahimi, M., and Webb, R. (1995). On the performance of a cascade of turbine rotor tip section blading in nucleating steam: part 1: surface pressure distributions. *Proceedings of the Institution of Mechanical Engineers, Part C: Journal of Mechanical Engineering Science*, 209(2):115–124.
- [6] Bakhtar, F. and Heaton, A. (1989). An examination of the effect of ‘wake chopping’ on droplet sizes in steam turbines. In *Technology of turbine plant operating with wet steam*, pages 197–200. Thomas Telford Publishing.
- [7] Bakhtar, F. and Heaton, A. V. (2005). Effects of Wake Chopping on Droplet Sizes in Steam Turbines. *Proceedings of the Institution of Mechanical Engineers, Part C: Journal of Mechanical Engineering Science*, 219(12):1357–1367.
- [8] Bakhtar, F., Rassam, S., and Zhang, G. (1999). On the performance of a cascade of turbin rotor tip section blading in wet steam part 4: Droplet measurements. *Proceedings of the Institution of Mechanical Engineers, Part C: Journal of Mechanical Engineering Science*, 213(4):343–353.
- [9] Bakhtar, F. and Webb, R. (1983). Tabular method of estimating nucleating steam flows. *International journal of heat and fluid flow*, 4(4):217–227.
- [10] Bakhtar, F., Young, J. B., White, A. J., and Simpson, D. A. (2005). Classical Nucleation Theory and Its Application to Condensing Steam Flow Calculations. *Proceedings of the Institution of Mechanical Engineers, Part C: Journal of Mechanical Engineering Science*, 219(12):1315–1333.
- [11] Balje, O. and Binsley, R. (1968). Axial turbine performance evaluation. part a—loss-geometry relationships. *Journal of Engineering for Power*, 90(4):341–348.

- [12] Bardon, M., Moffatt, W., and Randall, J. (1975). Secondary flow effects on gas exit angles in rectilinear cascades.
- [13] Barschdorff, D., Hausmann, G., and Ludwig, A. (1976). Flow and drop size investigations of wet steam at sub-and supersonic velocities with the theory of homogeneous condensation. *Pr. Inst. Maszyn Przeplwowych*, 241:70–72.
- [14] Baumann, K. (1912). Recent developments in steam turbine practice. *Journal of the Institution of Electrical Engineers*, 48(213):768–842.
- [15] Becker, R. and Döring, W. (1935). Kinetische behandlung der keimbildung in übersättigten dämpfen. *Annalen der Physik*, 416(8):719–752.
- [16] Binnie, A. and Woods, M. (1938). The pressure distribution in a convergent-divergent steam nozzle. *Proceedings of the Institution of Mechanical Engineers*, 138(1):229–266.
- [17] Binnie, A. M. and Green, J. (1942). An electrical detector of condensation in high-velocity steam. *Proceedings of the Royal Society of London. Series A. Mathematical and Physical Sciences*, 181(985):134–154.
- [18] Blasius, H. (1908). Boundary layers in fluids of small viscosity. *Z Math Physik*, 56(1):1–37.
- [19] Bohren, C. F. and Huffman, D. R. (2008). *Absorption and scattering of light by small particles*. John Wiley & Sons.
- [20] Buckley, J. and Winterton, R. H. (1999). The role of heterogeneous nucleation on the steam condensation process. In *VGB/EPRI Conference on Steam chemistry, Freiburg, Germany*.
- [21] Caporaloni, M., Tampieri, F., Trombetti, F., and Vittori, O. (1975). Transfer of particles in nonisotropic air turbulence. *Journal of the atmospheric sciences*, 32(3):565–568.
- [22] Chandler, K., Melas, M., and Jorge, T. (2015). A study of spontaneous condensation in an lp test turbine. In *ASME Turbo Expo 2015: Turbine Technical Conference and Exposition*. American Society of Mechanical Engineers Digital Collection.
- [23] Chandler, K. D. (2013). *Unsteady Wetness Effects in Low Pressure Steam Turbines*. PhD thesis, University of Cambridge.
- [24] Chandler, K. D., White, A. J., and Young, J. B. (2011). Unsteady wetness effects in LP steam turbines. In *Proc. ASME Turbo Expo*.
- [25] Crane, R. (1973). Deposition of fog drops on low pressure steam turbine blades. *International Journal of Mechanical Sciences*, 15(8):613–631.
- [26] Crane, R. (1978). Some aspects of wet steam flow in turbine cross-over pipes. *International Journal of Mechanical Sciences*, 20(4):237–246.
- [27] Crane, R. I. (2004). Droplet deposition in steam turbines. *Proceedings of the Institution of Mechanical Engineers, Part C: Journal of Mechanical Engineering Science*, 218(8):859–870.

- [28] Cunningham, E. (1910). On the velocity of steady fall of spherical particles through fluid medium. *Proceedings of the Royal Society of London. Series A, Containing Papers of a Mathematical and Physical Character*, 83(563):357–365.
- [29] Davies, C. N. (1945). Definitive equations for the fluid resistance of spheres. *Proceedings of the Physical Society*, 57(4):259.
- [30] Davies, C. N. and others (1966). *Aerosol science*, volume 1102. Academic Press London.
- [31] Délery, J., Marvin, J. G., and Reshotko, E. (1986). Shock-wave boundary layer interactions. Technical report, ADVISORY GROUP FOR AEROSPACE RESEARCH AND DEVELOPMENT NEUILLY-SUR-SEINE (FRANCE).
- [32] Denton, J. (1982). An improved time marching method for turbomachinery flow calculation. In *ASME 1982 International Gas Turbine Conference and Exhibit*. American Society of Mechanical Engineers Digital Collection.
- [33] Denton, J. and Dawes, W. (1998). Computational fluid dynamics for turbomachinery design. *Proceedings of the Institution of Mechanical Engineers, Part C: Journal of Mechanical Engineering Science*, 213(2):107–124.
- [34] Denton, J. D. (1978). Throughflow Calculations for Transonic Axial Flow Turbines. *Journal of Engineering for Power*, 100(2):212–218.
- [35] Denton, J. D. (1992). The calculation of three-dimensional viscous flow through multistage turbomachines. *Journal of Turbomachinery*, 114(1):18–26.
- [36] Denton, J. D. (2010). Tblock description and user manual. Version TBLOCK-10.0.
- [37] Denton, J. D. (2012). Throughflow program SLEQ manual. Version SLEQ-10.5.
- [38] Denton, J. D. and Xu, L. (2002). The effects of lean and sweep on transonic fan performance. In *ASME Turbo Expo 2002: Power for Land, Sea, and Air*, pages 23–32. American Society of Mechanical Engineers Digital Collection.
- [39] Dillmann, A. and Meier, G. (1991). A refined droplet approach to the problem of homogeneous nucleation from the vapor phase. *The Journal of chemical physics*, 94(5):3872–3884.
- [40] Dixon, S. L. and Hall, C. (2013). *Fluid mechanics and thermodynamics of turbomachinery*. Butterworth-Heinemann.
- [41] Dunham, J. (1970). A review of cascade data on secondary losses in turbines. *Journal of Mechanical Engineering Science*, 12(1):48–59.
- [42] Faeth, G. (1979). Current status of droplet and liquid combustion. In *Energy and Combustion Science*, pages 149–182. Elsevier.
- [43] Fahrenheit, D. G. (1724). Viii. experimenta & observationes de congelatione aquæ in vacuo factæ a dg fahrenheit, rs s. *Philosophical Transactions of the Royal Society of London*, 33(382):78–84.

- [44] Farkas, L. (1927). Keimbildungsgeschwindigkeit in übersättigten dämpfen. *Z. phys. Chem.*, 125(1):236–242.
- [45] Feder, J., Russell, K., Lothe, J., and Pound, G. (1966). Homogeneous nucleation and growth of droplets in vapours. *Advances in Physics*, 15(57):111–178.
- [46] Fendler, Y., Dorey, J.-M., Stanciu, M., Lance, M., and Léonard, O. (2012). Developments for Modeling of Droplets Deposition and Liquid Film Flow in a Throughflow Code for Steam Turbines. In *ASME Turbo Expo 2012: Turbine Technical Conference and Exposition*, pages 537–547. American Society of Mechanical Engineers.
- [47] Filippov, G. A., Saltanov, A., and Ignatevs, E. A. (1970). Analysing condensation of supersaturated steam in turbine stages. *Thermal Engineering*, 17(12):26–&.
- [48] Frenkel, J. (1946). Kinetic theory of liquids' clarendon press.
- [49] Friedlander, S. K. and Johnstone, H. F. (1957). Deposition of Suspended Particles from Turbulent Gas Streams. *Industrial & Engineering Chemistry*, 49(7):1151–1156.
- [50] Fung, K. H., Tang, I., and Munkelwitz, H. (1987). Study of condensational growth of water droplets by mie resonance spectroscopy. *Applied optics*, 26(7):1282–1287.
- [51] Guha, A. (2008). Transport and Deposition of Particles in Turbulent and Laminar Flow. *Annual Review of Fluid Mechanics*, 40(1):311–341.
- [52] Guha, A. and Young, J. (1991). Time-marching prediction of unsteady condensation phenomena due to supercritical heat addition.
- [53] Guha, A. and Young, J. (1994). The Effect of Flow Unsteadiness on the Homogeneous Nucleation of Water Droplets in Steam Turbines. *Philosophical Transactions of the Royal Society of London. Series A: Physical and Engineering Sciences*, 349(1691):445.
- [54] Gyarmathy, G. (1962). *Grundlagen einer theorie der nassdampfturbine*. PhD thesis, Swiss Federal Institute of Technology in Zurich, Zurich.
- [55] Gyarmathy, G. (1963). On the growth rate of droplets in a supersaturated atmosphere. *Zeitschrift für angewandte Mathematik und Physik*, 14(13):280–293.
- [56] Gyarmathy, G., Burkhard, H., Lesch, F., and Siegenthaler, A. (1973). Spontaneous condensation of steam at high pressure: first experimental results. In *Proceedings of IMechE Conference on Heat and fluid flow in steam and gas turbine plant*, volume 3, pages 182–186.
- [57] Gyarmathy, G. and Lesch, F. (1969). Paper 12: fog droplet observations in laval nozzles and in an experimental turbine. In *Proceedings of the institution of mechanical engineers, conference proceedings*, volume 184, pages 29–36. SAGE Publications Sage UK: London, England.
- [58] Gyarmathy, G. and Meyer, H. (1965). Spontaneous condensation phenomena. *VDI. ForschHft*, 508.

- [59] Gyarmathy, G. and Spengler, P. (1974). Flow fluctuations in multistage thermal turbomachines. *Traupel commemorative volume.(A 75-19051 06-02) Zurich, Juris-Verlag AG, 1974.*, page 95.
- [60] Harrison, S. (1989). Secondary loss generation in a linear cascade of high-turning turbine blades. In *Turbo Expo: Power for Land, Sea, and Air*, volume 79139, page V001T01A021. American Society of Mechanical Engineers.
- [61] Healy, D. and Young, J. (2010). An experimental and theoretical study of particle deposition due to thermophoresis and turbulence in an annular flow. *International Journal of Multiphase Flow*, 36(11-12):870–881.
- [62] Hertz, H. (1882). Ueber die verdunstung der flüssigkeiten, insbesondere des quecksilbers, im luftleeren raume. *Annalen der Physik*, 253(10):177–193.
- [63] Hesketh, J. and Walker, P. (2005). Effects of wetness in steam turbines. *Proceedings of the Institution of Mechanical Engineers, Part C: Journal of Mechanical Engineering Science*, 219(12):1301–1314.
- [64] Hill, P., Miyagawa, K., and Denton, J. (2000). Fast and accurate inclusion of steam properties in two-and three-dimensional steam turbine flow calculations. *Proceedings of the Institution of Mechanical Engineers, Part C: Journal of Mechanical Engineering Science*, 214(7):903–919.
- [65] Hirsch, C. and Denton, J. (1981). Propulsion and energetics panel working group 12 on through flow calculations in axial turbomachines. Technical report, ADVISORY GROUP FOR AEROSPACE RESEARCH AND DEVELOPMENT NEUILLY-SUR-SEINE (FRANCE).
- [66] HIRSCH, C. and Denton, J. (1981). Through flow calculations in axial turbomachines.
- [67] Holley, B. M., Becz, S., and Langston, L. S. (2006). Measurement and calculation of turbine cascade endwall pressure and shear stress.
- [68] Hughes, F. (2016). *Throughflow methods for two-phase flow in steam turbines*. PhD thesis, University of Cambridge.
- [69] Hulst, H. C. and van de Hulst, H. C. (1981). *Light scattering by small particles*. Courier Corporation.
- [70] IAPWS-IF97 (1997). Revised release on the IAPWS industrial formulation for thermodynamic properties of water and steam, internet resource, <http://www.iapws.org/release.html>.
- [71] IAPWS R1-76 (2014). Revised release on surface tension of ordinary water substance, internet resource, <http://www.iapws.org/relguide/surf-h2o.html>.
- [72] IAPWS R12-08 (2008). Release on the IAPWS formulation 2008 for the viscosity of ordinary water substance, internet resource, <http://www.iapws.org/relguide/viscosity.html>.
- [73] IAPWS R15-11 (2011). Release on the IAPWS formulation 2011 for the thermal conductivity of ordinary water substance, internet resource, <http://www.iapws.org/relguide/thcond.html>.

- [74] IEA (2020a). Carbon intensity of electricity generation in selected regions in the sustainable development scenario, 2000-2040, internet resource, <https://www.iea.org/data-and-statistics/charts/carbon-intensity-of-electricity-generation-in-selected-regions-in-the-sustainable-development-scenario-2000-2040>, all rights reserved.
- [75] IEA (2020b). Electricity generation by source, world 1990-2019, internet resource, <https://www.iea.org/data-and-statistics/data-browser?country=world&fuel=energy%20supply&indicator=elecgenbyfuel>, all rights reserved.
- [76] IEA (2020c). The paris agreement, internet resource, <https://unfccc.int/process-and-meetings/the-paris-agreement/the-paris-agreement>.
- [77] Jackson, R. and Davidson, B. (1983). An equation set for non-equilibrium two phase flow, and an analysis of some aspects of choking, acoustic propagation, and losses in low pressure wet steam. *International journal of multiphase flow*, 9(5):491–510.
- [78] Jameson, A. (1991). Time dependent calculations using multigrid, with applications to unsteady flows past airfoils and wings. In *10th Computational Fluid Dynamics Conference*, page 1596.
- [79] Jameson, A., Schmidt, W., Turkel, E., et al. (1981). 'numerical solutions of the euler equations by finite volume methods using runge-kutta time-stepping schemes,' aiaa paper 81-1259(1981). In *14th AIAA Fluid and Plasma Dynamic Conference, Palo Alto, California*.
- [80] Jones, W. and Launder, B. (1972). Some properties of sink-flow turbulent boundary layers. *Journal of Fluid Mechanics*, 56(2):337–351.
- [81] Kantrowitz, A. (1951). Nucleation in Very Rapid Vapor Expansions. *The Journal of Chemical Physics*, 19(9):1097–1100.
- [82] Kirkwood, J. G. and Buff, F. P. (1949). The statistical mechanical theory of surface tension. *The Journal of Chemical Physics*, 17(3):338–343.
- [83] Knudsen, M. (1915). Die maximale verdampfungsgeschwindigkeit des quecksilbers. *Annalen der Physik*, 352(13):697–708.
- [84] Koenig, F. O. (1950). On the thermodynamic relation between surface tension and curvature. *The Journal of Chemical Physics*, 18(4):449–459.
- [85] Kreitmeier, F., Greim, R., Congiu, F., and Faelling, J. (2005). Experimental and Numerical Analyses of Relaxation Processes in LP Steam Turbines. *Proceedings of the Institution of Mechanical Engineers, Part C: Journal of Mechanical Engineering Science*, 219(12):1411–1436.
- [86] Laaksonen, A., Ford, I., and Kulmala, M. (1994). Revised parametrization of the dillmann-meier theory of homogeneous nucleation. *Physical Review E*, 49(6):5517.
- [87] Langmuir, I. (1915). Chemical reactions at low pressures. *Journal of the American Chemical Society*, 37(5):1139–1167.

- [88] Langmuir, I. (1962). *The collected works of Irving Langmuir*, volume 12. Pergamon press.
- [89] Liu, B. Y. and Agarwal, J. K. (1974). Experimental observation of aerosol deposition in turbulent flow. *Journal of Aerosol Science*, 5(2):145–155.
- [90] Lothe, J. and Pound, G. M. (1962). Reconsiderations of nucleation theory. *The Journal of Chemical Physics*, 36(8):2080–2085.
- [91] Marshakov, A. V., Schetz, J. A., and Kiss, T. (1996). Direct measurement of skin friction in a turbine cascade. *Journal of propulsion and power*, 12(2):245–249.
- [92] Martin, H. M. (1918). *A new theory of the steam turbine*. Engineering.,
- [93] McDonald, J. E. (1962). Homogeneous nucleation of vapor condensation. I. Thermodynamic aspects. *American Journal of Physics*.
- [94] McDonald, J. E. (1963). Homogeneous nucleation of vapor condensation. II. Kinetic aspects. *American Journal of Physics*, 31(1):31–41.
- [95] Meacock, A. J. (2005). *Analysis of Water Injected Compressors*. PhD thesis, University of Cambridge.
- [96] Mills, A. and Seban, R. (1967). The condensation coefficient of water. *International Journal of Heat and Mass Transfer*, 10(12):1815–1827.
- [97] Moffat, R. and Kays, W. (1984). A review of turbulent-boundary-layer heat transfer research at stanford, 1958-1983. In *Advances in heat transfer*, volume 16, pages 241–365. Elsevier.
- [98] Moore, M., Langford, R., and Tipping, J. (1967). Paper 5: Research at cerl on turbine blade erosion. In *Proceedings of the Institution of Mechanical Engineers, Conference Proceedings*, volume 182, pages 61–68. SAGE Publications Sage UK: London, England.
- [99] Moore, M. and Sculpher, P. (1969). Conditions producing concentrated erosion in large steam turbines. In *Proceedings of the Institution of Mechanical Engineers, Conference Proceedings*, volume 184, pages 45–56. SAGE Publications Sage UK: London, England.
- [100] Moore, M., Walters, P., Crane, R., and Davidson, B. (1973). Predicting the fog drop size in wet steam turbines, institute of mechanical engineers (uk). In *The 4th Wet Steam Conf.*
- [101] Moore, M. J. and Sieverding, C. (1976). Two-phase steam flow in turbines and separators: theory, instrumentation, engineering.
- [102] Morsi, S. A. and Alexander, A. J. (1972). An investigation of particle trajectories in two-phase flow systems. *Journal of Fluid Mechanics*, 55(02):193.
- [103] Moses, C. and Stein, G. (1978). On the growth of steam droplets formed in a laval nozzle using both static pressure and light scattering measurements. *J. Fluids Eng.*, 100.
- [104] Muck, K., Hoffmann, P., and Bradshaw, P. (1985). The effect of convex surface curvature on turbulent boundary layers. *Journal of Fluid Mechanics*, 161:347–369.

- [105] Murpy, J. S. (1965). Extensions of the falkner-skan similar solutions to flows with surface curvature. *AIAA Journal*, 3(11):2043–2049.
- [106] Nadler, B., Hollerbach, U., and Eisenberg, R. (2003). Dielectric boundary force and its crucial role in gramicidin. *Physical Review E*, 68(2):021905.
- [107] Narasimha, R. and Ojha, S. K. (1967). Effect of longitudinal surface curvature on boundary layers. *Journal of Fluid Mechanics*, 29(1):187–199.
- [108] Němec, T., Maršík, F., and Palmer, D. A. (2006). Binary nucleation of water and sodium chloride. *The Journal of chemical physics*, 124(4):044509.
- [109] Owen, I. et al. (1985). Diffusion of aerosols onto a heated turbine blade. In *Proceedings of the International Symposium on Particulate and Multiphase Processes*. Hemisphere Publ Corp, Washington, DC, USA.
- [110] Papavergos, P. and Hedley, A. (1984). Particle deposition behaviour from turbulent flows. *Chemical engineering research & design*, 62(5):275–295.
- [111] Parker, G. and Lee, P. (1972). Studies of the deposition of sub-micron particles on turbine blades. *Proceedings of the institution of mechanical engineers*, 186(1):519–526.
- [112] Parker, G. and Ryley, D. (1969). Equipment and techniques for studying the deposition of sub-micron particles on turbine blades. In *Proceedings of the Institution of Mechanical Engineers, Conference Proceedings*, volume 184, pages 43–51. SAGE Publications Sage UK: London, England.
- [113] Patel, V. and Sotiropoulos, F. (1997). Longitudinal curvature effects in turbulent boundary layers. *Progress in Aerospace Sciences*, 33(1-2):1–70.
- [114] Penndorf, R. B. (1957). New tables of total mie scattering coefficients for spherical particles of real refractive indexes. *JOSA*, 47(11):1010–1015.
- [115] Peters, F. and Meyer, K. (1995). Measurement and interpretation of growth of monodispersed water droplets suspended in pure vapor. *International journal of heat and mass transfer*, 38(17):3285–3293.
- [116] Petr, V. and Kolovratnik, M. (2000). Modelling of the droplet size distribution in a low-pressure steam turbine. *Proceedings of the Institution of Mechanical Engineers, Part A: Journal of Power and Energy*, 214(2):145–152.
- [117] Petr, V. and Kolovratnik, M. (2001). Heterogeneous effects in the droplet nucleation process in lp steam turbines. In *4th European conference on turbomachinery, Firenze*.
- [118] Petr, V. and Kolovratnik, M. (2003). Diagnostics of wet steam in lp steam turbines. *ETC5, Praha*.
- [119] Petr, V. and Kolovratnik, M. (2014a). The assessment of the effect of binary homogeneous nucleation on wet steam energy loss in a low pressure steam turbine. *Proceedings of the Institution of Mechanical Engineers, Part A: Journal of Power and Energy*, 228(5):525–535.

- [120] Petr, V. and Kolovratnik, M. (2014b). Wet steam energy loss and related baumann rule in low pressure steam turbines. *Proceedings of the Institution of Mechanical Engineers, Part A: Journal of Power and Energy*, 228(2):206–215.
- [121] Pollard, D., Lord, M., and Stockton, E. (1983). Evaluation of low-pressure steam-turbine blade erosion. *J. Sci. Technol.;(United Kingdom)*, 49(1).
- [122] Poulson, B. (1997). Historical development in understanding of how fluid flow can damage metals. *BOOK-INSTITUTE OF MATERIALS*, 689:774–783.
- [123] Pullan, G. and Denton, J. (2003). Numerical simulations of vortex–turbine blade interaction. In *Proceedings of the 5th European Turbomachinery Conference*.
- [124] Reeks, M. W. (1983). The transport of discrete particles in inhomogeneous turbulence. *Journal of aerosol science*, 14(6):729–739.
- [125] Richardson, C., Lin, H.-B., McGraw, R., and Tang, I. (1986). Growth rate measurements for single suspended droplets using the optical resonance method. *Aerosol science and technology*, 5(1):103–112.
- [126] Ryley, D. and Davies, J. (1983). Effect of thermophoresis on fog droplet deposition on low pressure steam turbine guide blades. *International journal of heat and fluid flow*, 4(3):161–167.
- [127] Ryley, D. and El-Shobokshy, M. (1978). The deposition of fog droplets by diffusion onto steam turbine guide blades. In *International Heat Transfer Conference Digital Library*. Begel House Inc.
- [128] Saffman, P. G. (1965). The lift on a small sphere in a slow shear flow. *Journal of Fluid Mechanics*, 22(02):385.
- [129] Saffman, P. G. (1968). The lift on a small sphere in a slow shear flow - Corrigendum.
- [130] Schatz, M. and Eberle, T. (2014). Experimental study of steam wetness in a model steam turbine rig: presentation of results and comparison with computational fluid dynamics data. *Proceedings of the Institution of Mechanical Engineers, Part A: Journal of Power and Energy*, 228(2):129–142.
- [131] Schlichting, H. (1960a). *Boundary layer theory*, volume 960. Springer.
- [132] Schlichting, H. (1960b). Some developments in boundary layer research in the past thirty years. *The Aeronautical Journal*, 64(590):64–80.
- [133] Schrage, R. W. (1953). *A theoretical study of interphase mass transfer*. Columbia University Press.
- [134] Schraub, F. A. and Kline, S. J. (1965). A study of the structure of the turbulent boundary layer with and without longitudinal pressure gradients. Technical report, STANFORD UNIV CA THERMOSCIENCES DIV.
- [135] Schwendiman, L. and Postma, A. (1962). Turbulent deposition in sampling lines. *Rapport technique Tech. Inf. Div. TID-7628, USAEC*, 118.

- [136] Sehmel, G. A. (1968). Aerosol Deposition from Turbulent Airstreams in Vertical Conduits. Technical report, Battelle-Northwest, Richland, Wash. Pacific Northwest Lab.
- [137] Skillings, S. A., Moore, M. J., Walters, P. T., and Jackson, R. (1989). A reconsideration of wetness loss in LP steam turbines. In *Technology of turbine plant operating with wet steam*, pages 171–177.
- [138] Slater, S., Leeming, A., and Young, J. (2003). Particle deposition from two-dimensional turbulent gas flows. *International Journal of Multiphase Flow*, 29(5):721–750.
- [139] Smith, A. (1965). The influence of moisture on the efficiency of a one-third scale model low pressure steam turbine. In *Proceedings of the Institution of Mechanical Engineers, Conference Proceedings*, volume 180, pages 39–49. SAGE Publications Sage UK: London, England.
- [140] Smith Jr, L. (1966). Wake dispersion in turbomachines. *Journal of Basic Engineering*, 88(3):688–690.
- [141] Smits, A. J., Young, S., and Bradshaw, P. (1979). The effect of short regions of high surface curvature on turbulent boundary layers. *Journal of fluid mechanics*, 94(2):209–242.
- [142] Spalart, P. and Allmaras, S. (1992). A one-equation turbulence model for aerodynamic flows. In *30th aerospace sciences meeting and exhibit*, page 439.
- [143] Starzmann, J. (2016). Wet Steam Flow and Wetness Losses in Steam Turbines.
- [144] Starzmann, J., Casey, M. M., Mayer, J. F., and Sieverding, F. (2014). Wetness loss prediction for a low pressure steam turbine using computational fluid dynamics. *Proceedings of the Institution of Mechanical Engineers, Part A: Journal of Power and Energy*, 228(2):216–231.
- [145] Starzmann, J., Hughes, F. R., Schuster, S., White, A. J., Halama, J., Hric, V., Kolovratník, M., Lee, H., Sova, L., Št’astný, M., et al. (2018a). Results of the international wet steam modeling project. *Proceedings of the Institution of Mechanical Engineers, Part A: Journal of Power and Energy*, 232(5):550–570.
- [146] Starzmann, J., Hughes, F. R., Schuster, S., White, A. J., Halama, J., Hric, V., Kolovratník, M., Lee, H., Sova, L., Št’astný, M., Grübel, M., Schatz, M., Vogt, D. M., Patel, Y., Patel, G., Turunen-Saaresti, T., Gribin, V., Tishchenko, V., Gavrilov, I., Kim, C., Baek, J., Wu, X., Yang, J., Dykas, S., Wróblewski, W., Yamamoto, S., Feng, Z., and Li, L. (2018b). Results of the international wet steam modeling project. *Proceedings of the Institution of Mechanical Engineers, Part A: Journal of Power and Energy*, 232(5):550–570.
- [147] Starzmann, J., Hughes, F. R., White, A. J., Grübel, M., and Vogt, D. M. (2017). Numerical investigation of boundary layers in wet steam nozzles. *Journal of Engineering for Gas Turbines and Power*, 139(1).
- [148] Starzmann, J., Kaluza, P., Casey, M. V., and Sieverding, F. (2013). On Kinematic Relaxation and Deposition of Water Droplets in the Last Stages of Low Pressure Steam Turbines. *Journal of Turbomachinery*, 136(7):071001–071001–10.

- [149] Steltz, W. G., Lee, P. K., and Lindsay, W. T. (1983). The verification of concentrated impurities in low-pressure steam turbines. *Journal of Engineering for Power*, 105(1):192–198.
- [150] Talanquer, V. (1997). A new phenomenological approach to gas–liquid nucleation based on the scaling properties of the critical nucleus. *The Journal of chemical physics*, 106(23):9957–9960.
- [151] Talbot, L., Cheng, R. K., Schefer, R. W., and Willis, D. R. (1980). Thermophoresis of particles in a heated boundary layer. *Journal of Fluid Mechanics*, 101(04):737.
- [152] Tolman, R. C. (1949). The effect of droplet size on surface tension. *The journal of chemical physics*, 17(3):333–337.
- [153] Valha, J. and Ryley, D. (1977). Optical studies of nucleation in high pressure steam. In *Proceedings of the ASME Conference on Condensation in high speed flows (Ed. AA Pouring)*, pages 27–42.
- [154] Volmer, M. and Weber, A. (1926). Keimbildung in übersättigten gebilden. *Zeitschrift für physikalische Chemie*, 119(1):277–301.
- [155] von Helmholtz, R. (1886). Untersuchungen über dämpfe und nebel, besonders über solche von lösungen. *Annalen der Physik*, 263(4):508–543.
- [156] Von Karman, T. (1934). Turbulence and skin friction. *Journal of the Aeronautical Sciences*, 1(1):1–20.
- [157] Walters, P. (1973). Optical measurement of water droplets in wet steam flows. *Heat and Fluid Flow in Steam and Gas Turbine Plant*, page 216.
- [158] Walters, P. (1980). Practical applications of inverting spectral turbidity data to provide aerosol size distributions. *Applied Optics*, 19(14):2353–2365.
- [159] Walters, P. (1985). Wetness and efficiency measurements in lp turbines with an optical probe as an aid to improving performance. In *1985 Joint Power Generation Conference: GT Papers*, pages V001T03A001–V001T03A001. American Society of Mechanical Engineers.
- [160] Walters, P. (1987). Wetness and efficiency measurements in lp turbines with an optical probe as an aid to improving performance.
- [161] Webster, D., DeGraaff, D., and Eaton, J. (1996a). Turbulence characteristics of a boundary layer over a swept bump. *Journal of Fluid Mechanics*, 323:1–22.
- [162] Webster, D., DeGraaff, D., and Eaton, J. (1996b). Turbulence characteristics of a boundary layer over a two-dimensional bump. *Journal of Fluid Mechanics*, 320:53–69.
- [163] Wells, A. and Chamberlain, A. (1967). Transport of small particles to vertical surfaces. *British Journal of Applied Physics*, 18(12):1793.
- [164] White, A. J. (1992). *Condensation in steam turbine cascades*. PhD thesis, University of Cambridge.

- [165] Wilkinson, D. (1969). Paper 35: Stability, convergence, and accuracy of two-dimensional streamline curvature methods using quasi-orthogonals. In *Proceedings of the Institution of Mechanical Engineers, Conference Proceedings*, volume 184, pages 108–126. SAGE Publications Sage UK: London, England.
- [166] Williams, J. and Young, J. B. (2007). Movement of Deposited Water on Turbomachinery Rotor Blade Surfaces. *Journal of Turbomachinery*, 129(2):394.
- [167] Williams, J. C. (2003). *Water injection in jet engines*. PhD thesis, University of Cambridge.
- [168] Wilson, C. T. R. (1897). Xi. condensation of water vapour in the presence of dust-free air and other gases. *Philosophical Transactions of the Royal Society of London. Series A, Containing Papers of a Mathematical or Physical Character*, (189):265–307.
- [169] Wölk, J., Viisanen, Y., and Strey, R. (2000). Homogeneous nucleation rates for water. In *AIP Conference Proceedings*, volume 534, pages 7–10. American Institute of Physics.
- [170] Wood, N. B. (1973). Flow unsteadiness and turbulence measurements in the low-pressure cylinder of a 500 MW steam turbine. In *Proceedings of IMechE Conference, London*, volume 3. Mechanical Engineering Publications Bury St Edmunds and London.
- [171] Wood, N. B. (1981). A simple method for the calculation of turbulent deposition to smooth and rough surfaces. *Journal of aerosol Science*, 12(3):275–290.
- [172] Wu, C. H. (1952). general through flow theory of fluid flow with subsonic or supersonic velocity in turbo-machines of arbitrary hub and casing shapes', nacatn 2302, 1951. *Google Scholar*.
- [173] Wu, Z. and Young, J. B. (2003). Deposition of Small Particles From Turbulent Flows. In *Heat Transfer Summer Conference*, volume 36940, pages 731–741.
- [174] Wu, Z. and Young, J. B. (2012). The deposition of small particles from a turbulent air flow in a curved duct. *International Journal of Multiphase Flow*, 44:34–47.
- [175] Wyslouzil, B. E. and Wölk, J. (2016). Overview: Homogeneous nucleation from the vapor phase—the experimental science. *The Journal of chemical physics*, 145(21):211702.
- [176] Yamamoto, S. (2000). Numerical study of nonequilibrium condensation in unsteady transonic viscous flow problem. In *European Congress on Computational Methods in Applied Science and Engineering, ECCOMAS, Barcelona*.
- [177] Yau, K. K. and Young, J. B. (1987). The Deposition of Fog Droplets on Steam Turbine Blades by Turbulent Diffusion. *Journal of Turbomachinery*, 109(3):429–435.
- [178] Yellot, J. and Holland, C. (1937). The condensation of flowing steam: Condensation in diverging nozzles. *Engineering, Lond*, 143:647–703.
- [179] Young, J. (1984). Semi-analytical techniques for investigating thermal non-equilibrium effects in wet steam turbines. *International journal of heat and fluid flow*, 5(2):81–91.
- [180] Young, J. (1995). The fundamental equations of gas-droplet multiphase flow. *International journal of multiphase flow*, 21(2):175–191.

- [181] Young, J. and Leeming, A. (1997). A theory of particle deposition in turbulent pipe flow. *Journal of Fluid Mechanics*, 340:129–159.
- [182] Young, J. and Yau, K. (1988). The inertial deposition of fog droplets on steam turbine blades. *Journal of turbomachinery*, 110(2):155–162.
- [183] Young, J., Yau, K., and Walters, P. (1988). Fog droplet deposition and coarse water formation in low-pressure steam turbines: a combined experimental and theoretical analysis. *Journal of Turbomachinery*, 110(2):163–172.
- [184] Young, J. B. (1982). The Spontaneous Condensation of Steam in Supersonic nozzles. *Physico Chemical hydrodynamics*, 3:57–82.
- [185] Young, J. B. (1991). The Condensation and Evaporation of Liquid Droplets in a Pure Vapour at Arbitrary Knudsen Number. *International Journal of Heat and Mass Transfer*, 34:1649–1661.
- [186] Young, J. B. (1992). Two-dimensional, nonequilibrium, wet-steam calculations for nozzles and turbine cascades. *ASME J. Turbomach*, 114(3):569–579.
- [187] Zeldovich, Y. (1942). To the new phase formation theory. cavitation. *Zh Eksp Teor Fiz*, 12:525–538.

Appendix A

Scaling blade pressure curves based on blade loading

$$T = m(r_{LE}v_{\theta,LE} - r_{TE}v_{\theta,TE}) \quad (\text{A.1})$$

$$F(r_{LE} + r_{TE})/2 = m(r_{LE}v_{\theta,LE} - r_{TE}v_{\theta,TE}) \quad (\text{A.2})$$

$$\Delta pl(r_{LE} + r_{TE})/2 = \rho v_{x,LE} p(r_{LE}v_{\theta,LE} - r_{TE}v_{\theta,TE}) \quad (\text{A.3})$$

$$\text{assumption } r_{LE} \approx r_{TE} \approx r_{avg} \quad (\text{A.4})$$

$$\Delta plr = \rho v_{x,LE} p r (v_{\theta,LE} - v_{\theta,TE}) \quad (\text{A.5})$$

$$\Delta pl = \rho v_{x,LE} p (v_{\theta,LE} - v_{\theta,TE}) \quad (\text{A.6})$$

$$\Delta p = \rho v_{x,LE} \frac{p}{l} (v_{\theta,LE} - v_{\theta,TE}) \quad (\text{A.7})$$

$$\text{assumption } l = v_{x,avg} \Delta t, \Delta t = t_{TE} - t_{LE} \quad (\text{A.8})$$

$$\Delta p = \rho v_{x,LE} \frac{p}{v_{x,avg} \Delta t} (v_{\theta,LE} - v_{\theta,TE}) \quad (\text{A.9})$$

$$\Delta p = \rho v_{x,LE} \frac{p}{\Delta t} \left(\frac{v_{x,LE} \tan \beta_{LE}}{v_{x,avg}} - \frac{v_{x,TE} \tan \beta_{TE}}{v_{x,avg}} \right) \quad (\text{A.10})$$

$$\text{assumption } v_{LE} \approx v_{TE} \approx v_{avg} \quad (\text{A.11})$$

$$\Delta p = \rho v_{x,LE} \frac{p}{\Delta t} \left(\frac{v_{x,LE} \tan \beta_{LE}}{v_{x,avg}} - \frac{v_{x,TE} \tan \beta_{TE}}{v_{x,avg}} \right) \quad (\text{A.12})$$

$$(\text{A.13})$$

This ends up in:

$$\Delta p = \rho p \frac{v_{x,LE}}{\Delta t_{avg}} (\tan \beta_{LE} - \tan \beta_{TE}) \quad (\text{A.14})$$

Appendix B

Wake functional form derivation

In a model with multiple blade rows, in order to find the cumulative efficiency distribution at the final blade row $v_T(\psi)$, we need to know the functional form of the per-blade-row efficiency loss function $\eta(\psi)$. Since $\eta(\psi)$ is weakly increasing around zero, we take the inverse of it¹, and focus on the efficiency loss function $\xi(\psi) = 1 - \eta(\psi)$.

B.1 Linear function

Suppose that:

$$\xi_L(\psi) = \bar{\xi} \frac{1}{b} \left(1 - \frac{|\psi|}{b} \right), \quad \text{for } |\psi| \leq b. \quad (\text{B.1})$$

¹Since distribution functions usually have most of their mass around the centre and not away from it.

Let's verify that the expected value is equal to $\bar{\xi}$:

$$\mathbb{E}[\xi_L(\psi)] \equiv \mu_\xi = \mathbb{E}\left[\bar{\xi} \frac{1}{b} \left(1 - \frac{|\psi|}{b}\right)\right] \quad (\text{B.2})$$

$$= \bar{\xi} \int_{-b}^b \left(\frac{1}{b} - \frac{|\psi|}{b^2}\right) \cdot \underbrace{PDF(\psi)}_{=1} d\psi \quad (\text{B.3})$$

$$= 2\bar{\xi} \int_0^b \left(\frac{1}{b} - \frac{\psi}{b^2}\right) d\psi \quad (\text{B.4})$$

$$= 2\bar{\xi} \left[\frac{\psi}{b} - \frac{\psi^2}{2b^2}\right]_0^b \quad (\text{B.5})$$

$$= 2\bar{\xi} \left[1 - \frac{1}{2}\right] \quad (\text{B.6})$$

$$= \bar{\xi} \quad (\text{B.7})$$

Parameter b of the linear function is found by matching the Gaussian variance:

$$Var[\xi_L(\psi)] \equiv \sigma_\xi = Var\left[\bar{\xi} \frac{1}{b} \left(1 - \frac{|\psi|}{b}\right)\right] \quad (\text{B.8})$$

$$= \mathbb{E}\left[\left(\bar{\xi} \frac{1}{b} \left(1 - \frac{|\psi|}{b}\right)\right)^2\right] - \mu_\xi^2 \quad (\text{B.9})$$

$$= \bar{\xi}^2 \int_{-b}^b \left(\frac{1}{b} - \frac{|\psi|}{b^2}\right)^2 \cdot \underbrace{PDF(\psi)}_{=1} d\psi - \bar{\xi}^2 \quad (\text{B.10})$$

$$= 2\bar{\xi}^2 \int_0^b \left(\frac{1}{b} - \frac{\psi}{b^2}\right)^2 d\psi - \bar{\xi}^2 \quad (\text{B.11})$$

$$= 2\bar{\xi}^2 \int_0^b \frac{1}{b^2} \left(1 - \frac{2\psi}{b} + \frac{\psi^2}{b^2}\right) d\psi - \bar{\xi}^2 \quad (\text{B.12})$$

$$= 2\bar{\xi}^2 \frac{1}{b^2} \left[b - \frac{b^2}{b} + \frac{b^3}{3b^2}\right]_0^b - \bar{\xi}^2 \quad (\text{B.13})$$

$$= \frac{2\bar{\xi}^2}{3b} - \bar{\xi}^2 \quad (\text{B.14})$$

$$= \bar{\xi}^2 \left(\frac{2}{3b} - 1\right) \quad (\text{B.15})$$

Now impose:

$$\text{Var}[\xi_L(\psi)] = \text{Var}[\xi_G(\psi)] \quad (\text{B.16})$$

$$\Rightarrow \bar{\xi}^2 \left(\frac{2}{3b} - 1 \right) = \bar{\xi}^2 \left(\frac{1}{2\sigma\sqrt{\pi}} - 1 \right) \quad (\text{B.17})$$

$$\frac{2}{3b} = \frac{1}{2\sigma\sqrt{\pi}} \quad (\text{B.18})$$

$$\Rightarrow b = \frac{4\sqrt{\pi}\sigma}{3} \quad (\text{B.19})$$

B.2 Quadratic function

Suppose that:

$$\xi_Q(\psi) = \bar{\xi} (d - e\psi^2), \text{ for } |\psi| \leq \sqrt{\frac{d}{e}} := c. \quad (\text{B.20})$$

Here we have two parameters to find - d and e - so we have to use both the mean and the variance moment-matching equation.

Let's first use the mean equation:

$$\mathbb{E}[\xi_Q(\psi)] \equiv \mu_{\xi} = \mathbb{E} [\bar{\xi} (d - e\psi^2)] \quad (\text{B.21})$$

$$= \bar{\xi} \int_{-c}^c (d - e\psi^2) \cdot \underbrace{\text{PDF}(\psi)}_{=1} d\psi \quad (\text{B.22})$$

$$= 2\bar{\xi} \int_0^c (d - e\psi^2) d\psi \quad (\text{B.23})$$

$$= 2\bar{\xi} \left[d\psi - \frac{e\psi^3}{3} \right]_0^c \quad (\text{B.24})$$

$$= 2\bar{\xi} \left[d\sqrt{\frac{d}{e}} - \frac{e}{3} \frac{d^{3/2}}{e} \right] \quad (\text{B.25})$$

$$= \bar{\xi} \frac{4d}{3} \sqrt{\frac{d}{e}} \quad (\text{B.26})$$

We impose that the expected value of $\xi_Q(\psi)$ must be equal to $\bar{\xi}$, so:

$$\bar{\xi} \frac{4d}{3} \sqrt{\frac{d}{e}} = \bar{\xi} \quad (\text{B.27})$$

$$\implies \frac{4d}{3} \sqrt{\frac{d}{e}} = 1 \quad (\text{B.28})$$

$$\frac{16}{9} d^3 = e \quad (\text{B.29})$$

Using the equation above, the initial function can be rewritten only in terms of the parameter d :

$$\xi_Q(\psi) = \bar{\xi} d \left(1 - \left(\frac{4}{3} d \right)^2 \psi^2 \right) \quad (\text{B.30})$$

Finally, use the variance equation and impose that it needs to be equal to the Gaussian variance, in order to pin down the parameter d :

$$\text{Var}[\xi_Q(\psi)] \equiv \sigma_\xi = \text{Var} \left[\bar{\xi} d \left(1 - \left(\frac{4}{3}d \right)^2 \psi^2 \right) \right] \quad (\text{B.31})$$

$$= \mathbb{E} \left[\left(\bar{\xi} d \left(1 - \left(\frac{4}{3}d \right)^2 \psi^2 \right) \right)^2 \right] - \mu_\xi^2 \quad (\text{B.32})$$

$$= \bar{\xi}^2 d^2 \int_{-c}^c \left(1 - \left(\frac{4}{3}d \right)^2 \psi^2 \right)^2 \cdot \underbrace{\text{PDF}(\psi)}_{=1} d\psi - \bar{\xi}^2 \quad (\text{B.33})$$

$$= 2\bar{\xi}^2 d^2 \int_0^c \left(1 - \left(\frac{4}{3}d \right)^2 \psi^2 \right)^2 d\psi - \bar{\xi}^2 \quad (\text{B.34})$$

$$= \left\{ \text{Change of variable, define: } z = \frac{4a}{3}\psi \implies d\psi = \frac{3}{4a}dz \implies c \rightarrow 1 \right\} \quad (\text{B.35})$$

$$= 2\bar{\xi}^2 d^2 \int_0^1 (1-z^2)^2 \frac{3}{4a} dz - \bar{\xi}^2 \quad (\text{B.36})$$

$$= \frac{3\bar{\xi}^2 d}{2} \int_0^1 (1-2z^2+z^4) dz - \bar{\xi}^2 \quad (\text{B.37})$$

$$= \frac{3\bar{\xi}^2 d}{2} \left[z - \frac{2}{3}z^3 + \frac{z^5}{5} \right]_0^1 - \bar{\xi}^2 \quad (\text{B.38})$$

$$= \frac{4\bar{\xi}^2 d}{5} - \bar{\xi}^2 \quad (\text{B.39})$$

$$= \bar{\xi}^2 \left(\frac{4}{5}d - 1 \right) \quad (\text{B.40})$$

Now impose:

$$\text{Var}[\xi_Q(\psi)] = \text{Var}[\xi_G(\psi)] \quad (\text{B.41})$$

$$\implies \bar{\xi}^2 \left(\frac{4}{5}d - 1 \right) = \bar{\xi}^2 \left(\frac{1}{2\sigma\sqrt{\pi}} - 1 \right) \quad (\text{B.42})$$

$$\frac{4}{5}d = \frac{1}{2\sigma\sqrt{\pi}} \quad (\text{B.43})$$

$$\implies d = \frac{5}{8\sqrt{\pi}\sigma} \quad \text{and} \quad e = \frac{16}{9} \left(\frac{5}{8\sqrt{\pi}\sigma} \right)^3, \quad \text{for } |\psi| \leq \sqrt{\frac{d}{e}}. \quad (\text{B.44})$$

B.3 Step function

Suppose that:

$$\xi_L(\psi) = \begin{cases} \bar{\xi} \cdot \frac{1}{2a} & |\psi| \leq a \\ 0 & \text{otherwise.} \end{cases} \quad (\text{B.45})$$

Verify that the mean of $\xi_L(\psi)$ is equal to $\bar{\xi}$:

$$\mathbb{E}[\xi_L(\psi)] \equiv \mu_{\xi} = \mathbb{E}\left[\bar{\xi} \frac{1}{2a}\right] \quad (\text{B.46})$$

$$= \bar{\xi} \int_{-a}^a \bar{\xi} \frac{1}{2a} \cdot \underbrace{\text{PDF}(\psi)}_{=1} d\psi \quad (\text{B.47})$$

$$= 2\bar{\xi} \int_0^a \frac{1}{2a} d\psi \quad (\text{B.48})$$

$$= 2\bar{\xi} \left[\frac{\psi}{2a} \right]_0^a \quad (\text{B.49})$$

$$= \bar{\xi} \quad (\text{B.50})$$

Now calculate the variance and find parameter a such that the variance of $\xi_L(\psi)$ is equal to the Gaussian variance:

$$\text{Var}[\xi_L(\psi)] \equiv \sigma_{\xi} = \text{Var}\left[\bar{\xi} \frac{1}{2a}\right] \quad (\text{B.51})$$

$$= \mathbb{E}\left[\left(\bar{\xi} \frac{1}{2a}\right)^2\right] - \mu_{\xi}^2 \quad (\text{B.52})$$

$$= \int_{-a}^a \frac{\bar{\xi}^2}{4a^2} \cdot \underbrace{\text{PDF}(\psi)}_{=1} d\psi - \bar{\xi}^2 \quad (\text{B.53})$$

$$= \left[\frac{\bar{\xi}^2}{4a^2} \psi \right]_{-a}^a - \bar{\xi}^2 \quad (\text{B.54})$$

$$= \frac{\bar{\xi}^2}{2a} - \bar{\xi}^2 \quad (\text{B.55})$$

$$= \bar{\xi} \left(\frac{1}{2a} - 1 \right) \quad (\text{B.56})$$

Now equate with Gaussian variance:

$$\text{Var}[\xi_L(\psi)] = \text{Var}[\xi_G(\psi)] \quad (\text{B.57})$$

$$\implies \bar{\xi} \left(\frac{1}{2a} - 1 \right) = \bar{\xi}^2 \left(\frac{1}{2\sigma\sqrt{\pi}} - 1 \right) \quad (\text{B.58})$$

$$\frac{1}{2a} = \frac{1}{2\sigma\sqrt{\pi}} \quad (\text{B.59})$$

$$\implies a = \sigma\sqrt{\pi}. \quad (\text{B.60})$$

B.4 Summary of solved functions

1. Gaussian:

$$\xi_G(\psi) = \bar{\xi} \frac{1}{\sqrt{2\pi}\sigma} \cdot \exp\left(-\frac{1}{2} \frac{\psi^2}{\sigma^2}\right). \quad (\text{B.61})$$

2. Linear:

$$\xi_L(\psi) = \bar{\xi} \frac{3}{4\sqrt{\pi}\sigma} \left(1 - \frac{3|\psi|}{4\sqrt{\pi}\sigma} \right), \text{ for } |\psi| \leq \frac{4\sqrt{\pi}\sigma}{3}. \quad (\text{B.62})$$

3. Quadratic:

$$\xi_Q(\psi) = \bar{\xi} \left(\frac{5}{8\sqrt{\pi}\sigma} - \frac{16}{9} \left(\frac{5}{8\sqrt{\pi}\sigma} \right)^3 \psi^2 \right), \text{ for } |\psi| \leq \frac{\sigma\sqrt{\pi}}{30}. \quad (\text{B.63})$$

4. Step:

$$\xi_S(\psi) = \begin{cases} \bar{\xi} \cdot \frac{1}{2\sigma\sqrt{\pi}} & |\psi| \leq \sigma\sqrt{\pi} \\ 0 & \text{otherwise.} \end{cases} \quad (\text{B.64})$$

Appendix C

Drag coefficient expressions

Drag coefficient can be expressed as a function of Reynolds number. Langmuir's empirical drag coefficient relationship [88], often used in inertial deposition models (e.g., [54], [182]), provides good agreement with experiment, according to [42], and ensures the drag coefficient converges to the Stokes solution¹ at low Reynolds numbers.:

$$C_D = \frac{24}{Re} \cdot \Phi^{-1} = \frac{24}{Re} \left(1 + 0.197 Re^{0.63} + 0.00026 Re^{1.38} \right) \quad (C.1)$$

Morsi and Alexander [102] proposed a more detailed, composite formula for drag coefficient:

$C_D = 24/Re$	$Re \leq 0.1$	(C.2)
$C_D = 22.73/Re + 0.0903/Re^2 + 3.69$	$0.1 \leq Re \leq 1.0$	
$C_D = 29.1667/Re - 3.8889/Re^2 + 1.222$	$1.0 \leq Re \leq 10.0$	
$C_D = 46.5/Re - 116.67/Re^2 + 0.6167$	$10.0 \leq Re \leq 100.0$	
$C_D = 98.33/Re - 2778/Re^2 + 0.3644$	$100.0 \leq Re \leq 1000.0$	
$C_D = 148.62/Re - 4.75 \times 10^4/Re^2 + 0.357$	$1000.0 \leq Re \leq 5000.0$	
$C_D = -490.546/Re + 57.87 \times 10^4/Re^2 + 0.46$	$5000.0 \leq Re \leq 10000.0$	
$C_D = -1662.5/Re + 5.4167 \times 10^6/Re^2 + 0.5191$	$10000.0 \leq Re \leq 50000.0$	

where the experimental drag results were divided into a number of smaller regions and fitted with polynomials, improving the drag coefficient prediction. Considering the size of the droplets, the Reynolds number is likely to stay under $Re = 100$ for nucleated droplets, and under $Re = 1000$ for coarse water droplets. Both approaches are valid for $Re < 50000$,

¹Laminar viscous drag around a sphere at low Reynolds numbers yields $C_D = 24/Re$.

however, [95] reported better match with experimental data when using the composite formula, hence why this approach is adopted.

Appendix D

Correction for non-continuum gas effects

The derivation of Stokes law depends on the no-slip assumption, corresponding to continuum flow, which is no longer correct as the flow approaches free molecular regime and Knudsen number increases. Since nucleated droplets have a diameter well below the nanometre mark, drag coefficient deviation for a small spherical droplets needs to be taken into consideration. Non-continuum gas effects are accounted for using the Cunningham correction factor [28], with coefficients from [29].

$$C_C = 1 + \text{Kn} \cdot \left[1.257 + 0.4 \exp\left(-\frac{1.1}{\text{Kn}}\right) \right] \quad (\text{D.1})$$

Composite formula proposed by [54] is used to determine the force on an assumed constantly spherical droplet, including the drag correction for small droplets and rarefied gas effects, transforming eq. 4.2 into:

$$\mathbf{F}_D = \frac{3\pi d \mu_g (\mathbf{v}_g - \mathbf{v}_l)}{[\Phi_D(\text{Re}) + 2.7\text{Kn}]}, \quad \Phi_D = \frac{24}{\text{Re}} C_D^{-1} \quad (\text{D.2})$$

Inertial particle relaxation time from eq. 4.6 is corrected and transforms into:

$$\tau_d = \frac{\rho_l d^2}{18 \mu_g} [\Phi_D(\text{Re}) + 2.7\text{Kn}] \quad (\text{D.3})$$

In continuum flow conditions, where $\text{Kn} \ll 1$, with low Reynolds number, the denominator in eq. D.2 reduces to Stokes drag solution, $C_D = 24/\text{Re}$. Since τ_d in Stokes regime is independent of velocity slip, there is a linear relationship between velocity slip and drag force. Increasing the slip Reynolds number leads to deviations from that behaviour, which are

captured using either eq. C.1 or C.2. Equation D.2 reduces to the expression given by kinetic theory as Knudsen number becomes large ($\text{Kn} \gg 1$), and flow enters the free molecular regime.

Appendix E

Skin friction coefficient – CFD data

Table E.1

Re	α	C_f	p_1	Reynolds number variation				F_p
				T_1	$v_{g,1}$	p_2	T_2	
806185	0.00	0.001375	40969.92	376.45	88.17	17696.34	322.56	508.02
793359	0.00	0.001398	40970.25	397.83	90.69	17695.45	327.77	522.53
735465	0.00	0.001456	40970.95	417.74	92.93	17695.68	344.13	535.78
684612	0.00	0.001514	40971.63	437.64	95.11	17695.49	360.68	548.65
639678	0.00	0.001572	40973.02	457.55	97.20	17695.43	377.32	561.24
599358	0.00	0.001630	40974.31	477.46	99.26	17695.42	394.05	573.55
562754	0.00	0.001687	40975.54	497.37	101.2	17695.42	410.83	585.62
							0.083175	83.153853

Table E.2

Re	α	C_f	p_1	Incidence angle (α) variation				F_p
				T_1	$v_{g,1}$	p_2	T_2	
806473	-10.00	0.001376	40940.31	376.38	89.58	17696.42	322.49	508.01
806185	0.00	0.001375	40969.92	376.45	88.17	17696.34	322.56	508.02
806291	5.00	0.001367	40962.82	376.43	88.50	17696.37	322.54	508.02
806354	10.00	0.001357	40940.15	376.38	89.58	17696.40	322.53	508.02
806519	20.00	0.001320	40842.82	376.17	94.06	17696.46	322.49	508.02
							0.063104	82.683223

Appendix F

Comparison of measured and calculated static pressure variation with total inlet temperature

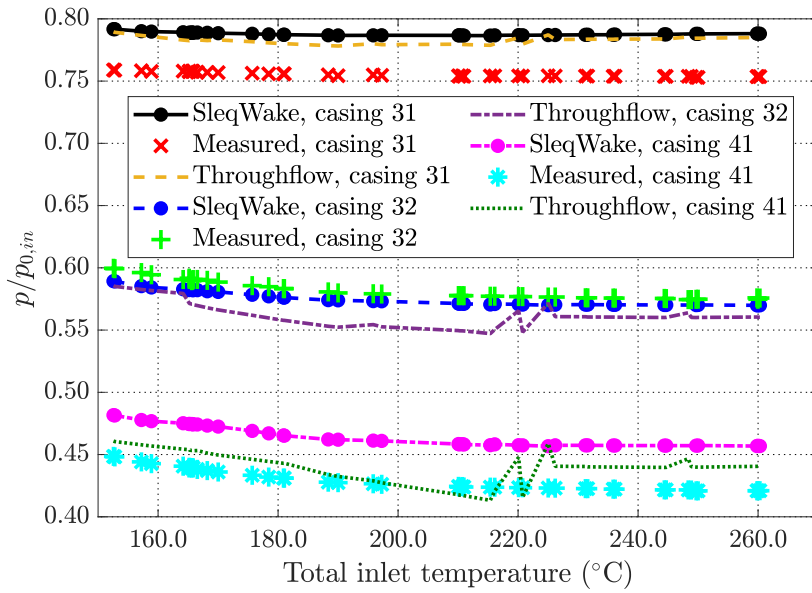


Fig. F.1 Static pressure at the casing on planes 31, 32, and 41, normalized with inlet total pressure.

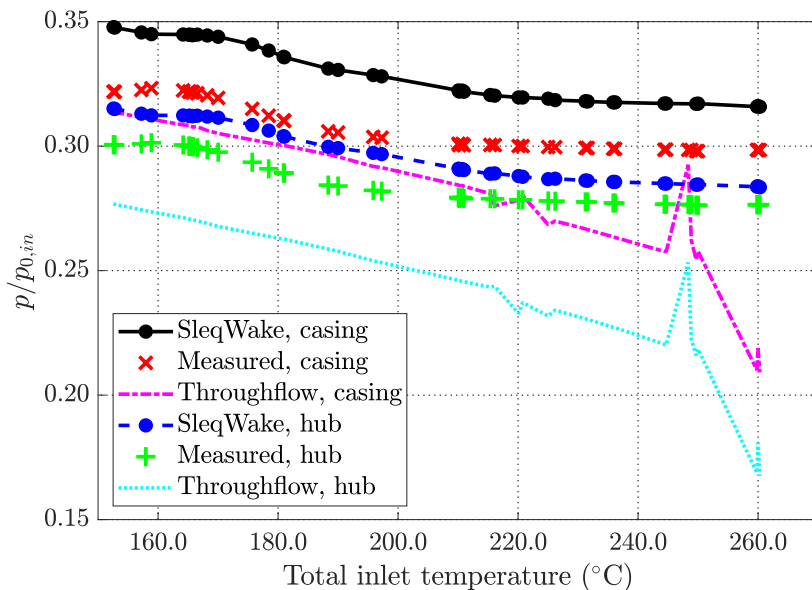


Fig. F.2 Static pressure at the hub and casing on plane 42, normalized with inlet total pressure.

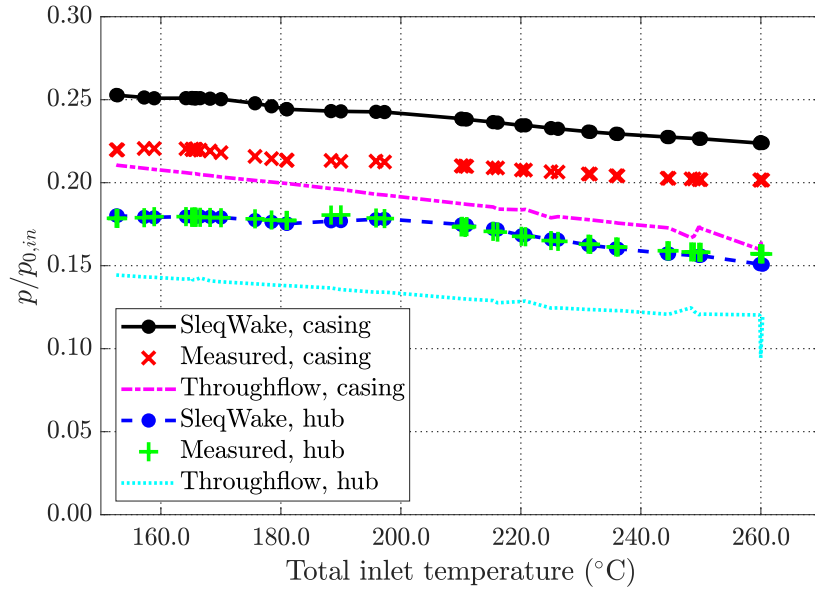


Fig. F.3 Static pressure at the hub and casing on plane 51, normalized with inlet total pressure.

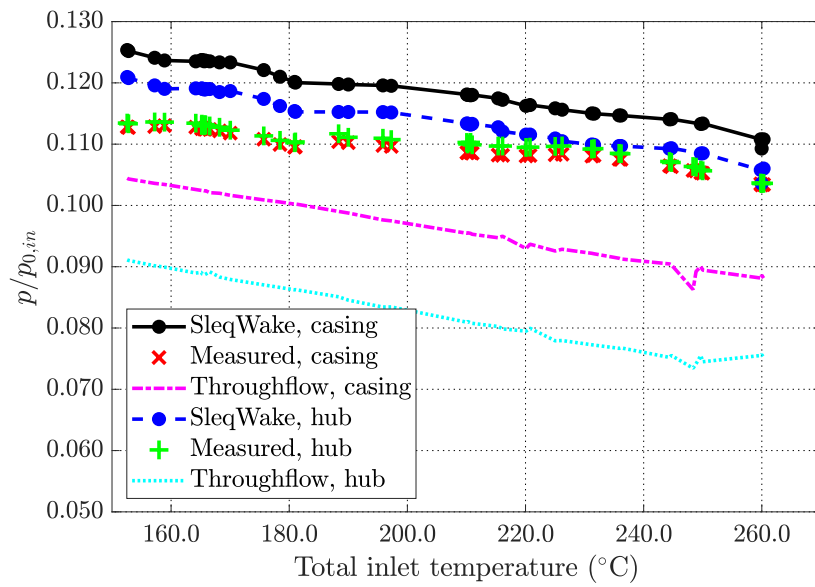


Fig. F.4 Static pressure at the hub and casing on plane 52, normalized with inlet total pressure.

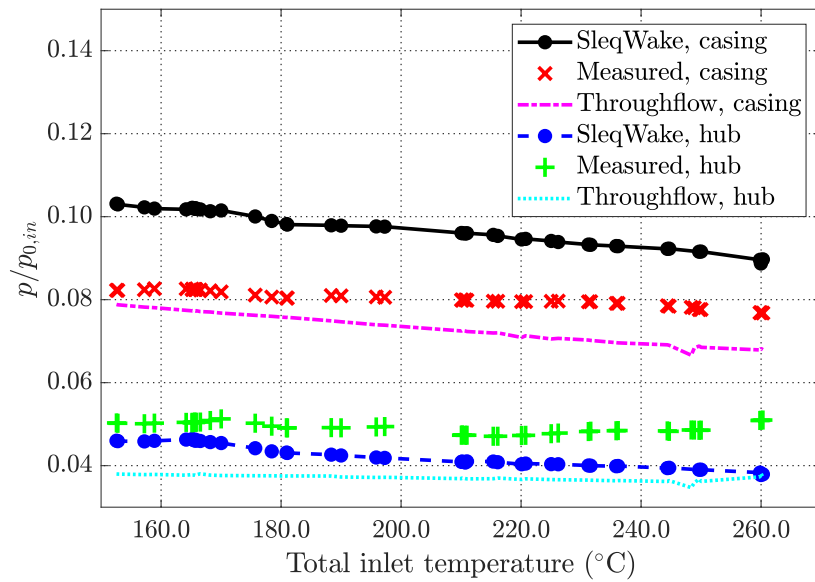


Fig. F.5 Static pressure at the hub and casing on plane 61, normalized with inlet total pressure.

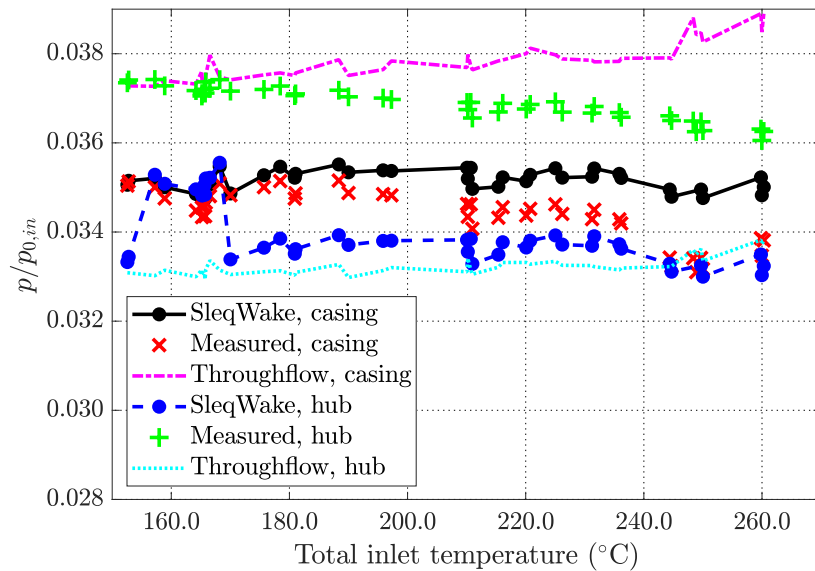
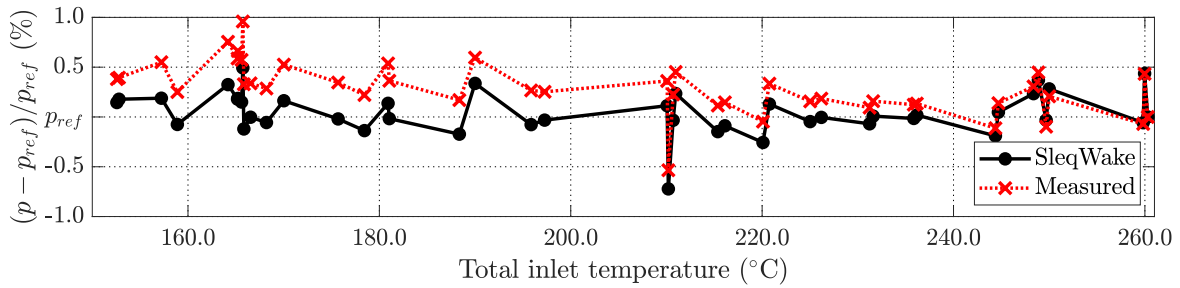
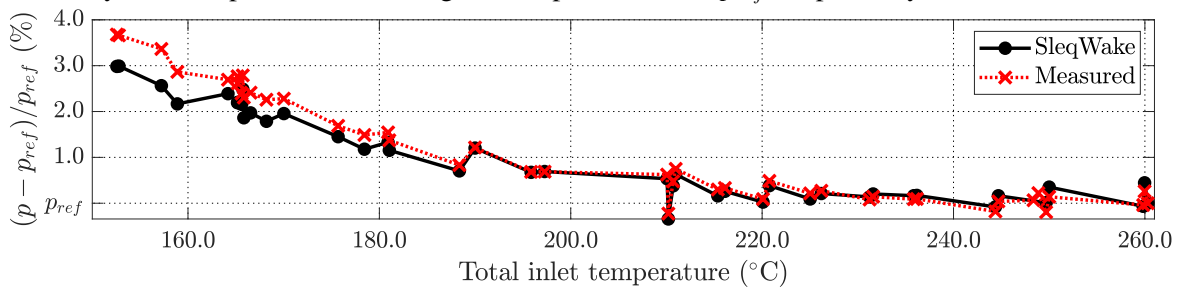


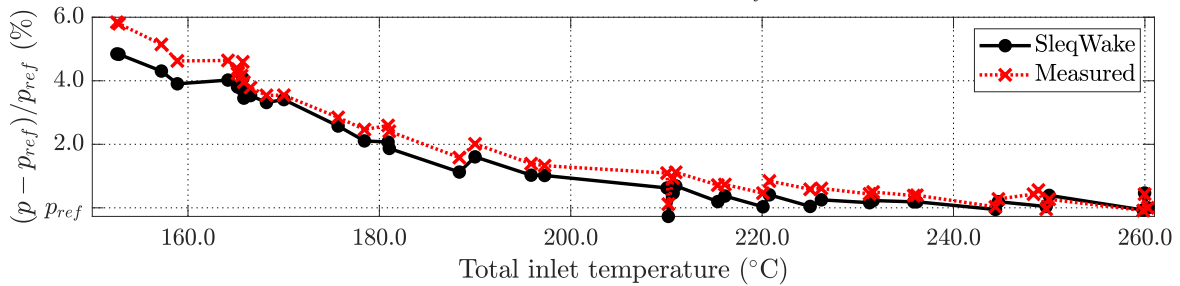
Fig. F.6 Static pressure at the hub and casing on plane 62, normalized with inlet total pressure.



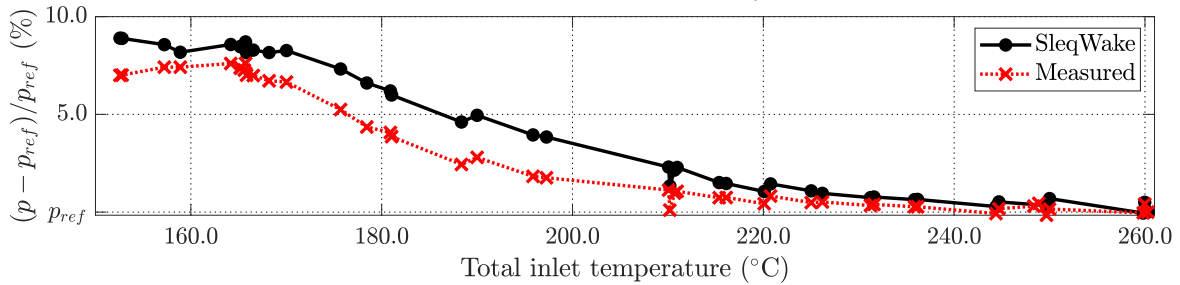
(a) Static pressure at the casing on plane 31 for a range of inlet total temperatures. Each curve is scaled by its static pressure for the highest temperature case, p_{ref} , respectively.



(b) Static pressure at the casing on plane 32 for a range of inlet total temperatures. Each curve is scaled by its static pressure for the highest temperature case, p_{ref} , respectively.

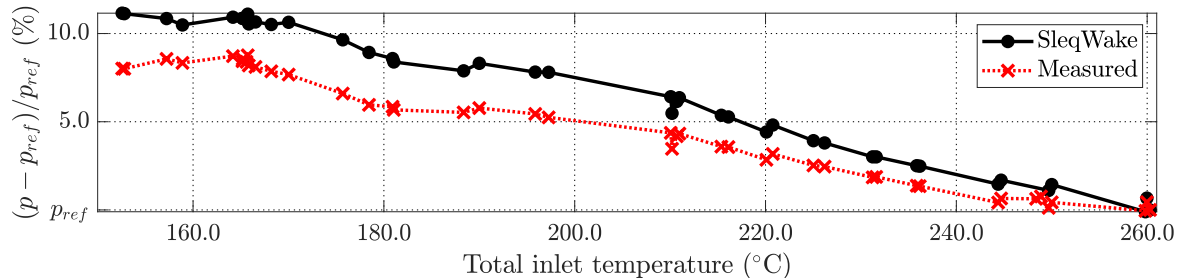


(c) Static pressure at the casing on plane 41 for a range of inlet total temperatures. Each curve is scaled by its static pressure for the highest temperature case, p_{ref} , respectively.

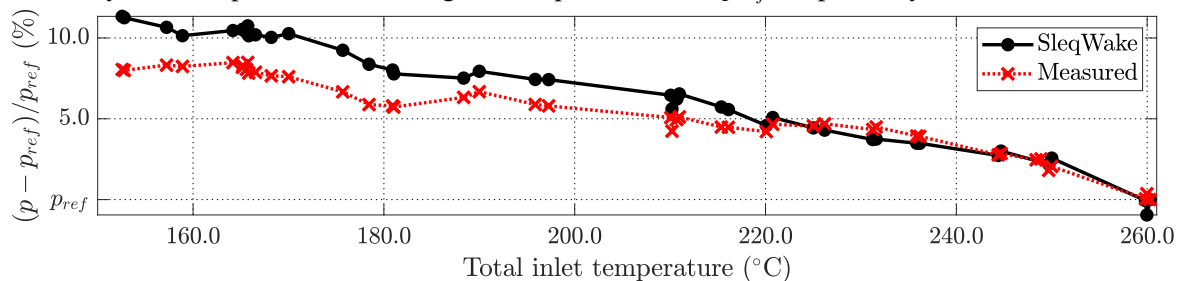


(d) Static pressure at the casing on plane 42 for a range of inlet total temperatures. Each curve is scaled by its static pressure for the highest temperature case, p_{ref} , respectively.

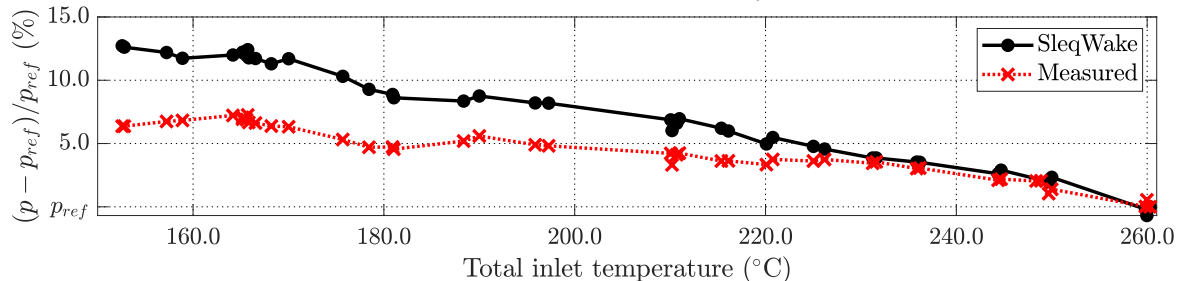
Fig. F.7 Casing static pressure variation with θ_{01} on planes 31 to 42.



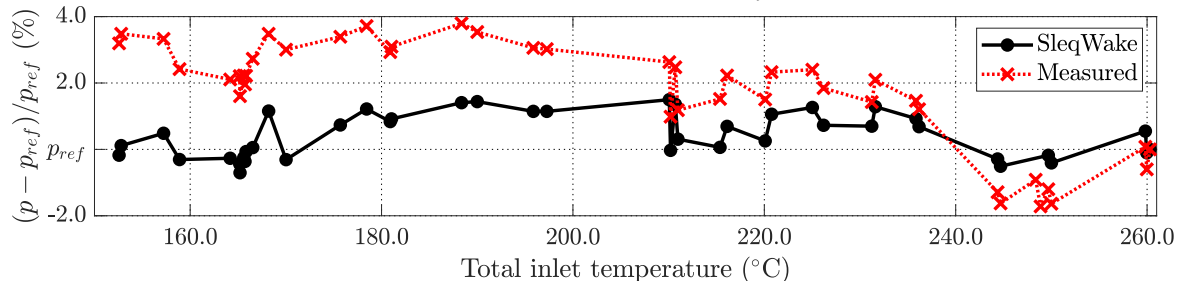
(a) Static pressure at the casing on plane 51 for a range of inlet total temperatures. Each curve is scaled by its static pressure for the highest temperature case, p_{ref} , respectively.



(b) Static pressure at the casing on plane 52 for a range of inlet total temperatures. Each curve is scaled by its static pressure for the highest temperature case, p_{ref} , respectively.

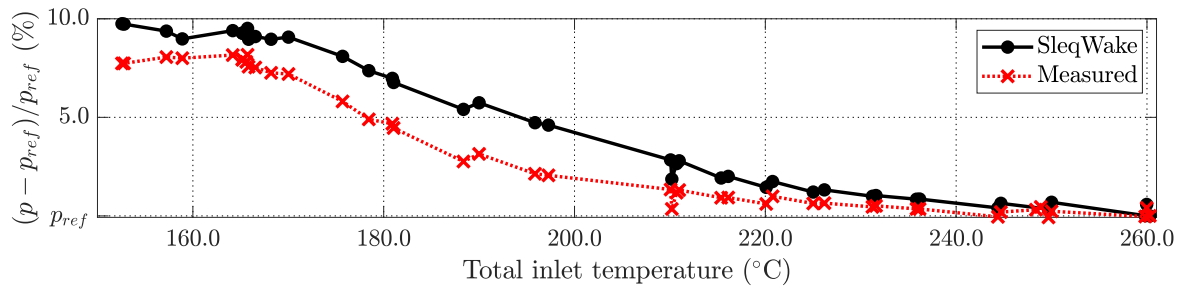


(c) Static pressure at the casing on plane 61 for a range of inlet total temperatures. Each curve is scaled by its static pressure for the highest temperature case, p_{ref} , respectively.

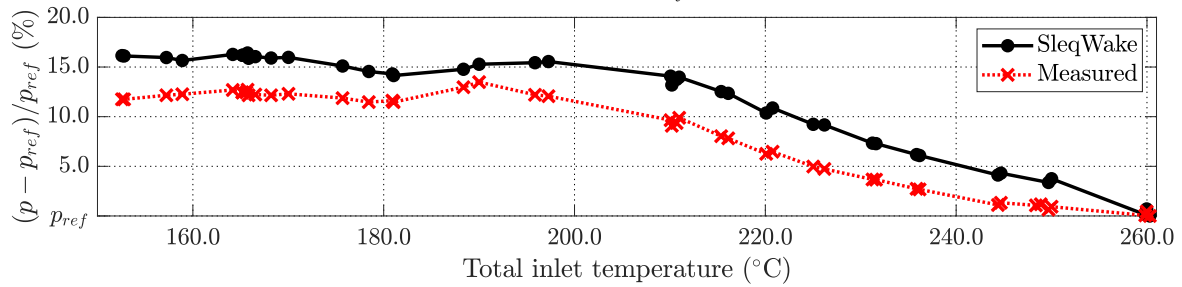


(d) Static pressure at the casing on plane 62 for a range of inlet total temperatures. Each curve is scaled by its static pressure for the highest temperature case, p_{ref} , respectively.

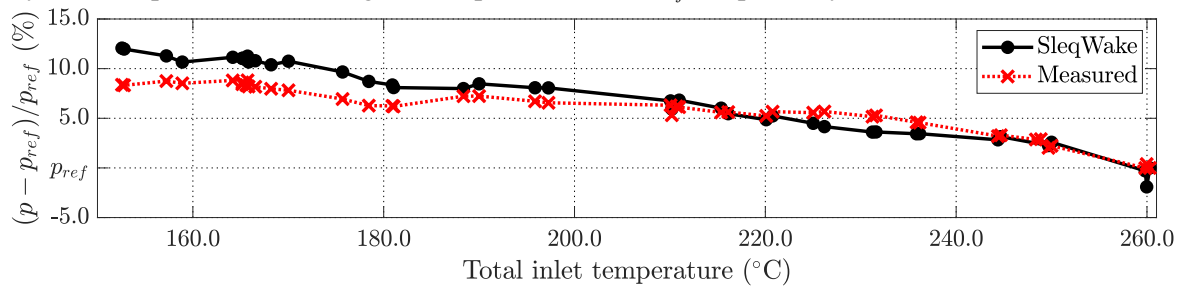
Fig. F.8 Casing static pressure variation with θ_{01} on planes 51 to 62.



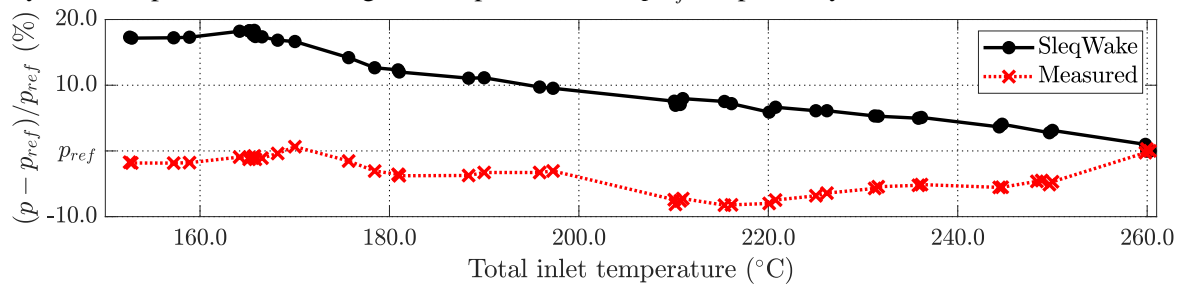
(a) Static pressure at the hub on plane 42 for a range of inlet total temperatures. Each curve is scaled by its static pressure for the highest temperature case, p_{ref} , respectively.



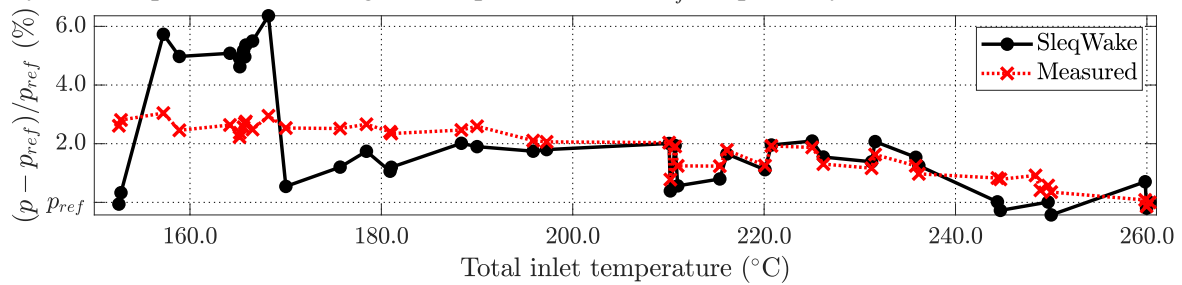
(b) Static pressure at the hub on plane 51 for a range of inlet total temperatures. Each curve is scaled by its static pressure for the highest temperature case, p_{ref} , respectively.



(c) Static pressure at the hub on plane 52 for a range of inlet total temperatures. Each curve is scaled by its static pressure for the highest temperature case, p_{ref} , respectively.



(d) Static pressure at the hub on plane 61 for a range of inlet total temperatures. Each curve is scaled by its static pressure for the highest temperature case, p_{ref} , respectively.



(e) Static pressure at the hub on plane 62 for a range of inlet total temperatures. Each curve is scaled by its static pressure for the highest temperature case, p_{ref} , respectively.

Fig. F.9 Hub static pressure variation with θ_{01} on planes 42 to 61.

